FERRIC PRECIPITATION AND METAL SORPTION IN BIOHYDROMETALLURGICAL PROCESSES

by

BABATUNDE OLADIPO

Thesis submitted in fulfilment of the requirements for the degree

Doctor of Engineering: Chemical Engineering

in the Faculty of Engineering & the Built Environment

at the

Cape Peninsula University of Technology

Cape Town, South Africa

October 2022

Supervisor

Prof. Tunde V Ojumu (PhD)

Professor and Head of Bioprocess and Environmental Engineering Research (BioPER)

Department of Chemical Engineering

Faculty of Engineering and the Built Environment

Cape Peninsula University of Technology

Bellville Campus, Cape Town

DECLARATION BY AUTHOR

I, **Babatunde Oladipo**, declare that the contents of this thesis are composed of my original work, and contain no material published or written by another person except where due reference has been made in the text. Furthermore, the thesis has not previously been submitted for academic examination towards any qualification and it represents my opinions and not necessarily those of the Cape Peninsula University of Technology.

October 17, 2022

Signed **Date**

ABSTRACT

Bioleaching is a well-known process for the efficient extraction of base metals from their mineral sulfides, and its long-term viability is reliant on the continual supply of ferric ions (Fe^{3+}). Due to the low solubility of ferric ions at higher pH levels, it tends to precipitate, resulting in the formation of ferric precipitates. The purpose of this work was to assess the impact of initial influent pH values on the surface properties of iron precipitate generated in a bio-oxidation operation and unravel the sorption mechanism by which these precipitates retain metal ions as it relates to a typical bioleach operation.

Ferrous ion bio-oxidation experiments mediated by mixed mesophilic culture were carried out in a continuous stirred tank reactor (CSTR) at pH levels of 1.7, 1.9, and 2.2 for 2 weeks at a fixed temperature of 35 °C and 550 rpm stirring speed. The results showed that the mass of iron precipitate generated increased as the initial solution pH increased. The X-ray powder diffraction (XRD) patterns of the recovered precipitates were identified as potassium jarosite (K-jarosite), $KFe_3(SO_4)_2(OH)_6$. The high-resolution X-ray photoelectron spectroscopy (XPS) analysis revealed the binding energies of elemental spectra assigned to Fe(III)–O, OH^-, SO_4^{2-}, and S^{2-} chemical states. The scanning electron microscopy (SEM) morphologies results are composed of aggregates of spherical/round and tabular particles. According to the energy-dispersive X-ray spectroscopy (EDS) results, a trend with a decrease in the total content of Fe, S, and K as the synthesis influent pH increased was observed. The Fourier transform infrared (FTIR) spectra of the precipitates showed the vibrational modes of SO_4^{2-}; H_2O and OH groups; and Fe–O vibrational mode in the jarosite. The thermogravimetric analysis (TGA) studies showed the dehydroxylation of K-jarosite and complete thermal decomposition of yavapaiite. Most importantly, the study revealed an increase in the surface area of the jarosites (from 8.32 – 11.00 m^2/g) and decrease in the pore size distribution (from 16.15 – 10.45 nm) as the influent solution pH increases from 1.7 – 2.2, confirming the mesoporous nature of the jarosite particles

The feasibility of improving typical biohydrometallurgical operations to minimize copper losses was investigated through the use of biogenic industrial iron precipitate for the

uptake of Cu(II) ions from aqueous solutions. The results show that the precipitate is highly heterogeneous. The surface area and average pore diameter were 4.74 m^2/g and 11.61 nm respectively. The Cu(II) ion adsorption can be described by both Freundlich and Langmuir adsorption isotherms, with a maximum adsorption capacity of 7.54 mg/g at 30 °C and 150 mg/L. The sorption followed pseudo-second-order kinetics, while the major presence of –OH and $–NH_2$ functional groups initiated a chemisorption mechanism. With estimated activation energy of 23.57 kJ/mol, the obtained thermodynamic parameters of $\Delta S°$ (0.034 – 0.050 kJ/mol K), $\Delta G°$ (8.37 – 10.64 kJ/mol), and $\Delta H°$ (20.07 – 23.81 kJ/mol) indicated the adsorption process was chemically favoured, non-spontaneous, and endothermic respectively.

The kinetics and sorption capacity of K-jarosite adsorption for copper ions from aqueous media were studied in relation to surface charge, surface area, and pore size. The point of zero charge of the jarosites was observed to be 2.14 and 2.37 for jarosite samples synthesized at pH 2.2 (Jar-2.2) and pH 1.7 (Jar-1.7) respectively. The results also demonstrated that jarosite could adsorb copper under both positively and negatively charged pH conditions, with more copper being adsorbed when the surface of the jarosite is more negatively charged (when the $pH_S > pH_{PZC}$). Jar-2.2 with a smaller particle size (higher surface area) gave the highest sorption capacity for copper as compared with Jar-1.7, under the same adsorption conditions. The mechanism of copper adsorption onto jarosite powder was by cation exchange and electrostatic attraction.

The results from this thesis may provide an insight into the management of biohydrometallurgical processes to minimize metal losses. Thus, the findings stated are applicable in the design and implementation of iron bio-oxidation, precipitation, and treatment of ferric precipitate residues.

DEDICATION

This thesis is dedicated to Jesus Christ, my Lord and Saviour, who is full of mercy and grace.

"Not that I am sufficient of myself to think of anything as being from myself, but my sufficiency is from God."

(2 Corinthians 3:5)

ACKNOWLEDGEMENTS

Without the support and encouragement of many people, I would not have been able to complete my doctorate thesis. As such, I would like to take this occasion to express my gratitude to those who have assisted me in countless ways.

To begin, I would like to express my heartfelt appreciation to my advising team. Firstly, my supervisor, Prof. Tunde V. Ojumu, for having faith in my ability and providing me with the great opportunity to embark on this interesting and somewhat challenging journey. I would like to thank him for his unwavering patience during the times I responded slowly, encouraging me to achieve more, and, most importantly, for his insightful criticism and correction when necessary. Secondly, Dr. Elaine Govender-Opitz, for her optimism and for giving me a proper introduction to the field of my research. I could not have asked for a more supportive advisory board during my doctorate journey.

I would want to convey my appreciation to Prof. Oluwaseun O. Oyekola for allowing me to participate in both course planning and teaching. Thank you for your friendly and genuine concern for my well-being throughout my programme.

To Prof. Eriola Betiku, I am grateful for your mentorship and support for my personal and professional development. You instilled in me an upright spirit toward the art and act of scientific investigation and encouraged me to persevere in pursuing the right path.

I greatly appreciate Dr. Mayowa Agunbiade, Dr. Dipo David, and my awesome friend, Engr. Martins Oyekanmi for their exceptional generosity towards my finances during my programme. I cannot thank you enough. My appreciation for you goes beyond the letters.

I would like to express my gratitude to Dr. Abiola Taiwo and Dr. Toyin Alabi, who gladly received me with open arms and made my settling in Cape Town a comfortable one. Thank you for your continuous support. I would like to extend my sincere thanks to Dr. Elizabeth Omodanisi for voluntarily proofreading my thesis.

To the pastorate, ministers, workers, and members of the Redeemed Christian Church of God (RCCG, Household of God Parish), I am grateful for your brotherly love and prayers.

I would also like to thank my postgraduate colleagues, as well as the administrative and academic staff of the department for their kindness and sense of community.

I gratefully acknowledged the Centre for Postgraduate Studies (CPGS) of CPUT for providing me with a postgraduate bursary for 3 years during my research. Additionally, I recognize the university research fund (URF) for funding the acquisition of several chemicals and materials utilized during my programme.

My sincere appreciation also goes to my friends, Toyin Shittu, Timilehin George, Moses Bisi-Johnson, Lanre Fajimi, AyoOluwa Akintola, Ibrahim Soremekun, Kayode Majekodunmi, Michael Aku, Ropo Omilakin, Rufus Oyemade, and Dr. Juvet Shabani whose timely calls, messages, and companionship encouraged me at some critical times. I would also like to thank my aunties, uncles, cousins, and mother-in-law for their support.

My special thanks go to my siblings, Olayemi, Olatomide, Abolade, and Ajibola, for your unswerving concern. I cherish the exemplary bond of love between us.

I want to convey my special gratitude to my parents, Mr. Lawrence and Mrs. Modupe Oladipo, for the love you bestowed on me in every way and for supporting my education from the basic level to this moment. Daddy and Mummy, I appreciate all you have done for me.

Finally, to my dearest wife, Eyitayo, thank you for your love, constant encouragement, and seemingly endless patience in making my vision a reality, and to my daughter, Oluwatomilola; you have been a blessing to me. It is impossible within the confines of this brief mention to convey all the gratitude I feel for your support.

Thank you all for being part of this journey with me. All glory and honour to God!

CONTRIBUTIONS BY OTHERS TO THE THESIS

Mrs. Hannelene Small (CPUT) provided training on laboratory instruments and assisted with the requisition and procurement of all chemical reagents throughout this thesis.

Mr. Alwyn Bester (CPUT) assisted with the design, fabrication, and repair of equipment, which led to a successful experimental setup.

Dr. Remy Bucher (Materials Research Department, iThemba LABS) assisted with the X-ray powder diffraction (XRD) analysis.

Mrs. Miranda Waldron (Centre for Imaging and Analysis, UCT) assisted with the scanning electron microscopy (SEM) and energy-dispersive X-ray spectroscopy (EDS) analyses.

Mrs. Rachel Cupido (Centre for Catalysis Research, UCT) assisted with the thermogravimetric analysis (TGA) of the samples.

Mr. Govender Sandeeran (The Analytical Laboratory, UCT) assisted with the Brunauer–Emmett–Teller (BET) and the BJH (Barrett–Joyner–Halenda) analyses.

Prof. Liza Coetsee-Hugo (Department of Physics, University of the Free State) assisted with the X-ray photoelectron spectroscopy (XPS) analyses.

Mr. Calleb Duya (Department of Chemistry, CPUT) assisted with the Fourier transform infrared (FTIR) spectroscopy analyses.

Mr. Bongolwethu Mabusela, Mr. Emmanuel Chukwuchendo, Mr. Tolbert Golela, and Mr. Afika Ndobeni supported various aspects of the project. Thank you all for sharing your time and knowledge with me.

RESEARCH OUTPUTS DURING CANDIDATURE

Published Journal Article

Babatunde Oladipo, Elaine Govender-Opitz and Tunde V. Ojumu (2021). Kinetics, Thermodynamics and Mechanism of Cu(II) Ion Sorption by Biogenic Iron Precipitate: Using the Lens of Wastewater Treatment to Diagnose a Typical Biohydrometallurgical Problem. *ACS Omega* (ACS), doi: 10.1021/acsomega.1c03855

This paper has been incorporated as Chapter 6.

Conference Publication

Babatunde Oladipo, Elaine Govender-Opitz and Tunde V. Ojumu (2021). Iron precipitation in biohydrometallurgical operations: An overview to heap operation of chalcopyrite dissolution. *XXX International Mineral Processing Congress-IMPC 2020*, 18–22 October, Cape Town, South Africa, pp. 2708–2721

This paper has been partly incorporated into Chapter 2.

Conference Presentations

Babatunde Oladipo, Mahabubur Chowdhury and Tunde V. Ojumu (2022). Minerals as materials I: Biogenic jarosite as catalytic and adsorbent materials. *11th International Conference of the African Materials Research Society*, 12–15th December 2022, Dakar, Senegal (Oral Presentation, Accepted).

Babatunde Oladipo, Elaine Govender-Opitz and Tunde V. Ojumu (2022). Sorption kinetics and thermodynamics of Cu(II) ion by biogenic iron precipitate. *The 24th International Biohydrometallurgy Symposium (IBS)*, 20–23 November 2022, Perth, Western Australia (Poster Presentation, Accepted).

Babatunde Oladipo and Tunde V. Ojumu (2022). Influence of solution pH on the surface properties of biogenic jarosite produced from ferrous ion bio-oxidation in a CSTR. *The 24th*

International Biohydrometallurgy Symposium (IBS), 20–23 November 2022, Perth, Western Australia (Oral Presentation, Accepted).

Babatunde Oladipo, Tunde V. Ojumu and Elaine Govender-Opitz (2022). Iron precipitate from bioleaching and ferrous ion bio-oxidation: surface characterization and metal sorption mechanism. *The Inter-institutional Chemical Engineering Postgraduate Symposium*, 30 September 2022, Stellenbosch, South Africa (Oral Presentation).

Babatunde Oladipo, Elaine Govender-Opitz and Tunde V. Ojumu (2019). Effect of operating conditions on iron precipitates during biohydrometallurgical processes. *The Southern African Institute of Mining and Metallurgy (SAIMM)*, Western Cape Branch Minerals Research Showcase, 11–12 November 2019, Cape Town, South Africa (Oral Presentation).

TABLE OF CONTENTS

LIST OF FIGURES

LIST OF TABLES

LIST OF ACRONYMS

Abbreviation	Description
BET	Brunauer–Emmett–Teller
BJH	Barrett–Joyner–Halenda
EDS	Energy dispersive X-ray spectroscopy
FTIR	Fourier transform infrared
K-jarosite	Potassium jarosite
pH_{PZC}	pH at point of zero charge
PFO	Pseudo-first-order
PSO	Pseudo-second-order
SEM	Scanning electron microscopy
SSA	Specific surface area
TGA	Thermogravimetric analysis
XRD	X-ray diffraction

LIST OF SYMBOLS

Symbol	Meaning	Unit
A	Arrhenius constant	
Å	Angstrom	Å
b	Langmuir's constant associated with Cu(II) ions affinity for adsorption sites and energy	L/mg
α	Initial Cu(II) adsorption rate	mg/g min
β	Degree of activation energy and surface coverage for chemisorptions	g/mg
C_i	Initial Cu(II) concentration	mg/L
C_e	Equilibrium Cu(II) concentration in solution	mg/L
C	Constant related to the thickness of the boundary layer of the intra-particle diffusion model	mg/g
$\Delta H°$	Standard enthalpy change	kJ/mol
$\Delta S°$	Standard entropy change	kJ/mol K
$\Delta G°$	Free energy change	kJ/mol
E_a	Activation energy	kJ/mol
K_D	The standard thermodynamic equilibrium constant	
K_f	Freundlich's constant in relation to the adsorption capacity	
k_1	Pseudo-first-order rate constant	min^{-1}
k_2	Pseudo-second-order rate constant	g/mg min
k_{id}	Intra-particle diffusion rate constant	mg/g $min^{1/2}$
m	Mass of iron precipitate residue	g
n_f	Heterogeneity factor of Freundlich isotherm	
q_e	Amount of Cu(II) adsorbed at equilibrium	mg/g
$q_{e, exp}$	Experimental values of Cu(II) adsorbed at equilibrium	mg/g
$q_{e, cal}$	Model estimated values of Cu(II) adsorbed at equilibrium	mg/g

q_m	Langmuir maximum adsorption capacity	mg/g
q_t	Amount of Cu(II) adsorbed at time *t*	mg/g
R	Gas constant (8.314)	J/mol K
R_L	Separation factor of Langmuir isotherm	
R^2	Coefficient of determination	
t	Time	min
T	Temperature	°C or K
V	Working solution volume	L

Degree Celsius	°C
Grams	g
Gram per litre	g/L
Gram per milligram	g/mg
Gram per milligram-minutes	g/mg min
Joule per mole-Kelvin	J/mol K
Kelvin	K
Litre	L
Litre per milligram	L/mg
Minutes	min
Per minutes	min^{-1}
Milligrams per gram	mg/g
Milligrams per gram-minutes	mg/g min
Millivolts	mV

GLOSSARY

Biohydrometallurgy: This is a branch of hydrometallurgy considered an eco-benign and cost-efficient technology for processing low-grade ores.

Bioleaching: Bioleaching is one of the important stages in biohydrometallurgy which exploits specific attributes of bacteria or archaea to aid the extraction of desired metals from their sulfide ores.

Bio-oxidation: Bio-oxidation is a crucial sub-process in the bioleaching operation. In this thesis, an emphasis was laid on microbial ferrous-ion oxidation.

Bacteria/Archaea: These are iron- and sulfur-oxidizing microorganism species that are mostly utilized in bio-oxidation and bioleaching processes. These microbes are mainly categorized as mesophiles, moderately thermophiles, and extreme thermophiles.

Heap bioleaching: This is irrigation-based leaching favoured as an energy-saving and cost-effective technique to process large quantities of low-grade ores.

Passivation: A common term used to report the formation of a layer associated with poor extraction of metals caused by the restriction of bacteria movement, nutrients, and oxidants to and from the mineral surface. Passivation is typical to less controlled conditions, especially in bioleaching and general heap leaching operations.

Iron precipitation: This describes a phenomenon/operation in biohydrometallurgical process streams where undesired iron in the circuit is commonly eliminated by oxidation to Fe^{3+}, followed by hydrolysis-precipitation of an iron compound.

Sorption: This is a wider term that embraces the physical and chemical phenomena of molecular interaction between two components. Other derived terms from this process are sorbent, sorbate, and sorptive. In the context of this thesis, sorption will be related to the retention of base metals by iron precipitates.

Jarosite: Jarosite is one of the major products linked with passivation and/or iron precipitate. The general formula for the jarosite-type compound is $A Fe_3(SO_4)_2(OH)_6$, where *A* is well established with several species such as: H_3O^+, Na^+, K^+, NH_4^+, etc.

Continuous stirred tank reactor: A continuous stirred tank reactor (CSTR) is a reactor that assumes the ideal mixing of the reactants (growth media and bacteria culture) while the product (iron precipitate) of the reaction concurrently exists in the reactor.

CHAPTER ONE

INTRODUCTION

"The environment and the economy are both two sides of the same coin. If we cannot sustain the environment, we cannot sustain ourselves." – Wangari Maathai

CHAPTER 1: INTRODUCTION

1.1 Background

Metals are widely employed in current technologies and construction, and the demand and dependency on metals are further increasing due to the continuous increase in industrialization and urbanization. For example, to manufacture new electronic devices like smartphones and tablets, around 60 different metals are required, ranging from platinum, gold, silver, and copper to rare earth elements (Kaksonen *et al.*, 2018). However, exploitable primary metal resources are becoming more limited, ore grades are becoming lower, and the mineralogy of the exploitable ores is becoming more complex. As ore grades get lower, the energy required and the environmental difficulties of conventional pyro- and hydro-metallurgical techniques for mineral processing increase (Norgate *et al.*, 2007; Prior *et al.*, 2012; Northey *et al.*, 2014).

Hydro- and pyro-metallurgy are the two most common techniques for processing mineral sulfides. Hydrometallurgical process involves leaching, concentration and purification, and metal recovery while pyrometallurgical process involves roasting, smelting, and refining. These processes result in a high quantity of chemicals used, a high rate of energy and water consumption, as well as air pollution (CO_2 and SO_2 emissions) with the generation of pollutants such as furans, dioxins, and highly acidic wastewater, which are harmful to the environment (Ruan *et al.*, 2010; Zhao and Wang, 2019). This necessitates the use of emission control devices and advanced wastewater treatment systems, which raises the capital and operational expenses of these technologies (Kulczycka *et al.*, 2016). Furthermore, conventional techniques are becoming less applicable due to the declining grade of ores (Panda *et al.*, 2015). This has further stimulated the attention of industrial stakeholders and researchers to seek an alternative technology that offers positive economic, environmental, and technical attributes relative to conventional methods.

Biohydrometallurgy, which involves bioleaching, solvent extraction, and electrowinning, is a branch of hydrometallurgy demonstrated to be relatively eco-friendly and cost-efficient

technology in the mineral processing industries for processing low-grade sulfide ores to extract metals (Brierley and Brierley, 2001; Zhao *et al.*, 2019). The simplified routes of pyro- and bio-hydrometallurgy operations are illustrated in Figure 1.1. In biohydrometallurgy, copper is the most extensively investigated metal followed by zinc, gold, nickel, cobalt, and uranium (Kaksonen *et al.*, 2018). However, biohydrometallurgy stages must be optimized to compete with conventional techniques.

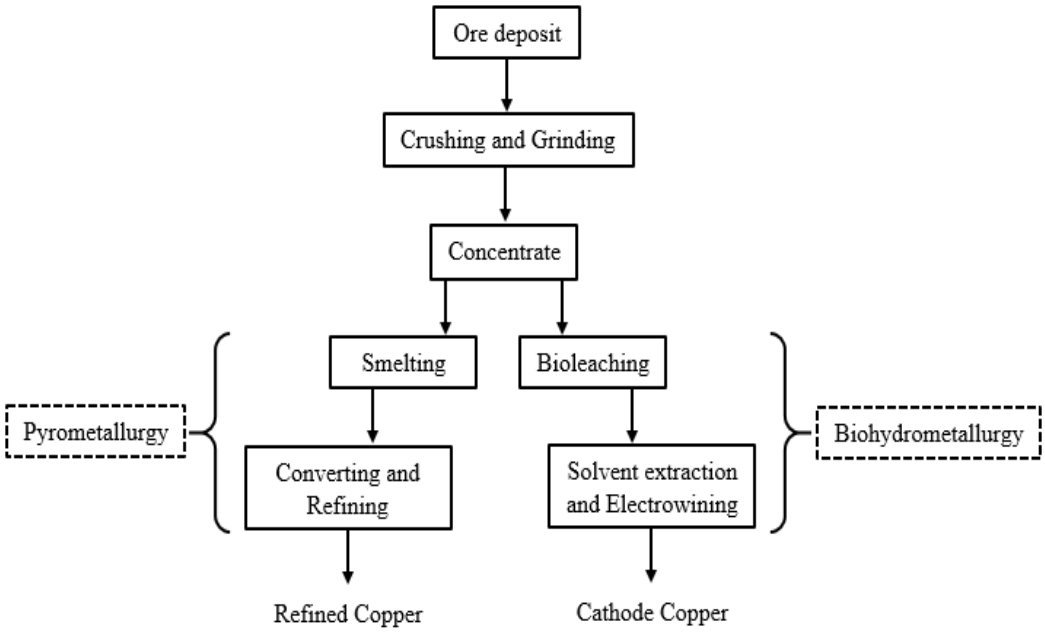

Figure 1.1: Simplified flowsheet of pyro- and bio-hydrometallurgical routes

Bioleaching of sulfide minerals is one of the stages within biohydrometallurgy and it has been understood by numerous researchers as a method that involves the oxidation and dissolution of metal-bearing minerals (such as copper sulfide ore) via the action of microorganisms (mainly bacteria and archaea) (Brierley and Brierley, 2001; Ehrlich, 2001). Simply put, bioleaching is the biological conversion of an insoluble metal compound into a water-soluble form. It involves chemical and biological reactions. Industrially, bioleaching is utilized as a pre-treatment procedure for refractory gold ores before cyanidation and for copper extraction from secondary copper sulfide ores. With continuous development, it is currently being used for the extraction of metals like copper, nickel, cobalt, gold, and zinc from their respective ores (Brierley and Brierley, 2013; Schippers *et*

al., 2013). Recent estimates indicate that about 20% of the global mined copper (Yin *et al.*, 2018) and approximately 5% of the global mined gold (Das *et al.*, 2017) are generated through the bioleaching process. Based on the ore grade, different bioleaching processes have been developed for metal extraction. These include stirred tank bioleaching, which is typically used for ground ore materials; heap bioleaching, which is primarily used for low-grade ore and concentrates; and irrigated dump leaching, which is commonly used for low-grade run-of-mine ores (Brierley and Brierley, 2001; Rawlings, 2002; Ghorbani *et al.*, 2016).

Ferrous ion (Fe^{2+}) bio-oxidation is a crucial sub-process in the optimization of bioleaching operations. It has been identified as the primary driving force for the oxidation of many industrially important sulfide minerals (Jones and Kelly, 1983; Boon, 1998; Meruane and Vargas, 2003). The bioleaching process involves a chemical leaching of the sulfide mineral with acid and ferric ions, which releases the valuable metal into solution, while the ferric ion is reduced back to ferrous ion with the formation of a range of sulfur species. The primary function of the microorganisms is to promote the oxidation of ferrous ions to ferric ions, and the reduced sulfur compounds to sulfur and/or sulfate (Schippers and Sand, 1999; Rohwerder *et al.*, 2003; Schippers, 2007), therefore maintaining the leaching operation. Thus, this necessitates the importance of ferrous ion bio-oxidation in bioleaching. It has likewise been demonstrated that under identical conditions, ferrous ion bio-oxidation occurs at a rate that is several orders of magnitude faster than abiotic oxidation (Lacey and Lawson, 1970; Ojumu, 2008).

While there have been several studies on biological iron oxidation (Nemati *et al.*, 1998; Boon *et al.*, 1999; Ojumu *et al.*, 2009; Chowdhury and Ojumu, 2014), it is well known that it results in both soluble and various forms of precipitated ferric ion, which are dependent on solution pH, temperature, iron concentration, and overall solution chemistry (Drouet and Navrotsky, 2003; Gramp *et al.*, 2008; Mabusela and Ojumu, 2017; Kaksonen *et al.*, 2019). Iron precipitation is an unavoidable phenomenon in many bio- and hydro-metallurgical operations, and in several of these processes, iron precipitates serve positively as an escape path for unwanted iron, alkali ions or sulfate ions from the processing circuit (Dutrizac and Jambor, 2000; Kaksonen *et al.*, 2018). However, recirculation of leach liquors over

continuous long-term operation of the bioleaching process may lead to the significant accumulation of dissolved iron and sulfate in heaps, which may interfere with process kinetics and biological stages due to precipitate formation.

1.2 Research motivation and problem statement

Precipitation occurs under controlled conditions in conventional hydrometallurgical flowsheets, yielding relatively well-defined compounds such as goethite, hematite, or crystalline jarosite. Under less controlled conditions, particularly in bioleaching and general heap leaching, a poorly-defined mixture of different forms of iron precipitate occurs, such as ferrihydrite, schwertmannite, jarosite, and so on. These precipitates are often rather amorphous with high surface area owing to their colloidal nature and surface charge (Nurmi *et al.*, 2010; Mabusela and Ojumu, 2017). While very low pH conditions have been demonstrated to reduce the generation of iron precipitates, it has been shown that precipitation occurs concurrently with ferrous ion bio-oxidation (Chukwuchendo and Ojumu, 2017) and in the bioleaching of sulfide minerals (Córdoba *et al.*, 2008b). The precipitates are known to cause severe blockage of pipes and heap beds. A major detrimental effect posed by precipitates during bioleaching operation is the reduction of extraction efficiency by scavenging valuable base metals of interest, thereby hindering the release of the metals into solution. To support this, studies have confirmed that a significant amount of metals can be recovered from iron precipitate residue of a preceding bioleaching process (Ju *et al.*, 2011; Liu *et al.*, 2017; Wang *et al.*, 2018). However, with respect to the solution chemistry and scavenging mechanism of iron precipitate, there is limited information and they are largely not well-understood. Thus, it is important to conduct studies that would provide fundamental knowledge of these precipitates and their interactions with desired metal ions, with a view to gain some insight into the management of biohydrometallurgical process such that loss of desired metals can be minimized.

1.3 Aims and objectives

This research aims to investigate the nature of iron precipitates generated during bio-oxidation processes under different initial pH values and to understand the sorptive mechanism for metal ions caused by iron precipitate during bioleach operation. More precisely, the objectives of this thesis are to:

(a) examine the effect of changes in influent pH on the surface properties of iron precipitate generated during microbial oxidation of ferrous ion;
(b) identify the mechanism and study the kinetics of metal ion sorption by iron precipitate from bioleaching and bio-oxidation processes;
(c) determine the effect of temperature and estimation of the pertinent activation energy and thermodynamic parameters for the sorption process of iron precipitate obtained from bioleaching and bio-oxidation processes;
(d) investigate the significance of surface charge, surface area, and pore size of biogenic iron precipitate on its kinetics and adsorption capacity for metal ion.

1.4 Research hypotheses and questions

The following are the hypotheses and questions posed in this study:

Hypothesis 1: Many factors influence the amount of iron precipitate and it is well known that microorganisms operate as a biocatalyst in bioleaching.

- How does change in pH affects the amount of iron precipitate formed due to microbial action?

Hypothesis 2: Metal retention on iron precipitate is intrinsically related to the surface properties of the precipitate. It is hypothesized that the ability of iron precipitate to scavenge desired metals depend on its morphology, surface charge, surface area, and pore size distribution.

- How do changes in solution pH affect the surface properties (such as surface charge, surface area, functional group, and pore size) of the iron precipitate generated?

Hypothesis 3: The sorption mechanism can be determined by having a good understanding of the chemical form of the adsorbate (metal ion) and the surface nature of the adsorbent (iron precipitate), as well as the interactions between them.

- What influence do the properties of iron precipitate have on its sorption mechanism and kinetics in the uptake of metal ions on its surface?
- What is(are) the mechanism(s) of sorption of metal ion by ferric ion precipitate in a typical biohydrometallurgical operation?

1.5 Significance of the study

The primary goal of this research is to gain an understanding of the link between operating parameters (primarily pH) and the surface properties of iron precipitates generated during the ferrous ion bio-oxidation by mixed mesophilic culture. The study provides a database of detail characterization of iron precipitate from bioleaching and bio-oxidation of ferrous ion that may be useful for laboratory or industrial applications. This study also investigates the kinetics and mechanisms of base metals sorption by iron precipitates generated during typical bio-oxidation and bioleaching operations. The lesson gleaned from this study may aid in ensuring less sorption of desired metals, thus enhancing their recovery while maintaining higher bio-oxidation rates. Furthermore, the outcome of the study may also help to reduce environmental pollution caused by the disposal of the biogenic iron precipitate residue. Ultimately, the results of this study will help improve the extraction efficiency of desired metals while also ensuring the sustainability of biohydrometallurgical processes.

1.6 Delineation of the study

This research investigated the surface properties of iron precipitate generated during microbial ferrous ion oxidation and pyrite bioleaching as well as their intrinsic sorption mechanism for valuable metals. While this work focused on the precipitate-metal interaction, it is assumed that the ferric precipitation can be decoupled from sorption process during bioleaching such that both precipitation and sorption can be investigated

separately. The results might not be directly translated to real bioleach case situations, but will provide some understanding of how changes in solution pH of the bioleach process influence the properties of iron precipitate and its sorption of desired metals in such operations. This study did not focus on bio-oxidation and bioleach experiments but rather on the iron precipitate generated from both processes. Also, the study did not focus on mass transfer operations intervening in both bio-oxidation and bioleach processes.

1.7 Thesis outline

This thesis is divided into eight chapters, four of which are dedicated to the study objectives (Chapters 4 to 7).

Chapter 1 (the current chapter) presents the fundamental background, motivation, and objectives to contextualize the proposed study.

Chapter 2 provides a literature review of the relevant knowledge as regards iron precipitation in biohydrometallurgical processes. The formation and impacts of iron precipitates in mineral ore processing are discussed. The characteristics of some iron minerals (oxides, oxyhydroxides, and hydroxysulfates) are also highlighted. The factors influencing ferrous ion bio-oxidation and bioleaching of mineral sulfide are discussed with major reference to solution pH, temperature, and redox potential. The chapter then identifies gaps and research problems that this research has to cover, particularly in the area of conditions that influence metal sorption and its mechanism by iron precipitate. Part of the overview described in this chapter was published in *IMPC 2020 Congress Proceedings*, (2022).

Chapter 3 describes the procedures employed in this thesis, including the typical set-up of the experimental rig, description of materials, mathematical tools, analytical solution techniques, and general characterization methods used for the analysis of products throughout the thesis.

Chapter 4 entails quantification experiments on the effect of initial influent pH values, redox potential, and reaction and/or aging time on the mass of iron precipitate produced during ferrous ion oxidation mediated by mixed mesophiles in a continuous stirred tank reactor (CSTR).

Chapter 5 describes the effect of initial solution pH values on the surface properties of the biogenic iron precipitates formed in Chapter 4. The precipitates were comprehensively characterized in terms of phase identification, surface morphology, elemental composition, chemical structure, thermal behaviour, surface area, and pore size distribution using various techniques. The scavenging mechanism of biogenic jarosite for metal ions as it relates to its surface properties was discussed in the context of mineral bioleaching.

Chapter 6 evaluates the performance of a highly heterogeneous industrial iron precipitate residue on the sorption of copper. The kinetics, thermodynamics, and mechanism of the sorption process were further used to diagnose a real biohydrometallurgical problem. The research discussed in this chapter was published in *ACS Omega* journal (Oladipo *et al.*, 2021a).

Chapter 7 investigates the influence of surface charge, surface area, and pore size of biogenic precipitates on the kinetics and mechanism of copper ion uptake by the precipitate at the precipitate-liquid phase interface.

Chapter 8 summarizes the main findings of this thesis and suggests recommendations for minimizing iron precipitation in biohydrometallurgical processes and future studies to reinforce the knowledge gained through this research.

A schematic illustration of the thesis structure is depicted in Figure 1.2.

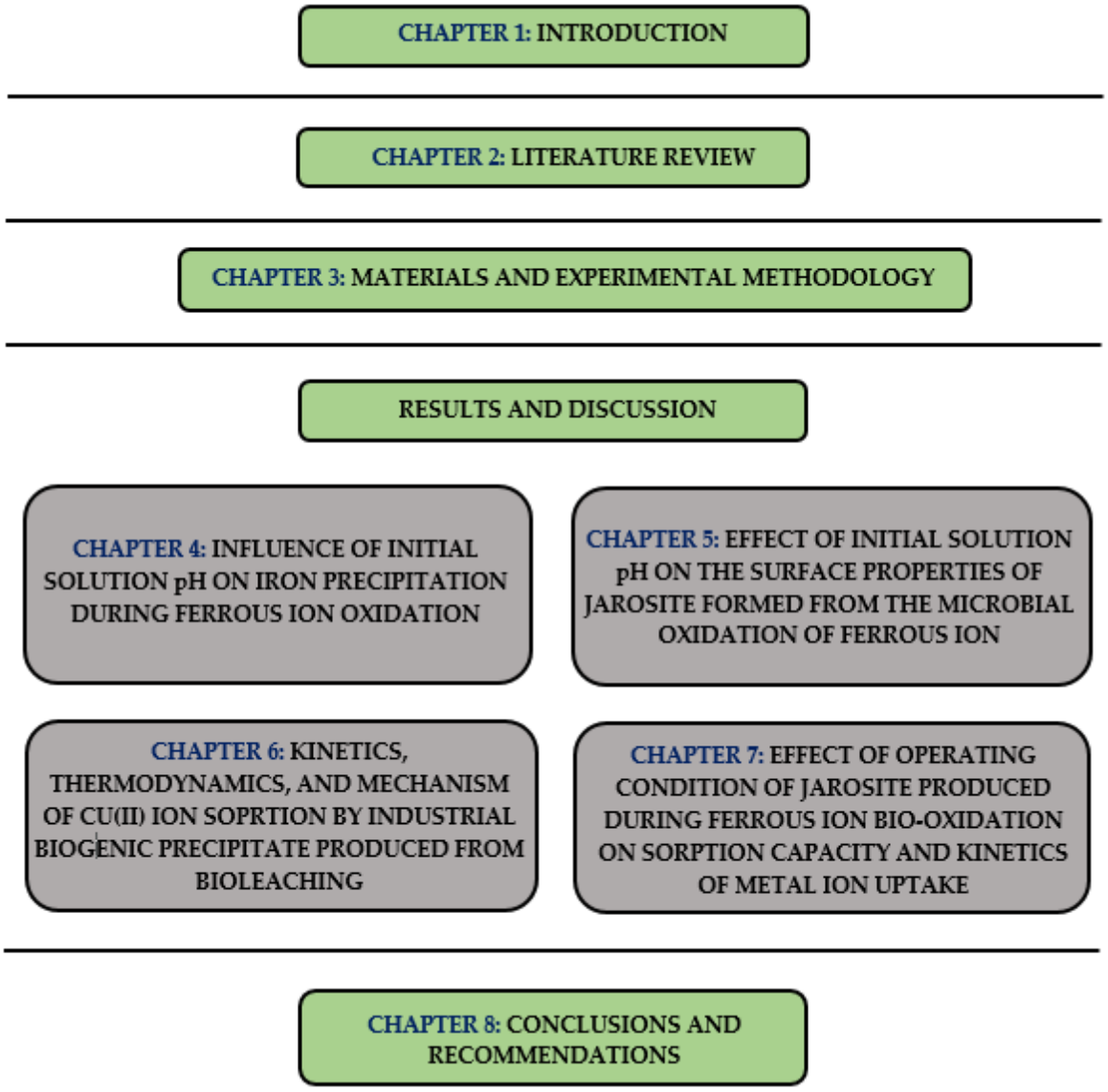

Figure 1.2: The thesis road map

CHAPTER TWO

LITERATURE REVIEW

Part of this chapter has been published in *IMPC 2020 Congress Proceedings* as

B. Oladipo, E. Govender-Opitz and T. V. Ojumu (2022). Iron precipitation in biohydrometallurgical operations: An overview to heap operation of chalcopyrite dissolution (pp. 2708–2721)

"The only way forward, if we are going to improve the quality of the environment, is to get everybody involved." – Richard Rogers

CHAPTER 2: LITERATURE REVIEW

This chapter reviews the relevant literature that underpins this thesis and highlights important research gaps that are addressed in this work. Most importantly, this chapter is targeted at developing a background into the nature and properties of iron precipitate as related to their scavenging of desired metals in biohydrometallurgical operations.

2.1 Iron precipitation in biohydrometallurgical processes

Iron precipitation is an unavoidable stage common in many biohydrometallurgical operations. These precipitates serve as the outlet path for unwanted iron, alkali ions, or sulfate ions from the processing circuit (Dutrizac and Jambor, 2000; Kaksonen *et al.*, 2018). The formation of iron precipitates, if not well managed, can exhibit negative impacts on the process kinetics and biological stages of bio-oxidation and bioleaching processes. Studies have even shown the recovery of a considerable amount of metals entrapped by these precipitates in bioleach residues, thereby reducing the overall efficiency of bioleach operation (Ju *et al.*, 2011; Liu *et al.*, 2017; Wang *et al.*, 2018).

During the bio-oxidation of ferrous ions under some prevailing process conditions, precipitates such as ferrihydrite, hematite, goethite, magnetite, schwertmannite, and jarosite are formed with a morphological attribute of adsorbing metal. Over continuous long term operation in bioleaching processes, these precipitates become very significant, accumulating in heaps and reducing permeability by forming a surface layer that hinders dissolution of sulfide ores, an effect generally known as "passivation" (Li *et al.*, 2013; Zhao *et al.*, 2019).

In proven research evidence reported in the literature, sulfur (S^0), disulfide (S_2^{2-}), polysulfide (also termed metal-deficient sulfide, S_n^{2-}), iron hydroxysulfates (otherwise known as jarosites), and other iron (oxyhydr)oxides identified on the surface of sulfide ores leached in various aqueous media (Zhao *et al.*, 2019), have all been suggested as major passivating species. Moreover, there is no generally admitted rationale as to their formation

mechanism. Furthermore, there is also no consensus in the literature on the precursors that lead to the formation of these passivating layers (Wang *et al.*, 2006; Córdoba *et al.*, 2008b). However, it appears that the nature of passivation depends on the physicochemical, biological, and mineralogical properties of the ore being leached, and operating conditions of the process (Kaksonen *et al.*, 2018).

2.2 Microbes used in biohydrometallurgical operations

Microorganisms have formed an important part of biohydrometallurgical processes by playing the role of a biocatalyst. The role of the microorganisms in the bioleaching process is to oxidize ferrous ions and sulfur compounds to provide ferric ions and protons, which are the necessary agents for metal sulfide dissolution (Sand *et al.*, 2001; Rohwerder and Schippers, 2007; Schippers, 2007). The diverse range of well-known acidophilic microbes mostly isolated from natural leaching surroundings (e.g. acid mine drainage) is utilized in bio-oxidation and bioleaching processes at the industrial level (Olson *et al.*, 2003; Schippers, 2007). The microbes employed in biohydrometallurgical operations are mainly categorized according to the range of optimal temperature growth, namely mesophiles (24 – 40 °C), moderate thermophiles (40 – 60 °C), and extreme thermophiles (60 – 80 °C). Table 2.1 shows the iron- and sulfur-oxidizing acidophiles employed in biohydrometallurgical operations (Schippers, 2007).

Table 2.1: Some selected iron- and sulfur-oxidising acidophilic microbes in bio-oxidation and bioleaching processes*

Specie	pH	Temperature (°C)	Growth mode (ability to oxidize Fe^{2+}, S^{-}, or S^{2-})
Mesophiles			
Acidithiobacillus ferroxidans	2.5	30 – 35	Autotroph (S^{-}, S^{2-})
Acidithiobacillus thiooxidans	2.0 – 3.0	28 – 30	Autotroph (Fe^{2+}, S^{-})
Leptospirillum ferriphilum	1.3 – 1.8	30 – 37	Autotroph (Fe^{2+}, S^{2-})
Leptospirillum ferroxidans	1.5 – 3.0	28 – 30	Autotroph (Fe^{2+}, S^{2-})
Thiobacillus prosperus	~ 2	33 – 37	Autotroph (Fe^{2+}, S^{-}, S^{2-})
Thiomonas cuprina	3.5 – 4	30 – 36	Facultative (S^{-}, S^{2-})
Moderate thermophiles			
Acidimicrobium ferroxidans	30 – 37	45 – 50	Facultative (Fe^{2+})
Acidithiobacillus caldus	2.0 – 2.5	45	Facultative (S^{-}, S^{2-})
Sulfobacillus acidophilus	~ 2	45 – 50	Facultative (Fe^{2+}, S^{-}, S^{2-})
Sulfobacillus sibiricus	2.2 – 2.5	55	Facultative (Fe^{2+}, S^{-}, S^{2-})
Sulfobacillus thermosulfidooxidans	~ 2	45 – 48	Facultative (Fe^{2+}, S^{-}, S^{2-})
Extreme thermophiles			
Acidianus brierleyi	1.5 – 2.0	~ 70	Facultative (Fe^{2+}, S^{-}, S^{2-})
Acidianus infernus	~ 2	~ 90	Autotroph (Fe^{2+}, S^{-}, S^{2-})
Metallosphaera sedula	2 – 3	75	Facultative (Fe^{2+}, S^{-}, S^{2-})
Sulfolobus metallicus	2 – 3	65	Autotroph (Fe^{2+}, S^{-}, S^{2-})
Sulfurococcus mirabilis	2 – 2.6	70 – 75	Facultative (Fe^{2+}, S^{-}, S^{2-})
Sulfurococcus yellowstonensis	2 – 2.6	60	Facultative (Fe^{2+}, S^{-}, S^{2-})

*Source: adapted from Schippers (2007)

2.3 Ferrous ion bio-oxidation and iron precipitation

Microbial oxidation of ferrous (Fe^{2+}) to ferric ion (Fe^{3+}) has proved to be a crucial sub-process for the efficient oxidative processing of sulfide minerals. Ferric sulfate is the most commonly applied lixiviant in leaching owing to its operational simplicity and low cost (Li *et al.*, 2013). A good understanding of Fe^{2+} bio-oxidation and Fe^{3+} precipitation process would aid in the efficient bioleaching of sulfide minerals, especially the low-grade ores such as chalcopyrite.

2.3.1 How do iron precipitates form?

The microbial oxidation of Fe^{2+} to Fe^{3+} is according to Equation (2.1). The production of Fe^{3+} is important as it performs the function of an important leaching agent. Due to the consumption of H^+ in the formation of Fe^{3+}, the pH of the aqueous media at first increases (Daoud and Karamanev, 2006). However, this increase in pH is later counteracted by the hydrolysis of Fe^{3+} in aqueous solutions, as shown in Equations (2.2) – (2.4) respectively.

$$4Fe^{2+} + 4H^+ + O_{2(aq)} \xrightarrow{\text{Fe-oxidising bacteria}} 4Fe^{3+} + 2H_2O \quad (2.1)$$

$$Fe^{3+} + H_2O \leftrightarrow FeOH^{2+} + H^+ \quad (2.2)$$

$$Fe^{3+} + 2H_2O \leftrightarrow Fe(OH)_2^+ + 2H^+ \quad (2.3)$$

$$Fe^{3+} + 3H_2O \leftrightarrow Fe(OH)_3 + 3H^+ \quad (2.4)$$

The degree of Fe^{2+} oxidation and Fe^{3+} hydrolysis is dependent on and strongly impacted by the pH of the medium. Typically, Fe^{3+} has a very low solubility at pH > 2.5 (Nurmi *et al.*, 2010). In sulfate-rich systems, Fe^{3+} precipitates mainly as jarosite (Fe(III)-hydroxysulfate) compounds at pH 1 – 3.

Depending on the nature of precipitates, the general conversion of ferrous-ion to soluble and precipitated ferric sulfate may be acid-neutral, as shown in Figure 2.1.

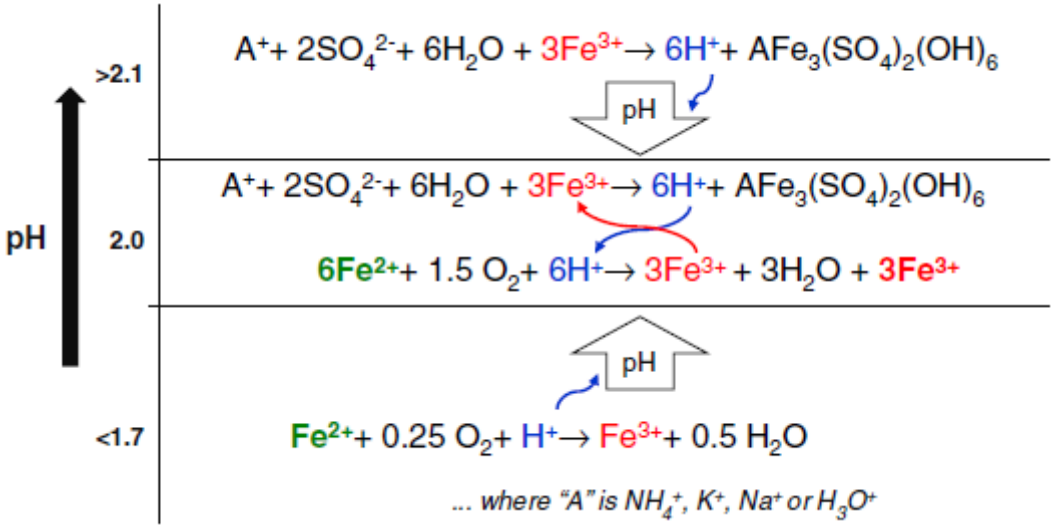

Figure 2.1: Diagrammatic representation of the link between ferrous ion oxidation and ferric ion precipitation processes

Source: adapted from Kaksonen *et al.* (2014b)

The formation of jarosite (a form of iron precipitate) which is an acid-generating reaction has been reported to compete with the hydrolysis reactions (Grishin *et al.*, 1988; Daoud and Karamanev, 2006). End-member jarosite in the narrow sense consists of potassium (K) and it is described by the formula $KFe_3(SO_4)_2(OH)_6$, whereas other end-members in the jarosite class consist of iron (Fe^{3+}) and sulfur (S^{6+}) (Jambor, 1999; Dutrizac and Jambor, 2000).

The lower threshold pH for jarosite formation is close to pH 1; however, it relies on the ionic constituents and temperature of the medium solution (Nurmi *et al.*, 2010). The formation of jarosite is summarized in Equation (2.5).

$$K^+_{(aq)} + 3Fe^{3+}_{(aq)} + 2SO_4^{2-} + 6H_2O_{(l)} \leftrightarrow KFe_3(SO_4)_2(OH)_{6(s)} + 6H^+_{(aq)} \quad (2.5)$$

In other end-member jarosite minerals, K^+ is substituted by other monovalent cations, such as Na^+, NH_4^+, H_3O^+, or Ag^+ (Jambor, 1999; Dutrizac and Jambor, 2000) depending on the nature of excess available cation in the medium solution (Daoud and Karamanev, 2006; Nazari *et al.*, 2014). The end-member minerals of the jarosite family frequently found in bio-oxidation and bioleach residues are presented in Table 2.2 (Dutrizac and Jambor, 2000; Watling, 2015).

Table 2.2: Mineral names and the synthetic analogue of jarosite precipitates*

Formula	Mineral name	Synthetic equivalent
$KFe_3(SO_4)_2(OH)_6$	jarosite	potassium jarosite
$(H_3O)Fe_3(SO_4)_2(OH)_6$	hydronium jarosite	hydronium jarosite
$NaFe_3(SO_4)_2(OH)_6$	natrojarosite	sodium jarosite
$(NH_4)Fe_3(SO_4)_2(OH)_6$	ammoniojarosite	ammonium jarosite
$AgFe_3(SO_4)_2(OH)_6$	argentojarosite	silver jarosite
$Pb_{0.5}Fe_3(SO_4)_2(OH)_6$	plumbojarosite	lead jarosite

*Source: adapted from Dutrizac and Jambor (2000) and Watling (2015)

It should be noted that the stability of jarosite is significantly dependent on pH and temperature, as illustrated in Figure 2.2 (Das *et al.*, 1996). With increasing temperature, the stability domain narrows and shifts towards the more acidic zone. Jarosite, for example, is more stable at 120 °C than at 90 °C in solutions with pH around 0 (Figure 2.2). Furthermore, the pH-redox potential (Eh) phase-stability diagram of iron minerals compiled from thermodynamic data has also been given in the literature (Bigham *et al.*, 1996; Dutrizac and Jambor, 2000). This is shown in Figure 2.3. More details on the influence of pH, temperature, and redox potential on iron precipitate are given in Section 2.5.

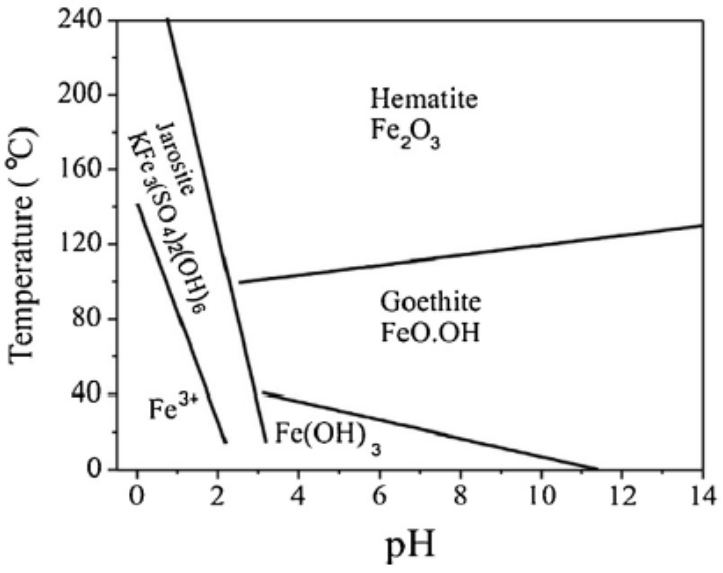

Figure 2.2: Iron minerals stability as a function of temperature and pH

Source: adapted from Das *et al.* (1996)

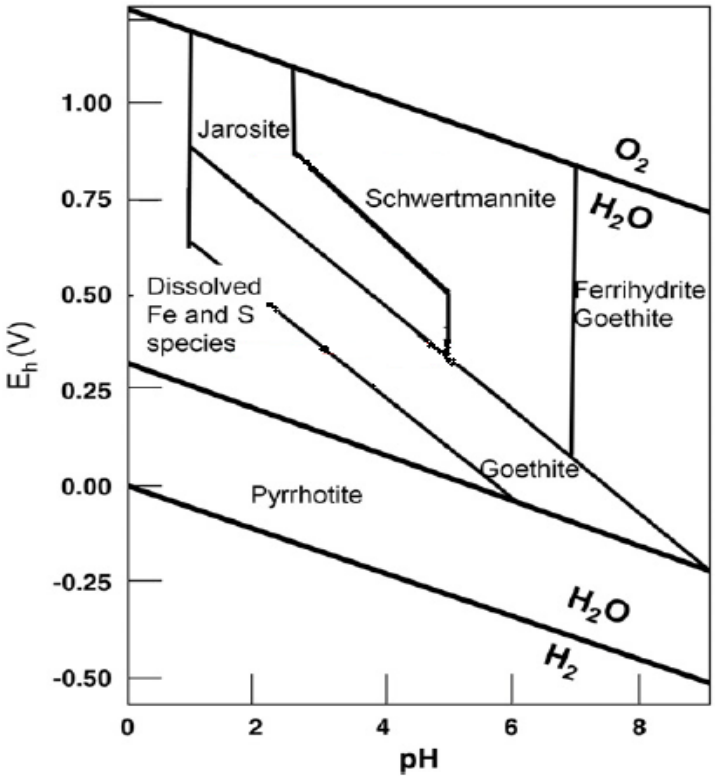

Figure 2.3: Predicted thermodynamic stability for iron minerals as a function of Eh and pH

Source: adapted from Bigham *et al.* (1996)

At higher pH values, oxyhydroxides and oxides are formed. For example, the formation of ferrihydrite [$Fe_2O_3(OH)_9$] is promoted in solutions of pH > 5. Ferrihydrite is a poor crystalline compound that changes to goethite in solutions of pH 2 – 5 (Watling, 2015). Goethite, an Fe(III)-oxyhydroxide (α-FeOOH) has a wide pH range, precipitating at acidic to neutral conditions pH (< 4, > 10) with low sulfate concentration (Watling, 2015). The precipitation of schwertmannite [$(Fe_{16}O_{16}(OH)_{12}(SO_4)_2$] is aided in solutions of pH 3 – 4 that contain moderate to high ferric sulfate but low monovalent cations (Jones *et al.*, 2014). Schwertmannite is a poor crystalline mineral that is unstable and changes to either goethite or jarosite. The characteristics of these iron oxides, oxyhydroxides, and hydroxysulfates are further described in Section 2.4.

Several studies have reported the formation of jarosites in both bio-oxidation and bioleaching of sulfide minerals. Liu *et al.* (2009) identified the presence of dark-yellow precipitates formed during Fe^{2+} oxidation by *Thiobacillus ferrooxidans* to be ammoniojarosite. Nazari *et al.* (2014) reported the formation of potassium jarosite in their study on the

production of jarosite and its influence on crucial ions for *Acidithiobacillus ferrooxidans* bacteria. Grishin *et al.* (1988) characterized jarosite formed in a packed bed reactor, inoculated with *Thiobacillus ferrooxidans*; the results revealed the absence of ammonium traces even though the medium was rich in NH_4^+. This led the authors to report mixed jarosite of K^+ and NH_4^+, which was attributed to the preferential precipitation of potassium-hydronium jarosite over ammonium jarosite. The above findings questioned the suggestions of Nazari *et al.* (2014) and Daoud and Karamanev (2006) on the cations present in abundance determining the nature of the precipitate. Grishin *et al.* (1988) stated that the synthesis of hydronium jarosite is only possible in the absence of an alkali over a temperature range of 25 – 170 °C.

The initial stage of the formation of an iron precipitate is necessary for a proper understanding of the kinetics of precipitate formation. According to Pina *et al.* (2005), Fe^{3+} precipitation is initiated at pH 2; however, Córdoba *et al.* (2008a) stated that Fe^{3+} precipitation was pronounced at pH as low as 0.9. Liu *et al.* (2007) stated that precipitation of Fe^{3+} begins when microbes undergo their logarithmic growth phase. This was contrary to the report of Liu *et al.* (2009) which found that the precipitation of Fe^{3+} begins when its concentration in solution starts to decrease and is evident long after the logarithmic growth phase has started. From the results reported by Liu *et al.* (2009), it can be deduced that the initial formation stage of Fe^{3+} precipitation begins when the microbes reach their peak in the logarithmic growth phase and this can be corroborated by the subsequent decrease in the concentration of Fe^{3+}.

More concisely, Sasaki and Konno (2000) proposed the initial formation stages of Fe^{3+} precipitation to proceed in three distinct steps: (1) the oxidation of Fe^{2+} by iron-oxidizing microbes to Fe^{3+}, (2) the formation of crystal nuclei (embryos) and lastly, (3) the development of crystals of jarosite-type compounds. In the oxidation of Fe^{2+} by *Thiobacillus ferroxidans*, Lazaroff *et al.* (1982) stated that the formed polymeric intermediates are the primary precursors to the formation of jarosite-like compounds. However, in a study of Fe^{2+} bacterial oxidation in a packed-bed reactor, Grishin *et al.* (1988) reported that a jarosite-like group could form from solution without the initial formation of solid precursors. Casas

et al. (2000) further reported that jarosite formation is initiated from iron hydroxides ($Fe(OH)_3$) produced by hydrolysis of Fe^{3+} (refer to Equations (2.2)–(2.4)). In another study, Jiang and Lawson (2004) stated that the initial production of $FeSO_4^+$ and $Fe(OH)_3$ species is necessary for the production of jarosite, thus, corroborating the findings of Casas and co-workers. In addition, it was also reported that $(Fe(OH)_2)_2SO_4$ and $Fe(OH)SO_4$ are the precursors for jarosite formation. Wang *et al.* (2006) reported schwertmannite (a poorly crystalline Fe(III) phase) to be the precursor for the production of jarosite. To the contrary, Córdoba *et al.* (2008b) observed that geothite (FeOOH) was the main precursor in jarosite formation.

2.4 Characteristics of iron oxides, oxyhydroxides, and hydroxysulfates

In this section, iron oxides (magnetite, hematite, maghemite), oxyhydroxides (goethite, akaganéite, lepidocrocite, ferrihydrite), and hydroxysulfates (schwertmannite, jarosite) are sometimes collectively referred to as iron minerals and/or compounds for convenience. The retention of metal ions on iron compounds is fundamentally linked to their distinct structural attributes and morphology of the mineral surface (Fernandes and Baeyens, 2019). For example, all iron oxyhydroxides have a fundamental structural unit of $Fe(O, OH)_6$–octahedral, which contains six O_2 atoms surrounding individual Fe atoms. Crystallographic analysis indicates that the surface hydroxyl groups may be coordinated to one, two, or three underlying Fe atoms. These singly, doubly, and triply coordinated groups (Figure 2.4) are also known as A, B, and C type respectively (Cornell and Schwertmann, 2003a). These surface hydroxyl groups exhibit significantly varying acidic and reactive properties toward sorbates. Because of the disparities in total density and arrangement of these surface hydroxyls on individual crystal planes, the sorption methods and metal capacity of various iron compounds should differ (Shi *et al.*, 2020). Furthermore, iron oxyhydroxides can retain considerable quantities of several heavy metals in the crystal lattice, because of the distinctive positioning of the $Fe(O, OH)_6$–octahedral in space. Selected properties of iron compounds are summarized in Table 2.3 (Cornell and Schwertmann, 2003a; Guo and Barnard, 2013; Shi *et al.*, 2020). The individual iron compounds are summarized in the next section.

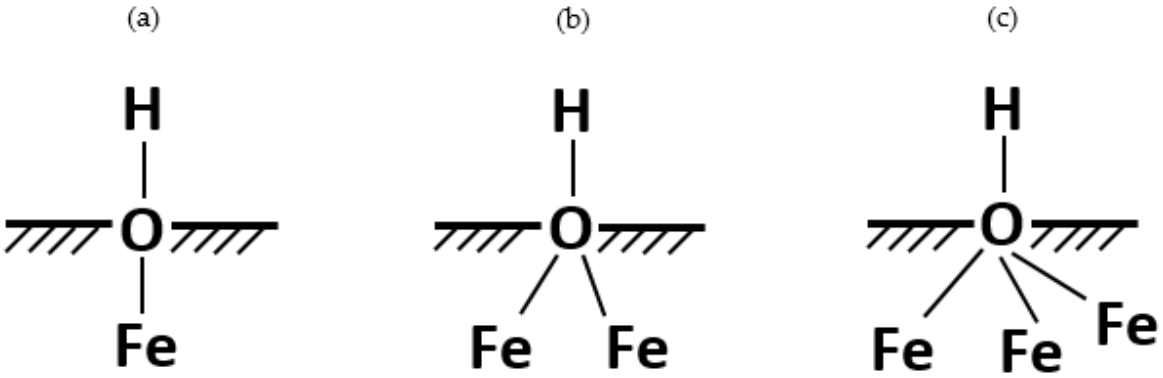

Figure 2.4: Schematic illustration of surface hydroxyl groups on iron oxides and oxyhydroxides: (a) singly, (b) doubly, and (c) triply coordinated types

Source: adapted from Shi *et al.* (2020)

Table 2.3: Formation, occurrence, structure, and retained metals on iron oxides, oxyhydroxides, and hydroxysulfates*

Minerals (chemical formula)	Formation conditions	Environments	Shape	Cell dimensions	Point of zero charge	Sorbed metals
Ferrihydrite ($Fe_{10}O_{14}(OH)_2.nH_2O$)	At circumneutral pH	Soils, sediments, and mine-drainage channels	Irregular and spherical	Hexagonal a = ~0.595 nm, c = ~0.906 nm	~7.6–8.5	Sb, Mn, As, Pb, Zn, Se, U, Cr, Np, Ni, Cd, Cu
Hematite (α-Fe_2O_3)	At near-neutral pH and high temperatures	Tropical and subtropical soils	Rounded, rhombohedral and platy	Rhombohedral hexagonal, a = 0.5034 nm, c = 1.375	~8.2–9.3	Cr, Ni, Pb, As, Co, Zn, V, U, Sb, Mn, Cd, Cu, Se, Np
Goethite (α-FeOOH)	At high and low pH and lower temperatures	Many ores, sediments and soils	Acicular	Orthorhombic a = 0.9956 nm, b = 0.30215 nm, c = 0.4608 nm	~9.1–9.6	Mn, Zn, Ni, As, Cr, U, Co, Pb, Sb, Cd, Cu
Magnetite (Fe_3O_4)	Under circumneutral to alkaline conditions in anoxic environments	Anoxic soils and sediments	Octahedron, rhombo-dodecahedron	Cubic a = 0.8396 nm	~7.1–7.5	Al, Zn, Cu, Cr, Mg, U, Co, Hg, V, Pb, Mn, As, Ti, Ni
Schwertmannite ($Fe_8O_8(OH)_{8-2x}(SO_4)_x$)	In acidic (pH 3–4), sulfate-rich waters	Acid mine drainage and acid sulfate soil systems	Hedgehog or pin-cushion like	Tetragonal a = 1.065 nm, c = 0.604 nm	~6.6–7.2	Zn, As, Se, Cd, Cu, Pb, Cr
Jarosite ($AFe_3(SO_4)_2(OH)_6$)	In strong acidity (pH ~1–3) and moderate to highly oxidized sulfate-rich waters	Acid rock drainage and acid mine drainage, mine tailings, and acidic soils	Spherical, hollow-shaped and cenosphere	Hexagonal a = ~0.73 nm, c = ~1.71 nm	~1.9	Ga, Zn, As, Pb, Sb, Ni, Cr, Ag, Al, Cu, V, Cd

*Source: modified from Cornell and Schwertmann (2003b), Guo and Barnard (2013), and Shi *et al.* (2020)

2.4.1 Ferrihydrite

Ferrihydrite ($Fe_{10}O_{14}(OH)_2 \cdot nH_2O$) is the most common iron oxyhydroxide mineral in soil and sediment (Thomasarrigo *et al.*, 2019). Since it is thermodynamically unstable, ferrihydrite is often the initial mineral generated when ferric iron precipitates from solution and is a precursor to other iron minerals like hematite and goethite (Meng *et al.*, 2014). Both synthetic and natural ferrihydrite is poorly crystalline. Each ferrihydrite particle is usually found as a cluster that is made up of irregular to spherical morphologies with a small size distribution of less than 7 nm (Wang *et al.*, 2016b). Ferrihydrite mineral contains 20% tetrahedral Fe^{3+} and 80% octahedral Fe^{3+} with a local morphological pattern associated with the δ-Keggin cluster (Michel *et al.*, 2007; Weatherill, 2018). Due to its extraordinarily huge surface area (between 120 and 850 m^2/g), strong attraction for metal or metalloid ions, and a high density of defects (vacant sites, stacked fault), it demonstrates great potential for sequestering significant quantities of metal cations and oxyanions (Guo and Barnard, 2013; Wang *et al.*, 2015; Liu *et al.*, 2016b). Ferrihydrite can form strong complexes with common heavy metals (e.g., Cr(VI) and As(V)) (Johnston and Chrysochoou, 2016; Xiu *et al.*, 2018). As ferrihydrite progressively changes into the crystalline phase, the surface area and the capacity to scavenge metal ions decrease. Consequently, the ferrihydrite-sorbed metals would undergo remobilization or redistribution (Perez *et al.*, 2019).

2.4.2 Goethite

Goethite (α-FeOOH) is found in nearly all weathering surroundings and is common in sediment, ore and soil (Randall *et al.*, 1999; Guo *et al.*, 2016). Goethite has good thermodynamic stability and forms from the recrystallization of ferrihydrite, which takes place at extreme conditions of pH (<4, >10), lower temperature, and ionic strength (Schwertmann and Murad, 1983). The transformation of goethite from other relatively metastable oxyhydroxides such as ferrihydrite and lepidocrocite usually occurs via the dissolution-precipitation mechanism (Vu *et al.*, 2010). Commonly, the morphological shape of goethite is often acicular (Kakuta *et al.*, 2014), while its structure is made up of double bands of edge-sharing $FeO_3(OH)_3$–octahedral, that are connected by corner-sharing to construct octahedral tunnels (Parkman *et al.*, 1999; Randall *et al.*, 1999).

Goethite demonstrates a strong capacity for the sorption of heavy metals due to its large number of hydroxyl groups and high specific surface area, varying from 18 to 132 m^2/g (Villalobos *et al.*, 2003; Ganta *et al.*, 2021). For example, cations (e.g., Co, Zn, Cd, Cu, Ni) are absorbed onto the surface of goethite (Coughlin and Stone, 1995; Angove *et al.*, 1999). Furthermore, different varieties of cations (e.g., Zn, Cd, Cu, Co, Ni) can also be attached to goethite through Fe^{3+} partial substitution (Manceau *et al.*, 2000).

2.4.3 Hematite

Hematite (α-Fe_2O_3) has a high degree of thermodynamic stability and is typically the end-product of the transition of all other iron oxides (Al-Hakkani *et al.*, 2021). Hematite belongs to the space group of $R\bar{3}c$ and has a structure made up of hexagonally close-packed arrays of the O^{2-} group in the (001) direction. With the normal positioning of two Fe^{3+} sites adjacent to a vacant site, the Fe^{3+} ions fill two-thirds of the octahedral crevices (Bolanz *et al.*, 2013). Hematite (nano)crystals often have platy, rounded, and rhombohedral morphologies (Cornell and Schwertmann, 2003a).

Hematite nanoparticles can be formed as a result of ferrihydrite transition at circumneutral pH conditions, high ionic strength, and temperature, or low water activity (Börsig *et al.*, 2017). Ferrihydrite particle aggregation, particle development, recrystallization through reprecipitation, and dissolution activities, have all been reported as part of the formation process (Shi *et al.*, 2020). The crystallization entails several events, such as oxy-linkage formation, ferrihydrite particle dehydration, cation vacancy repartition, and hydroxyl group deprotonation (Shaw *et al.*, 2005). In the course of the complicated transition process and high specific surface area (10 to 90 m^2/g), heavy metals (e.g., Ni, Sb, Zn, Cd, As, Pb, Cr) can be entrapped mainly through adsorption into the matrix of hematite (Jeon *et al.*, 2003; Al-Hakkani *et al.*, 2021).

2.4.4 Magnetite

Magnetite (Fe_3O_4) is usually found around igneous rocks in prevalently iron-reducing media e.g. soil and sediments (Wu *et al.*, 2019; Huang *et al.*, 2020). It is formed through

various mechanisms, such as biological degradation of ferric oxides, biomineralization of magnetotactic bacteria, iron metal corrosion, and chemical coprecipitation of Fe^{2+} and Fe^{3+} salts (Mirabello *et al.*, 2016). Magnetite morphology differs depending on the formation mechanisms (Guo and Barnard, 2013). In terms of thermodynamics, magnetite is more stable in suboxic to anoxic environments (Huang *et al.*, 2020) and is susceptible to oxidation and transformation into maghemite under aerated environments (Jolivet *et al.*, 2004).

Magnetite has a stoichiometric ratio of 1:2 for Fe^{2+} and Fe^{3+} ions respectively. It has a cubic inverse spinel structure and belongs to the space group of $Fd\bar{3}m$ (Sebastian *et al.*, 2019). Half of the Fe^{3+} ions in the unit cell, which contains 8 Fe^{2+} cations, 16 Fe^{3+} cations, and 32 O^{2-} anions, fill the tetrahedral spaces, whereas the remaining half and all the Fe^{2+} ions take up octahedral spaces (Lavina *et al.*, 2002). Magnetite has been frequently utilized to sequester redox-responsive toxic metallic ions (e.g., U(VI), Cr(VI), and Hg(II)) due to the structural ability of Fe^{2+} to behave as an electron donor (Zhang *et al.*, 2017; Li *et al.*, 2020). Additionally, because of its non-stoichiometric form and its oxygen structure flexibility, magnetite has a high capacity to retain diverse metal ions through Fe ion substitution, such as divalent ions (e.g., Mn^{2+}, Ni^{2+}, Zn^{2+}, Co^{2+}, Mg^{2+}), trivalent ions (e.g., Cr^{3+}, Al^{3+}, V^{3+}), and also tetravalent ions (e.g., Ti^{4+}) (Li *et al.*, 2020). In certain situations, substitution may raise the superficial hydroxyl groups and surface area of magnetite, hence enhancing its adsorption capacity towards metal ions (Liang *et al.*, 2013).

2.4.5 Schwertmannite

Schwertmannite is well-known to have a formula of $Fe_8O_8(OH)_{8-2x}(SO_4)_x$, where $1.0 \leq x \leq 1.75$. It is typically seen in acid mine drainage and natural sulfate-rich surroundings (Antelo *et al.*, 2013). It forms in acidic and oxic (pH 3 – 4) environs and has irregular crystals that are poorly defined (Song *et al.*, 2015). Schwertmannite is metastable and easily transforms over time to other phases of more stable Fe^{3+} oxides, such as goethite, under the right pH and oxidizing conditions (Choppala and Burton, 2018). Schwertmannite has clusters of

quasi-spherical particles (Qiao *et al.*, 2017) or hedgehog-shaped morphologies (Feng *et al.*, 2021).

Schwertmannite is structurally similar to akaganéite, consisting of FeO_6 octahedral unit cells that form double chains with the presence of SO_4^{2-} ions as tunnel and adsorbed sulfate (Knorr and Blodau, 2007). Besides surface complexation with the hydroxyl groups, it has been shown that heavy oxyanions can be sequestered via ion and/or ligand exchange with tunnel sulfate on the surface of schwertmannite (Antelo *et al.*, 2012). Thus, schwertmannite demonstrates a high capacity for the retention of toxic metals (e.g., Cr, Cu, and As) and is of great ecological importance (Sánchez-España and Reyes, 2019).

2.4.6 Jarosite

Jarosite is a mineral that occurs naturally in acidic, sulfate-rich surroundings, and is also produced as processing wastes in the biohydrometallurgical industry. Jarosites are often formed at low pH (~1 – 3) in high-sulfate surroundings and change into goethite when pH increases (Zolotov and Shock, 2005; Desborough *et al.*, 2010). Jarosites can be quickly converted to green rust sulfate intermediate by high Fe^{2+} concentrations under moderately acidic to circumneutral media, and afterwards displaced by goethite; while when Fe^{2+} concentrations are low, it changes to lepidocrocite (Karimian *et al.*, 2018).

Jarosites are known to have a generic expression of $AB_3(TO_4)_2(OH)_6$, where *A*-site is typically a monovalent ion (e.g., K^+, Na^+, Ag^+, H_3O^+, and NH_4^+); *B*-site is often occupied by Fe^{3+} with octahedral coordination, while the tetrahedrally coordinated *T*-site is typically comprised of S^{6+} (Kendall *et al.*, 2013). Jarosite has a crystal framework in the rhombohedral space group of $R\bar{3}m$ (Zhao *et al.*, 2016). Ion diffusion may be facilitated by the open channel structure (Zhao *et al.*, 2016). Jarosite crystals typically have a compact texture and are composed of rounded and intergrown hexagonal, pyramidal, rhombohedral, and dipyramidal rhombs (Gasharova *et al.*, 2005; Cogram, 2017). Due to the three crystallographic cation sites with varied coordinating environs (Savage *et al.*, 2005), toxic metal ions (e.g., As, Cd, Zn, Cr, Cu, and Pb) can be successfully integrated into the crystal lattice of jarosite by filling the A-, B-, and T-sites (Kendall *et al.*, 2013; Cogram, 2017;

Aguilar-Carrillo *et al.*, 2018). Jarosite can also scavenge metal ions at the mineral interface via adsorption or coprecipitation (Smith *et al.*, 2006).

In summary, the formation of iron compounds (oxides, oxyhydroxides, and hydroxysulfates) involves two basic mechanisms (Cornell and Schwertmann, 2003a):

(1) *direct precipitation* from Fe^{2+} or Fe^{3+} containing solutions, and

(2) *transformation of* an iron compound precursor, either by a dissolution/reprecipitation or via a solid-state transformation process involving internal arrangements within the structure of the solid precursor.

Various pathways of the formation are depicted in Figure 2.5 (Barrón and Torrent, 2013).

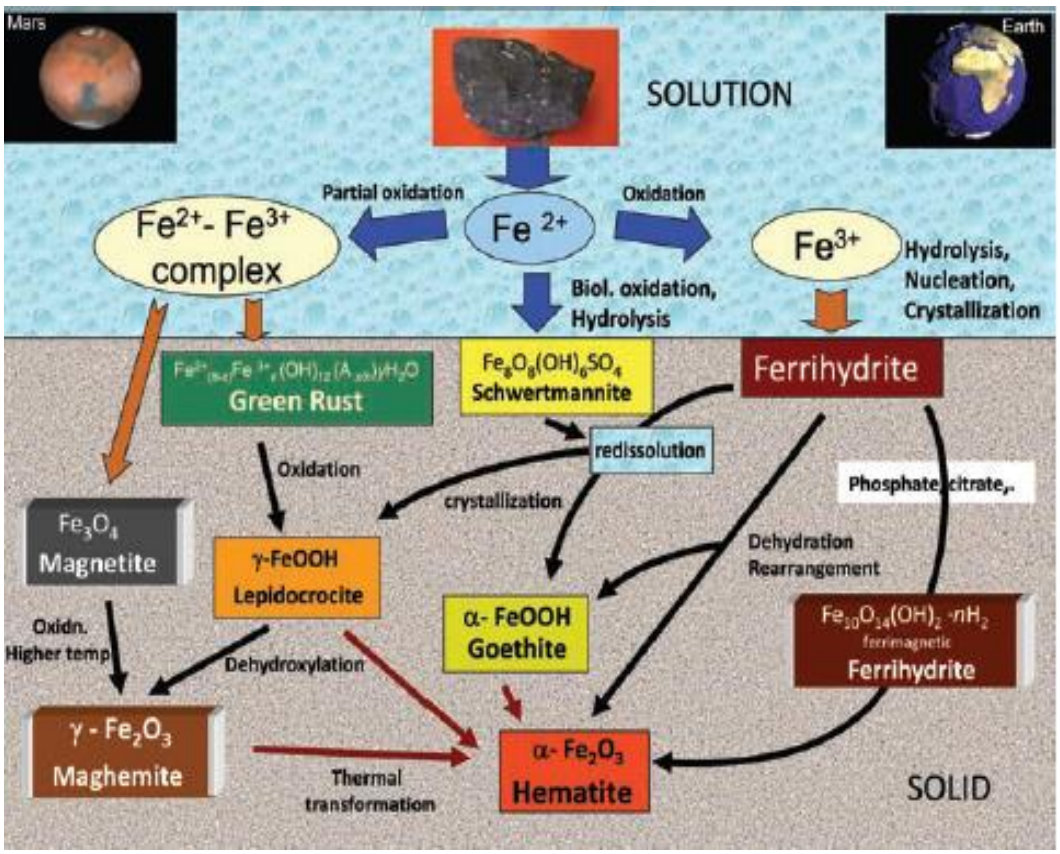

Figure 2.5: Schematic representation of major formation and transformation pathways for common iron oxides, oxyhydroxides, and hydroxysulfates

Source: adapted from Barrón and Torrent (2013)

2.5 Process conditions influencing heap bioleaching and the formation of iron precipitates

Mineral dissolution and iron precipitation as related to typical heap bioleaching are influenced by several factors (Table 2.4), such as the physicochemical parameters, biological factors, ore properties, and processing conditions (Ghorbani *et al.*, 2011).

Table 2.4: Parameters influencing heap bioleaching operations and the formation of iron precipitates

Factors	Properties influencing bioleaching
Physical and chemical factors	Redox potential, H_2O potential, CO_2 content, pH, O_2 content and availability, temperature, Fe(III) concentration, surface tension, light, nutrient availability, presence of inhibitors, pressure
Biological factors	Microbial diversity, metal tolerance, microbial activities, spatial distribution of microbes, microbial adaptation strength, population density, attachment to ore particles
Ore properties	Porosity, acid consumption, galvanic interactions, grain size, formation of secondary minerals, surface area, mineral type, hydrophobicity, mineral dissemination
Processing conditions	Rest periods, heap geometry, circulation of bacterial lixiviant and flow rates to heap, pulp density, weather conditions

While careful consideration of all these factors are quite important, significant impacts of pH, temperature, and redox potential are further discussed as applied to bio-oxidation and bioleaching processes and their corresponding influence on the amount of iron precipitate formed.

2.5.1 Effect of pH

The stability of jarosite and the amount to which it precipitates are both affected by the solution pH (Dutrizac and Jambor, 2000). Dutrizac and Jambor (2000) reported that increasing the acid concentrations reduces the extent to which synthetic jarosite precipitates. Furthermore, the authors explained that the degree of precipitation increases with increasing pH until other Fe compounds are precipitated, which occurs at pH > 2 at 100 °C. At 100 °C, a pH of 1.5 – 1.6 appears to be ideal for the formation of jarosite. Higher temperatures can be utilized in practice to offset excessive acidity. In another work on the effect of the initial solution pH on the precipitation of sodium jarosite at 97 °C, Dutrizac (1982) found that a nearly constant amount of jarosite was precipitated for pH values < 1.5, although, the amount of precipitate decreases sharply at lower pH values. Furthermore, when the initial pH was ~0.5, no precipitate forms because the equilibrium has been displaced in favour of solution species. Although it has been demonstrated that the amount of jarosite is strongly influenced by the acidity of the solution, the composition of the precipitate remains nearly constant.

pH can greatly influence the aqueous reaction chemistry, particularly the formation of jarosite, which has been considered a major product specie responsible for passivation in mineral bioleaching such as chalcopyrite. A low pH is advantageous to inhibiting jarosite production. However, several thermophilic microbes are unable to withstand very low pH (< 1.0), signifying that the formation of jarosite cannot be completely avoided (Vilcáez *et al.*, 2008). In a work carried out by Ojumu and Petersen (2011) on the impact of solution pH (0.8 – 2.0) on the kinetics of Fe^{2+} oxidation using *Leptospirillum ferriphilum* in continuous culture, the results demonstrated that Fe^{3+} ion precipitation increases with an increase in solution pH. In a study carried out by Nazari *et al.* (2014), it was found that the highest amount of Fe^{3+} ion precipitated at above pH 2.2, and a decrease in the solubility of phosphate ion was observed at pH 1.6, which was attributed to co-precipitation as a constituent element of jarosite. Wanjiya *et al.* (2015) reported a 33 and 52% decrease in the mass of Fe^{3+} ion precipitate following a decrease in pH from 1.7 to 1.5 and 1.3 respectively, after operating for 10 days. Small-scale experiments on bio-oxidation of Fe^{2+} demonstrated schwertmannite as the main Fe^{3+} mineral phase to precipitate at pH 3.0 (Bigham *et al.*, 1996).

Moreover, Liao *et al.* (2009) reported the production of pure schwertmannite by *Acidithiobacillus ferrooxidans* at pH 2.0, when NH_4^+ concentration was < 10 mM with the absence of other alkali cations from the cultures. Thus, it is quite evident that the pH of the medium performs a vital function in the formation of an iron precipitate. The relationship between solution potential and pH can determine precipitate formation (refer to Figure 2.3). Through electrochemical analysis, Warren *et al.* (1992) studied the passivation of chalcopyrite in an anodic polarized system. In their work, chalcopyrite was responsive to pH at high potential while it was less responsive to pH at low potential, and as a result of the electrolysis of H_2O in the ultra-passivation area, an increased current was observed within the condition of a higher potential.

2.5.2 Effect of temperature

Temperature is an important parameter that affects the precipitation of jarosite. Jarosite is an important iron precipitate in the hydrometallurgical industry. Among other ranges of conditions likely to be encountered in hydrometallurgical practice, Dutrizac (2008) investigated the effect of temperature on the precipitation of potassium jarosite in sulfate media. The amount of precipitate in sulfate solutions at 97 °C increases with increasing retention times up to approximately 10 h, although nearly constant product yields are attained for extended durations of reaction. Despite the differences in the precipitate amount, the composition remains nearly consistent and is typical of potassium jarosite, the only phase discovered by XRD analysis of the products. Dutrizac (2008) further explained that the amount of potassium jarosite precipitate increases with increasing temperature to ~100 °C over a 24 h reaction time but remains relatively constant at higher temperatures. The product composition, on the other hand, is the same at all investigated temperatures.

The kinetic rate of mineral sulfide bioleaching is enhanced by an increase in temperature. Based on the optimum temperature, the microbes employed in chalcopyrite bioleaching vary. Generally, the maximum dissolution of chalcopyrite in a bioleach process can be achieved in an extreme thermophile Archaea system, then a moderate thermophile system, and finally the mesophile system (Fu *et al.*, 2008; Gautier *et al.*, 2008). The rate of iron precipitation depends on temperature, and it is widely accepted that rapid and complete

precipitation occurs with an increase in temperature. Leduc *et al.* (1993) studied the characterization of ten different isolates of *Thiobacillus ferrooxidans* in the temperature range of 2 – 35 °C. It was reported that Fe^{3+} ion precipitation was reduced at temperatures less than 10 °C and no formation of Fe^{3+} ion precipitate was observed at 2 °C. Daoud and Karamanev (2006) reported the minimal formation of Fe^{3+} ion precipitate at 35 °C. Bigham *et al.* (2010) in their work characterized the jarosites synthesized via a chemical process over a temperature range from 2 – 40 °C. It was observed that the precipitation of Fe^{3+} ions increases with temperature. With an increase in temperature from 36 – 45 °C, Wang *et al.* (2006) observed the transformation of schwertmannite to jarosite. It is noteworthy to state that the study of the influence of temperature on Fe^{3+} ion precipitation is strictly dependent on pH (refer to Figure 2.2). Daoud and Karamanev (2006) stated that the precipitation of Fe^{3+} ions at higher pH values could be minimized at lower temperatures.

Enhanced leach rate in acidic chloride media was achieved by raising the process temperature from 60 to 70 °C, with considerable stability of leaching kinetics noticeable between 70 and 90 °C (Dreisinger and Abed, 2002). In the work of Sokić *et al.* (2009), it was reported that the chalcopyrite dissolution rate improved by 42% in 1.5 M H_2SO_4 within 240 min as the leaching temperature was raised from 70 to 90 °C. Córdoba *et al.* (2008a) also reported the impact of temperatures between 35 and 68 °C, with significant Cu leaching increased from < 30 to > 80%.

2.5.3 Effect of redox potential (E_h)

Redox potential is an important process factor in the dissolution of mineral ore, such as chalcopyrite. A low potential promotes the disintegration of chalcopyrite while a high potential hinders the release of copper and can result in the passivation of chalcopyrite (Third *et al.*, 2002; Wang *et al.*, 2016a). Velásquez-Yévenes *et al.* (2010) in their work explained the influence of media potential on the leach rate of chalcopyrite. In a controlled experiment at 0.2 M HCl with 0.5 g/dm^3 Cu^{2+} at 35 °C, it was reported that the leached products greatly depend on the solution potential. Within the range of 540 – 580 mV (SHE, standard hydrogen electrode), the leaching rate increased while the active potential range

was proposed to be between 550 – 620 mV (SHE). At a potential > 630 mV (SHE), the dissolution rate of chalcopyrite was observed to be slow. In an experiment conducted with sulfuric acid media, Sandström *et al.* (2005) suggested that at redox potential of 620 mV (SHE), chalcopyrite leach rate was improved. Passivation occurs within the potentials of 690 – 840 mV (SHE) at a low temperature of 25 °C or at 840 mV and higher temperature (> 65 °C). Koleini *et al.* (2011) reported that the highest copper extraction could be achieved between 610 – 640 mV (SHE). This is well corroborated by the result of other researchers (Sandström *et al.*, 2005; Viramontes-Gamboa *et al.*, 2010). In addition, Viramontes-Gamboa and co-workers concluded that irrespective of acidity, impurities or temperature, chalcopyrite will always remain in the active state below 685 mV (SHE); however, dissolution slows down due to the passive nature of chalcopyrite for a potential of 750 mV (SHE) upward (Viramontes-Gamboa *et al.*, 2007; Viramontes-Gamboa *et al.*, 2010). Several methods have been demonstrated to control the redox potential to benefit metal extraction, such as the addition of a chemical oxidizing agent (e.g. H_2O_2) or reducing agent (e.g. Na_2SO_3), employing electrochemical reactors and controlling the dissolved O_2 (Zhao *et al.*, 2019).

2.6 Precipitation in bioleaching: a case of chalcopyrite mineral

This section reviews the negative impact of iron precipitation in bioleaching operations using chalcopyrite (a copper-bearing mineral) as a case study.

Due to rapid industrialization, high-grade and oxides of copper resources have been extensively exploited and are fast depleting while the world demand for copper is increasing tremendously. This has consequently led the mineral industry to a major challenge regarding the urgency of processing low-grade copper ores, especially chalcopyrite ($CuFeS_2$), which is the most enriched copper-containing ore in the world. However, the slow development of $CuFeS_2$ bioleaching at the industrial level is due to its refractory nature and low dissolution kinetics. This behaviour has been reported to be provoked by a passivation layer identified on the surface of $CuFeS_2$. The passivation layer has been investigated (Yu *et al.*, 2011; Zeng *et al.*, 2011; Zhu *et al.*, 2011; Zhao *et al.*, 2015)

with the aid of technical analyzing tools such as Fourier transform infrared (FT–IR), X-ray diffraction (XRD), X-ray photoelectron spectroscopy (XPS), X-ray absorption near edge spectroscopy (XANES), scanning electron microscopy/energy-dispersive X-ray spectroscopy (SEM/EDX), electrochemical impedance spectroscopy (EIS), and (AFM) atomic force microscopy. The passivation layer was believed to contain some species which are mainly polysulfides (S_n^{2-}), elemental sulfur (S^0), and insoluble sulfate (SO_4^{2-}) (mainly jarosite). They are reviewed in this section.

2.6.1 Polysulfides

Polysulfides (chiefly metal-deficient polysulfides) can notably lead to passivation during chalcopyrite dissolution. In the early work conducted by Linge (1976) on the dissolution of chalcopyrite in acidic ferric nitrate, it was observed that the metal-deficient polysulfide produced which resulted in the recalcitrant nature of chalcopyrite was caused by the immediate dissolution of Fe ahead of Cu at the initial stage of the leaching operation. This observation was also confirmed in a later work by Fu *et al.* (2012) on chalcopyrite bioleaching using *Acidithiobacillus ferrooxidans*. The authors concluded that polysulfide ($Cu_4Fe_2S_9$) should be the principal product responsible for the passivating nature of chalcopyrite during the microbe-mediated leach process. Some authors reported the thickness of the passive film to be less than 1 μm (Parker *et al.*, 1981; Hackl *et al.*, 1995). Another work explained that the favoured disintegration of Fe resulted in the production of Fe-deficient polysulfide, and thus, hindered the diffusive movement of ion from the juncture of chalcopyrite/passive layer to the juncture of passive layer/solution, which led to passivation (Yang *et al.*, 2018). In recent work by Peng *et al.* (2019) on the dissolution of chalcopyrite at low temperatures using *Acidithiobacillus ferrivorans*, it was revealed that polysulfide was the main possible passivating specie at 6 °C. Several other authors also reported polysulfide as the main passivating specie in chalcopyrite bioleaching (Peng *et al.*, 2019; Zeng *et al.*, 2020; Liao *et al.*, 2021; Lv *et al.*, 2021). On the contrary, Parker *et al.* (2003) and Klauber (2008) believed that polysulfides cannot be linked as the specie accountable for the passive attribute of chalcopyrite because of its instability.

2.6.2 Elemental sulfur

Elemental sulfur was reported to be the major passivating species during chalcopyrite microbial dissolution. In the work of Dutrizac (1989), it was suggested that elemental sulfur should be the major specie responsible for the passivation of chalcopyrite. In a leaching experiment performed at 95 °C in the presence of ferric sulfate, it was observed that > 94% of sulfur was in elemental form (S^0) while < 6% was in the form of sulfate. This elemental sulfur obstructs the free flow of electrons at the mineral/solution interface, thus it inhibits the redox reactions (Munoz *et al.*, 1979). Bevilaqua *et al.* (2004) observed the principal constituents of the sorption film to be chiefly comprised of cells, biomolecules, and the sulfur element. It was noted that the sorption film behaved as a capacitor, prohibiting the diffusive movement of ions and molecules on the surface of the mineral. In a study carried out by Khoshkhoo *et al.* (2014), an increase in the amount of elemental sulfur with the leaching time was observed. It was concluded in the study that the goethite (FeOOH) generated jointly with the elemental sulfur led to the formation of a passive layer which later interfered with the dissolution of chalcopyrite. Other authors also reported elemental sulfur as the main passivating specie in chalcopyrite bioleaching (Yang *et al.*, 2020; Zeng *et al.*, 2020; Liao *et al.*, 2021; Nourmohamadi *et al.*, 2021; Zhang *et al.*, 2021a). Nevertheless, some studies have suggested that elemental sulfur should not be the passivating specie in chalcopyrite leaching because of the ease with which it oxidized to sulfate (Gu *et al.*, 2013; Liu *et al.*, 2015).

2.6.3 Iron hydroxysulfates

In several studies conducted, iron hydroxysulfates (predominantly jarosite) have likewise been identified as the chief specie causing passivation in the dissolution of chalcopyrite. At low potential, Sandström *et al.* (2005) observed the oxidation of elemental sulfur to sulfate in work carried out on the characterization of the surface products of chemically and bioleached chalcopyrite. The authors concluded that the main cause of passivation was jarosite. Klauber (2008) argued that polysulfide was highly reactive and that oxygen could aid its oxidation to elemental sulfur. However, it was also stated that the formed elemental sulfur might also be responsible for the passivating nature of chalcopyrite. Despite this,

elemental sulfur could easily fall away from the surface of chalcopyrite, hence, it was concluded that the principal specie responsible for the passivation should be jarosite. The electrons can be displaced to Fe^{3+} as a result of the disulfide oxidation via surface protonation and hydration reactions, hence generating thiosulfate. By oxidation, the thiosulfate can be changed to ferric sulfates, which act as a crystal nucleus provoking the production of jarosite, which later leads to the recalcitrant attribute of chalcopyrite (Parker *et al.*, 2003). In a study of the electrochemical behaviour of chalcopyrite, Zeng *et al.* (2011) reported that the initial stage of chalcopyrite dissolution was an acid-consuming stage that needed a constant supply of acid to the process to make certain of a steady and low pH. It was concluded that the passivation layer was chiefly comprised of jarosite. Other authors have also reported jarosite as the main passivating specie in chalcopyrite bioleaching (Sasaki *et al.*, 2009; Zhang *et al.*, 2014; Masaki *et al.*, 2018; Ma *et al.*, 2021; Zhang *et al.*, 2021a). However, a few authors believed that the bioleaching of chalcopyrite should not be inhibited, notwithstanding the considerable quantity of jarosite produced. This was attributed to the fact that the porous and loosely attached jarosite could easily fall from the surface of chalcopyrite (Gu *et al.*, 2013; Liu *et al.*, 2015).

According to the existing literature, the dissolution and passivation mechanism of chalcopyrite bioleaching can be illustrated according to Figure 2.6 (modified from Zhao *et al.* (2019)). In path 1, chalcopyrite degrades into copper (I) sulfide (Cu_2S), which enhances the dissolution rate. In path 2, chalcopyrite readily releases Fe^{2+} and Cu^{2+}, forming a metal-deficient polysulfide. In path 3, a film of elemental sulfur is generated. In path 4, jarosite precipitates on the surface of chalcopyrite. Paths 2, 3, and 4 have been reported to cause the passivation of chalcopyrite.

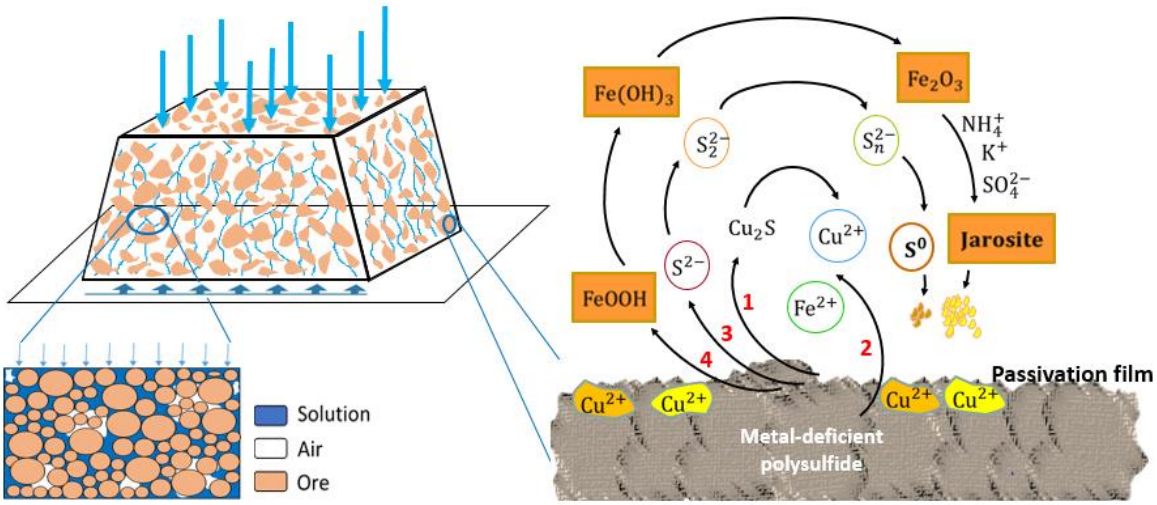

Figure 2.6: Dissolution and passivation mechanisms of chalcopyrite bioleaching

Source: modified from Zhao *et al.* (2019)

Based on these reviewed works, it may be concluded that the major products responsible for the passive nature of chalcopyrite are the species that contained sulfur as a constituent. It is therefore essential to characterize these transitional species containing sulfur in chalcopyrite dissolution. Table 2.5 shows some selected works on possible passivating species during the bioleaching of chalcopyrite.

Table 2.5: Selected publications on passivating species identified during chalcopyrite bioleaching

Microbes	Ore chemical analysis	Cause of passivation	Residue analysing tool	References
Acidithiobacillus ferrooxidans	-	Elemental sulfur	EIS and AFM	Bevilaqua *et al.* (2004)
Acidithiobacillus ferrooxidans	Cu (31.91%), Fe (23.20%), and S (27.14%)	Jarosite	XRD	Fu *et al.* (2008)
Acidithiobacillus ferrooxidans	Cu (35.41%), Fe (29.56%), S (30.27%), and Si (0.82%)	Jarosite	Raman spectroscopy, XRD and FT-IR	Sasaki *et al.* (2009)
Leptospirillum ferriphilum and *Acidithiobacillus caldus*	-	Jarosite	XRD	Zhou *et al.* (2009)
Mixed thermophiles	Cu (34.63%), Fe (25.35%), and S (30.45%)	Jarosite	XRD, Raman spectroscopy, and XANES	Zhu *et al.* (2011)
Acidithiobacillus caldus and *Leptospirillum ferriphilum*	$CuFeS_2$ (98%) and silicate (2%)	EPS and jarosite	SEM/EDX	Zeng *et al.* (2011)
Acidithiobacillus ferrooxidans	Cu (33.15%), Fe (29.86%), and S (33.22%)	EPS and jarosite	XRD	Yu *et al.* (2011)
Acidithiobacillus caldus	Cu (34.46%), Fe (31.53%), and S (33.12%)	Iron-deficient polysulfide	XRD and XPS	Zhao *et al.* (2015)
Sulfobacillus thermosulfidooxidans and *Leptospirillum ferriphilum*	Cu (34.46%), Fe (31.53%), and S (33.12%)	Polysulfide and jarosite	XRD and XPS	Zhao *et al.* (2015)
Acidithiobacillus caldus and *Leptospirillum ferriphilum*	Cu (34.46%), Fe (31.53%), and S (33.12%)	Polysulfide	XPS	Wang *et al.* (2016a)

2.7 Effect of iron precipitation on bio-oxidation and bioleaching processes

Iron precipitation has both positive and negative influences on the bio-oxidation and processing of sulfide ores in the mineral industry. In zinc hydrometallurgical operation, the precipitation of jarosite-type compounds is beneficial as it serves as the exit route for undesired iron, sulfate ions, alkali ions, and other impurities (such as lead and silver) from the processing circuit (Dutrizac and Jambor, 2000; Murphy *et al.*, 2009). It has been observed that jarosite precipitate performs a vital function in the development and stabilization of biofilms during the generation of Fe^{3+} ion, which is a significant leaching agent in hydrometallurgical operations (Kinnunen and Puhakka, 2004). Furthermore, it has also been reported that jarosite precipitate acts as a support for microbial attachment, which helps in enhancing the bio-oxidation rate (Chowdhury and Ojumu, 2014). Jarosite precipitate has also been used for remediating polluted sites (Welch *et al.*, 2007) and as a raw material in the production of pigments and construction materials (Das *et al.*, 1996; Dutrizac and Jambor, 2000). From the perspective of material science, schwertmannite has great potency as an adsorbent for the uptake of heavy metals from polluted water (Liao *et al.*, 2009). The management of jarosite production has also been reported through variations in solution pH during the microbial ferrous ion oxidation process (Wanjiya *et al.*, 2015). While there seem to be highlighted advantages of the iron precipitation process in the biohydrometallurgical industry, there are proofs that its disadvantages are of great impart.

Apart from the negative impacts on leach kinetics and biological processes, the production of iron precipitates in the microbial oxidation of Fe^{2+} and bioleaching processes may affect the overall efficiency of such operations. The negative influence of iron precipitate formation, particularly jarosite, in the context of the bio-oxidation and bioleach heap are highlighted below:

- It causes the pumps, valves, pipes, and other peripheral equipment in the processing setup to become clogged.
- It deprives the system of vital ferric ions, which serve as an important agent for chemical oxidative reactions in the mineral sulfide dissolving process (Rawlings, 2002).

- It occupies most of the available space in the immobilization matrices, thus, limiting the amount of biomass retention (Jensen and Webb, 1995).
- It clogs up the heap bed system resulting in partial, or at times, complete blockage of the passageway of liquid and gas flow in the heap system (Jensen and Webb, 1995; Daoud and Karamanev, 2006).
- It interferes with the respiratory mechanism of the bacteria by denying them complete access to available nutrients (Nazari *et al.*, 2014).
- It adheres its crystal-like structures to the surface of the sulfide ores, forming a compact thin layer of membrane that inhibits the transfer of the substrate and metabolites.
- It takes up accessible sites on the surface of minerals, preventing bacteria from adsorbing onto the mineral deposits and, as a result, impeding a successful bio-oxidation process.
- It leads to the development of the kinetic barrier by impeding the reactants and products from diffusing across the precipitation region (Meruane and Vargas, 2003; Liu *et al.*, 2009).

Most notably, the formation of iron precipitates has been reported to decrease the leaching efficiency by scavenging/entrapping the target metal in the prevailing bioleach conditions. The large surface area owing to the colloidal attribute of these precipitates is one of the factors responsible for their reduction in the extraction efficiency of bioleaching operations by scavenging metals of interest, thereby, hindering the release of desired metals into solution. While sulfur, disulfur, polysulfide, and jarosite have all been found to hinder the solution of different mineral sulfides, jarosite has also frequently been reported to entrap some metals during the bioleach operation. Recently, some studies have shown that a considerable quantity of metals could be recovered from the treatment of industrial jarosite residue formed during hydrometallurgy processes. For example, in a study conducted by Ju *et al.* (2011), 97 and 87% of Zn and Cu respectively, could be directly recovered from jarosite residue generated through zinc hydrometallurgy. Further, in a work conducted by Liu *et al.* (2017) on the recovery of metals from jarosite via sulfuric acid roasting using microwave and water leaching, it was reported that 89.4, 80.7, 85.1, 90.7, 61.3, and 48.8% of

Fe, Zn, In, Cu, Ag, and Cd respectively, could be recovered. Córdoba *et al.* (2008b) stated that controlling the formation of Fe^{3+} precipitate might be difficult to attain because of the spontaneous generation of the precipitates. Table 2.6 shows some valuable metals recovered from industrial jarosite residue.

Table 2.6: Source, chemical composition, and recovery of metals from various industrial jarosite residue

Source of jarosite residue	Chemical composition of jarosite residue	Phase present	Recovery technique	Percentage recovery of metal	Reference
Baiyin Nonferrous Metals Group (China)	Zn (7.06%), Pb (4.00%), Fe (19.92%), Ag (0.009%), Cu (0.21%), As (0.18%), Cd (0.11%), SiO_2 (10.12%), SO_4^{2-} (38.17%)	$K_2Fe_6(SO_4)_4(OH)_{12}$, $ZnO.Fe_2O_3$, $PbSO_4$, $CaSO_4.0.5H_2O$, SiO_2	Roasting, NH_4Cl leaching, reduction with Zn powder, and NaOH leaching	Zn (97.5%), Pb (95.3%), Cu (95.4%), Cd (100%), Ag (100%)	Ju *et al.* (2011)
Impala Base Metal Refinery (Gauteng, South Africa)	Ni (4.9%), Fe (38.6%), Cu (0.02%), and other minor elements	$NH_4Fe_3(SO_4)_2(OH)_6$, Fe_2O_3	Leaching with hydrochloric acid	Ni (60%)	Nheta and Makhatha (2013)
Zijin Smelting Plant (Neimenggu, China)	Pb (8.48%), Zn (5.94%), Ag (0.022%), Fe (28.81%), Cu (0.2%), Cd (3.64%), Ba (0.18%), S (10.79%), Si (1.17%), others (40.77%)	$KFe_3(SO_4)_2(OH)_6$, $PbSO_4$, $ZnFe_2O_4$	Roasting and sulfidization-flotation	Pb (66.86%), Ag (81.60%)	Han *et al.* (2014)
Zinc hydrometallurgical plant (Yunnan, China)	Fe (19.79%), Zn (4.55%), Cu (0.15%), Cd (0.12%), Pb (7.37%), S (10.65%), Ag (427.5 g/t), In (92.5 g/t)	$(K,H_3O)Fe_3(SO_4)_2(OH)_6$, $NH_4Fe_3(SO_4)_2(OH)_6$, $(NH_4)_3Fe(SO_4)_3$, $ZnFe_2O_4$	Sulfuric acid roasting using microwave and water leaching	Fe (89.4%), Zn (80.7%), In (85.1%), Cu (90.7%), Ag (61.3%), Cd (48.8%)	Liu *et al.* (2017)
Shanxi Province, China	Fe (26.76%), Zn (6.95%), Pb (3.01%), S (10.16%), Al_2O_3 (1.78%), As (0.33%), SiO_2 (4.74%), MgO (0.50%), CaO (1.83%)	$NH_4Fe_3(SO_4)_2(OH)_6$, $Pb(Fe_3(SO_4)_2(OH)_6)_2$, $ZnFe_2O_4$	Direct reduction and magnetic separation	Pb (96.97%), Zn (99.89%), Fe (91.97%)	Wang *et al.* (2018)
Baiyin Nonferrous Metals Group (China)	Pb (3.24%), Zn (7.19 %), Cu (0.24%), S (10.9%), Fe (19.8%), Ag (0.0017 %), Ca (1.79 %), Si (3.97%)	Fe_2O_3, $KFe_3(SO_4)_2(OH)_6$ $ZnO.Fe_2O_3$, $ZnSO_4$, $PbSO_4$, Cu_2S, $CaSO_4.0.5H_2O$	Reducing-matting smelting-thermal decomposition reduction	Cu (98.82%), Zn (98.84%), Pb (90.35 %), Ag (97.17%)	Tang *et al.* (2018)

2.8 Retention mechanism of metal ions onto iron compounds

Numerous investigations employing various experimental procedures and techniques have been conducted on the mechanism of interaction between metal and iron compounds (oxides, oxyhydroxides, and hydroxysulfates). Based on literature findings, metal ion retention happens mostly during adsorption, precipitation/coprecipitation, and mineral phase change processes (Hu *et al.*, 2018). Figure 2.7 summarizes all of the retention mechanisms described in the literature, such as structural incorporation, surface complexation, surface precipitation, etc.

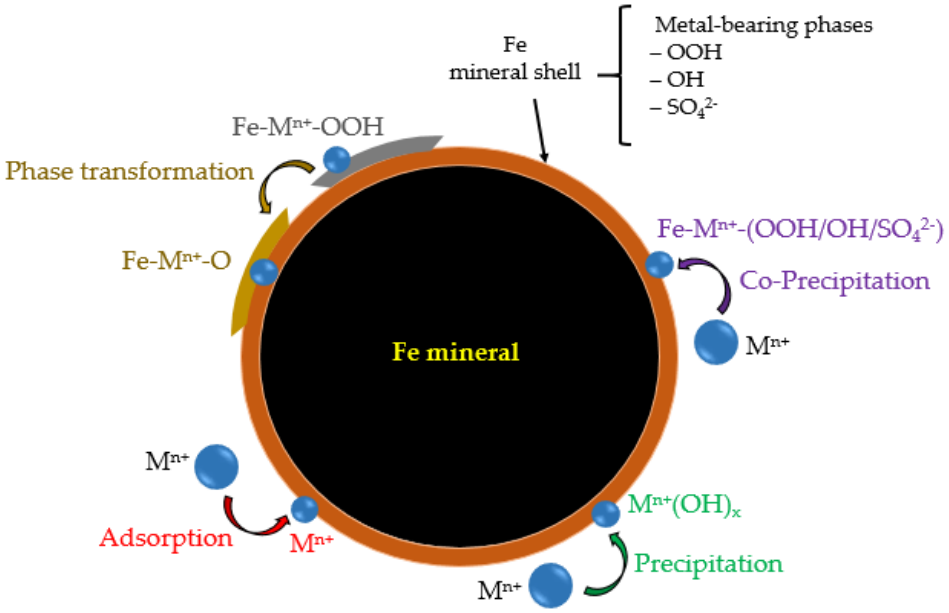

Figure 2.7: Mechanisms involved in the retention of metal ions by iron minerals

2.8.1 Iron mineral transformation process

Iron mineral transformation is often influenced by reaction pH, temperature, and solution chemistry (Hu *et al.*, 2018). At high temperatures, some iron minerals transform, particularly those containing water molecules and/or hydroxyl groups. Ferrihydrite, goethite, lepidocrocite, akaganéite, and schwertmannite are examples of these minerals (Rzepa *et al.*, 2016). During the process of formation and transformation, iron precipitates can uptake metal ions. Although the general course of the transformation processes are

well understood, the influence of numerous crystal-chemical and chemical variables on the transformation mechanisms and product attributes is still widely debated (Cornell and Schwertmann, 2003a; Wells *et al.*, 2006).

2.8.2 Surface precipitation/coprecipitation process

Surface precipitation, on the other hand, may occur when metal sorption densities increase (Ford *et al.*, 1997). In long-term sorption investigations, initially sorbed metals can be incorporated into the structure of iron minerals via lattice diffusion or pore diffusion (Barrow *et al.*, 2012). Coprecipitation is a similar process that involves the simultaneous removal of metal ions during the formation of iron minerals (Lee *et al.*, 2002). This can be accomplished through adsorption, mechanical occlusion, precipitation, and/or structural incorporation (Karthikeyan *et al.*, 1997; Tokoro *et al.*, 2010). Mechanical occlusion happens during the coprecipitation process when discrete metal-bearing phases (e.g. oxide, hydroxide, sulfate, etc.) develop and become occluded inside iron precipitate nanoparticles (Francisco *et al.*, 2018). Iron minerals can be structurally reordered to various crystalline forms under specific conditions. As a result, metals that were initially retained can be redistributed by release and subsequently by readsorption or incorporation into crystalline structural locations (Ford *et al.*, 1997).

2.8.3 Adsorption process

Adsorption is defined as the two-dimensional complexation of metal ions at the interface between a pre-existing solid and the aqueous phase, which frequently includes inner-sphere and outer-sphere surface complexes (Liu *et al.*, 2016b). It is widely accepted that the adsorption of specie on a solid surface occurs in three stages: (i) transport of the adsorbate (ions in the case of solutions) from the bulk to the external surface of the adsorbent, (ii) passage through the liquid film attached to the solid surface, and (iii) interactions with the surface atoms of the solid resulting to chemisorption (strong adsorbate–adsorbent interaction corresponding to covalent bonding) or weak adsorption (weak adsorbate–adsorbent interaction, somewhat comparable to van der Waals forces), in which case desorption may be the outcome (Gupta and Bhattacharyya, 2011). In the case of porous

solids, after passing through the liquid layer adhering to the external surface, the adsorbate slowly diffuses into the pores and becomes entrapped (adsorbed). Any of the abovementioned steps could be the slowest (defining the overall rate of the interaction), and thus, influencing the kinetics of the adsorption process.

In conclusion, apart from the retention mechanism being integrally linked to the structural type of iron mineral species, it is also significantly depending on the physicochemical characteristics of metal ions (e.g. ionic radius, hydration energy, solubility, electronegativity, etc), and the operating conditions (e.g. pH, metal ion concentration, ionic strength, etc.) (Fernandes and Baeyens, 2019; Shi *et al.*, 2020), thereby complicating the interaction between metal ions and iron precipitates.

2.8.3.1 Analytical techniques in identifying adsorption mechanism

Metal ions can be integrated into the mineral structure during the formation of iron precipitates. Additionally, these metals can be adsorbed onto the surfaces or trapped in the interfacial regions between aggregated nanoparticles of precipitates during or after their formation (Zhu *et al.*, 2012). As a result, gaining a better knowledge of the mechanisms by which metals interact with iron precipitates will be vital for minimizing metal loss during sulfide mineral bioleaching.

It should be noted that adsorption mechanisms can only be determined by: (1) employing a variety of analytical techniques and (2) having a good understanding of the chemical form of the adsorbate and adsorbent, the surface nature of the adsorbent, and the chemical or physical interactions between the adsorbent and adsorbate (Volesky, 2007; Lima *et al.*, 2015; Lima *et al.*, 2016). Such analytical techniques include Fourier transform infrared (FTIR) spectroscopy, scanning electron microscopy (SEM), transmission electron microscopy (TEM), energy dispersive spectroscopy (EDS), Raman spectroscopy, X-ray photoelectron spectroscopy (XPS), X-ray diffraction (XRD), thermogravimetric analysis (TGA)/differential thermal analysis (DTA), differential scanning calorimetry (DSC), nitrogen adsorption-desorption isotherms, pH at the point of zero charge (pH_{PZC}), pH at the isoelectric point (pH_{IEP}), solid-state ^{13}C nuclear magnetic resonance (NMR), carbon-

hydrogen-nitrogen (CHN) analysis, Boehm titration, and solution calorimetry (Tran *et al.*, 2017). The application of analytical techniques together with adsorptive thermodynamic data (i.e., change in enthalpy (ΔH) and change in entropy (ΔS)) as well as energies of activation and adsorption, are required to determine if adsorption of adsorbate in aqueous solution is a chemical or physical process (Lima *et al.*, 2015; Tran *et al.*, 2016). The analytical techniques employed in this thesis are further described in Chapter 3.

2.9 Adsorption modeling

Adsorption modeling is a critical component of any adsorption study because it uses adsorption models to interpret experimental data to obtain useful information that aids in the understanding of process mechanisms, process equilibrium dynamics, predicting responses to changes in operational conditions, and optimizing the adsorption process. Kinetic models, isotherm models, and thermodynamic models are frequently utilized to improve the knowledge of adsorption investigations (Tran *et al.*, 2017; Al-Ghouti and Da'ana, 2020; Wang and Guo, 2020).

2.9.1 Kinetics of adsorption of metal ions: theoretical basis

The study of kinetics gives insight into the likely mechanism of adsorption as well as the reaction routes. It is usually difficult to arrive at a definite rate law, which necessitates an accurate understanding of all the molecular information of the adsorbate-adsorbent interactions, along with the energy requirements and stereochemical considerations, as well as the elementary steps that lead to the adsorption of the solute via a specific mechanism (Gupta and Bhattacharyya, 2011).

Kinetics is the study of the rates of chemical processes to understand the factors that govern them. The study of chemical kinetics entails careful monitoring of the experimental circumstances that influence the speed of a chemical reaction and thus aid in the attainment of equilibrium in an acceptable amount of time. Such investigations provide information about the likely mechanisms of adsorption and the various transition stages that occur on the path to the formation of the final adsorbate–adsorbent complex, as well as assist in the

development of suitable mathematical models to explain the interactions (Gupta and Bhattacharyya, 2011).

The rates are determined by the concentrations of the species participating in the adsorption process, and the standard rate law may take the following form:

$$R = k[A]^a[B]^b \ldots \quad (2.6)$$

where k is the rate coefficient and a, b... etc. denote the order of the species, A, B, etc. The precise form of the rate law can reveal information about the reaction mechanism.

The following sub-sections review the important adsorption reaction kinetic models in the literature, namely the pseudo-first-order (PFO) model, pseudo-second-order (PSO) model, and Elovich model.

2.9.1.1 Pseudo-first-order model

The Lagergren equation (Lagergren, 1898) is most likely the first known example of a rate equation for adsorption in liquid-phase systems, especially for PFO kinetics. The model was established on adsorbent capacity. It describes the rate of change in adsorbate uptake with time directly proportional to the difference in saturation concentration levels. The linear form of the PFO equation is expressed below:

$$\ln (q_e - q_t) = \ln q_e - k_1 t \quad (2.7)$$

where q_e and q_t are the quantities of adsorbate uptake (mg/g) at equilibrium and at time t (min) respectively, and k_1 represents the PFO rate constant (min^{-1}). The values of k_1 and q_e can be evaluated from the slope and intercept respectively, of the linearity plot of ln (q_e–q_t) vs t.

The true test of the veracity of Equation (2.7) is established by comparing how experimentally measured q_e values are compared to those derived from plots of ln (q_e–q_t) versus t (Ho and Mckay, 1999; Mckay *et al.*, 1999). If this test is shown to be invalid, higher-level kinetic models must be applied to the experimental data. If the Lagergren equation

does not fit well across the entire range of interaction time, then the adsorption process is much more complex than the basic first-order kinetics-based mechanism.

2.9.1.2 Pseudo-second-order model

The PSO model can adequately describe adsorption kinetic experimental data. It describes the rate of occupation of adsorption sites to be proportional to the square of the number of non-occupied sites. The linearized form of the model is given in Equation (2.8) (Blanchard *et al.*, 1984):

$$\frac{t}{q_t} = \frac{1}{q_e^2 k_2} + \frac{t}{q_e} \tag{2.8}$$

where q_e and q_t are the quantities of adsorbate uptake (mg/g) at equilibrium and at time t (min) respectively, and k_2 represents the equilibrium PSO rate constant (g/mg min). The linear plots of t/q_t versus t can be generated. The values of q_e and k_2 can then be evaluated from the slope and intercept of the plots respectively.

Both theoretical and experimental investigations show that the value of k_2 is typically determined by the initial adsorbate concentration in the bulk phase. As a general rule, the rate coefficient, k_2, decreases as the initial adsorbate concentration increases, where k_2 is regarded as a time-scaling factor (Gupta and Bhattacharyya, 2011).

The initial adsorption rate, h, of a second-order process as $t \rightarrow 0$ is described as

$$h = k_2 q_e^2 \tag{2.9}$$

It is critical to have a clear knowledge of q_e when applying Equations (2.8) and (2.9) to experimental data (Ho *et al.*, 2001). One advantage of using the PSO equation to estimate q_e values is its low sensitivity to the impact of random experimental mistakes.

2.9.1.3 Elovich model

The Elovich equation is based on the assumption that the true solid surfaces are energetically heterogeneous and that neither desorption nor interactions between adsorbed species may significantly impact adsorption kinetics even at low surface coverage. The Elovich equation describes the kinetics of chemical adsorption systems. The linearized expression for the Elovich model is shown in Equation (2.10) (Chien and Clayton, 1980):

$$q_t = \frac{1}{\beta}\ln \alpha\beta + \frac{1}{\beta}\ln t \qquad (2.10)$$

where q_t denotes the amount of adsorbate uptake (mg/g) onto the adsorbent powder at time t, α represents the initial metal ion adsorption rate (mg/g min) and β represents the degree of activation energy and surface coverage for chemisorptions (g/mg). The linear plots of q_t versus ln t can be generated. The parameters α and β can then be estimated from the slope and intercept of the plots respectively.

In practice, the relevance of the Elovich equation is limited to the early stages of the adsorbate–adsorbent interaction process, when the system is quite far from equilibrium (Gupta and Bhattacharyya, 2011).

2.9.1.4 Intra-particle diffusion model

The intra-particle diffusion model can be useful for determining reaction routes and adsorption mechanisms, as well as predicting the rate-controlling step. Adsorbate transfer in a solid/liquid sorption process is frequently characterized by film diffusion (sometimes referred to as external diffusion), surface diffusion, pore diffusion, or a combination of surface and pore diffusion. The linearized expression for the intra-particle diffusion model is shown in Equation (2.11) (Weber and Morris, 1963):

$$q_t = k_{id}t^{0.5} + C \qquad (2.11)$$

where k_{id} (mg/g × $min^{1/2}$) is the rate constant of the intra-particle diffusion model and C (mg/g) is a constant related to the thickness of the boundary layer, with a larger value of C corresponding to a stronger influence on the limiting boundary layer.

The significance of Equation (2.11) is that if the linear plots of q_t versus $t^{0.5}$ are linear and pass through the origin (zero intercepts), the adsorption is completely governed by intra-particle diffusion. If, on the other hand, the intra-particle diffusion plot shows multiple linear regions, then the adsorption process is controlled by a multistep mechanism.

2.9.2 Modeling of adsorption isotherm systems

The term "adsorption isotherm" refers to the relationship between the concentration of adsorbate in solution (liquid phase) and adsorbent (solid phase) at a constant temperature under specified parameters (i.e., pH and ionic strength, fixed mass, and particle size of adsorbent) (Tran *et al.*, 2016). Over the years, a wide range of equilibrium isotherm models has been developed in terms of three core methods (Malek and Farooq, 1996). The first approach is the kinetic consideration, which defines adsorption equilibrium as being in a state of dynamic equilibrium, with both adsorption and desorption rates equal (Langmuir, 1916). The second approach which is based on thermodynamics can provide a framework for developing various forms of adsorption isotherm models (Deboer, 1953; Myers and Prausnitz, 1965). The third approach is the potential theory which usually conveys the main notion in the development of characteristic curves (Dubinin, 1960).

The next section reviews the two-parameter isotherm model widely used for modeling sorption isotherm systems, which are the Langmuir and Freundlich isotherm models.

2.9.2.1 Langmuir isotherm model

The Langmuir isotherm model is valid for monolayer adsorption of solutes at definite homogeneous sites on the surface layer of the adsorbent, with no more than one adsorbate molecule occupying a site (Langmuir, 1918). The linearized form of the model is expressed below:

$$\frac{C_e}{q_e} = \frac{1}{q_m b} + \frac{C_e}{q_m} \quad (2.12)$$

where q_e is the equilibrium quantity of adsorbate uptake onto the adsorbent powder (mg/g), C_e denotes equilibrium metal ion concentration in the solution (mg/L), q_m denotes the maximum adsorption capacity (mg/g) and b represents Langmuir's constant associated with metal ion affinity for adsorption sites and energy (L/mg). The linear plots of C_e/q_e versus C_e can be generated. The values of q_m and b can then be estimated from $1/q_m$ and $1/q_m b$, which represent the slopes and intercepts of the plots respectively.

An important feature of the Langmuir isotherm which indicates the type of adsorption is expressed through a dimensionless constant termed separation factor (R_L):

$$R_L = \frac{1}{1 + bC_0} \quad (2.13)$$

where b is Langmuir constant and C_0 is the initial metal ion concentration (mg/L). Adsorption is unfavourable, linear, irreversible when $R_L > 1$, $R_L = 1$, $R_L = 0$, and favourable when $0 < R_L < 1$ (Weber and Chakravorti, 1974; Tran *et al.*, 2017).

2.9.2.2 Freundlich isotherm model

The Freundlich isotherm model holds for multilayer adsorption of solutes onto a heterogeneous adsorbent surface with non-uniform adsorption sites (Freundlich, 1906). The linearized form for this isotherm model is represented in Equation (2.14):

$$\log q_e = \log K_f + \frac{1}{n_f} \log C_e \quad (2.14)$$

where n_f and K_f represent the heterogeneity factor and Freundlich constant in relation to the adsorption intensity and adsorption capacity respectively. The linear plots of log q_e versus log C_e can be generated. Freundlich constants K_f and n_f are evaluated from the plots with a slope of $1/n_f$ and intercept of log K_f.

Adsorption is deemed easier when $2 < n_f < 10$, mildly difficult when $1 < n_f < 2$, and unfavourable when $n_f < 1$ (Ali *et al.*, 2016).

2.9.3 Estimation of activation energy

Activation energy allows the determination of an energetic barrier that metal ions must overcome before being attached to the adsorption sites. The activation energy is determined using the linearized form of the Arrhenius equation as expressed in Equation (2.15):

$$\ln k_2 = \ln A - \left(\frac{E_a}{R}\right)\frac{1}{T} \tag{2.15}$$

where E_a (kJ/mol) is the activation energy, K_D represents the equilibrium rate constant, A is the Arrhenius constant, R (8.314 J/mol K) represents the gas constant, and T (K) is the absolute solution temperature. Based on Equation (2.14), the value of E_a can be estimated from the slope of the plot of ln k_2 versus $1/T$.

The type of adsorption can be determined by the magnitude of the activation energy. Physical adsorption requires activation energy of less than 4.184 kJ/mol (Hill and Root, 2014) and no more than 17.573 KJ/mol (Saha and Chowdhury, 2011). A chemical adsorption process has an activation energy in the range of 4 – 40 kJ/mol (Maleki *et al.*, 2017).

2.9.4 Thermodynamic adsorption modeling

Evaluation of thermodynamic parameters helps in predicting the feasibility and mechanism of an adsorption system. After the adsorption equilibrium of the studied systems has been established, the thermodynamic parameters, namely standard enthalpy change (ΔH°), standard entropy change (ΔS°), and free energy change (ΔG°), can be estimated using the van't Hoff equation (Khan and Singh, 1987; Tran *et al.*, 2017).

The van't Hoff equation measures changes in the equilibrium constant as temperature varies. The expression is shown below:

$$\Delta G° = -RT \ln K_D \tag{2.16}$$

where R represents the gas constant (8.314 J/mol K), T represents the absolute solution temperature (K), and K_D is the standard thermodynamic distribution coefficient (Khan and Singh, 1987; Tran *et al.*, 2017).

$$K_D = \frac{q_e}{C_e} \tag{2.17}$$

where q_e is the quantity of metal ion (mg/g) adsorbed onto the adsorbent at equilibrium and C_e, is the equilibrium concentration (mg/L) in solution.

Taking into account the third principle of thermodynamics, it implies that:

$$\Delta G° = \Delta H° - T\Delta S° \tag{2.18}$$

Combining Equations (2.16) and (2.18) results in:

$$\ln K_D = \frac{\Delta S°}{R} - \frac{\Delta H°}{RT} \tag{2.19}$$

By constructing a linear plot of ln K_D versus $1/T$, values of $\Delta H°$ and $\Delta S°$ can be estimated from the slope and intercept respectively.

2.10 Review of reported studies on the management of iron precipitate formation

To prevent the iron precipitate formation and/or minimize it, some authors have suggested operating the bioleaching systems under thermophilic microorganisms (Wang *et al.*, 2012; Feng *et al.*, 2013); controlling redox potentials (Yu *et al.*, 2011; Lotfalian *et al.*, 2015); operating with a low pH (Ojumu and Petersen, 2011; Liu *et al.*, 2016a); and the addition of catalysts like silver and activated carbons (Zhang and Gu, 2007; Abdollahi *et al.*, 2015). These are beneficial to minimize the formation of iron precipitates, while some other researchers have attempted novel integrated methods for the bioleaching systems to minimize the negative impact of iron precipitation. For example, Kaksonen *et al.* (2014b) developed a two-stage bioreactor system that enables continuous iron oxidation and the removal of excess iron sulfate. The authors suggested that in the case of heap bioleaching, the technique of bioreactors for excess iron removal can be applied either to pregnant or barren leach liquor before or after metal recovery respectively. The improvements gained

from all the studies cited above truly helped in high activity of bacteria, high reaction efficiency, and even complete dissolution. Notwithstanding, it should be noted that each method has specific drawbacks such as a low metal tolerance capacity, high acid consumption, complicated process, or high operation cost, which limit their application in industry. In fact these methods do not yet resolve the scavenging of metals by iron precipitate, as analysis of the bioleach residue from such bioleach heap systems shows that it still contains valuable metals. To this effect, Table 2.6 illustrates the considerable amount of metals recovered from industrial jarosite obtained from heap bioleach.

2.11 Knowledge gaps

In industrial heap bioleaching operations, strictly speaking, it is very difficult to control the prevailing operating conditions (such as pH and temperature) since the bioleaching system experiences a gradient of changes in these operating conditions across different depths of heap. This difficulty entirely disturbs the biogeophysicochemistry of the whole operation, thereby making iron precipitation an unavoidable phenomenon. From the knowledge of environmental remediation, it has been shown that the retention and/ or uptake of metals could depend on the nature of these iron precipitates which are greatly dependent on mineral species, metal ion species, and reactive conditions (i.e., pH, heavy metal concentration, ionic strength, etc.). Thus, it is hypothesized that the sorption mechanisms and metal sorption capacities of the various iron precipitates may differ. Besides, disposal of these iron residues requires many acres of land and this poses an environmental risk with the potential for heavy metal pollution of the soil and groundwater systems (Oladipo *et al.*, 2021a).

These knowledge gaps have motivated this work to further understand the scavenging and/or retention of valuable metals on iron minerals. This knowledge would require carefully designed sets of fundamental studies under certain relatable operating conditions to generate iron precipitates, investigate their properties, and conduct sorption studies with the precipitates, at least in microbial oxidation of ferrous ions, which is an important process for the efficient oxidation of sulfide minerals. Consequently, getting a better

understanding of the mechanisms of metal ions interacting with iron precipitates could help in diagnosing the relationship between these two (metal ions and iron precipitates) and predicting their long-term behaviour bioleaching operations. This knowledge may be applicable in the design and may provide some understanding of a typical biohydrometallurgical system with respect to metal-precipitate interaction and treatment of residues in operations.

2.12 Summary

This chapter summarizes the relevant literature that underpins this thesis. The chapter provided basic information on the nature and behaviour of iron precipitate in relation to their scavenging of desirable metals in biohydrometallugical operations.

It can be inferred from this chapter that the formation of iron precipitate hinders the biological stages of bio-oxidation and bioleaching operations, and most importantly, it affects the downstream metal recovery. Precipitates such as those containing ferric hydroxides, oxyhydroxides, schwertmannite, jarosite, and at times complex mixtures of iron species can be formed. These precipitates have morphological attributes that hinder the permeability of leaching agents for dissolution and also entrap valuable metals of interest, thereby preventing metal ions from getting into the solution for further processing.

CHAPTER THREE

MATERIALS AND EXPERIMENTAL METHODOLOGY

"The environment is no one's property to destroy; it's everyone's responsibility to protect." – Mohith Agadi

CHAPTER 3: MATERIALS AND EXPERIMENTAL METHODOLOGY

This chapter details the general description of materials and experimental methods used to achieve the objectives of the research in the thesis. The specific experimental conditions, methodology, and mathematical tools are presented in the relevant chapters.

3.1 Materials

3.1.1 Microbial culture analysis

Mesophilic microorganisms were employed in this research. The mesophilic mixed culture was obtained from the Centre for Bioprocess Engineering Research (CeBER) at the University of Cape Town (UCT), Cape Town, South Africa. The mixed mesophiles collected from the stock culture contains the following microorganisms: *Ferroplasma acidiphilum* – 0.1%, *Cuniculiplasma divulgatum* – 3.5%, Archaea (JTC1/2 – *Thermoplasmatales*) – 3.9%, *Acidithiobacillus cupricumulans* – 4.7%, *Acidithiobacillus caldus* – 32.2%, and predominantly *Leptospirillum ferriphilum* – 55.5%. The microorganisms present were confirmed by a quantitative Real-Time Polymerase Chain Reaction (qPCR) with species-specific primers (or primer sets) (Ngoma, 2015). The microbial distribution of the stock culture is displayed in Figure 3.1. The microorganisms were maintained in a 1 L batch stirred tank reactor at 35 °C and 550 rpm on a ferrous ion substrate supplied as 5 g/L of $FeSO_4.7H_2O$ of total iron. Once the microorganisms reached their exponential phase (> 600 mV), they were subcultured to ensure their continued viability. This was accomplished by withdrawing 100 mL of stock and replacing it with 100 mL of growth medium.

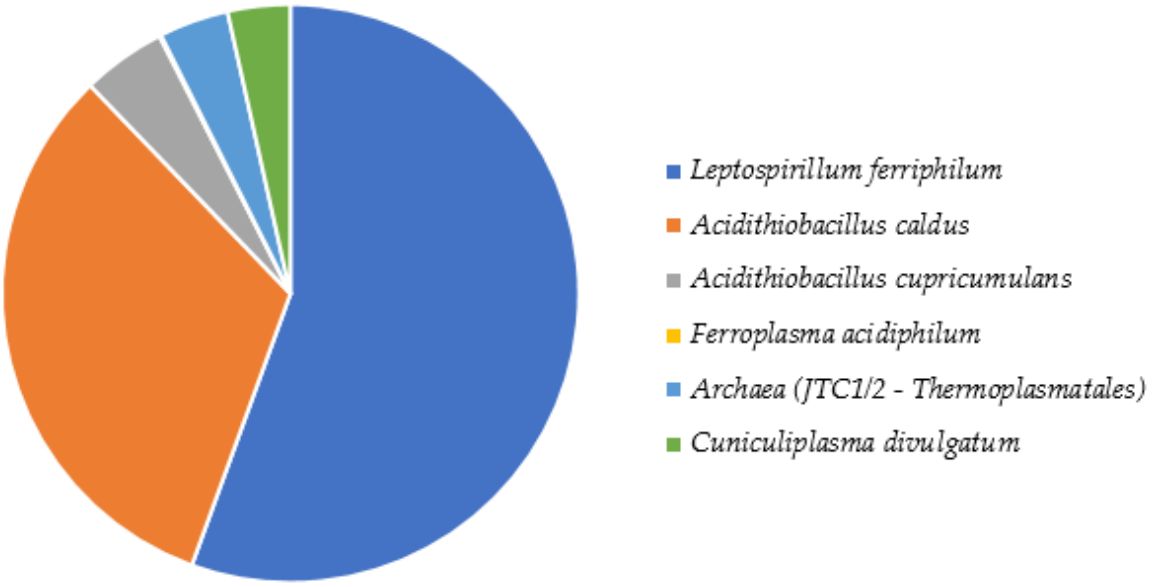

Figure 3.1: Microbial distribution of the stock culture

3.1.2 Growth media composition

The ferrous media contained 5 g/L of Fe^{2+} (added as $FeSO_4.7H_2O$), 5.55 g K_2SO_4, 9.15 g $(NH_4)_2SO_4$, 2.65 g $(NH_4)_2HPO_4$, and 50 mL of Vishniac trace element solution (Vishniac and Santer, 1957) (Appendix A). The trace element solution contained 50 g/L EDTA ($C_{10}H_{14}N_2Na_2O_8.2H_2O$, M = 372.24 g/mol), which was dissolved in 200 mL of 6% (w/v) KOH solution (Chowdhury, 2012). In a separate container, the following chemicals were added in succession: 22 g $ZnSO_4.7H_2O$, 9.24 g $CaCl_2.2H_2O$, 5.06 g $MnCl_2.4H_2O$, 5.0 g $FeSO_4.7H_2O$, 1.1 g $(NH_4)_6Mo_7O_{24}.4H_2O$, 1.58 g $CuSO_4.5H_2O$, 1.62 g $CoCl_2.6H_2O$, and thereafter dissolved in 400 mL distilled H_2O. The EDTA solution was added after the contents were fully dissolved. Following that, the Vishniac solution was added and diluted to 1 L with distilled H_2O (Chowdhury, 2012). Afterwards, the pH of the growth medium was adjusted to the desired value ($0.9 < pH < 1.3$) using concentrated H_2SO_4 (98%). This is detailed in Appendix A. There was no attempt to keep sterile conditions. The resultant solution was refrigerated to prevent ferrous ion oxidation. All studies were conducted using reagents of analytical grade.

3.2 Experimental methodology

3.2.1 Experimental rig

A schematic diagram of the experimental rig for the batch culture experiments is depicted in Figure 3.2. It was fabricated of borosilicate jacket glass and featured a lid with four openings, each for the condenser, blade agitator, air sparger, and sample point. The bioreactor had a 1 L working volume (Table 3.1). An SMC water-bath was connected to the reactor to maintain the desired temperature of the reactor by circulating water through the bioreactor jacket. Agitation and gas dispersion was attained using an inclined (60°) three-blade turbine impeller operated at 550 rpm which was placed a little distance from the basement of the reactor. Air was delivered from the laboratory via an outlet line and regulated at a flow rate of 3 mL/s using a Dwyer bubble airflow meter (Rotameter). Evaporation was decreased by connecting a condenser to a refrigerator (Julabo, FL300) set at 7 °C. The redox potential and pH of the reactor were determined using a CRISON GLP 21 redox and pH meters that were readily available in the laboratory. The typical experimental set-up is shown in Figure 3.3.

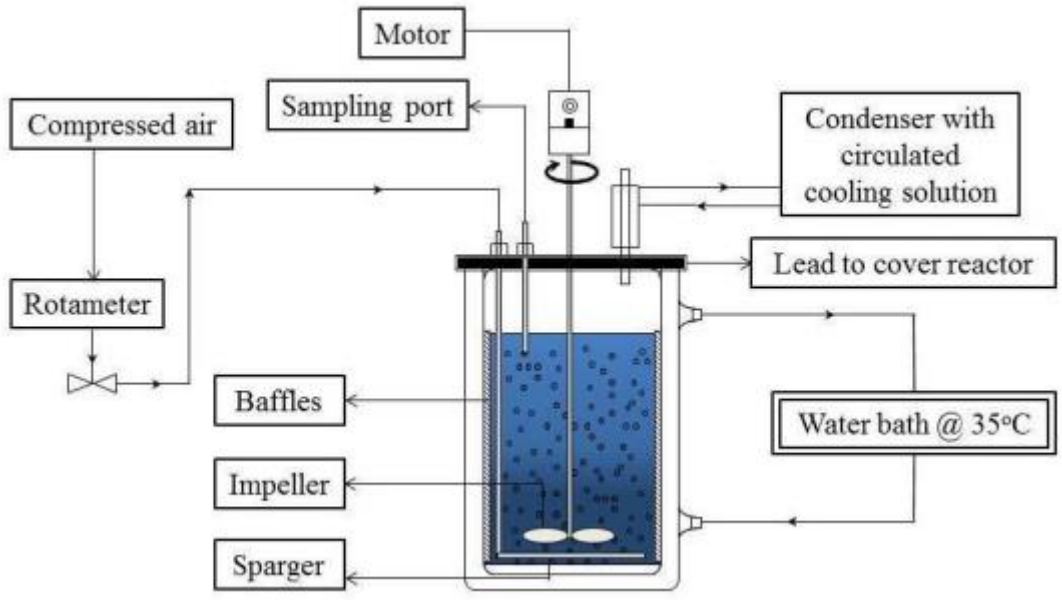

Figure 3.2: Schematic representation of the stirred tank reactor

Table 3.1: Stirred tank reactor specifications

Parameter	Specification
Total volume	1300 mL
Working volume	1000 mL
Total height	200 mm
Vessel diameter	100 mm
Impeller design	Axial 3 pitched blade propeller
Impeller diameter	57 mm
Impeller clearance	10 mm

Figure 3.3: Stirred tank experimental set-up for ferrous ion bio-oxidation

3.2.2 Experimental study on the effect of initial pH on iron precipitate formation

Strictly speaking, for copper solubility, industrial heap copper bioleaching is performed at pH 2.0 or lower to maintain a high concentration of the principal bioleaching agent–Fe(III) (Ruan *et al.*, 2011; Gentina and Acevedo, 2013). Thus, in this present study, batch experiments on ferrous ion bio-oxidation experiments would be performed at initial pH values of 1.7, 1.9, and 2.2 to generate iron precipitates.

Batch culture studies with the mixed mesophiles were conducted in a CSTR bioreactor, while the working temperature was maintained at 35 °C using a temperature-controlled water bath. The cell suspension was agitated at 550 rpm while being aerated with dry air at a flow rate of 3 mL/s. The bioreactor was allowed to run for 14 days, and pH and redox potential measurements were taken daily. Three reactors were operated under identical conditions, and the mean value was computed. To begin new experiments, 20% of the inoculum (with redox potential > 600 mV) was mixed with 80% of the growth media. After each experiment, the bioreactor was cleaned with concentrated HCl (32%), to ensure that all the precipitates and any wall growth were completely removed. After that, the bioreactor was rinsed with dilute H_2SO_4 (50%) to eliminate the HCl, which is toxic to bacteria. Finally, the pH in the reactor was neutralized by rinsing the bioreactor with distilled H_2O. Every experiment was repeated three times to ensure that the results were reproducible.

During the studies, the following assumptions were made:

- Effects of shear forces and hydrodynamic conditions were constant throughout the experiments.
- There was minimal cell loss due to adhesion to the reactor walls.
- There was a negligible temperature differential between different sets of experiments.

3.3 Preparation of iron precipitate for analysis

After the completion of the experiment at the pre-defined time, iron precipitates were collected by sedimentation, followed by Büchner filtration with a vacuum pump utilizing Whatman polycarbonate filters. The precipitates on the filter paper were washed back into the reactor with distilled H_2O. This was done to merge the filtered precipitates with those adhering to the reactor wall. Following that, approximately 100 mL of 0.1 N H_2SO_4 was added to dissolve both the suspended precipitate and those on the wall. Additionally, the precipitates clinging to the air sparger and impeller surfaces were removed. After allowing the filtrate containing the cells and precipitate to settle, it was decanted, and the precipitate-

containing part was filtered (Mabusela, 2017). The precipitates were dried to a constant weight at 80 °C. Following the drying phase, the solids were gently crushed to a fine powder using a porcelain mortar and pestle. The final product was then sent for analysis.

3.4 Characterization of iron precipitate

To have a good understanding of the nature of the precipitates, numerous techniques based on different properties such as thermal stability, morphology, surface chemistry, elemental composition, textural property, and crystalline structure were used to characterize the iron precipitate produced in this study (Figure 3.4).

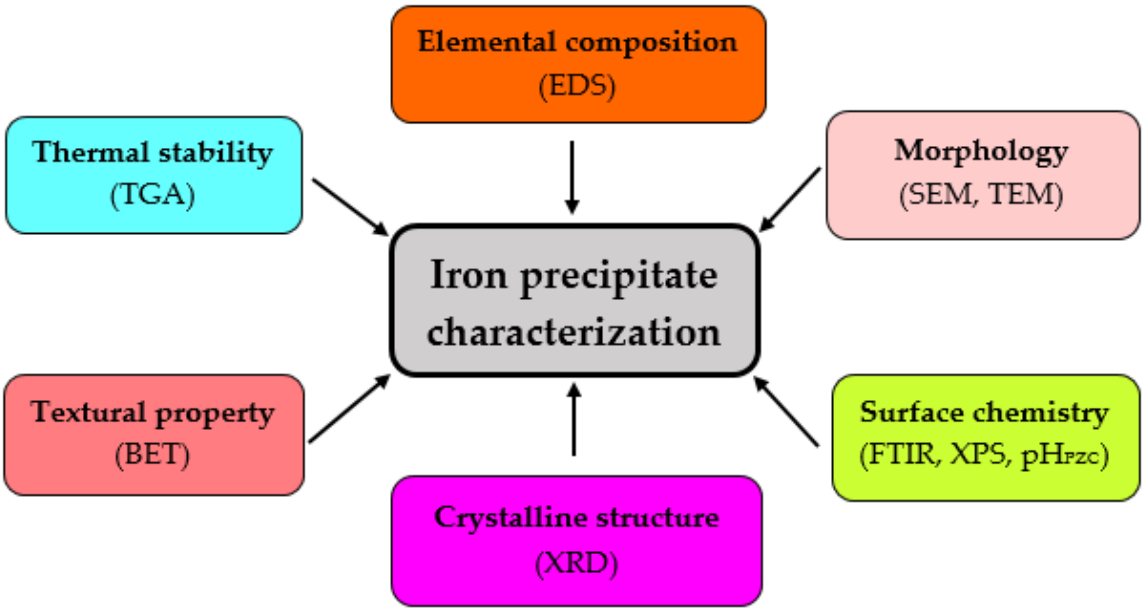

Figure 3.4: Iron precipitate characterization determined by various techniques

3.4.1 X-ray diffraction (XRD)

XRD analysis, in order to study the crystal structure, was performed to identify the crystalline phases present in the precipitate samples under investigation, thus, revealing the chemical information of the sample. Measurements were performed using a multi-purpose X-ray diffractometer D8-Advance from BRUKER AXS (Germany), operated in a continuous θ-θ scan in locked coupled mode with Cu-K$_\alpha$ radiation ($\lambda K_{\alpha 1}$=1.5406Å). The

sample was mounted in the centre of the sample holder on a glass slide and leveled up to the correct height. The measurements ran within a 2θ range of 5 – 80° with a typical step size of 0.034° in 2θ. The tube voltage and tube current were operated at 40 kV and 40 mA respectively. A position-sensitive detector (PSD), LYNXEYE, was used to record diffraction data at a typical speed of 0.5 sec/step, which was equivalent to an effective time of 92 sec/step for a scintillation counter. Data were background subtracted so that the phase analysis was carried out for diffraction patterns with zero background after the selection of a set of possible elements from the periodic table. Phases were identified from the match of the calculated peaks with the measured ones until all phases were identified within the limits of the resolution of the results.

The crystallite size of the iron precipitate which is the smallest, most likely single-crystal in powder form, was measured by X-ray diffraction broadening. Scherrer's equation was used for the determination of the crystallite size as follows (Holzwarth and Gibson, 2011):

$$d = \frac{k\lambda}{\beta \cos\theta} \tag{3.1}$$

where d is the crystallite size (nm) in the direction perpendicular to the lattice planes, k is the crystallite-shape factor (0.9), λ is the wavelength (0.15406 nm) of the X-rays; β is the width (full-width at half-maximum intensity-FWHM) of the X-ray diffraction peak in radians, and θ is the Bragg angle (radians).

3.4.2 Fourier transform infrared (FTIR) spectroscopy

FTIR was employed for qualitative and quantitative analysis of the precipitate samples. It helped to identify the functional groups present in the samples. Measurement of samples was carried out with a universal attenuated total reflectance (UATR) Two PerkinElmer spectrophotometer (Llantrisant, UK) and recorded over the range of 4000 and 400 cm^{-1} in ambient conditions. The crystal area of the instrument was cleaned with isopropanol before analysis and background corrections were made. The samples were placed directly on the crystal area of the diamond UATR top plate. The pressure arm was positioned over the crystal-sample area, then locked into a precise position above the diamond crystal. A force

was applied to the sample, pushing it onto the diamond surface. The sample was thereafter scanned to obtain the spectrum.

3.4.3 Scanning electron microscope (SEM)/Energy-dispersive X-ray spectroscopy (EDS)

SEM analysis was done to study the surface morphology of the precipitate samples. Images were taken with the Tescan MIRA SEM. The equipment has an in-beam secondary electron (SE) detector which is placed in the objective lens that allows imaging at very short working distances for better resolution. A small amount of the sample was mounted on carbon glue on a 12 mm aluminium SEM stub. The stubs were then carbon-coated in an evaporation coater before being loaded into the SEM. The operating conditions are SEM high voltage (HV) of 5.0 kV with different SEM magnifications (5, 10, 20, and 50 kx). ImageJ, a Java-based open-source software was used to process the SEM images for particle size measurement.

EDS was performed to provide the elemental composition of the precipitate samples. EDS was done on the Nova NanoSEM at 20kV using an Oxford X-max 20mm^2 detector (Oxfordshire, UK) and patterns were recorded using Oxford INCA software.

3.4.4 Brunauer-Emmett-Teller (BET) and Barrett-Joyner-Halenda (BJH)

The textural properties (surface area, total pore volume, and pore size) of the precipitate samples were determined using automated TriStar II 3020 (Micromeritics Corp.) surface area and porosity analyzer equipment. The samples were degassed overnight under a vacuum in an oven operated at 383 K to remove moisture before N_2 adsorption-desorption analysis at –195.8 °C bath temperature. MicroActive 5.02 software (TriStar II Version 2.00) was employed to generate the BET surface area and the BJH pore distribution of the samples.

3.4.5 Thermogravimetric analysis (TGA)

TGA was used to study the thermal stability of the precipitate samples with the percentage of weight loss at different phases of the sample decomposition. The TGA was carried out using an SDT 650 simultaneous thermal analyzer (TA Instruments, Inc. USA). A sample mass of 20 mg was introduced and measurement was performed at the process condition of a dry airflow rate of 50 mL/min and a heating rate of 10 °C/min between 20 to 900 °C temperature range.

3.4.6 X-ray photoelectron spectroscopy (XPS)

The XPS spectra of the precipitate samples were collected using a PHI Versaprobe 5000 Scanning ESCA Microprobe. A 100 μm diameter monochromatic Al Kα X-ray beam (hv = 1486.6 eV) generated by a 25 W, 15 kV electron beam at constant pass energy of 187 eV and step width of 1 eV was used to analyze the different binding energy peaks. The spectra were recorded in the range 0 – 1400 eV.

3.4.7 pH at point of zero charge (pH_{pzc}) determination

The pH_{pzc} is the value at which the surface charge density equals zero. The experiments were carried out using the salt addition method (Bakatula *et al.*, 2018). In different 250 mL Erlenmeyer flasks, 40 mL of 0.1 M $NaNO_3$ solutions were prepared, with initial pH (pH_i) readings adjusted to an initial pH range between 2 – 11 (±0.1 pH unit), using either 0.1 N NaOH or 0.1 N HNO_3. Samples of 0.2 g were then added to the flasks and were shaken at 150 rpm and 303 K for 24 h. On completion, the suspensions were centrifuged, and the final pH (pH_f) measurement of the supernatants was determined. The pH_{pzc} was determined from the plot of ΔpH (= pH_f – pH_i) versus pH_i values. The pH_i at which ΔpH is zero was taken to be the PZC.

3.5 Batch adsorption studies

The variations in ore composition across habitats differ due to the diversity of geological and environmental conditions of the source of location. This was the case as presented in Table 2.5 of Chapter 2. Thus, in this study different initial concentrations of copper would be investigated for the adsorption studies.

The retention capacity of iron precipitate was tested with Cu(II) ions. Stock solutions of 1000 mg/L of Cu(II) were prepared by dissolving predefined quantities of $CuSO_4.5H_2O$ in Milli-Q ultrapure water with a resistivity ≥ 18 MΩ cm. The initial concentration range (150–500 mg/L) was further prepared from the stock solutions by dilution. Solution pH was adjusted with 0.1 N NaOH or 0.1 N HCl to give desired values. Laboratory experimental runs were performed in several 250-mL Erlenmeyer flasks, which were placed inside a thermostatic temperature-controlled shaker until equilibrium was attained. A working solution of 50 mL Cu(II) at the studied initial concentrations (150, 300, 400, and 500 mg/L), contact time (5, 10, 15, 20, 40, 60, and 120 min), and sorption temperature (30, 40, 45, 50, and 55 °C) were all investigated at pH 5, 150 rpm mixing speed and 1 g adsorbent dosage. All chemicals employed were of analytical reagent grade.

3.5.1 Analysis of solution

After equilibrium time, suspensions were passed through a 0.45 μm syringe filter. The concentrations of Cu(II) were carried out calorimetrically on a CE 2021 UV/VIS spectrophotometer (2000 series). The percentage removal of Cu(II) ($\%R_{Cu}$) in solution was estimated below:

$$\%R_{Cu} = \frac{C_i - C_e}{C_i} \times 100 \tag{3.2}$$

where C_i denotes initial Cu(II) concentration (mg/L) and C_e represents equilibrium Cu(II) concentration (mg/L) in solution. The amount of Cu(II) adsorbed onto iron precipitate powder at equilibrium, q_e (mg/g), was determined below:

$$q_e = \frac{(C_i - C_e)V}{m} \tag{3.3}$$

where m (g) is the mass of dried iron precipitate residue and V (L) is the working solution volume. For the validity of data results, adsorption experiments were performed three times and mean values were recorded.

3.6 Adsorption kinetics

An adsorption kinetics investigation was performed to evaluate the contact time needed to reach equilibrium. For the adsorption kinetic study, 1 g adsorbent was added to 50 mL working solutions of initial Cu(II) concentrations (150, 300, 400, and 500 mg/L) at contact times (5, 10, 15, 20, 40, 60, and 120 min), at process condition of 30 °C temperature, 150 rpm stirring speed and pH 5. Pseudo-first-order, pseudo-second-order, and Elovich models were appraised for the process kinetic studies. These models were described in Section 2.9.1 of Chapter 2.

3.7 Adsorption isotherms

Adsorption isotherms are useful in explaining the interaction between the adsorbate and the adsorbent, and in defining optimal adsorbent application (Oladipo *et al.*, 2021b). The adsorption isotherms were examined with the Langmuir and Freundlich models for initial Cu(II) concentrations (150, 300, 400, and 500 mg/L) and temperatures (30, 40, 45, 50, and 55 °C) using 1 g iron precipitate powder in a 50 mL working solutions of Cu(II) at 60 min contact time, 150 rpm shaking speed and pH 5. The models employed were described in Section 2.9.2 of Chapter 2.

3.8 Activation energy and adsorption thermodynamics

Adsorption thermodynamic experiments were conducted under the same process conditions for the adsorption isotherm study. Thermodynamic parameters, namely standard enthalpy change (ΔH°), standard entropy change (ΔS°), and free energy change (ΔG°) were all studied. The equations used for estimating the activation energy and adsorption thermodynamics were described in Sections 2.9.3 and 2.9.4 of Chapter 2.

The goodness of fit of the applied models to experimental data was checked by the coefficient of determination (R^2). Microsoft Excel and OriginPro 2018 (OriginLab Corp., Northampton, MA) graphing software were used to plot and analyse the data generated.

The general approach of the research methodology in the thesis is summarised in Figure 3.5.

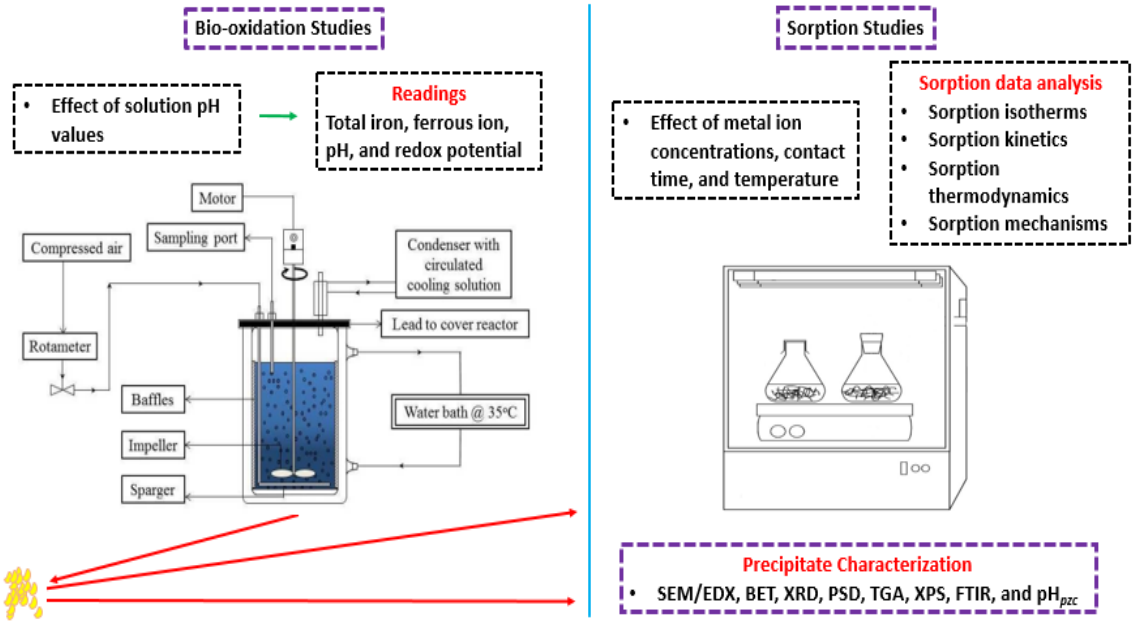

Figure 3.5: Synopsis of research approach

CHAPTER FOUR

INFLUENCE OF INITIAL SOLUTION pH ON IRON PRECIPITATION DURING FERROUS ION BIO-OXIDATION

"The greatest threat to our planet is the belief that someone else will save it." – Robert Swan

CHAPTER 4: INFLUENCE OF INITIAL SOLUTION pH ON IRON PRECIPITATION DURING FERROUS ION BIO-OXIDATION

4.1 Introduction

Mineral sulfides, such as chalcopyrite ore, require an oxidizing agent for dissolution, and adequate concentrations of ferric ion are typically used for this purpose. Bio-oxidation of ferrous ion produces precipitated ferric ion, which is pH and solution-chemistry-dependent (Kaksonen *et al.*, 2019). High concentrations of ferric ions generate various forms of precipitate on the surface of ore particles which reduces the accessibility of the leaching agent and bacteria cells to the mineral surfaces (Nazari *et al.*, 2014). In the bioleaching process, oxidation of ferrous ions results in precipitates containing schwertmannite, ferrihydrite, and various forms of jarosite minerals, which may reduce bioleaching efficiency due to their ability to entrap desired metals. Thus, the management of iron precipitates during operation is important.

Studies aimed at quantifying iron precipitates have been undertaken over the last decades (Daoud and Karamanev, 2006; Mousavi *et al.*, 2006; Sasaki *et al.*, 2006; Liu *et al.*, 2009). Nonetheless, these investigations were performed in shake flasks that do not accurately represent typical heap operations. The findings of these investigations are not relevant on an industrial scale, where reactor volumes range between 440×10^3 and 21.6×10^6 L with operations that can last up to a year (Rawlings *et al.*, 2003; Watling *et al.*, 2009). It has been reported that the parameters affecting microbial oxidation of ferrous ions would have a direct effect on ferric ion precipitation, among which factors is reactor configuration (Daoud and Karamanev, 2006; Mabusela, 2017). Notably, heaps and stirred tank reactors are two distinct techniques primarily used in bioleaching and bio-oxidation (Tao and Dongwei, 2014), thus, quantification of iron precipitate in systems such as a CSTR is necessary.

Microorganisms are widely used as biocatalysts during microbial oxidation of ferrous ions (Mazuelos *et al.*, 2010; Mabusela, 2017). It is worth noting that most of the quantification

experiments used *Acidithiobacillus ferrooxidans* to mediate the process. However, the high ferric-ferrous ion ratio present in bio-oxidation tanks inhibits *A. ferrooxidans* (Meruane and Vargas, 2003). Thus, it is necessary to investigate the characteristic of another oxidizing microbe. *Leptospirillum ferriphilum* is a gram-negative, mesophilic, thermotolerant (up to 45 °C) ferrous ion oxidizer. It uses ferrous ions as its sole electron donor and oxygen as its electron acceptor. *L. ferriphilum* is less inhibitory to ferric ions and has a kinetic advantage over *A. ferrooxidans* due to its prevalence in stirred bioreactor operations. In fact, it has been reported that optimum leaching efficiency is obtained at lower substrate concentrations for an *L. ferriphilum* mediated process than for *A. ferrooxidans* (Coram and Rawlings, 2002; Gao *et al.*, 2007; Kaksonen *et al.*, 2014a). *L. ferriphilum* has risen in importance and is now routinely employed to study the kinetics of ferrous ion oxidation (Nurmi *et al.*, 2009; Ojumu *et al.*, 2009; Penev and Karamanev, 2010; Ojumu and Petersen, 2011; Mabusela, 2017). Therefore, quantification studies using *L. ferriphilum* as a biocatalyst in a CSTR are of great interest.

4.2 Objective

This chapter discusses the quantification of iron precipitate generated during bio-oxidation of ferrous ion in a CSTR mediated by mesophilic culture dominated by *L. ferriphilum* as a function of pH (1.7 – 2.2) and process time (14 days). The goal of this part of the study was to understand how initial pH and time influenced the amount of iron precipitate produced during bio-oxidation, and thus provide insight into the management of greater scales encountered in biohydrometallurgical processes. It is important to state that this part of the study was very significant because it would provide the precipitate required to carry out further studies in this thesis.

4.3 Methodology

The experimental design, quantification, and analysis of data were described in detail in Sections 3.1 and 3.2 of Chapter 3.

4.4 Results and discussion

4.4.1 Variations in the redox potential with time

The time-dependent variations of the redox potential at the initial pH values investigated are illustrated in Figure 4.1. The changes in the redox potential were directly related to the bio-oxidation of ferrous ions and reflected the relative concentrations of ferrous and ferric ions present at different times (Smith and Johnson, 2018). Given that increase in redox potential is associated with an increase in ferrous oxidation (Ojumu and Petersen, 2011), the pH values examined in this study resulted in high oxidation rates as well as high ferric ion production rates. Thus, iron precipitation is dependent on the redox potential of the solution and accelerates when it exceeds a critical point, around 450 mV. This is due to the tendency of Fe^{3+}/Fe^{2+} solutions to reach a state of chemical equilibrium in which the activities of both ions are equal (Córdoba *et al.*, 2008b). Additionally, at the investigated initial pH values, maximum oxidation occurred in less than 4 days. In all the pH values studied, ferrous ion was oxidized rapidly and the redox potential values increased to > 650 mV and remained as such for the duration of the experiment.

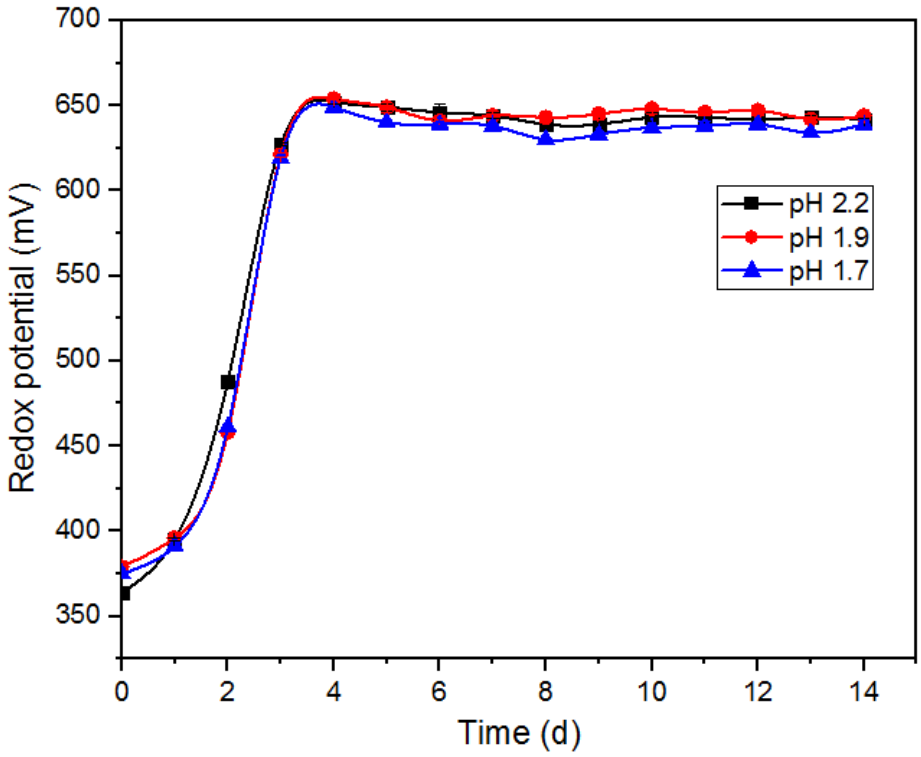

Figure 4.1: Time-dependent variations of redox potential at the studied initial pH values

4.4.2 Variations in the pH values with time

The changes in solution pH over time for the initial solution pH values are illustrated in Figure 4.2. The typical pattern observed is an increase in the pH of the solution followed by a decrease in pH. The increase in pH is caused by the consumption of hydronium ions during ferrous ion oxidation, whereas the decrease is due to ferric ion precipitation, which causes the release of hydronium ions. The sharp decrease in pH 1.7 on the 5th day is probably a result of a high amount of precipitated iron on the day. Similar to the changes in the redox potential, the increase in solution pH can be correlated with the extent of ferrous ion oxidation, since it is the only reaction responsible for the increase in solution pH (Qiu *et al.*, 2005). Due to the fact that a high concentration of ferric ion is required to cause a decrease in solution pH (Jin *et al.*, 2013), it can be affirmed that at the studied initial pH values, ferrous ion was almost completely oxidized on day 2, leaving the medium rich in ferric ion.

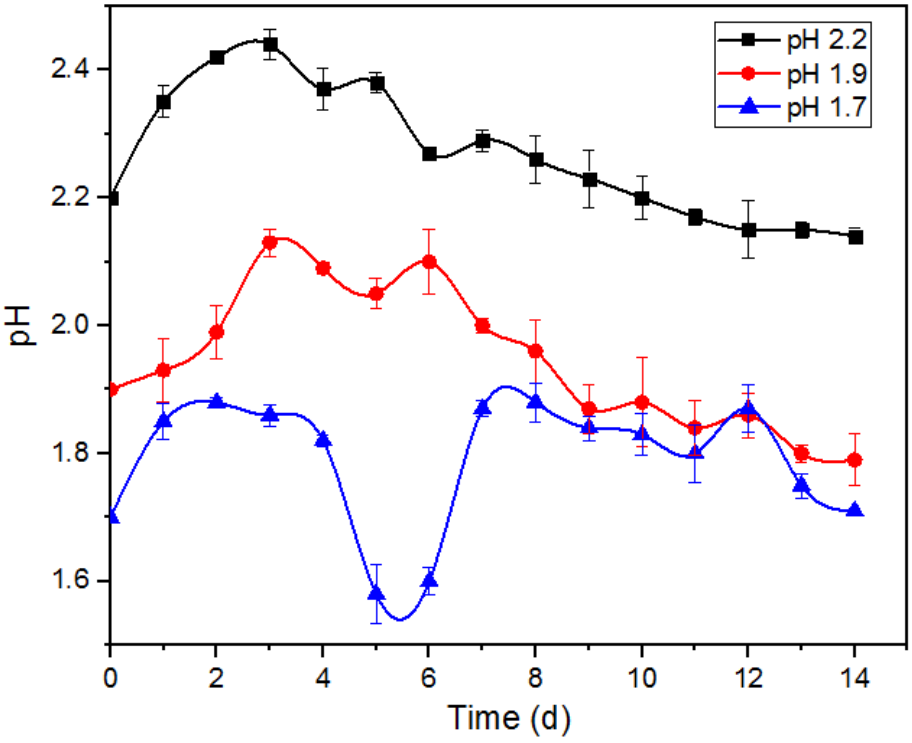

Figure 4.2: Variation of solution pH with time during ferrous ion bio-oxidation

4.4.3 Effect of initial solution pH on the amount of iron precipitate

The mass of iron precipitate formed as a function of the initial pH values after 14 days of operation is depicted in Figure 4.3. The results indicate that the mass of iron precipitate increased with an increase in the initial solution pH. This observation corroborates with previous studies (Daoud and Karamanev, 2006; Liu *et al.*, 2009; Wanjiya *et al.*, 2015; Mabusela, 2017). At an initial pH of 1.7, the lowest amount of iron precipitate (7.34 g) was obtained, followed by 9.62 g generated at the initial pH of 1.9, and finally, the initial pH of 2.2 produced the largest amount of iron precipitate (11.49 g).

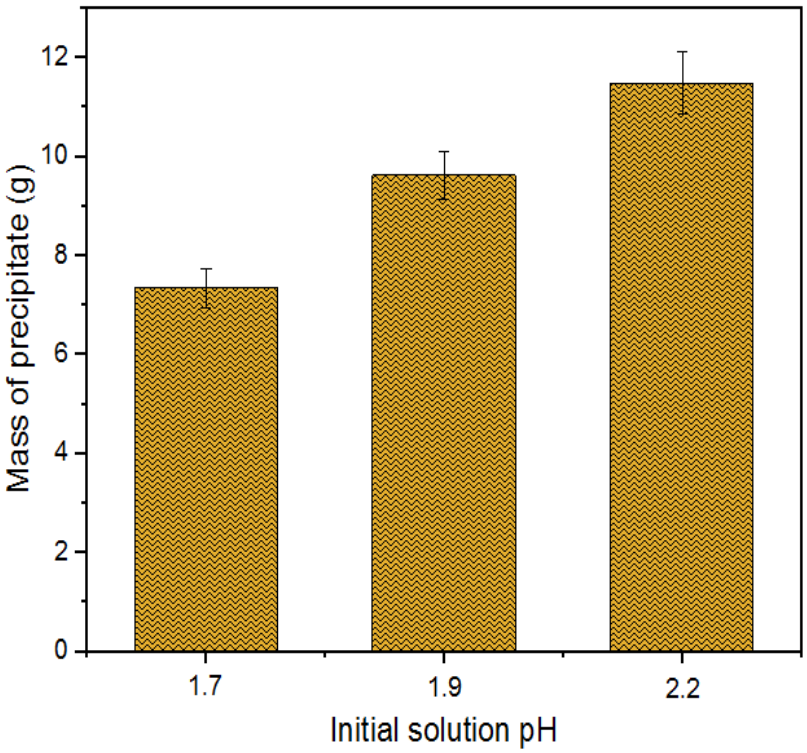

Figure 4.3: Mass of iron precipitate obtained at the studied initial pH values

The amount of iron precipitated at the pH values investigated correspond to high redox potential values that are within the threshold range for significant precipitation (Córdoba *et al.*, 2008b). Based on this, it is hypothesized that the amount of iron precipitated is proportional to the time allowed for a solution medium rich in ferric ions to continue when the redox potential remains within critical levels. According to Figure 4.2, the decrease in solution pH as the bio-oxidation progresses was ascribed to the ensuing precipitation of

ferric ions. From Figures 4.2 and 4.3, it is possible to deduce that the intensity of the reducing pH gradient was proportional to the amount of iron precipitated.

This study obtained a higher amount of iron precipitate than most of the previous investigations (Table 4.1).

Table 4.1: Comparison of literature studies in relation with precipitate formation during ferrous ion bio-oxidation

Bacteria employed	Reactor type	Experimental conditions	Precipitate amount	References
Thiobacillus ferrooxidans	Packed-bed reactor	23 °C, pH 1.35	0.24 g after 1 month	Grishin *et al.* (1988)
Acidithiobacillus ferrooxidans	Erlenmeyer flask	260 rpm, 35 °C, pH 2.0	0.17 g after 46 h	Daoud and Karamanev (2006)
Acidithiobacillus ferrooxidans	Erlenmeyer flask	180 rpm, 30 °C, pH 2.0	2.64 g after 46 h	Liu *et al.* (2007)
Thiobacillus ferrooxidans	Erlenmeyer flask	110 rpm, 28 °C, pH 1.99	~13.00 g after 7 days	Liu *et al.* (2009)
Acidithiobacillus ferrooxidans	Packed-column bioreactor	38.6 °C, 20 mL/s, 0.05 h^{-1}, pH 1.7	7.08 g after 10 days	Wanjiya *et al.* (2015)
Leptospirillum ferriphilum	Continuous stirred tank reactor	350 – 400 rpm, 35 °C, pH 2.0	13.26 g after 14 days	Mabusela (2017)
Leptospirillum ferriphilum	Continuous stirred tank reactor	550 rpm, 35 °C, pH 2.2	11.49 g after 14 days	This study

For example, in the work of Daoud and Karamanev (2006), it was reported that no iron precipitate formation was observed at pH 1.6. The most likely explanation for this is that

their study was conducted over a short period and smaller working volume, which is quite typical of most literature studies. In addition to this, *A. ferrooxidans* used by the authors is not as effective as a biocatalyst when compared with *L. ferriphilum* employed in this present study. This is probably because *L. ferriphilum* has higher affinity for ferrous ions and is more tolerant to high ferric ions (Petersen and Ojumu, 2007; Johnson, 2009). In a very strong oxidizing condition such as in high redox potentials (> 650 mV), *Leptospirillum* spp. are known to be significantly more efficient iron oxidizers than *A. ferrooxidans* (Johnson, 2009). Another key factor could be the temperature and pH of the operating environment. *L. ferriphilum* is more tolerant of lower pH and higher cultivation temperature than *A. ferrooxidans* (Rawlings, 2002; 2005), which explains why it is more important in stirred tank operations, which typically operate at 40 °C. Elsewhere, it was reported that a significant iron loss was reported at pH 1.3 in a process mediated by *L. ferriphilum* (Ojumu and Petersen, 2011). Figure 4.4 shows the precipitate obtained in this study.

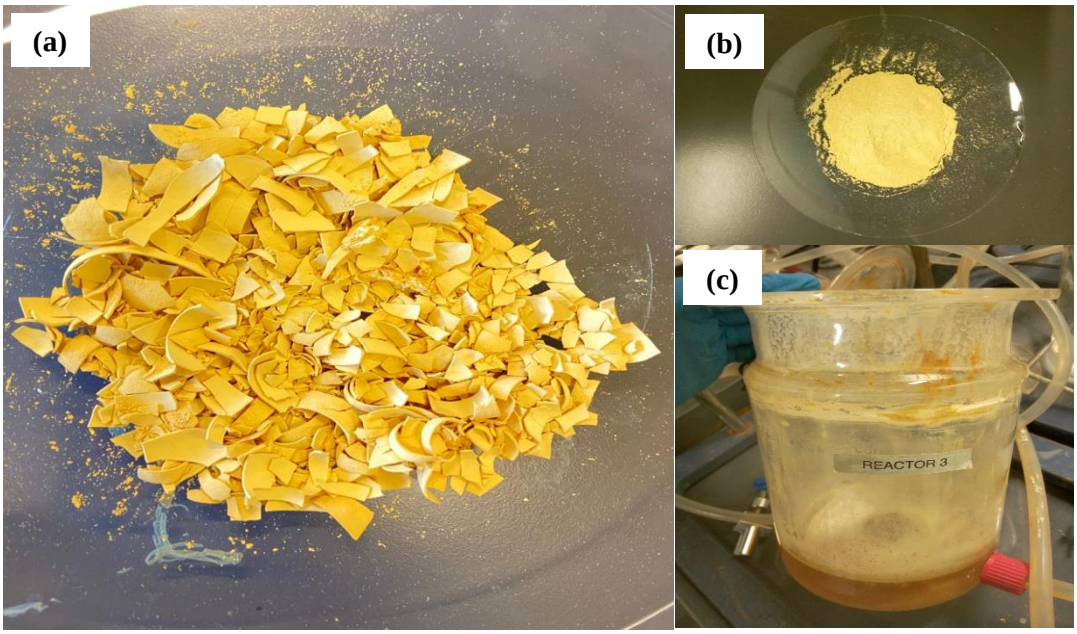

Figure 4.4: (a) Sample of the iron precipitate obtained after filtration and drying processes, (b) iron precipitate powder, and (c) traces of precipitate present in bioreactor

However, substantial precipitation occurred on the fifth and eighth days of operation, when the highest redox potential fluctuated between 403 and 624 mV. This range corresponds with the exponential phase of the microorganism. This indicates that to avoid

the accumulation of iron precipitate in batch systems operating for an extended period, the redox potential should be either above or below the critical levels. If this could be possible, the difficulty associated with iron precipitation management might be alleviated.

4.5 Conclusions

This chapter aimed to quantify iron precipitate generated as a result of initial solution pH and reaction time. The findings indicate that the amount of iron precipitate increased with an increase in the initial solution pH. The mass of precipitated iron in this study exceeded the amount documented in previous studies. This is due to the large reactor capacity utilized in this study and the bacteria strain employed, which was less susceptible to high concentrations of ferric ions than other microorganisms. The findings of this study will aid in estimating the quantity and in the minimization of iron precipitate on an industrial level where processes span for days, months, and even years.

CHAPTER FIVE

EFFECT OF INITIAL SOLUTION pH ON THE SURFACE PROPERTIES OF BIOGENIC JAROSITE FORMED FROM THE BIO-OXIDATION OF FERROUS ION IN A CSTR BY *Leptospirillum ferriphilum*

"The optimal use of natural resources can be made only if there is a well-thought-out policy framework for their exploitation towards a particular end-use." – Kapil Sibal

CHAPTER 5: EFFECT OF INITIAL SOLUTION pH ON THE SURFACE PROPERTIES OF JAROSITE FORMED FROM THE MICROBIAL OXIDATION OF FERROUS ION

5.1 Introduction

During bio-oxidation of ferrous ion, ferric precipitate is formed and ferric ion solubility has been reported to be solution pH dependent (Drouet and Navrotsky, 2003; Gramp *et al.*, 2008; Mabusela and Ojumu, 2017; Kaksonen *et al.*, 2019). pH is a critical operating parameter since it has a substantial effect on the chemical reactions occurring in solution, particularly in the formation of iron precipitates. Studies have demonstrated the recovery of a significant quantity of metal trapped in some iron precipitate minerals, which may reduce the overall extraction efficiency of a typical bioleach operation (Ju *et al.*, 2011; Liu *et al.*, 2017; Wang *et al.*, 2018). Thus, the mobility of desired metal ions in the bioleaching system is limited by the nature of the iron precipitate formed on the surface of the mineral ore as the bioleach operation proceeds. This necessitates further research into the surface characteristics of biogenic iron precipitates.

5.2 Objective

The main goal of the study in this chapter is to investigate the surface properties of biogenic iron precipitate produced from the mixed mesophile mediated oxidation of ferrous ion under different initial solution pH in a CSTR. The biogenic precipitates were characterized using surface-specific analytical techniques, namely XRD, SEM/EDS, FTIR, XPS, TGA, and BET. The results of this study may provide more insight into understanding the retention of metal ions onto iron precipitates in hydrometallurgical and bio-hydrometallurgical processes. The information obtained from this present chapter may be applicable in the design and implementation of iron bio-oxidation for minimal iron precipitate formation.

5.3 Methodology

The biogenic iron precipitate was obtained from the experiments carried out in Chapter 4. The characterization procedures used in this study have been previously described in Section 3.3 and 3.4 of Chapter 3. In this thesis, the precipitate samples synthesized at the investigated solution pH values of 1.7, 1.9, and 2.2 are code-named Jar-1.7, Jar-1.9, and Jar-2.2 respectively.

5.4 Results and discussion

5.4.1 XRD analysis

The XRD patterns of the iron precipitate are illustrated in Figure 5.1. The patterns matched the International Centre for Diffraction Data (ICDD) indexed to potassium jarosite (K-jarosite), $KFe_3(SO_4)_2(OH)_6$ (PDF: 22-0827 and 71-1777) with (113) being the favoured orientation. A comparison of all the XRD patterns revealed that, regardless of the increase in pH in this study, all the diffraction peaks were of similar structure, suggesting that an increase in pH does not probably affect the strain of the crystal visibly, which may have influenced the stability of their crystallinity. All the jarosite samples exhibited the rhombohedral structure that belongs to the space group of $R\bar{3}m$. The lattice parameters obtained are shown in Table 5.1. With an increase in the influent solution pH, a slight increase in peak intensity was observed. In addition, a slight decrease in the unit cell parameters (a and c) of the jarosites was also observed as the pH increased from 1.7 to 2.2. The crystallinity of the biogenic jarosites was well-defined and there was no other detection of poorly crystalline or crystalline phases (such as hematite, goethite, etc) associated with jarosite forms or products related to precursor residues. Thus, it demonstrates that solid precipitates of potassium jarosites were produced. The crystal size reflects growth conditions and determines the surface area which in turn, is important for all types of surface reactions. The average crystallite sizes were calculated using Scherrer's equation (Equation 3.1) (Holzwarth and Gibson, 2011) and were found to be 8.68, 8.42, and 8.08 nm for pH 1.7, 1.9, and 2.2 respectively (Table 5.1). A decrease in the average crystallite size as the influent solution pH increased was observed. This is likely because, at higher pH, the

presence of OH^- ions is less dominant than SO_4^{2-} ions in the jarosite structure owing to its smaller ionic radius (r_{OH^-} = 0.119 nm < $r_{SO_4^{2-}}$ = 0.244 nm) (Shannon, 1974). This may be attributed to having facilitated the decrease in crystallite size. The decrease in lattice parameters and the crystallite sizes as the synthesis pH values increased observed in this study corroborates well with the recent findings of Hernández-Lazcano *et al.* (2021). During the precipitation process, smaller crystallites came closer and grew larger due to kinetics. Thus, the pH of the solution influenced the crystallite size, which depends on the nucleation and growth kinetics during iron precipitation.

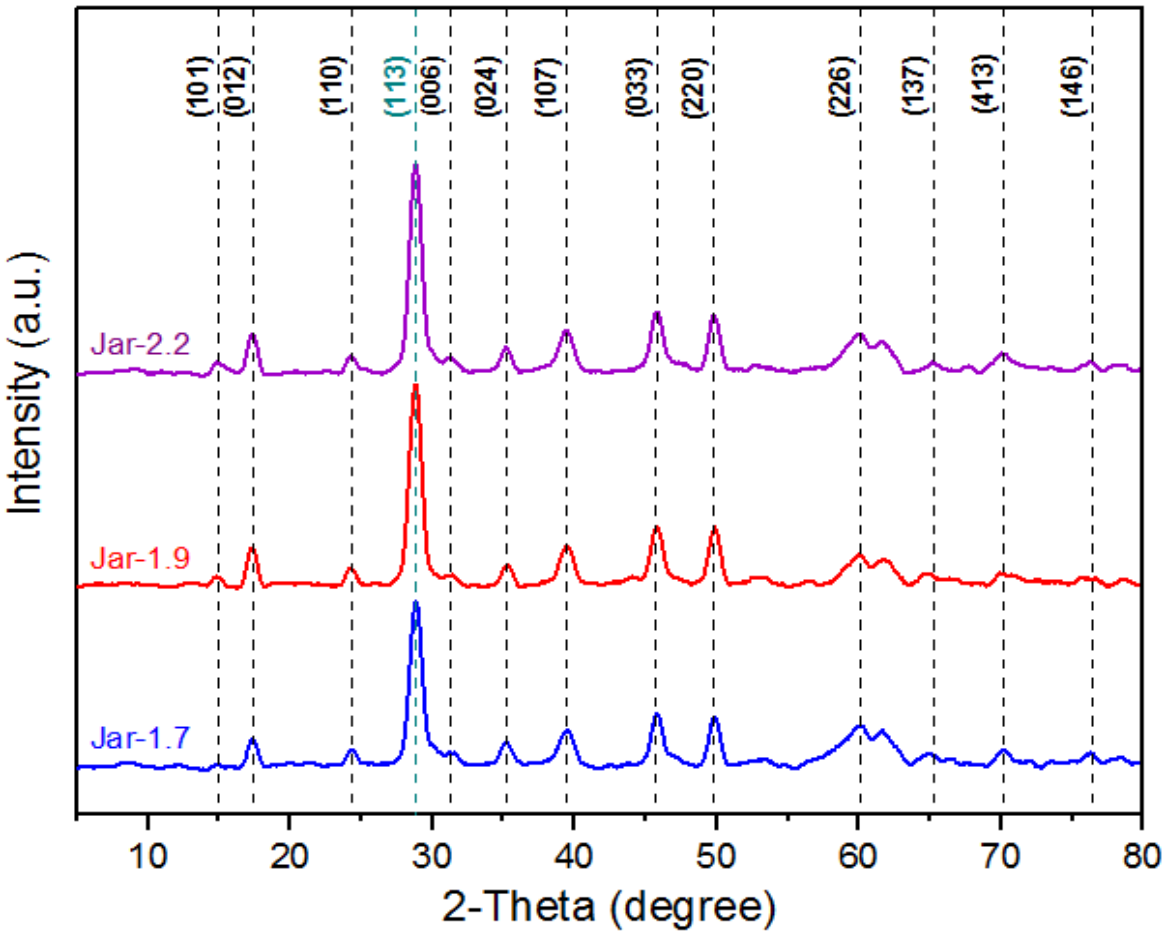

Figure 5.1: XRD patterns of biogenic potassium jarosites

Table 5.1: Crystallite size and lattice parameters of biogenic jarosite synthesized at different pH values

Jarosite sample	Average crystallite size (nm)	*a=b* (Å)*	*c* (Å)
Jar-1.7	8.68	7.32	17.22
Jar-1.9	8.42	7.29	17.16
Jar-2.2	8.08	7.29	17.16

**a=b* trigonal (hexagonal) lattice

5.4.2 SEM analysis

There exists a similar but evident variation in the surface morphology (external shape) of the jarosite crystal formed, as shown in Figure 5.2(a–c). All the jarosites formed are dense light ochreous yellow residues. The morphologies are typical of K-jarosite, composed of aggregates of round, elliptical and/or tabular, and granular particles, with no pronounced sharp edges. The well-defined crystallinity of the tabular and round shapes observed could be attributed to the presence of large cell concentrations (Sasaki *et al.*, 2006) used in the study. To further explain the morphology, the pH of the prepared solution (inoculum and growth medium) was acidic, and as the pH of the solution was raised by adding a strong concentration of base (NaOH); mainly K^+ and OH^- ions were liberated, increasing the solubility of the solution. These OH^- ions are located on the facets of the produced nuclei (Basciano and Peterson, 2008; Hernández-Lazcano *et al.*, 2021). Subsequently, OH^- ions inhibit development and agglomeration, resulting in some elliptical and/or tabular particles of the produced jarosite at all pH values tested, which are well pronounced at pH 2.2. It is worth noting that some voids emerged on the surface of the particles, which could be a result of the melting of hydroxysulfates after electron beam interaction (Jiménez *et al.*, 2019). However, the poor crystallinity of some crust-like small/tiny particles was observed as clusters on the surface of the individual particle, especially on precipitate formed at pH 1.7. This might have been a result of slow precipitation time and some smaller concentration of the cell numbers, which may have led to the unripened crystal units (Sasaki and Konno, 2000; Kaksonen *et al.*, 2014a). The proportion of poorly crystallized particles decreased with increasing solution pH, thus, enhancing the formation of distinct

particles. It has been observed that the morphology of jarosite is impacted by the type of the monovalent cation and/or the rate of Fe^{3+} supply (Sasaki and Konno, 2000). Interestingly, it should be noted that even though NaOH was used to control pH values in this study, Na-jarosite was not formed during the microbial synthesis. The preferential precipitation of K-jarosite over other types of monovalent jarosites could be attributed to its thermodynamic stability ($K^+ > Na^+ \sim H_3O^+ > NH_4^+$) and ionic radius ($r_{K^+} = 1.64$ Å > $r_{Na^+} =$ 1.39 Å) (Gaboreau and Vieillard, 2004; Sasaki *et al.*, 2006; Aguilar-Carrillo *et al.*, 2018). In conclusion, it can be said that changes in surrounding pH had a significant role in the nucleation and development of jarosite crystallites, which determined the final morphology of the precipitate. Thus, the surface morphology was pH dependent.

Particle size analysis provides information on the size distribution of particles. The size distribution of the precipitated particles obtained at different initial pH values is shown in Figure 5.2(d–f). The average particle size decreased as the pH of the influent solution increased. For the initial solution pH of 1.7, 1.9, and 2.2, the average particle size distribution was 726.83 ± 43.13, 641.84 ± 37.17, and 597.76 ± 28.95 nm respectively. The observation of an increase in pH leading to a decrease in particle size has also been reported elsewhere (Mabusela and Ojumu, 2017; Hernández-Lazcano *et al.*, 2021). The obtained particle size fell within the values reported in a recent study. In a study by Hernández-Lazcano *et al.* (2021) on the effect of pH and aging time on jarosite synthesis in the chemical oxidation of ferrous ion, a particle size range of ~1000 – 200 nm was observed between 0 – 7 days aging time, for jarosite synthesized at pH 2.1. In this present study, the distribution of particles at pH 2.2 revealed the formation of distinct smaller particles whereas precipitates generated at pH 1.7 showed the formation of large particles. The smaller particles formed at pH 2.2 are attributed to rapid precipitation while the large particles formed at pH 1.7 are attributed to the relatively slow precipitation reaction rates. The particle size distribution of jarosite has been reported to be affected by the rate of crystallization (Sasaki and Konno, 2000) and the level of agglomeration (Kaksonen *et al.*, 2014a). The effect of crystallization was visible from SEM results in Figure 5.2(a–c). Crystallization became more significant with an increase in initial solution pH as evidenced by the well-developed crystals formed at pH 2.2. By comparing SEM particle sizes to XRD

crystallite sizes, it is evident that the particles identified in SEM were made up of smaller crystallites. Therefore, the initial pH value could be used to obtain the desired particle size distribution range.

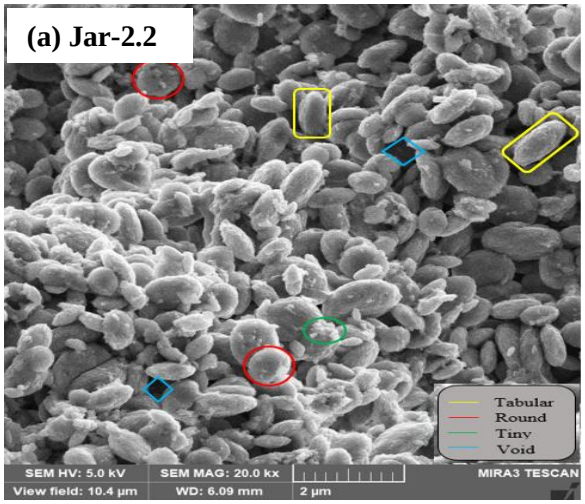

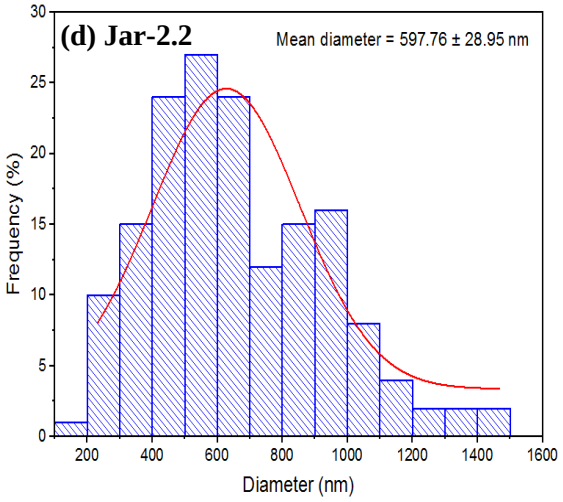

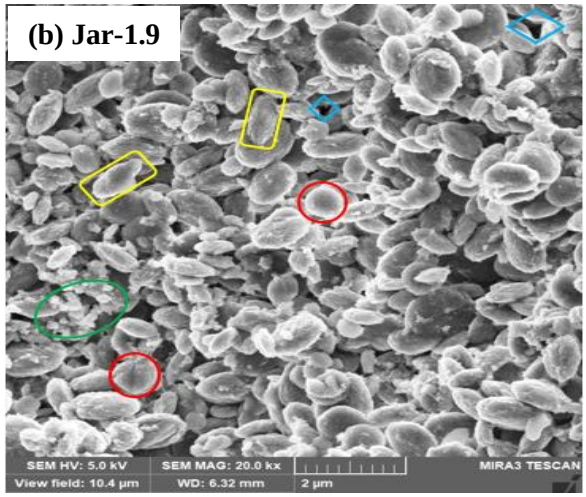

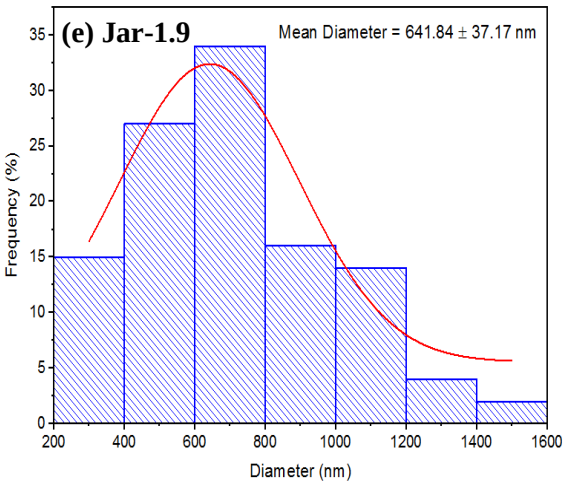

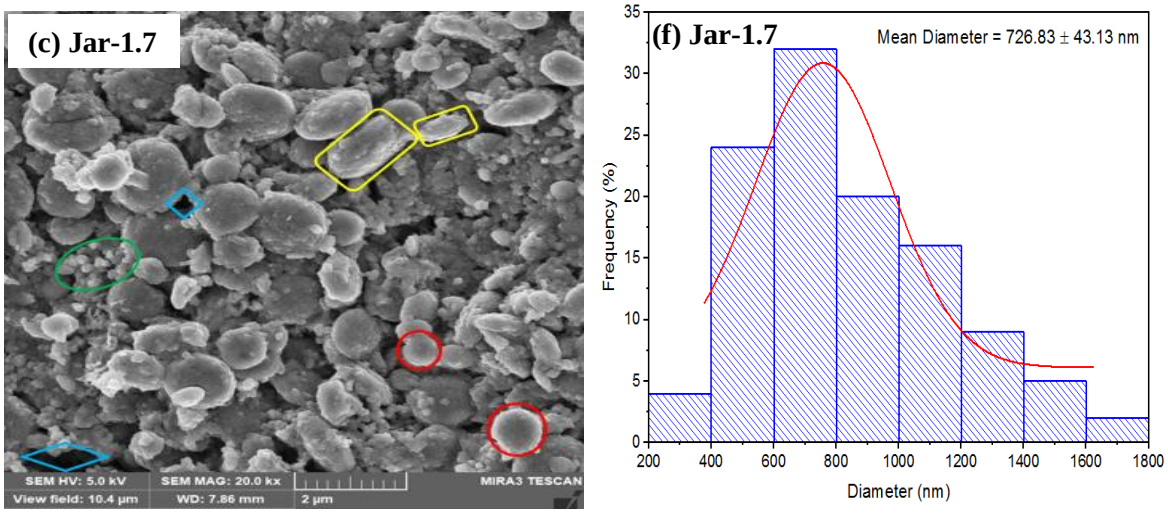

Figure 5.2: SEM images (a–c) and corresponding particle size distribution (d–f) of biogenic potassium jarosite formed at different pH values

5.4.3 EDS analysis

EDS was employed to identify the elemental composition and specific cations of the jarosite. The results are presented in Figure 5.3(a–c) and Table 5.2. The signals of iron, sulfur, oxygen, and potassium pronounced in K-jarosite were also found on the EDS spectra. The appearance of the P element was further confirmed, which shows that phosphate may be integrated into the structure of jarosite (Table 5.2). It has previously been reported that phosphate is frequently chemisorbed to the surfaces of Fe minerals, particularly at pH values where the surface functional groups are positively charged (Bigham *et al.*, 2010). At pH 2.2, the Fe/S molar ratio of 1.42 obtained in this present study is closer to the Fe/S standard stoichiometric ratio of 1.5 for K-jarosite, than the Fe/S molar ratios of 1.35 and 1.04 obtained at pH 1.9 and pH 1.7 respectively. This result also demonstrated that there may be a direct relationship between an increase in initial pH and Fe/S ratio. According to the EDS results, a trend was observed with regard to the increase in both the total content of Fe, S, and K, and the Fe/S molar ratio as the synthesis influent pH increased. However, the extent to which this tendency relates to K-jarosite is unknown.

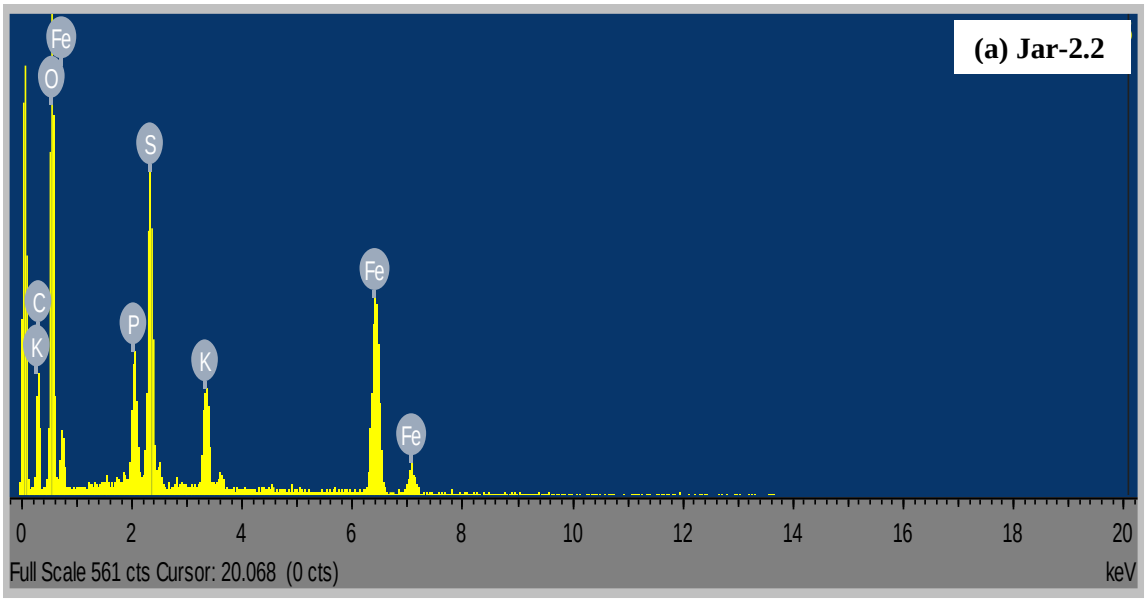
(a) Jar-2.2
Fe
O
S
C
K
P
K
Fe
Fe
0
2
4
6
8
10
12
14
16
18
20
Full Scale 561 cts Cursor: 20.068 (0 cts)
keV

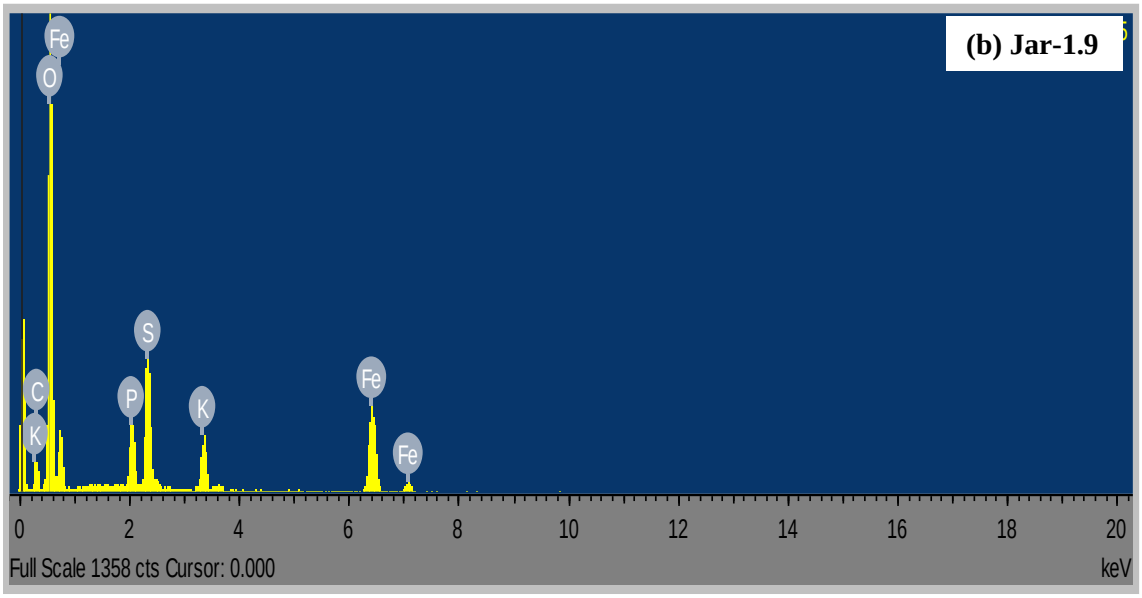
(b) Jar-1.9
Fe
O
S
C
K
P
K
Fe
Fe
0
2
4
6
8
10
12
14
16
18
20
Full Scale 1358 cts Cursor: 0.000
keV

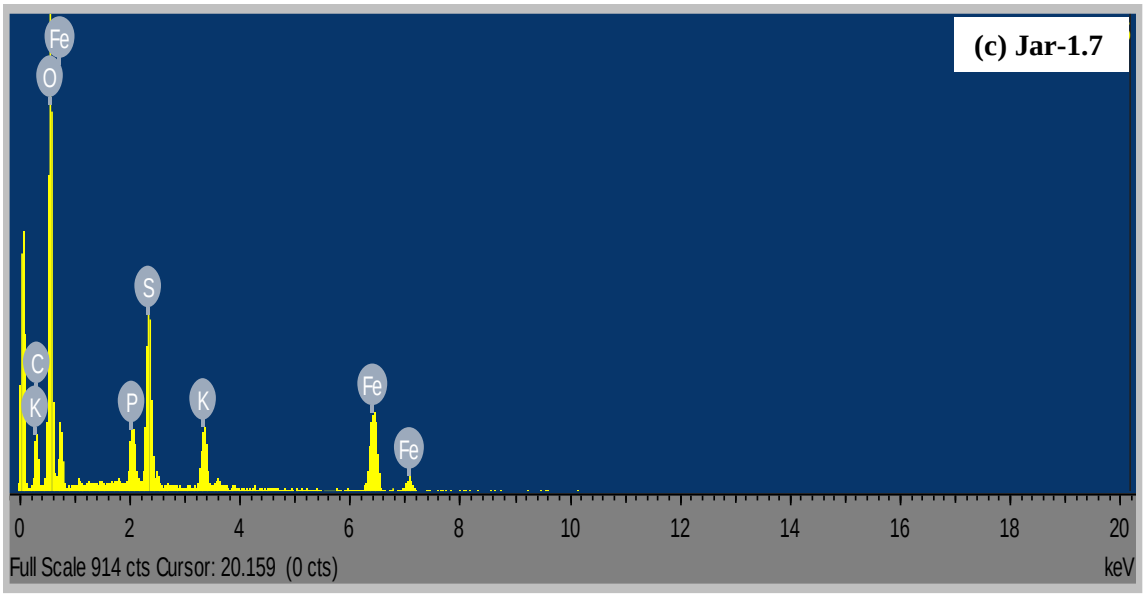

Figure 5.3: Figure 5.4: EDS spectra of biogenic potassium jarosite formed at different pH values

Table 5.2: Elemental weight composition (F, S, and K) and ratios in biogenic potassium jarosite

	Elemental composition (%)			Molar ratio		
Jarosite	F	S	K	Fe/S	Fe/K	S/K
Jar-1.7	11.21	6.21	2.73	1.04	2.88	2.78
Jar-1.9	14.94	6.34	2.86	1.35	3.66	2.71
Jar-2.2	16.45	6.63	2.93	1.42	3.94	2.76

5.4.4 XPS analysis

To validate the chemical composition and surface species of the produced biogenic K-jarosite, the samples were further studied via the XPS analysis. The wide survey scan of the XPS spectra is shown in Figure 5.4a. It can be seen that the major presence of iron, sulfur, and oxygen are revealed which are peculiar to jarosite. According to the high-resolution XPS spectra, the peaks at binding energies of 531.40 eV (pH 1.7), 531.47 eV (pH 1.9), and 531.55 eV (pH 2.2) observed in the spectra of O 1s (Figure 5.4b) indicate the elemental oxygen of the hydroxides (Dupin *et al.*, 2000) present in the crystalline network of jarosite. In the Fe 2p spectra (Figure 5.4c), two doublets, i.e., Fe $2p_{1/2}$ and Fe $2p_{3/2}$ (of an approximate area ratio of 2:1) were observed with a spin-orbit splitting energy of 13.19 eV

(pH 1.7), 13.45 eV (pH 1.9), and 13.39 eV (pH 2.2). The peaks of the Fe $2p_{3/2}$ is the most intense peak of the Fe 2p doublet, thus revealing peaks at 711.29 eV (pH 1.7), 711.03 eV (pH 1.9), and 710.78 eV (pH 2.2), which are all assigned to the binding energy of the Fe(III)–O chemical state. This further confirmed Fe(III) bulk presence in the biogenic jarosite (Wang *et al.*, 2014; Deng *et al.*, 2020). While in the spectra of S 2p (Figure 5.4d), the appearance of two doublets was also observed for the K-jarosite. The peaks with intense signals at 168.87 eV (pH 1.7), 168.76 eV (pH 1.9), and 168.72 eV (pH 2.2) are all attributed to the presence of sulfate ion (SO_4^{2-}) (Fantauzzi *et al.*, 2015; Deng *et al.*, 2020). The characteristic peaks in the S 2p spectra with lower energies of 162.25 eV (pH 1.7), 162.74 eV (pH 1.9), and 162.85 eV (pH 2.2) are all attributed to contributions from polysulfide (S^{2-}) in the jarosite samples (Fantauzzi *et al.*, 2015; Zhang *et al.*, 2021b). The peaks at binding energies of 133.46 eV (pH 1.7), 133.58 eV (pH 1.9), and 133.61 eV (pH 2.2) identified in the spectra of P 2p (Figure 5.4e) are indicative of the presence of phosphate ion (PO_4^{3-}) (Siow *et al.*, 2018). The high-resolution XPS spectra of K 2p are also depicted in Figure 5.4f. The slight shifts in the binding energies and intensities can be attributed to changes in the oxidation states of the elements present in the jarosite (Rao *et al.*, 1980). The higher binding energies correspond to higher oxidation states. Table 5.3 summarises the binding energies and their corresponding chemical state.

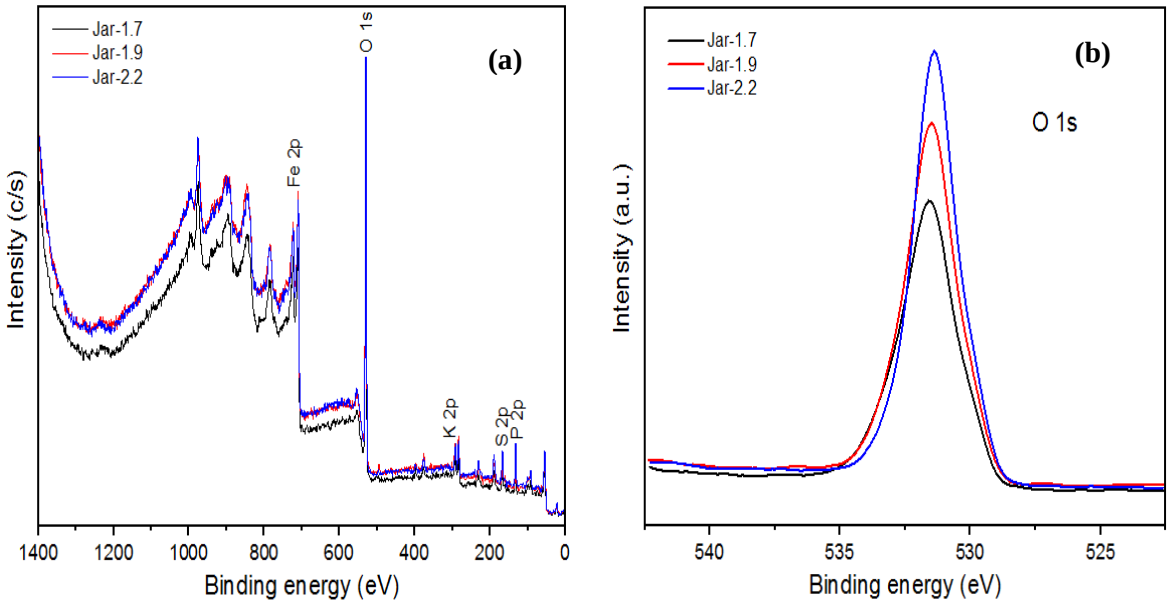

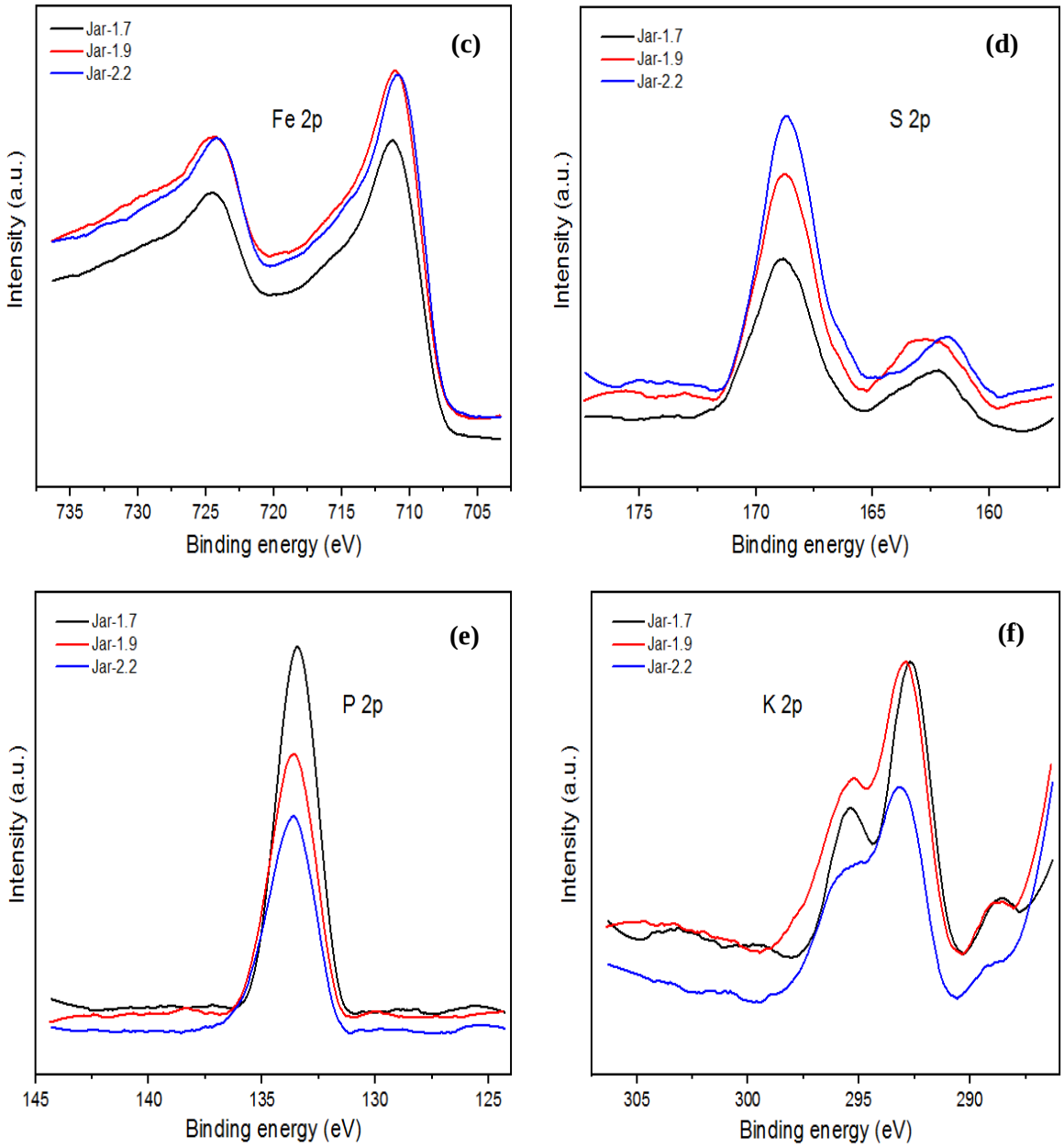

Figure 5.4: (a) XPS survey spectra of biogenic potassium jarosite at different influent solution pH; (b) high-resolution XPS spectra of O 1s; (c) Fe 2p, (d) S 2p, (e) P 2p, and (f) K 2p

Table 5.3: Binding energies (eV) of element lines of biogenic jarosite formed at different solution pH values

Element line	Binding energy (eV)			Chemical state (group)
	Jar-1.7	Jar-1.9	Jar-2.2	
O 1s	531.40	531.47	531.55	OH^- (hydroxide)
P 2p	133.46	133.58	133.61	PO_4^{3-} (phosphate)
Fe $2p_{3/2}$	711.29	711.03	710.78	Fe(III)–O
S $2p_{3/2}$ (I)	162.25	162.74	162.85	S^{2-} (polysulfide)
S $2p_{3/2}$ (II)	168.87	168.76	168.72	SO_4^{2-} (sulfate)

Diffusive processes can also induce a shift in intensity since the depth distribution of the atoms affects the intensity (Wiltner and Linsmeier, 2008). An increase in intensity was observed when the atoms diffused towards the surface and a decrease in intensity was observed when the atoms diffused towards the bulk, which could all be linked to the changes in the investigated influent solution pH values.

5.4.5 FTIR analysis

FTIR spectra obtained to identify the functional groups of the biogenic jarosite are illustrated in Figure 5.5. The peak positions in the spectra are nearly the same. The v_1, v_3, and v_4 of sulfate (SO_4^{2-}) modes are indicated, where v_1 and v_3 are the stretching modes, while v_4 is the bending mode. The bands identified between 3362 – 3369 cm^{-1} for the spectra are ascribed to *v*OH stretching vibrational mode in jarosite originating from water and hydroxyl groups (Sasaki *et al.*, 1998; Aguilar-Carrillo *et al.*, 2018). Bands detected between 1624 – 1637 cm^{-1} could be attributed to the δ(H_2O), water-bending vibrations. The bands present in the region 1189 – 1196 cm^{-1} and 1077 – 1080 cm^{-1} could be linked to the $v_3(SO_4^{2-})$ stretching vibration (Bishop and Murad, 2005). Specifically, the bands near ~1100 cm^{-1} are cation sensitive. The bands observed at 1077 – 1080 cm^{-1} in this study are in strong agreement with the reports of Spratt *et al.* (2013) and Aguilar-Carrillo *et al.* (2018) for K-jarosite. Identification of strong bands located in the region of 997 – 1000 cm^{-1} is on account of the stretching vibrational modes of $v_1(SO_4^{2-})$ and OH deformation (δ_{OH}) (Aguilar-Carrillo

et al., 2018). The sharp bands identified at 629 cm^{-1} showed the bending vibrational mode of $v_4(SO_4^{2-})$ in jarosite-group. The bands at lower energies found between 470 – 506 cm^{-1} on the spectra are attributed to the Fe–O lattice stretching vibrational mode of FeO_6 octahedral component in jarosite crystal (Breitinger *et al.*, 1997; Aguilar-Carrillo *et al.*, 2018). It should be noted that $v_2(SO_4^{2-})$, which is a bending vibrational mode, was not observed, most likely owing to its overlap with other neighbouring high absorption modes (Zhu *et al.*, 2013). A summary of the absorption peaks detected in the FT-IR spectra is given in Table 5.4.

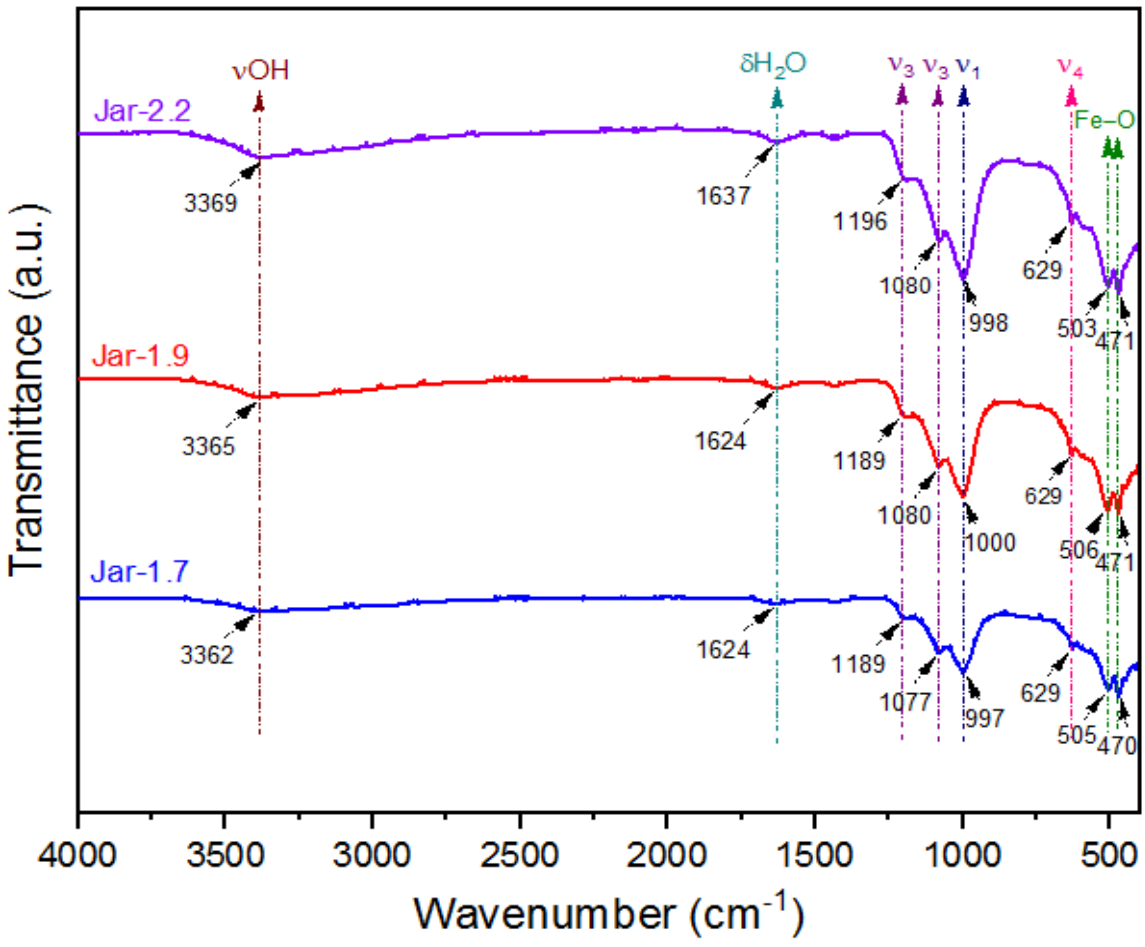

Figure 5.5: FTIR spectra of biogenic potassium jarosite

Table 5.4: Infrared bands of biogenic jarosite formed at different solution pH values

Wave numbers (cm^{-1})			Functional group	Mode of vibration
Jar-1.7	Jar-1.9	Jar-2.2		
3362	3365	3369	υOH	stretching
1624	1624	1637	$\delta(H_2O)$	bending
1189	1189	1196	$v_3(SO_4^{2-})$	stretching
1077	1080	1080	$v_3(SO_4^{2-})$	stretching
997	1000	998	$v_1(SO_4^{2-})$, δ_{OH}	stretching
629	629	629	$v_4(SO_4^{2-})$	bending
505	506	503	Fe–O	stretching
470	471	471	Fe–O	stretching

5.4.6 TGA analysis

The thermal stability of the biogenic K-jarosites was tested by the TGA technique. The TGA and the first derivative thermogravimetry analysis (DTA) curves are depicted in Figure 5.6(a–c). The TGA/DTA profiles are similar, although with observable narrow differences in the positions and intensities of some endothermic peaks.

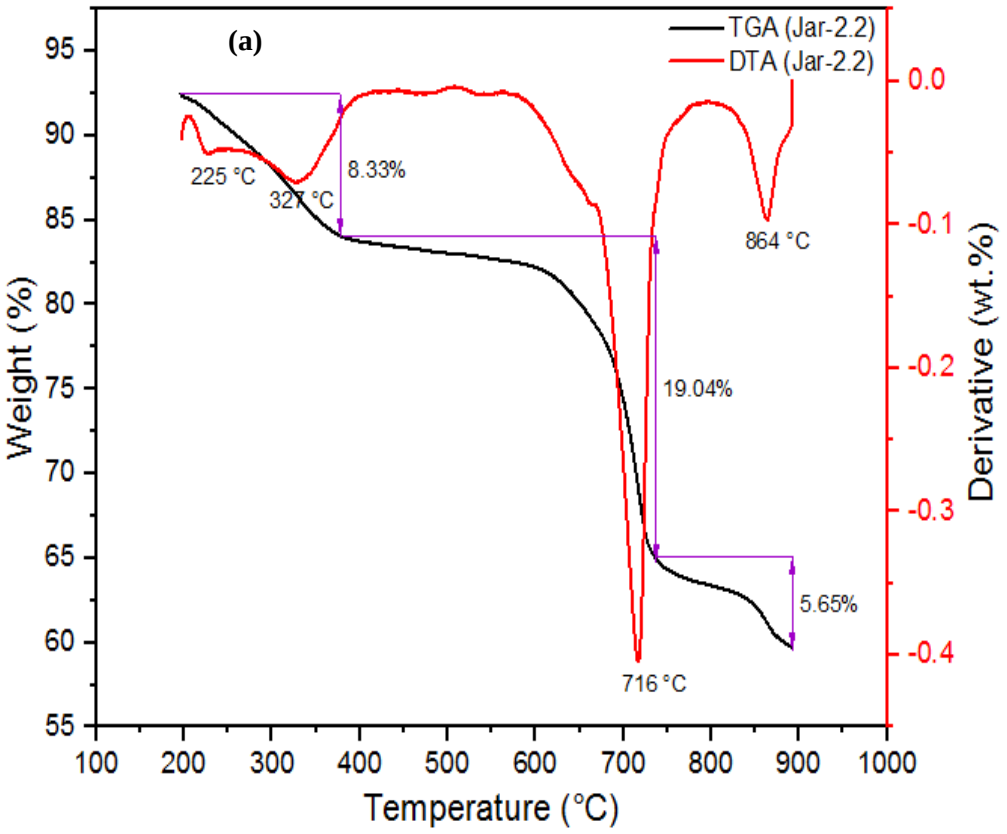
(a)
TGA (Jar-2.2)
DTA (Jar-2.2)
225 °C
327 °C
8.33%
864 °C
19.04%
5.65%
716 °C
Weight (%)
Derivative (wt.%)
Temperature (°C)

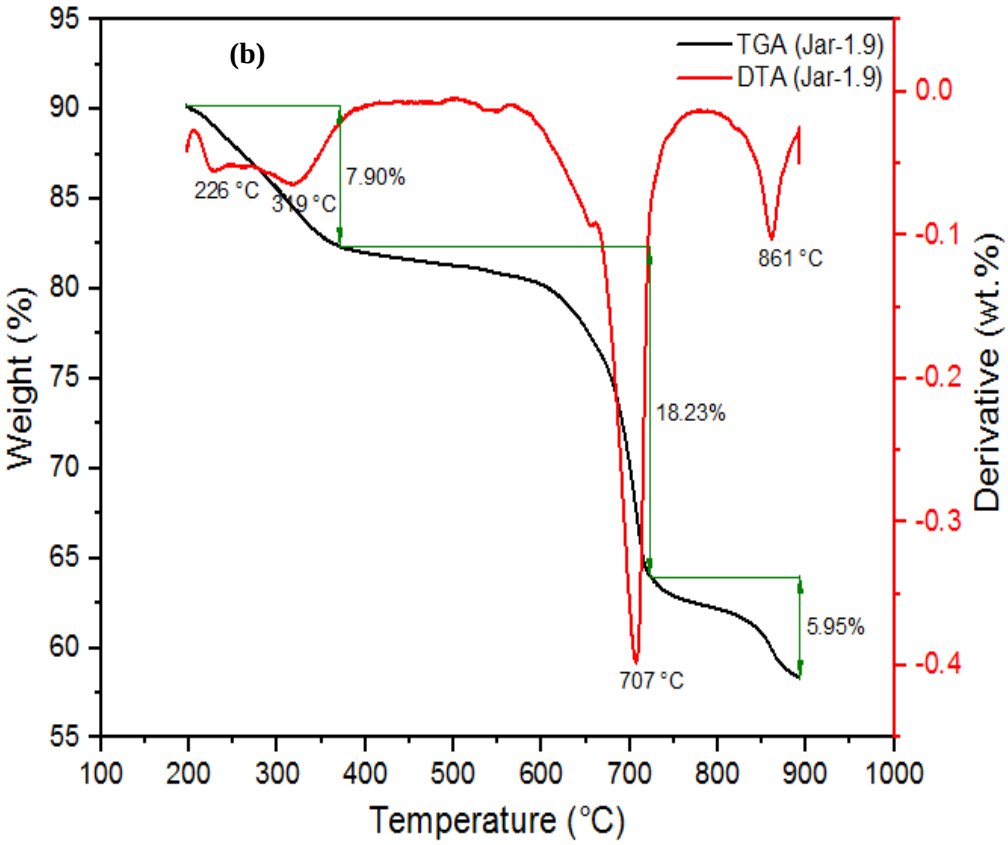
(b)
TGA (Jar-1.9)
DTA (Jar-1.9)
226 °C
319 °C
7.90%
861 °C
18.23%
5.95%
707 °C
Weight (%)
Derivative (wt.%)
Temperature (°C)

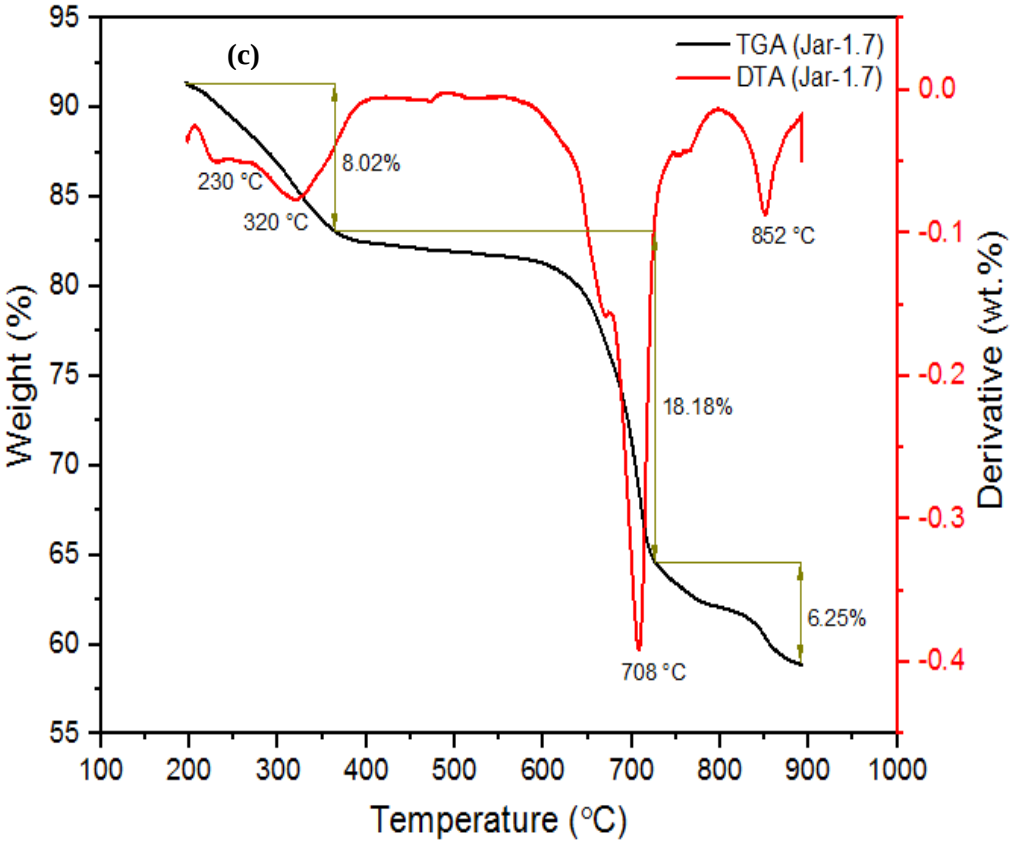

Figure 5.6: TGA/DTA analysis of biogenic potassium jarosite

All the profiles showed three distinct mass loss phases marked notably with four endothermic peaks. Pronounced first mass losses of 8.02% (pH 1.7), 7.90% (pH 1.9), and 8.33% (pH 2.2) are observed with weak endothermic peaks at 230 and 320 °C for pH 1.7; 226 and 319 °C for pH 1.9; and lastly, at 225 and 327 °C for pH 2.2. These two endothermic temperature peaks are attributed to the removal of adsorbed water molecules and dehydroxylation of potassium jarosite respectively (Drouet and Navrotsky, 2003; Zhu *et al.*, 2013). This led to the formation of a yavapaiite compound, $KFe(SO_4)_2$, and the crystallization of hematite (α-Fe_2O_3) in all the jarosite samples. The process is described as follows:

$$KFe_3(SO_4)_2(OH)_6 \rightarrow KFe(SO_4)_2 + Fe_2O_3 + 3H_2O \quad (5.1)$$

The second mass losses of 18.18% (pH 1.7), 18.23% (pH 1.9), and 19.04% (pH 2.2) with sharp endothermic peaks observed at ~708 °C (pH 1.7), ~707 °C (pH 1.9), and ~716 °C (pH 2.2),

are all attributed to the complete thermal decomposition of yavapaiite (Zhu *et al.*, 2013) and the release of sulfur oxides (Jiménez *et al.*, 2019), as given by the following expression:

$$KFe(SO_4)_2 \rightarrow 1/2\,Fe_2O_3 + 1/2\,K_2SO_4 + SO_{3(g)} \quad (5.2)$$

Furthermore, the maximum endothermic peaks at ~852 °C (pH 1.7), ~861 °C (pH 1.9), and ~864 °C (pH 2.2), which show the third mass losses of 6.25%, 5.95%, and 5.65% respectively, are indicative of the decomposition of some intermediate products. In addition, they demonstrate the major presence of α-Fe_2O_3 and K_2SO_4 (Drouet and Navrotsky, 2003). In the work of Kubisz (1971) on jarosite decomposition, it was noted that SO_3 can stay in the system up to 1000 °C, whereas K_2SO_4 decomposes only above 1000 °C. The slight changes in decomposition over the temperature range observed in Figure 5.7(a–c) could be due to particle size distribution and kinetic control effect during the bio-oxidation process, which can probably be influenced by the solution condition, such as the initial pH.

5.4.7 BET analysis

The specific surface area (SSA) and porosity of a crystal are highly influenced by the conditions in which it grows. BET technique was used to estimate the SSA, while the BJH method was employed to determine the pore size distribution and pore volume of the jarosite samples. Because adsorption is a surface phenomenon, SSA is one of the most essential parameters of an adsorbent material because it shows the required active sites for adsorption. The adsorptive performance of a material is directly related to its surface area (Lv *et al.*, 2018; Yin *et al.*, 2020). Porosity (pore volume) is the sum of all the pores in an adsorbent and contributes to the internal surface area of the material, which might affect the kinetics of adsorption. The jarosite obtained at pH 1.7, 1.9, and 2.2 showed BET surface areas of 8.32, 8.58, and 11.00 m^2/g with total pore volumes of 0.03, 0.03, and 0.04 cm^3/g respectively. The observed increase in surface area as solution pH increases could be attributed to smaller particles formed at pH 2.2 compared to the large particles formed at pH 1.7. This also demonstrated that the degree of agglomeration affects particle size and, consequently, the surface area of the jarosite particles. This is consistent with the morphology and particle size results reported in section 5.4.3. The SSA of biogenic K-

jarosite obtained in this present study are higher than the reported values of 1.62 m^2/g at pH 3.0 (Bhaskar *et al.*, 2019) and 7.27 m^2/g at pH ~2.5 (Wei *et al.*, 2020). Even though the investigated pH values in this present study are lower than those reported in the cited literature, the higher SSA obtained in this present work could be linked to the technical and microbial advantages of the reactor type and the bacteria strain employed here. N_2 adsorption-desorption isotherms are depicted in Figure 5.7(a–c). The plots revealed type-IV isotherm and H3 hysteresis loop patterns (Sing, 1985), showing that the biogenic K-jarosites are mesoporous in structure. The pore size of a material is defined as the gap or stretch of its pores. The average pore sizes of the jarosite were estimated to be 16.15, 13.36, and 10.45 nm, for initial solution pH of 1.7, 1.9, and 2.2 respectively. These values are consistent with the Brunauer–Deming–Deming–Teller (BDDT) classification methodology, which classifies pores with a diameter of 2 – 50 nm as mesopores (Sing, 1985). According to the adsorption pore-size distribution plots (Figure 5.7(d–f)), the majority of the average pore sizes were within the range of 2 – 25 nm, confirming that the jarosites are composed predominantly of mesoporous particles. Jarosite samples generated at a higher pH readily become loose and porous, which facilitates metal ion diffusion and transport (Guo *et al.*, 2020). The increased surface area of jarosites as influent pH increases is another surface property influenced by the overall solution conditions for metal scavenging in bioleaching processes. Table 5.5 gives the summary of the surface areas and pore size distribution.

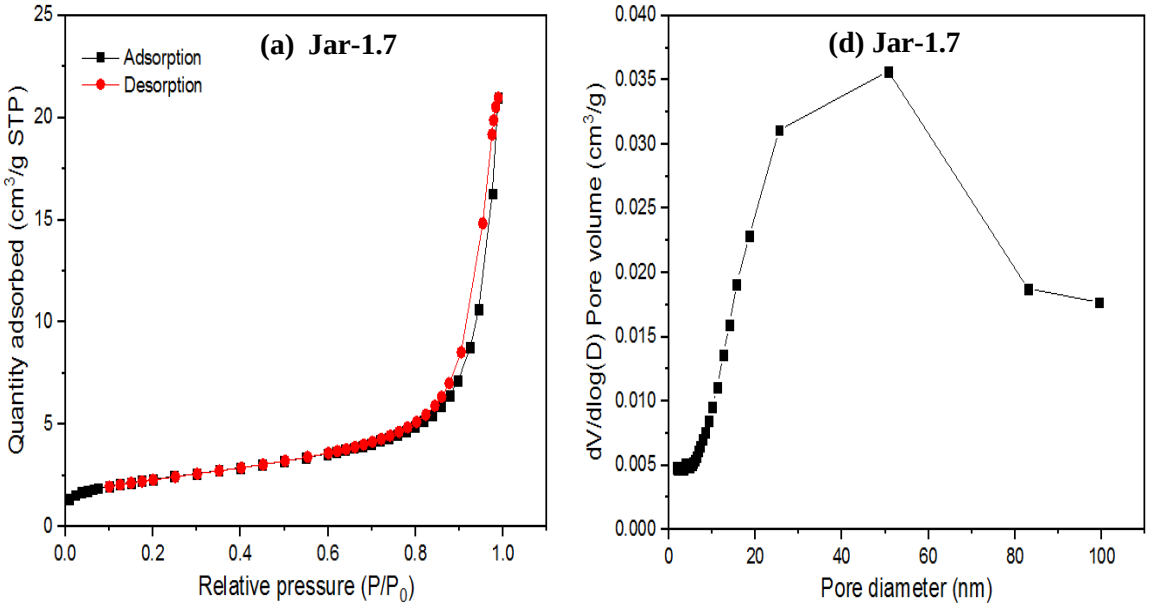

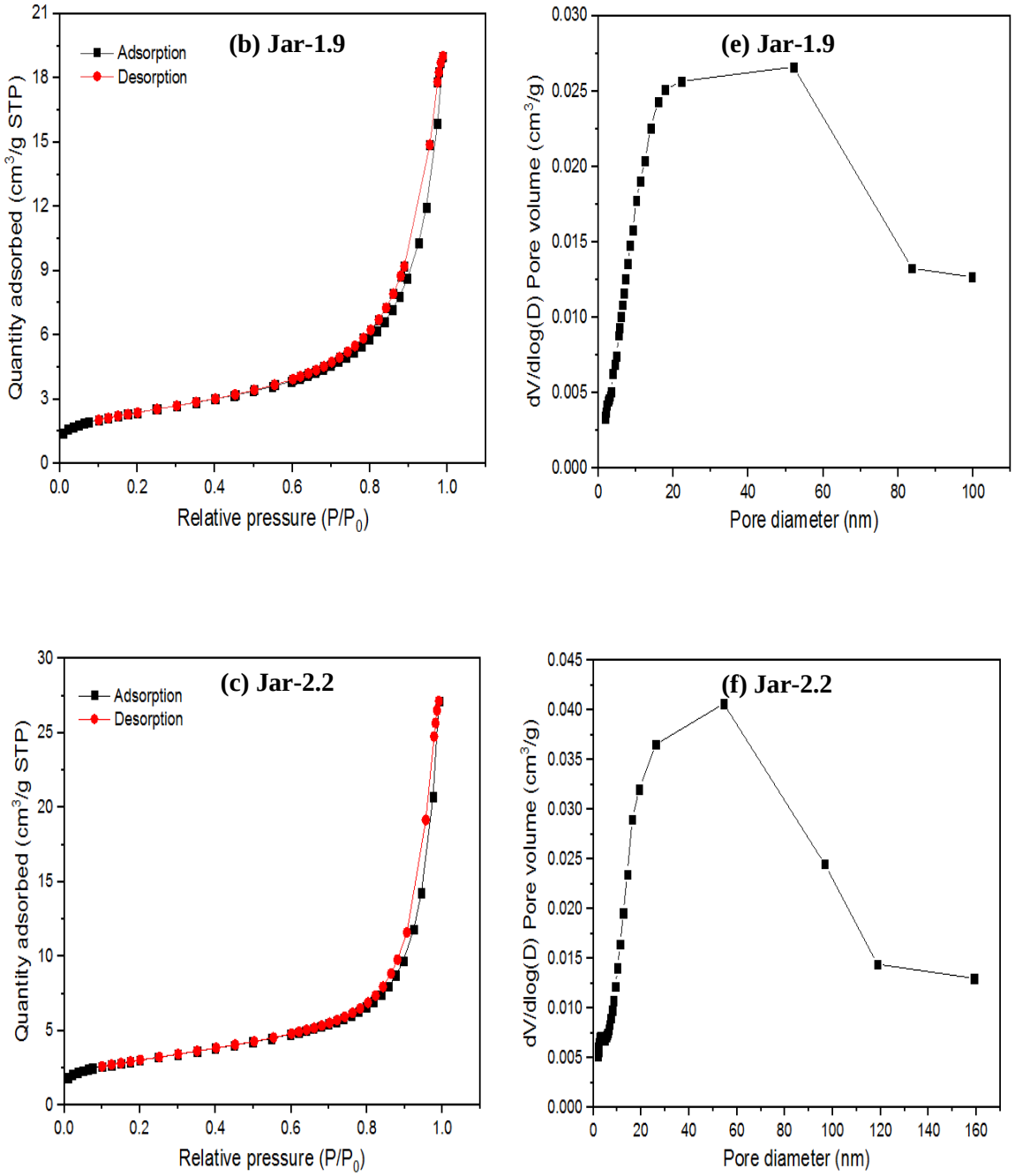

Figure 5.7: N2 adsorption/desorption isotherm (a–c) and pore-size distribution (d–f) of biogenic potassium jarosite

Table 5.5: Surface area, pore volume, and pore diameter of biogenic potassium jarosite

Jarosite	BET surface area (m^2/g)	Total pore volume (cm^3/g)	BJH average pore size (nm)
Jar-1.7	8.32	0.03	16.15
Jar-1.9	8.58	0.03	13.36
Jar-2.2	11.00	0.04	10.45

5.5 Conclusions

In this chapter, the effect of pH on the surface properties of biogenic jarosite generated at a temperature of 35 °C and an aging time of 14 days was successfully investigated. The results indicate that the surface properties of biogenic jarosite have a strong dependency on the pH of the solution. All the precipitates formed are dense light ochreous yellow residues. The XRD patterns of the precipitates were identified as potassium jarosite (K-jarosite), $KFe_3(SO_4)_2(OH)_6$, with (113) being the favoured orientation. There was no other detection of other poorly crystalline or crystalline phases (such as hematite, goethite, etc). A slight decrease was observed in the unit cell parameters (*a* and *c*) of the jarosites as the pH increased from 1.7 to 2.2. Likewise, with an increase in influent solution pH, a decrease in the average crystallite sizes was observed and was found to be 8.68, 8.42, and 8.08 nm for pH 1.7, 1.9, and 2.2 respectively. The SEM morphologies are composed of aggregates of spherical/round, tabular, and granular particles. The proportion of poorly crystallized particles decreased with increasing solution pH, thus, enhancing the formation of distinct particles. The EDS results revealed a trend with the decrease in the total content of Fe, S, and K as the synthesis influent pH increased. Most importantly, the changes in the solution pH impacted the BET surface area analyses of the K-jarosites, which ranged from 8.32, 8.58, and 11.00 m^2/g; while the pore size distribution ranged from 16.15, 13.36, and 10.45 nm for pH values 1.7, 1.9, and 2.2 respectively, confirming that the jarosite residues are composed mainly of mesoporous particles. In conclusion, it can be said that changes in surrounding pH have a significant role in the crystallite size, growth kinetics, nucleation and development of jarosite crystals, which determine the final morphology, pore size distribution, porosity, and surface area of the precipitate.

CHAPTER SIX

KINETICS, THERMODYNAMICS AND MECHANISM OF Cu(II) ION SORPTION BY BIOGENIC IRON PRECIPITATE

This chapter has been published in *ACS Omega* (ACS), doi: 10.1021/acsomega.1c03855 as

Oladipo, B., Govender-Opitz, E. and Ojumu, T. V. (2021). Kinetics, thermodynamics and mechanism of Cu(II) ion sorption by biogenic iron precipitate: using the lens of wastewater treatment to diagnose a typical biohydrometallurgical problem

"If you are fearful of the destruction of the environment, then learn to quit being an environmental parasite." – Wendell Berry

CHAPTER 6: KINETICS, THERMODYNAMICS, AND MECHANISM OF CU(II) ION SORPTION BY INDUSTRIAL BIOGENIC PRECIPITATE PRODUCED FROM BIOLEACHING

6.1 Introduction

Extensive literature studies have shown that iron precipitation during the dissolution of sulfide minerals using hydro- and bio-hydrometallurgical treatment, is an inevitable phenomenon (Qiu *et al.*, 2005; Nurmi *et al.*, 2010). Authors have suggested that precipitate formation serves as the outlet path for unwanted iron, alkali ions or sulfate ions from the processing circuit (Dutrizac and Jambor, 2000; Malenga *et al.*, 2015). While precipitate formation can be minimised (Van Hille *et al.*, 2010; Wu *et al.*, 2016), significant accumulation over continuous long term operation may lead to slow kinetics and reduce the efficiency of bioleaching processes, by occluding desired metals within the precipitate residue (Deveci *et al.*, 2004; Nurmi *et al.*, 2010). In recent times, due to the absence of efficient technology to treat these iron residues, they are stored in waste dams, occupying large areas of land (Ju *et al.*, 2011). This poses an environmental risk with the potential for heavy metal pollution of the soil and groundwater systems (Oladipo *et al.*, 2020).

Due to the continuous increase in industrialization and urbanization, the world's copper mining capacity has been on the increase, with approximately 20% of the global copper production through biohydrometallurgy (Yin *et al.*, 2018). It is well-known that the production of iron precipitate is unavoidable and will continue to persist in biohydrometallurgical operations; however, there is an opportunity to harness these waste residues as a low-cost precursor for the recovery of heavy metal ions. The large surface area, enhanced porosity and good surface chemistry and reactive properties (Gramp *et al.*, 2008) make the precipitate a good sorption candidate for the removal of heavy metal contaminants such as copper from wastewater systems.

Since the toxic metals present in the iron residues have an intrinsic value, the opportunity for recovery of desired metal will also result in the mitigation of environmental pollution. A few studies have shown the recovery of heavy metals from iron precipitate-metallurgical

byproducts, such as goethite (Rodriguez *et al.*, 2020) and jarosite (Ju *et al.*, 2011; Liu *et al.*, 2017). Ju *et al.* (2011) reported that 97% Zn and 87% Cu, could be directly recovered from jarosite waste produced during zinc hydrometallurgical operations. In the work by Liu *et al.* (2017), the authors found that 89.4% Fe, 80.7% Zn, 90.7% Cu and 48.8% Cd could be recovered from jarosite using microwave-assisted sulfuric acid roasting and water leaching. In another study, Li *et al.* (2015) reported that 95.4% In and 95.5% Cu could be extracted from zinc residue leach liquor by solvent extraction.

Although there are several studies (Dou *et al.*, 2013; Jaiswal *et al.*, 2013; Castro *et al.*, 2018; Liu *et al.*, 2018) on sorption isotherms with respect to the use of synthesized and/or biogenic iron compounds in the treatment of wastewater systems, none investigated the nature of the sorption at solid/liquid interfaces. For example, Castro *et al.* (2018) studied heavy metal adsorption from aqueous solutions using biogenic iron compounds (mainly siderite and magnetite) obtained from a natural microbial consortium of an abandoned mine; Jaiswal *et al.* (2013) synthesized goethite mineral as an adsorbent for the uptake of copper and cadmium from synthetic wastewater; while Dou *et al.* (2013) experimented on the sorption of arsenate on different types of granular schwertmannite from aqueous solutions. However, the mode of sorption may provide some understanding of how biohydrometallurgical operation can be better managed at least in the context of minimising copper losses in bioleach operation.

6.2 Objective

The objective of this chapter is to investigate the kinetics, thermodynamics, and mechanism of the sorption of copper ions from an aqueous solution by industrial biogenic iron precipitate. The influence of several sorption factors namely, solution pH, temperature, contact time and initial metal ion concentration were investigated. The aim is to provide an understanding of sorption mode which may be explored to improve and manage a typical biohydrometallurgical operation more efficiently. The result may also help to reduce environmental pollution caused by biogenic iron precipitate residue disposal.

6.3 Methodology

Iron precipitate residue was obtained from a pilot plant used for bioleaching pyrite concentrate using mixed mesophilic cultures. The residue was dried in a temperature-controlled Labcon incubator with a shaker (Labcon 5081U) at 80 °C for 18 h, to ensure a constant weight. The oven-dried powder was then preserved in a desiccator for further use. To demonstrate the adsorption capacity of the precipitate for Cu(II), the residue was utilized with no physical or chemical modification. The characterization methods used in this study were previously described in Section 3.4 of Chapter 3. The details of the methods used for the batch adsorption studies and the analysis of solution for Cu(II) concentrations in this study are described in Section 3.5 of Chapter 3. The adsorption kinetics, isotherms, and thermodynamics studies are described in Sections 3.6, 3.7, and 3.8 respectively of Chapter 3.

6.4 Results and discussion

6.4.1 Characterization of iron precipitate

The procured iron precipitate residue was characterized with FTIR, SEM/EDS, XRD, TGA, and BET analyses, to demonstrate its adsorption capacity for Cu(II) in an aqueous solution.

The N_2 adsorption-desorption isotherm of the sample is depicted in Figure 6.1(a).

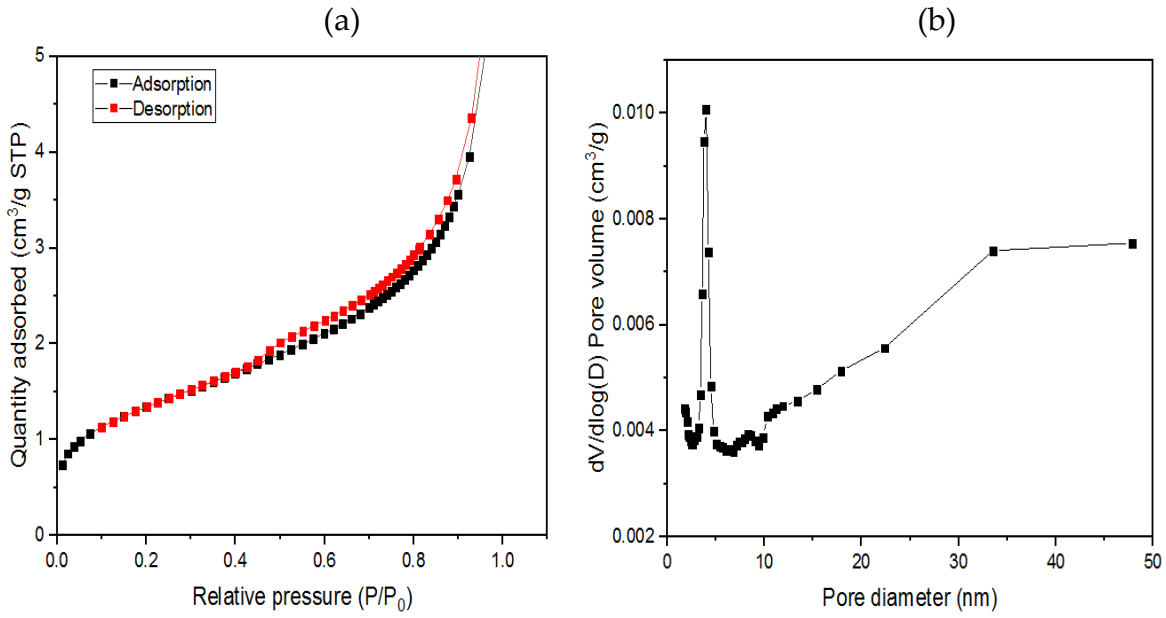

Figure 6.1: Plots of (a) N2 adsorption/desorption isotherms; and (b) adsorption pore-size distribution

The plot displays principal type-IV pattern and hysteresis loop-type (Sing, 1985), signifying that the powdered residue was mesoporous. The BET surface area and BJH pore volume analyses of the sample were evaluated to be 4.74 m^2/g and 0.014 cm^3/g respectively, whereas the average pore diameter value was determined to be 11.61 nm. In comparison with the iron precipitate powder used in this study, Cu(II) ion has an ionic diameter of 0.072 nm (0.72 Å) (Tang *et al.*, 2017), indicating that Cu(II) ions could easily be adsorbed by ion-exchange onto the pores of the adsorbent in a given pore volume. In the context of physisorption, pore size between 2 – 50 nm is referred to as mesopore (Sing, 1985). Based on the adsorption pore-size distribution curve (Figure 6.1(b)), it was observed that most of the average pore sizes are ranged between 2 – 15 nm, which confirmed that the powdered iron precipitate consisted mainly of mesopores. This suggests there would be easy access for Cu(II) ion adsorption into the active sites of the adsorbent due to favourable surface area and pore size.

The XRD pattern of iron precipitate powder is depicted in Figure 6.2. The result showed that the powdered sample was heterogeneous in composition and mainly dominated by talc. Other phases identified were quartz, cronstedtite and potassium jarosite. The peaks at 2θ = 11, 23 and 33° were assigned to the characteristic peaks of talc ($Mg_3Si_4O_{10}(OH)_2$) with

an average crystallite size of 290 nm. The peaks at 2θ = 24 and 31° corresponded to the characteristic peaks of quartz (SiO_2) with an average crystallite size of 284 nm. The appearance of peaks at 2θ = 14 and 29° were indexed to the peculiar peaks of cronstedtite ($Fe_3((Si_{0.711}Fe_{0.289})_2O_5)(OH)_4$) with an average crystallite size of 172 nm. The peaks identified at 2θ = 33 and 34° was ascribed to the characteristic peaks of potassium jarosite ($KFe_3(SO_4)_2(OH)_6$) with an average crystallite size of 143 nm. The strong presence of talc is an indication of the high surface area and ion-exchange properties of the biogenic iron precipitate.

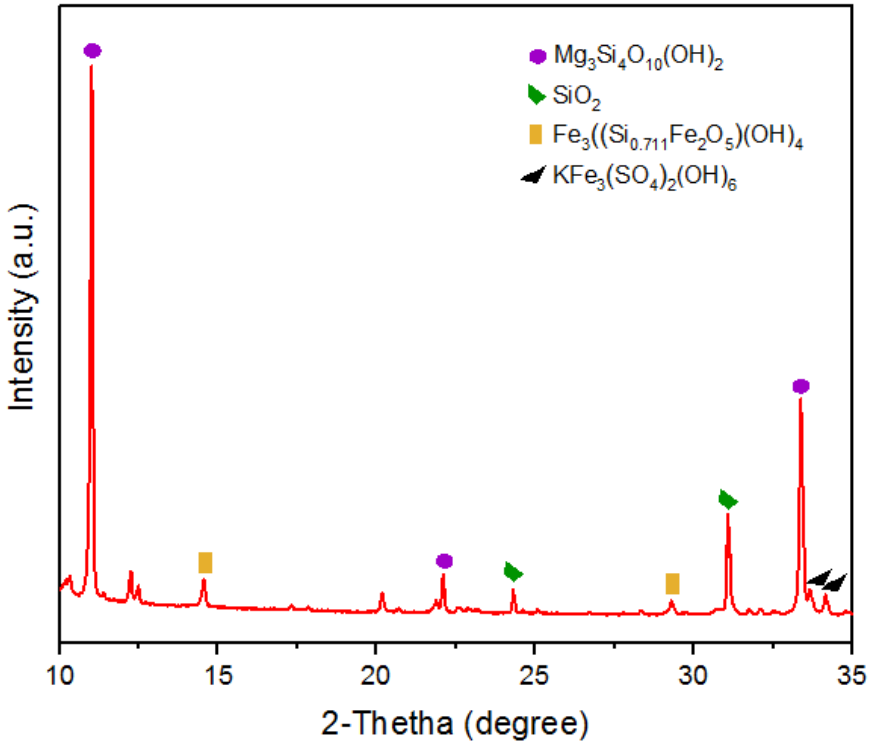

Figure 6.2: XRD pattern of iron precipitate residue sample

The thermal behaviour of iron precipitate residue powder was checked with the TGA curve is displayed in Figure 6.3.

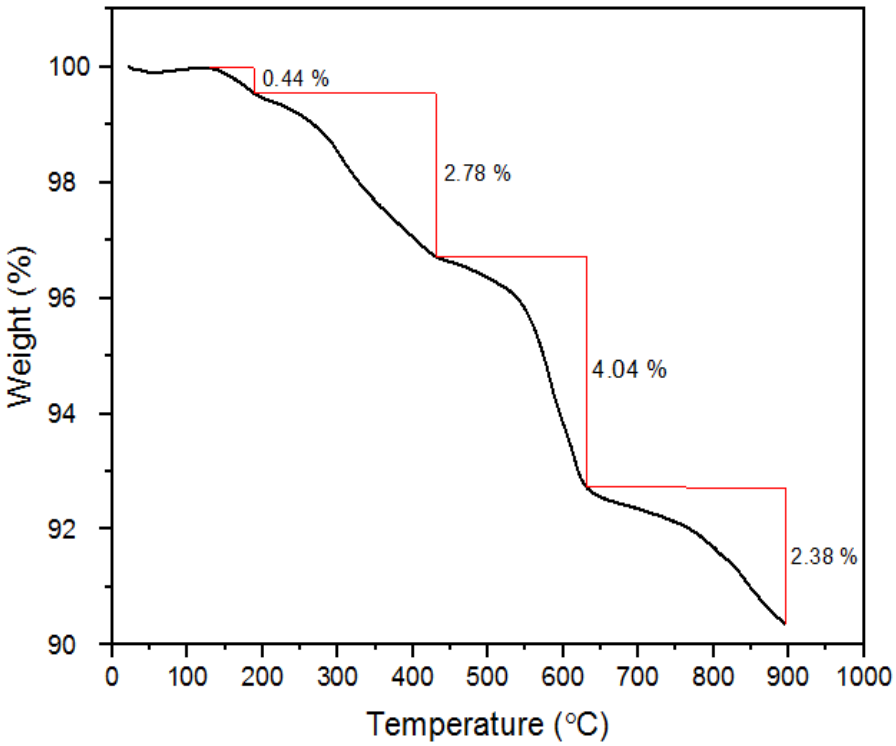

Figure 6.3: TGA curve of iron precipitate residue sample

The plot revealed four distinct weight loss phases. Noticeable at 180 and 425 °C were the first two weight losses of 0.44 and 2.78% respectively, which can be ascribed to loss of physically adsorbed water and inter-layered water within the lattice crystals respectively. Mass loss of $Fe_3((Si_{0.711}Fe_{0.289})_2O_5)(OH)_4$ and $KFe_3(SO_4)_2(OH)_6$ in the temperature range between 425 and 625 °C could be attributed to the likely formation of γ-Fe_2O_3 and loss of SO_2 respectively. The third mass loss of 4.04% at 625 °C is assumed to be due to the transformation of SiO_2 present in the residue sample, while the final weight loss of 2.38% is linked to the decomposition of $Mg_3Si_4O_{10}(OH)_2$ observed at > 830 °C. Moreover, the loss of weight at each stage is marked by an endothermic process. The negligible mass loss observed at the high-temperature range of the TGA profile indicated that iron precipitate powder has good thermal stability. Thus, it could be used as an adsorbent for high-temperature adsorption processes.

FTIR spectra obtained to check the qualitative attribute and modification of surface functional groups of the iron precipitate powder, before and after adsorption, are illustrated in Figure 6.4.

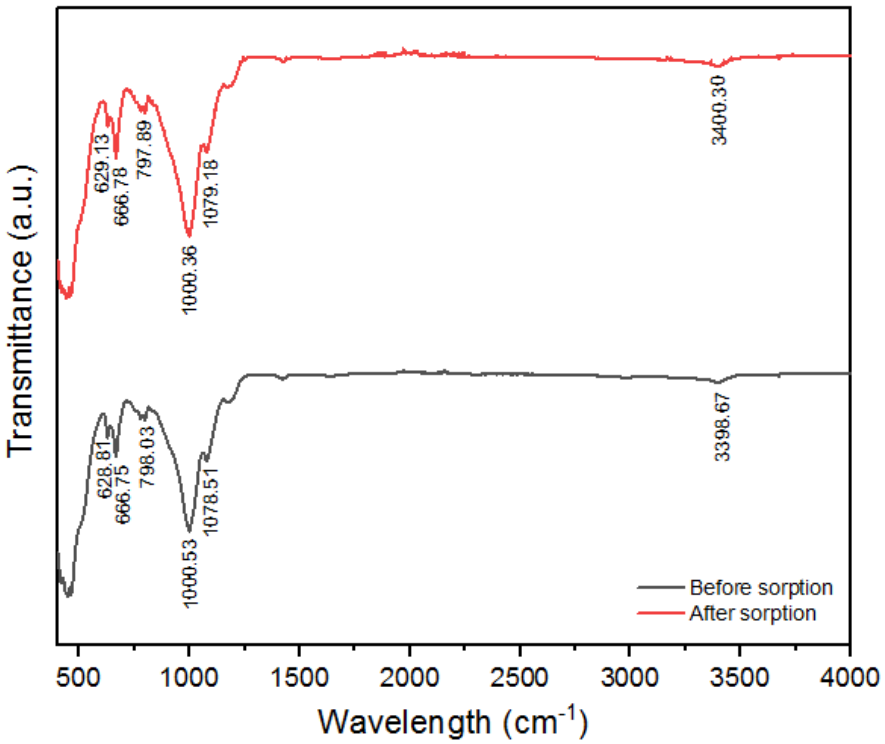

Figure 6.4: FTIR spectra of iron precipitate samples

The broad peaks at 3398.67 and 3400.30 cm^{-1}, before and after Cu(II) adsorption, are ascribed to both the stretching vibrations of the hydroxyl (–OH) and symmetrical aliphatic amine ($–NH_2$) of polymeric compounds (Coates, 2000; Silverstein *et al.*, 2014; Adebisi *et al.*, 2017). The slight shift in wavelength of the peak after adsorption is due to the attachment of Cu^{2+} onto –OH and $–NH_2$ groups. The polar functional group identified on the top layer of iron precipitate powder facilitates chemisorption process with cation exchange capacity. The occurrence of out-of-plane C–H bending vibrations identified at 798.03 cm^{-1} indicated the presence of mononuclear aromatic hydrocarbons. Before adsorption, bands detected at 1078.51 and 1000.53 cm^{-1} could both be ascribed to the stretching vibrations of silicate (SiO_4^{4-}) and phosphate (PO_4^{3-}) ions (Coates, 2000), suggesting the presence of silicon and phosphorus compounds in the iron precipitate powder. A slight shift was observed in these bands after adsorption. Identification of bands present in the region of 666.75–628.81 cm^{-1} before Cu(II) adsorption were ascribed to the presence of sulfate ion (SO_4^{2-}) of sulfur functional groups or alkyne C–H bending vibration of alkynes group (Coates, 2000; Silverstein *et al.*, 2014). FTIR spectra of the samples showed either a slight increase or

reduction in the wavelength of sorption peaks after adsorption, which indicates that an ion-exchange mechanism could be the sorption pathway for the uptake of Cu(II). Besides, the major presence of the negatively charged ionizable functional groups of hydroxyl (–OH) and amino (–NH_2) located on the surface of the adsorbent has a strong ability to interact with a proton or metal ion (Munagapati *et al.*, 2010), whereby a covalent chemical bond is established via the interaction of the adsorbed Cu(II) ions with the adsorbent.

The sites accountable for the adsorption process can be expressed as shown in Equations (6.1) – (6.2):

$$S-OH+M^{n+} \rightarrow S-OM^{(n-1)+}+H^{+} \quad (6.1)$$

$$S-NH_2+M^{n+} \rightarrow S-NM^{(n-2)+}+2H^{+} \quad (6.2)$$

where S represents the surface of the adsorbent.

The SEM/EDS surface morphology and identified elements on iron precipitate powder before and after adsorption are displayed in Figure 6.5.

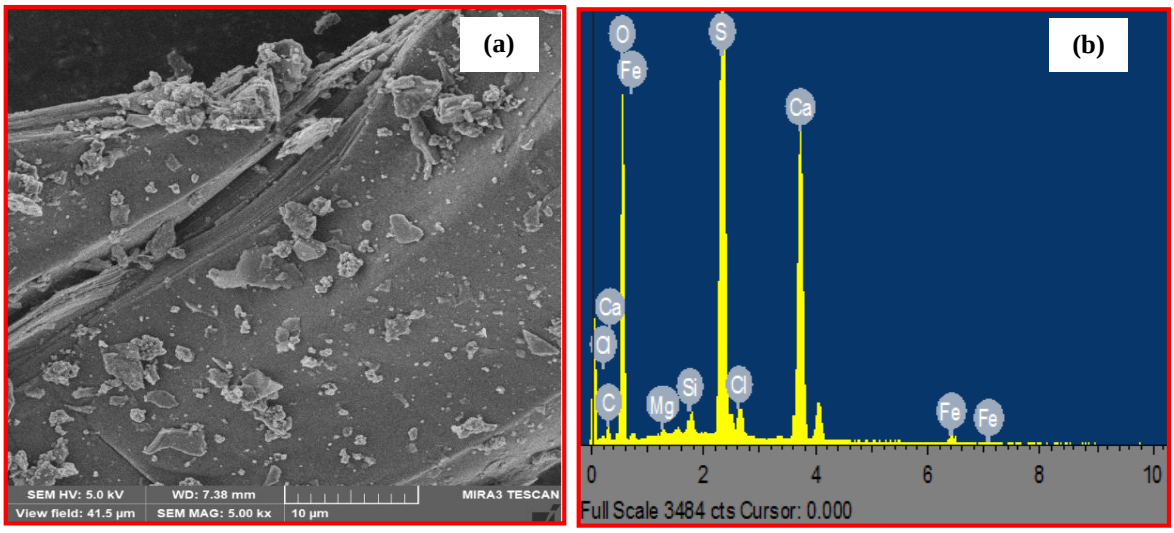

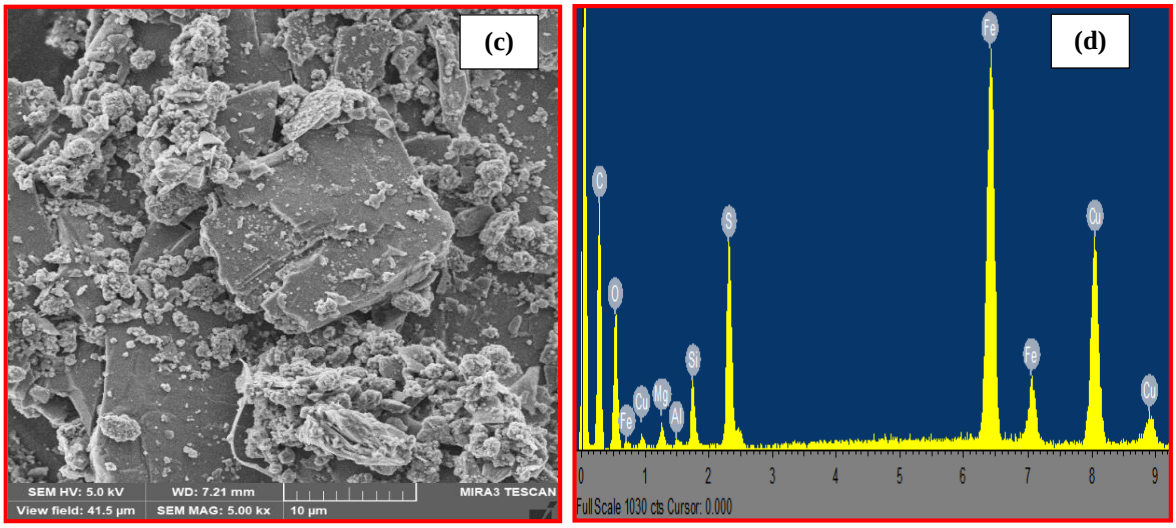

Figure 6.5: (a) SEM image before Cu(II) adsorption, (b) EDS image before Cu(II) adsorption, (c) SEM image after Cu(II) adsorption, and (d) EDS image after Cu(II) adsorption for iron precipitate residue powder

Observed on the SEM image before adsorption (Figure 6.5(a)) is a smooth surface with noticeable scattered, irregular and elongated flat pieces compared to the SEM image after adsorption (Figure 6.5(c)). The EDS elemental composition of the sample before adsorption is shown in Figure 6.5(b), with the presence of some metallic ions. In Figure 6.5(c), the observed clusters of agglomerated particles on the surface of the biogenic precipitate may be attributed to agitation and random site selection during the adsorption process. Iron precipitate powder has a large surface area primarily due to its crystalline form which may be ascribed to its ability to entrap metallic ions. After adsorption, there was a shift in valencies of the metallic ions and the presence of Cu(II) ions could be observed on the surface (Figure 6.5(d)), indicating the feasibility of iron precipitate to adsorb metals. The percentage elemental composition before and after copper adsorption is displayed in Table 6.1.

Table 6.1: Elemental composition of iron precipitate residue before and after Cu(II) adsorption

Element	Before adsorption (%)	After adsorption (%)
C	9.17	24.80
O	54.36	40.20
Mg	8.69	5.17
Al	0.81	0.57
Si	13.72	9.08
S	4.83	7.15
Cl	0.42	-
K	0.03	-
Ca	5.23	-
Fe	2.74	7.68
Cu	-	5.35

6.4.2 Study of adsorption factors

Adsorption factors, namely initial solution pH, adsorption time, initial Cu(II) concentrations and solution temperatures, as they influenced the batch adsorption process in this study, are discussed below.

The pH of the solution governs the sorption affinity of the adsorbent by influencing the: type of charge on the surface of the adsorbent, speciation of the metal in the solution, and ionizing strength of the adsorbent. In this study, pH-dependent experimental runs were not conducted at pH values > 5 to prevent Cu(II) precipitating as insoluble copper hydroxide, which can hinder true adsorption studies. The influence of pH could also be described through the point of zero charge (PZC). pH_{PZC} refers to the pH at which the surface of the adsorbent has a net charge of zero. The value of pH_{PZC} obtained in this study is 4.02 (Figure 6.6).

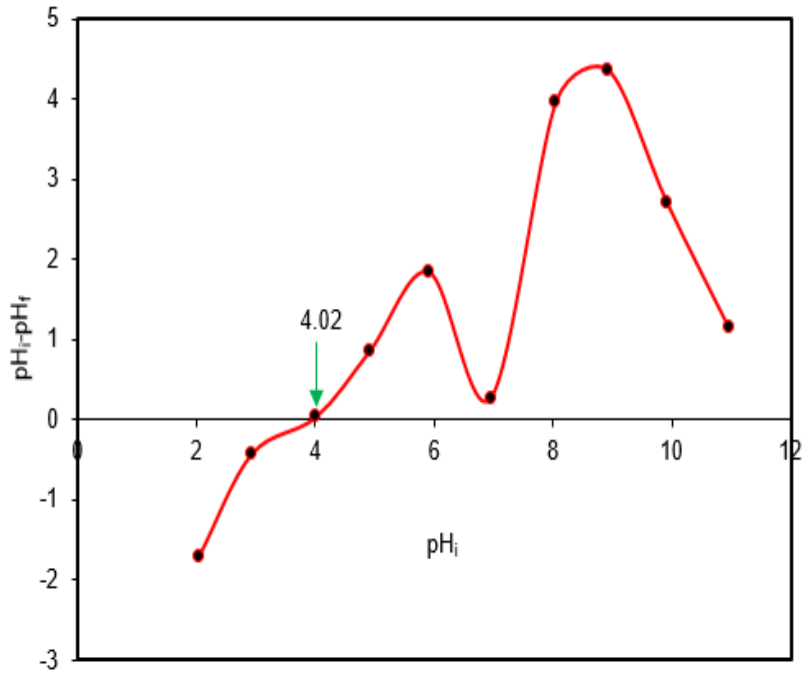

Figure 6.6: pHpzc of iron precipitate powder

This suggests that the surface of the adsorbent is positively charged and favours sorption of anions for solution pHs < pH_{PZC} (4.02), while it becomes negatively charged to favour sorption of cations for solution pHs > pH_{PZC} (4.02). This property of the adsorbent further supports the finding that optimum Cu(II) adsorption onto iron precipitate powder takes place at pH 5 (> pH_{PZC}), under which conditions the surface of the adsorbent is negatively charged.

The impact of initial Cu(II) concentration on the sorption capacity of iron precipitate powder was investigated for adsorption time values from 5 – 120 min and concentration values of 150 – 500 mg/L at 30 °C solution temperature, pH 5, 150 rpm agitation speed and 1 g dosage of iron precipitate powder. As presented in Figure 6.7, the increase in initial Cu(II) concentration from 150 to 500 mg/L led to (i) an increase in the adsorption capacity from 3.20 to 5.80 mg/g; and (ii) a decrease in adsorption rate and removal of Cu(II) efficiency from 42.73 to 23.20%. These observations suggest that at lower concentrations, Cu(II) ions in the reaction system experience higher interaction with the top layer of the adsorbent due to the large ratio of unoccupied sorption sites to initial Cu(II) concentration.

In contrast, the ratio of available sites for Cu(II) ions decreases at higher concentrations, due to saturation of the binding sites.

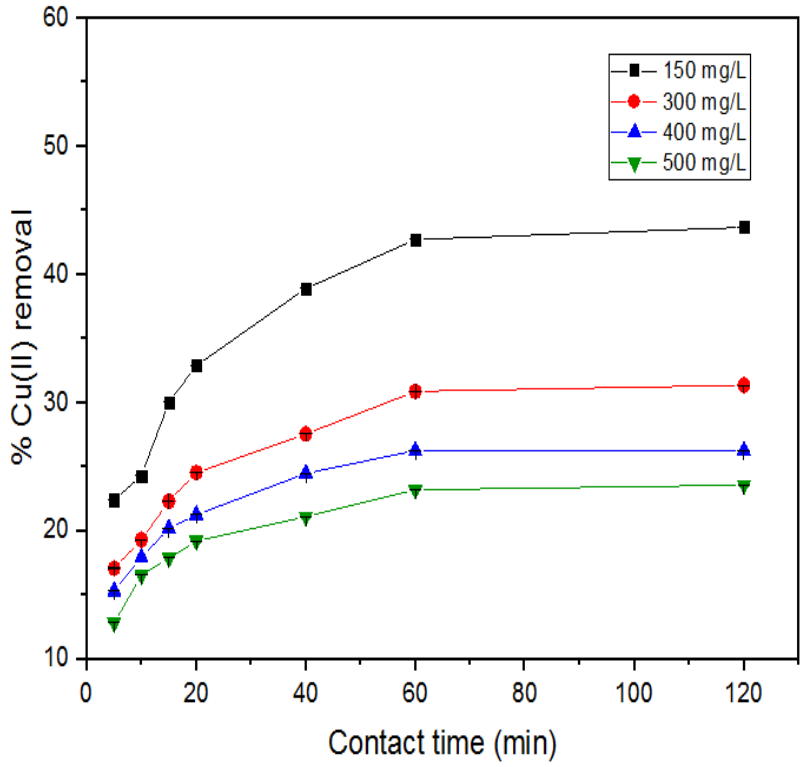

Figure 6.7: Influence of contact time on percentage Cu(II) removal at various Cu(II) ion concentrations (data are expressed as the mean of three replicate ± standard deviations)

The relationship between the adsorption of Cu(II) onto the surface of the iron precipitate and contact time is presented in Figure 6.7. It was observed that the adsorption capacity and percentage removal of the adsorbent increased as the contact time increased, after which equilibrium was attained at 60 min. Beyond this equilibrium point, the adsorption capacity of iron precipitate was in dynamic equilibrium with the adsorbed quantity of Cu(II), as indicated by an insignificant increase in percentage Cu(II) uptake after 60 min. The percentage removal of Cu(II) was rapid at the beginning of the adsorption process (Figure 6.6), due to the available rich active sites of the adsorbent and the small diameter of Cu(II) ion. After 60 min, the Cu(II) ions could not easily penetrate the inner pores of the adsorbent, which were assumed to be linked to Cu(II) monomolecular saturation of the surface pores as shown on the SEM image after adsorption (Figure 6.5d). The results shown

in Figure 6.7 further demonstrate that equilibrium time was independent of the initial Cu(II) concentration.

The influence of temperature on the sorption capacity of iron precipitate was examined for temperature values between 30 – 55 °C at pH 5, 150 mg/L initial Cu(II) concentration, 150 rpm agitation speed, 1 g adsorbent dosage, and 60 min contact time. As shown in Figure 6.8, Cu(II) adsorption onto iron precipitate powder is considerably affected by temperature over the range of Cu(II) ion concentrations under investigation in this study. As observed for the test with an initial Cu(II) concentration of 150 mg/L, adsorption efficiency increased from 42.73 to 60.51% with an increase in temperature from 30 to 55 °C. This indicates that higher temperatures enhanced the adsorption process for metal ion binding, suggesting that Cu(II) adsorption by iron precipitate is an endothermic process. Furthermore, increasing the temperature could lead to an expansion in the pore size of the adsorbent, which helps to ease the diffusion of Cu(II) ions onto the sites difficult to access.

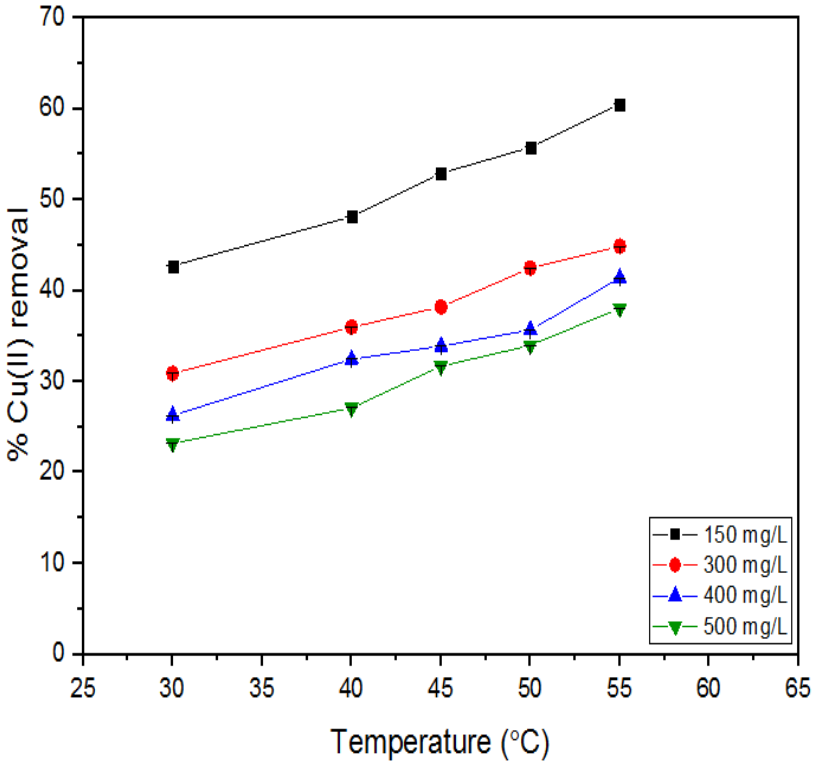

Figure 6.8: Influence of temperature on percentage Cu(II) removal at various Cu(II) ion concentrations (data are expressed as the mean of three replicate ± standard deviations)

6.4.3 Adsorption isotherms and model fitting

The adsorption isotherms were examined with the Langmuir and Freundlich models.

For the Langmuir isotherm model, the linear plots of C_e/q_e versus C_e are depicted in Figure 6.9, and the estimated constants of the equation are displayed in Table 6.2.

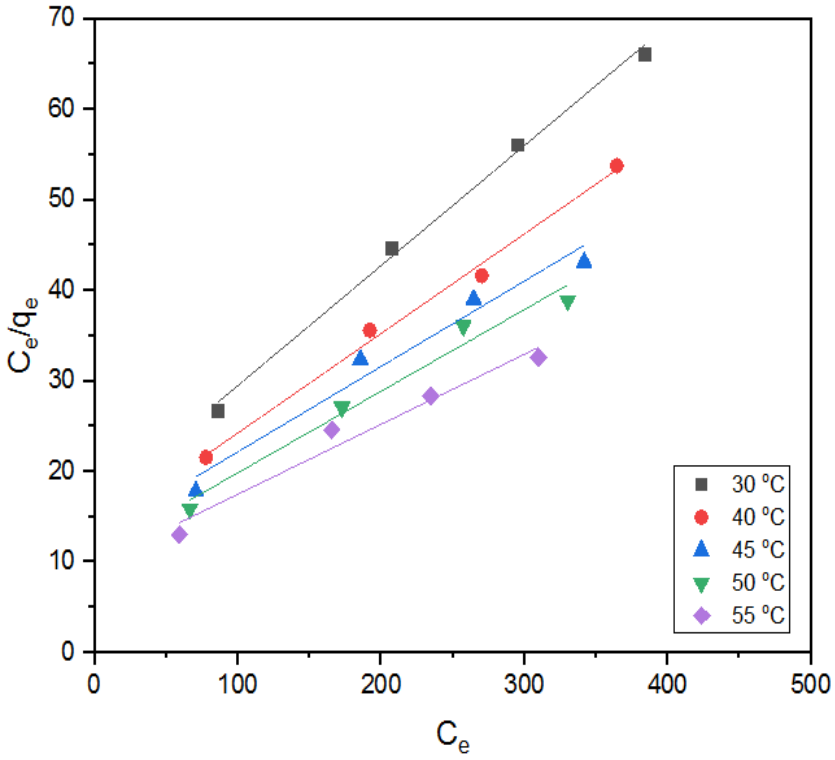

Figure 6.9: Langmuir plots of Cu(II) adsorption onto iron precipitate powder at the investigated temperatures

Table 6.2: Langmuir isotherm model correlations and separation factor (RL) values for Cu(II) adsorption onto iron precipitate powder at the studied temperatures

T (K)	Langmuir isotherm model						
	Langmuir correlations			R_L at various initial Cu(II) concentrations			
	q_m (mg/g)	b	R^2	150 mg/L	300 mg/L	400 mg/L	500 mg/L
303	7.541	0.0082	0.996	0.450	0.290	0.234	0.197
313	9.091	0.0083	0.993	0.446	0.287	0.232	0.191
318	10.593	0.0074	0.967	0.474	0.310	0.252	0.213
323	11.086	0.0083	0.974	0.445	0.286	0.231	0.194
328	12.937	0.0079	0.965	0.457	0.296	0.240	0.202

High values of R^2 obtained were within the range of 0.965 – 0.996, with R^2 value obtained at 303 K to be 0.996. The high R^2 values suggest that the model predictions are accurate within the variance of the experimental data. Langmuir maximum adsorption capacity of 7.54 mg/g was obtained at 30 °C, 150 mg/L, 1 g adsorbent dosage and pH 5 within 60 min. It was also observed that the values of q_m increased with increasing temperature, signifying that Cu(II) adsorption by iron precipitate powder is indeed an endothermic process.

The calculated R_L values in this study ranged between 0 and 1 (Table 6.2), indicating that the adsorption system of Cu(II) ions onto iron precipitate powder is favourable. Adsorption is unfavourable, linear, irreversible or favourable when $R_L > 1$, $R_L = 1$, $R_L = 0$ or $0 < R_L < 1$ respectively (Weber and Chakravorti, 1974; Tran *et al.*, 2017).

For the Freundlich isotherm model, the linear plots of log q_e versus log C_e are depicted in Figure 6.10. Very high R^2 values within the range of 0.991 – 0.999 were estimated, with the R^2 value obtained at 303 K to be 0.999. These values are listed in Table 6.3, which also provides the model correlations for n_f and K_f at each temperature investigated. The increase in K_f values with increasing temperature also demonstrates the endothermic nature of Cu(II) adsorption process.

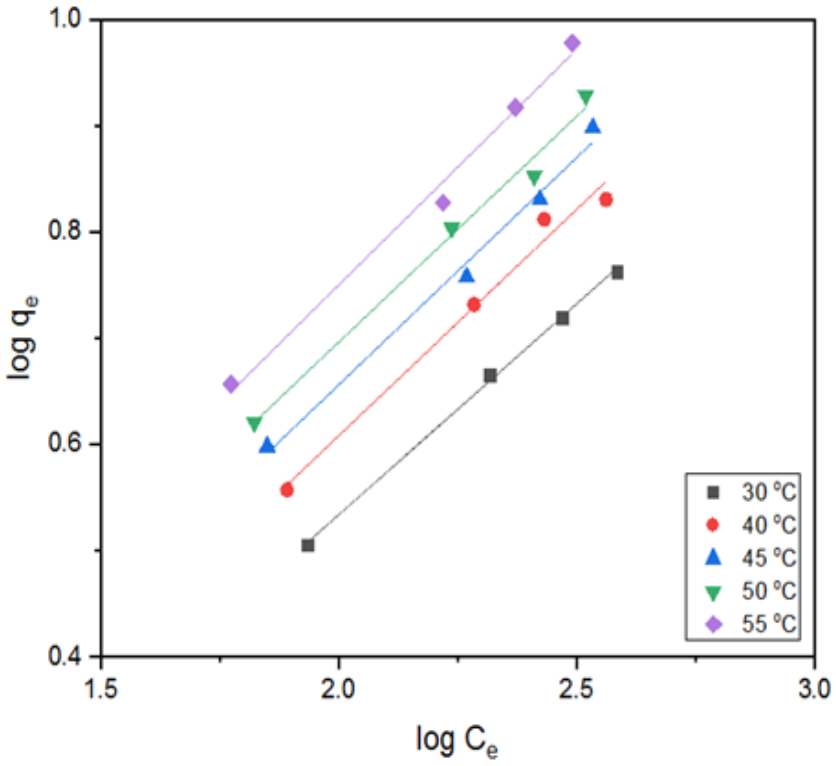

Figure 6.10: Freundlich isotherm plots of Cu(II) adsorption onto iron precipitate powder at the investigated temperatures.

Table 6.3: Freundlich isotherm model correlations for Cu(II) adsorption onto iron precipitate powder at the studied temperatures

T (K)	Freundlich model			
	K_f	$1/n_f$	n_f	R^2
303	0.549	0.397	2.518	0.999
313	0.570	0.426	2.346	0.985
318	0.632	0.428	2.336	0.991
323	0.701	0.425	2.351	0.990
328	0.730	0.444	2.254	0.991

The values of n_f indicate the feasibility of the adsorption process. Adsorption is deemed easier when $2 < n_f < 10$, mildly difficult when $1 < n_f < 2$ and unfavourable when $n_f < 1$ (Ali *et al.*, 2016). Since $n_f > 2$ for all conditions covered in this study, it suggests that utilising iron precipitate powder as a sorbent of Cu(II) recovery is a technically feasible process. Also, the

values of $1/n_f < 1$ signify a more heterogeneous adsorption site and a feasible chemisorption process (Kumar *et al.*, 2016; Tang *et al.*, 2017).

Based on the comparison of R^2 values, both Langmuir and Freundlich models fit the experimental data well. The very high R^2 values obtained according to the Freundlich model indicate that the iron precipitate powder is highly heterogeneous, which is corroborated by the XRD analysis of the sample. It further suggests that, at high Cu(II) concentration, adsorption probably occurs at the multilayer surface of the iron precipitate.

6.4.4 Adsorption kinetics and model fitting

The kinetics of Cu(II) adsorption by iron precipitate powder was investigated with the pseudo-first-order (PFO), pseudo-second-order (PSO), and Elovich kinetic models.

For the PFO model, the linear plots of ln (q_e–q_t) versus t are depicted in Figure 6.11.

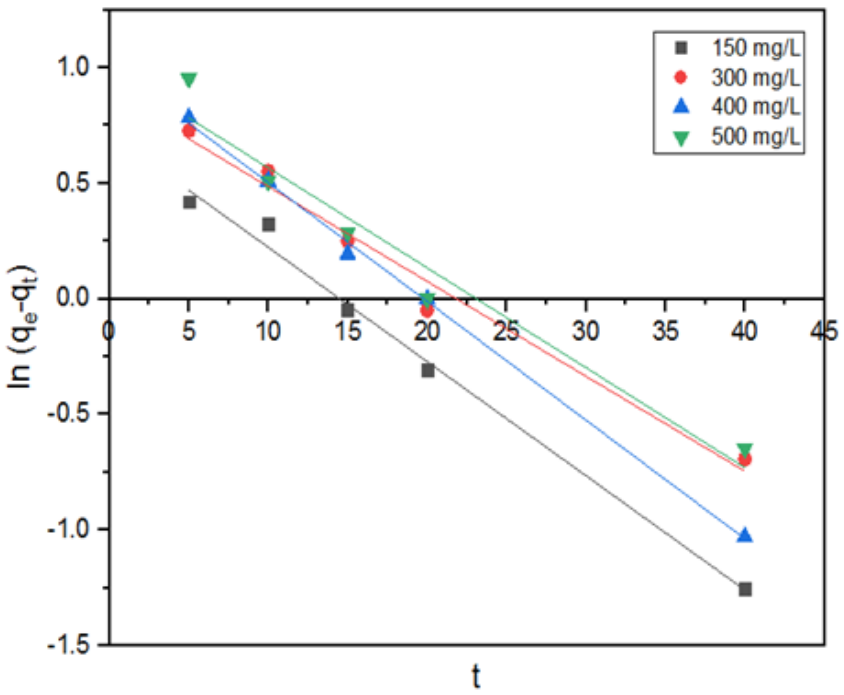

Figure 6.11: Pseudo-first-order kinetic plots at the studied Cu(II) concentrations for Cu(II) adsorption onto iron precipitate powder

The estimated model parameters in the studied conditions are summarized in Table 6.4. Although the fitted model gave high R^2 values between 0.957 – 0.998, the calculated $q_{e,\,cal}$ values of the model differed greatly from the experimental $q_{e,\,exp}$ values at initial Cu(II) concentrations. This deviation indicates that the pseudo-first-order equation may not adequately explain the adsorption pathway of Cu(II) onto the surface of iron precipitate powder, which suggests the need to assess the efficacy of another kinetic model.

Table 6.4: Pseudo-first-order estimated model parameters for Cu(II) adsorption onto iron precipitate powder at studied initial Cu(II) concentrations

C_0 (mg/L)	$q_{e,exp}$ (mg/g)	Pseudo-first-order		
		$q_{e,cal}$ (mg/g)	k_1 (min^{-1})	R^2
150	3.205	2.049	0.049	0.992
300	4.633	2.454	0.041	0.980
400	5.252	2.765	0.051	0.998
500	5.800	2.717	0.043	0.957

For the PSO model, the linear plots of t/q_t versus t are shown in Figure 6.12.

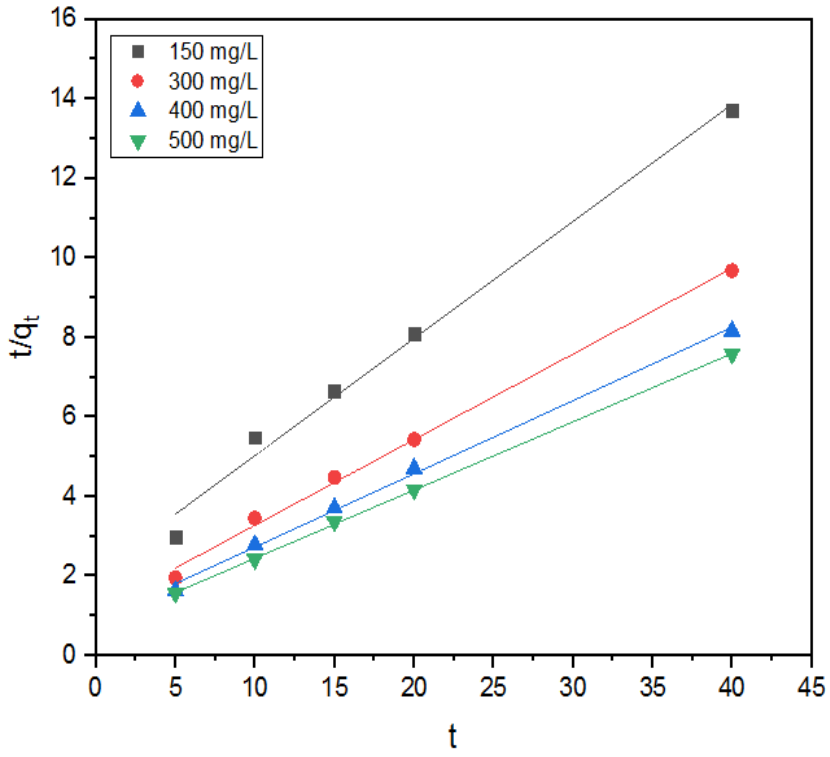

Figure 6.12: Pseudo-second-order kinetic plots at the studied Cu(II) concentrations for Cu(II) adsorption onto iron precipitate powder

The very high R^2 values obtained were in the range of 0.990 – 0.999, with the calculated model parameters presented in Table 6.5. The results indicate a better fit with the pseudo-second-order equation than the pseudo-first-order model. This may be observed by the negligible differences between the model estimated $q_{e,\,cal}$ values and the experimental $q_{e,\,exp}$ values for the initial Cu(II) concentrations being studied. Thus, pseudo-second-order being the best fit suggests that both the concentration of Cu(II) in solution and the amount of available active sites on the iron precipitate powder can be used to mathematically describe the intrinsic kinetic adsorption constant (Tran *et al.*, 2017; Hevira *et al.*, 2020).

Table 6.5: Pseudo-second-order estimated model parameters for Cu(II) adsorption onto iron precipitate powder at studied initial Cu(II) concentrations

C_0 (mg/L)	$q_{e,exp}$ (mg/g)	Pseudo-second-order		
		$q_{e,cal}$ (mg/g)	k_2 (g/mg min)	R^2
150	3.205	3.392	0.042	0.990
300	4.633	4.640	0.041	0.997
400	5.252	5.429	0.038	0.998
500	5.800	5.821	0.041	0.999

For the Elovich model, the plots of q_t versus ln t for Cu(II) removal by iron precipitate powder is displayed in Figure 6.13, and the estimated constants of the equation are presented in Table 6.6.

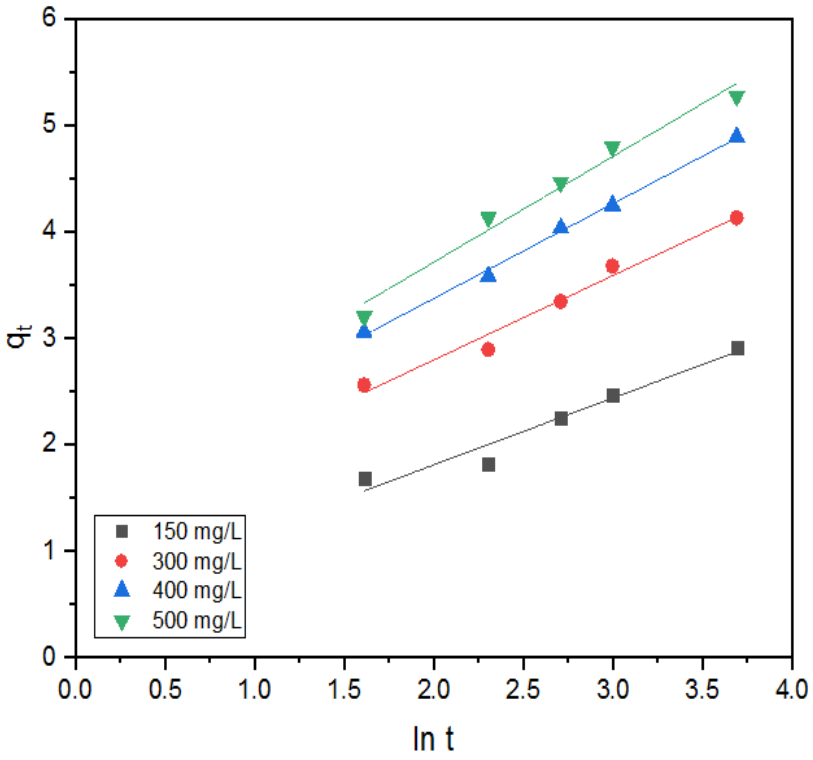

Figure 6.13: Elovich model kinetic plots of Cu(II) adsorption onto iron precipitate powder at the studied initial Cu(II) concentrations

Table 6.6: Pseudo-second-order estimated model parameters for Cu(II) adsorption onto iron precipitate powder at studied initial Cu(II) concentrations

C_0 (mg/L)	$q_{e,exp}$ (mg/g)	Elovich		
		β (g/mg)	α (mg/g min)	R^2
150	3.205	1.591	1.523	0.952
300	4.633	1.261	3.662	0.978
400	5.252	1.123	5.355	0.997
500	5.800	1.006	5.677	0.978

The high R^2 values obtained for the Elovich model signify the involvement of a chemisorption mechanism in the system, which may involve valence forces via the sharing or exchange of electrons between Cu(II) ions and iron precipitate powder. The expected interactions with the –OH and $–NH_2$ functional groups further validate the FTIR results, suggesting that the ion-exchange mechanism also plays a vital part in the adsorption process.

6.4.5 Activation energy and thermodynamic parameters

The value of the activation energy (E_a), was estimated from the slope of the plot of ln k_2 versus $1/T$ (Figure 6.14).

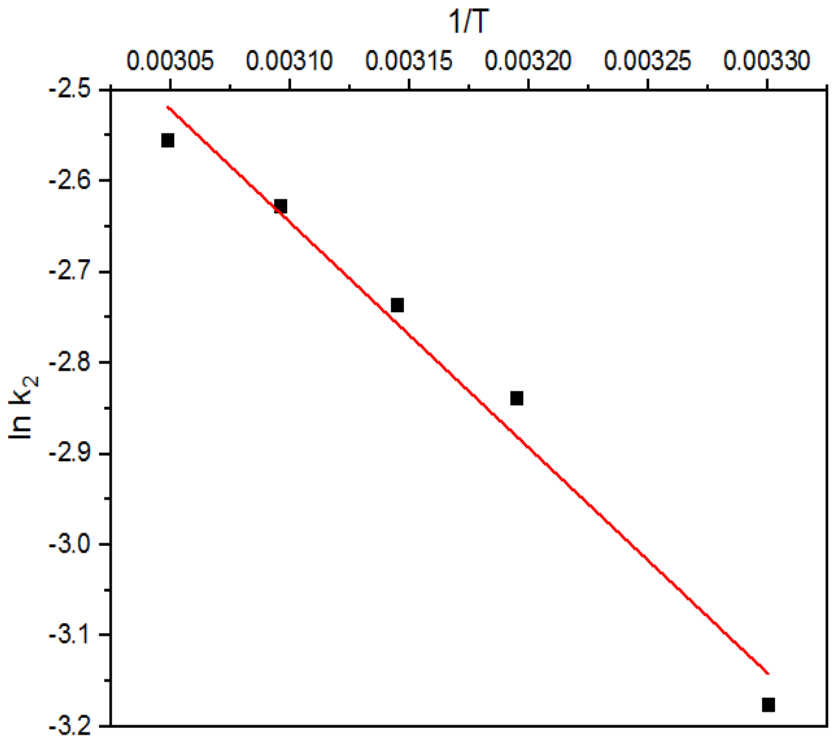

Figure 6.14: Arrhenius plot at 303–328 K and 150 mg/L, for Cu(II) adsorption onto iron precipitate powder

The type of adsorption can be determined by the magnitude of the activation energy. A chemical adsorption process has an activation energy in the range of 4 – 40 kJ/mol (Maleki *et al.*, 2017). In this study, the activation energy was evaluated to be 20.61 kJ/mol, indicating a chemical adsorption process.

The relationship between k and T can be expressed in an Arrhenius form as follows:

$$k = 154.28 \; exp\left(-\frac{20.61}{8.314T}\right) \tag{6.3}$$

The positive value obtained for the activation energy also implies that an increase in temperature favours the adsorption process. This further supported that the adsorption of Cu(II) ions onto iron precipitate powder is endothermic in nature.

After adsorption equilibrium of the studied systems was established, thermodynamic data, namely $\Delta G°$, $\Delta S°$, and $\Delta H°$ were evaluated for Cu(II) adsorption onto iron precipitate powder.

The respective values of $\Delta H°$ and $\Delta S°$ were estimated from the slope and intercept of linear van't Hoff plots of ln K_D versus $1/T$ (Figure 6.14). A summary of the model predictions for $\Delta H°$ and $\Delta S°$ are provided in Table 6.7.

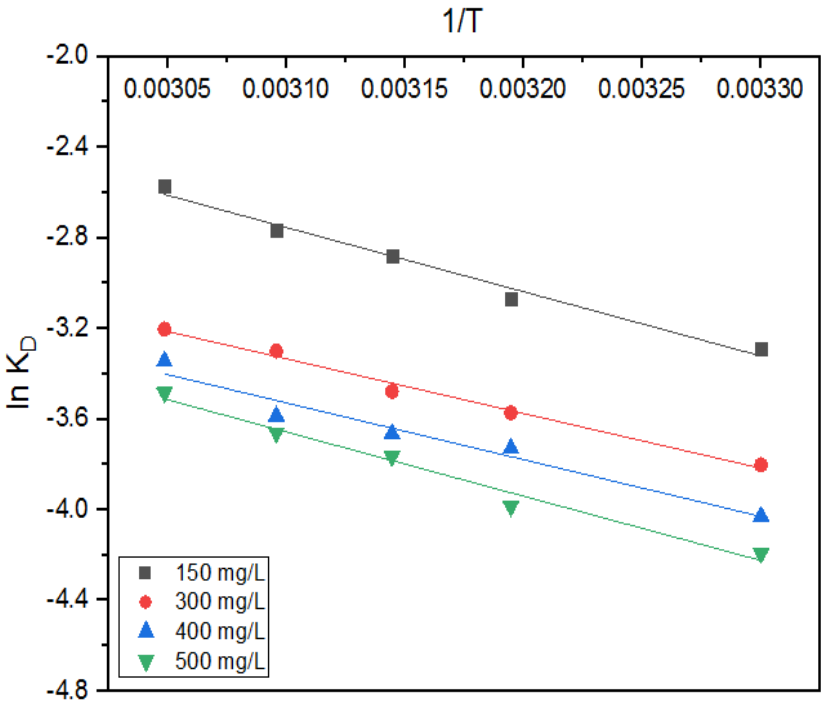

Figure 6.15: van't Hoff plots at various Cu(II) concentrations for Cu(II) adsorption onto iron precipitate powder

Table 6.7: Thermodynamic parameters for Cu(II) adsorption onto iron precipitate powder

Initial Cu(II) concentrations (mg/L)	ΔH (kJ/mol)	ΔS (kJ/mol K)	ΔG (kJ/mol) at investigated temperatures				
			303 K	313 K	318 K	323 K	328 K
150	23.57	0.050	8.37	7.87	7.61	7.36	7.11
300	20.07	0.034	9.61	9.27	9.10	8.92	8.75
400	23.81	0.044	10.33	9.88	9.66	9.44	9.22
500	23.59	0.043	10.64	10.21	10.00	9.79	9.57

ΔH (kJ/mol) is the enthalpy change, ΔS (kJ/mol K) is the entropy change and ΔG (kJ/mol) is Gibb's free energy change.

The positive values of $\Delta H°$ further support the finding that the adsorption process is endothermic, which is unequivocally attributable to chemisorption. The positive values of $\Delta S°$ demonstrate increased dissociation and randomness at the solid/liquid boundary during the adsorption process. This suggests that Cu(II) ions replaced some water molecules in the solution earlier adsorbed on the surface of the adsorbent. Likewise, positive values of $\Delta G°$ is an indication of the non-spontaneity and ion exchange process in the adsorption system. This suggests that energy and agitation are required for the adsorption process to be carried out in this study. The decrease in $\Delta G°$ values observed as the temperature increased show that a higher sorption rate occurred at elevated temperatures.

6.4.6 Implications of Cu(II) adsorption in biohydrometallurgical process

It has been demonstrated in this study that biogenic iron precipitate adsorb Cu(II) ions via combined mechanisms of chemisorption and ion-exchange, with the adsorption process requiring estimated activation energy of 20.61 kJ/mol. In the bioleaching of low-grade copper sulfide, such as chalcopyrite, high temperature (60 – 80 °C) operation promotes rapid adsorption of copper onto iron precipitate, thereby preventing the release of the entrapped copper into solution for further processing (Vilcáez *et al.*, 2008; Sokić *et al.*, 2009). In this study, it has been shown that during Cu(II) adsorption onto iron precipitate, there

appears to be competition for the active sites between the ionic Cu(II) (radius (0.72 Å)) and the hydrated Cu(II) (radius (4.19 Å)) (Tang *et al.*, 2017), with the former easily adsorbed to the pores of the biogenic precipitate due to its smaller radius. This entrapment of copper during the high-temperature dissolution of copper-bearing chalcopyrite mineral is expected to affect the overall extraction and recovery of the process. Given that it has been shown in Chapter 5 that operating conditions such as pH affect the particle size of iron precipitate, it may be important also to investigate whether there is a relationship between solution pH and particle pore sizes; such that process conditions in bioleaching operations may be used to manipulate pore size with a view to limit Cu(II) sorption in the pores (if this exists at all). This could thus provide a better route for increasing copper extraction in biohydrometallurgical processes.

6.5 Conclusions

The intrinsic mechanism of biogenic iron precipitate entrapment of desired metals, produced during biohydrometallurgical operation, was investigated in this study through the lens of its sorption in the removal of Cu(II) from aqueous solutions. Analyses of the iron precipitate sample showed it is highly heterogeneous in terms of composition, has a large surface area and possesses negatively charged functional groups for the uptake of Cu(II), demonstrating a chemisorption process via an ion-exchange mechanism. The pseudo-second-order model best fits the experimental data, signifying its high precision in describing the kinetic constant for Cu(II) adsorption onto biogenic iron precipitate. Thermodynamic parameters showed that the process is non-spontaneous and endothermic. More importantly, the lessons gleaned from this study provide new insights into the rationale for the management of a typical biohydrometallurgical operation to minimise copper losses for efficient mineral processing. Moreover, the results would help reduce land and water pollution caused by the disposal of iron precipitate residues.

CHAPTER SEVEN

EFFECT OF OPERATING CONDITIONS OF JAROSITE PRODUCED DURING FERROUS ION BIO-OXIDATION ON SORPTION CAPACITY AND KINETICS OF METAL ION UPTAKE

"We won't have a society if we destroy the environment." – Margaret Mead

CHAPTER 7: EFFECT OF OPERATING CONDITIONS OF JAROSITE PRODUCED DURING FERROUS ION BIO-OXIDATION ON SORPTION CAPACITY AND KINETICS OF METAL ION UPTAKE

7.1 Introduction

In sulfate-rich environments, ferric ion precipitates mostly as jarosite. Jarosites are seen in the oxidized areas of sulfide ore deposits, acid sulfate soils, bioleaching processes, as well as contaminated fluvial surroundings from acid mine drainage (Craddock, 1995; Becker and Gasharova, 2001; Welch *et al.*, 2008). Precipitates of comparable nature are also prevalent in cultures of iron-oxidizing bacteria like *Acidithiobacillus ferrooxidans* (Li et al., 2021; Zhan et al., 2021) and *Leptospirillum ferriphilum* (Chowdhury and Ojumu, 2014; Mabusela and Ojumu, 2017). In bioleaching of mineral sulfides, the accumulation of jarosite precipitate may cause slow kinetics, impart negatively on process dynamics (Nazari *et al.*, 2014), and lower the efficiency of bioleaching operations by occluding desired metals (Keeling *et al.*, 2005; Rouchalova *et al.*, 2020), with an extensively described underlying sorption mechanism (Oladipo *et al.*, 2021a).

It has been shown recently that the presence of –OH and $–NH_2$ functional group initiated a chemisorption mechanism through an ion-exchange pathway for the adsorption of copper ions to the active sites of an industrially generated biogenic precipitate (Oladipo *et al.*, 2021a). Since adsorption is a surface phenomenon, the specific surface area is one of the most essential parameters of iron minerals, often seen to be directly related to its adsorption capacity. The surface area of such minerals is contributed by pores of varying sizes which can also influence the availability of active sites for adsorption. Depending on the size of the pores as well as their arrangement, their accessibility for metal ions could be affected, which in turn can affect the adsorption kinetics.

It has been shown above (in Chapter 5) that an increase in initial solution pH led to an increase in the surface area of the generated ferric ion precipitate. Likewise, the pH of the solution influenced the sorption affinity of the adsorbent by influencing the type of charge

on the surface of the adsorbent, speciation of the metal in the solution, and ionizing strength of the adsorbent. The point of zero charge (PZC) could be used to describe the effect of pH. The PZC is the pH value (pH_{PZC}) at which the surface of an adsorbent has a net charge of zero (Mahmood *et al.*, 2011; Bakatula *et al.*, 2018), and it is an important factor in determining the pH sensitivity spectrum, surface form, and adsorption capacity.

7.2 Objective

This chapter aims to give insights into the influence of initial pH of jarosite produced during ferrous ion bio-oxidation on its sorption capacity and kinetics for copper ion uptake from aqueous solutions. The results of the investigation in this chapter will help to clarify if the adsorption capacity of jarosite for metal is consistently sensitive to increase and/or decrease its surface area. It also seeks to identify if a pore-filling mechanism occurs in the adsorption process. In addition, the chapter compares the surface properties of precipitate produced from mineral bioleaching and the precipitate generated from ferrous ion bio-oxidation.

7.3 Methodology

The jarosite precipitates used in this present chapter were obtained from the experiments carried out in Chapter 4. The characterization procedures for the precipitates are described in Section 3.4 of Chapter 3. The methods utilized in this chapter for batch adsorption experiments and solution analysis for Cu(II) concentrations are described in Section 3.5 of Chapter 3. The adsorption kinetics, isotherms, and thermodynamic methods are documented in Sections 3.6, 3.7, and 3.8 respectively of Chapter 3.

The jarosite obtained at pH 1.7 (Jar-1.7) and 2.2 (Jar-2.2) were used for the adsorption studies to understand the influence of surface area and porosity of the precipitate on the adsorption of copper. The Jar-1.7 and Jar-2.2 samples were reported (Section 5.4.7 of Chapter 5) to have BET surface areas of 8.32 and 11.00 m^2/g with total pore volumes of 0.03 and 0.04 cm^3/g respectively.

7.4 Results and discussion

7.4.1 Point of zero charge (PZC) analysis

The pH at PZC of the biogenic jarosite generated at initial pH values of 1.7 and 2.2 is illustrated in Figure 7.1 and was determined within pH ranges of 2 to 11. It was observed that the pH_{PZC} for the jarosite samples decreases with an increase in initial solution pH synthesis. The values of pH_{PZC} obtained for the jarosite samples, Jar-2.2 and Jar-1.7 are 2.14 and 2.37 respectively (Figure 7.1). This implies that the net surface charge on the jarosite would be positive for a solution pH value less than the pH_{PZC} value, and negative for a solution pH value above the pH_{PZC} value. When the net surface charge is positive, electrostatic repulsion exists between the jarosite particles and cations whereas when the net surface charge is negative, electrostatic attraction exists (Smith, 1999). In other words, this connotes that the surface of the jarosite particles is positively charged and favours anion sorption for solution pHs < pH_{PZC} (2.14 for Jar-2.2 and 2.37 for Jar-1.7), but becomes negatively charged and favours cation sorption for solution pHs > pH_{PZC}. Xu *et al.* (2013) reported pH_{PZC} value of 5.6 for biosynthesized jarosite. The difference in pH_{PZC} between the jarosite precipitate formed in this study and that synthesized by Xu *et al.* (2013) could be due to differences in PZC analysis method, medium, and solution chemistry in which the precipitates were formed (which may have contained a variety of anions and cations), and the bacteria strain used. It has previously been reported that conducting adsorption experiments for copper at pH values > 5 can lead to the precipitation of Cu(II) as insoluble $Cu(OH)_2$, which can hinder true adsorption studies (Ali *et al.*, 2016; Oladipo *et al.*, 2021a). Thus, in this study, pH-dependent experimental runs for the sorption process were conducted at pH 4.

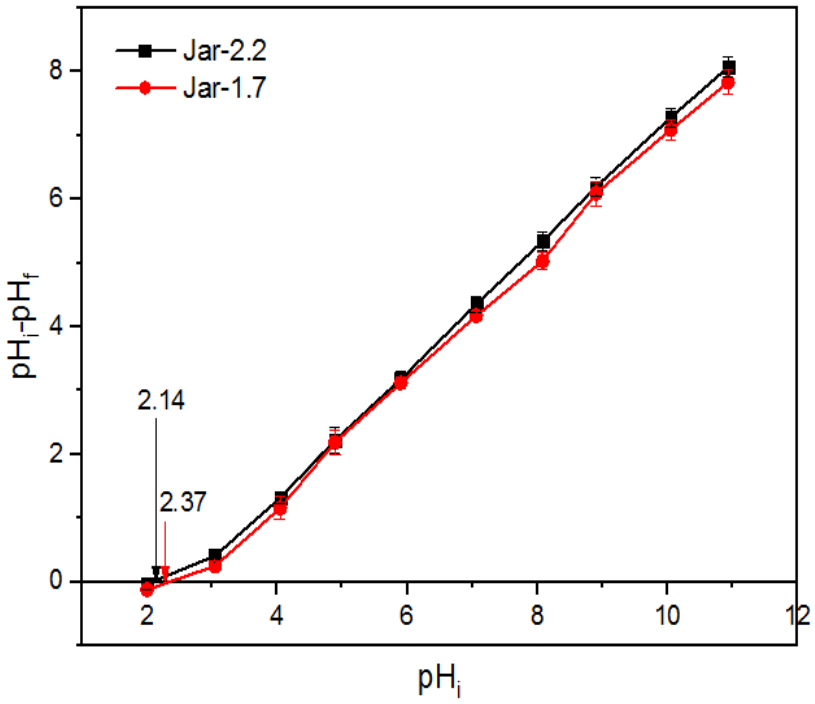

Figure 7.1: pH point of zero charge (pHPZC) of biogenic jarosite

7.4.2 Parametric study on jarosite sorption capacity

The effect of adsorption variables on copper removal is investigated in parametric studies. A parametric study is a critical component of process systems engineering that studies the impact of various parameters on processes and aims to establish optimal levels for these parameters.

7.4.2.1 Effect of contact time

The effect of contact time (5 – 140 min) on the removal of Cu(II) by biogenic jarosite was studied at an initial copper concentration of 150 mg/L Cu(II), 1 g jarosite dosage, 150 rpm stirring speed, pH 4, and at a solution temperature of 30 °C. The Cu(II) uptake increased rapidly from 10 – 40 min and a further slow increment was observed with time until equilibrium was achieved at 80 min (Figure 7.2). The rapid uptake of Cu(II) at the start of adsorption was due to the presence of more active sites. Due to the saturation of these active sites, the jarosite uptake of copper decreased over time. Additionally, the high Cu(II) concentration at the onset of sorption promoted a strong mass transfer driving force, resulting in a faster sorption rate. The mass transfer driving force helped to overcome the

diffusion constraint at the liquid film surrounding the jarosite adsorbent. The maximum time for the uptake of Cu(II) was 80 min and this was used for other experiments.

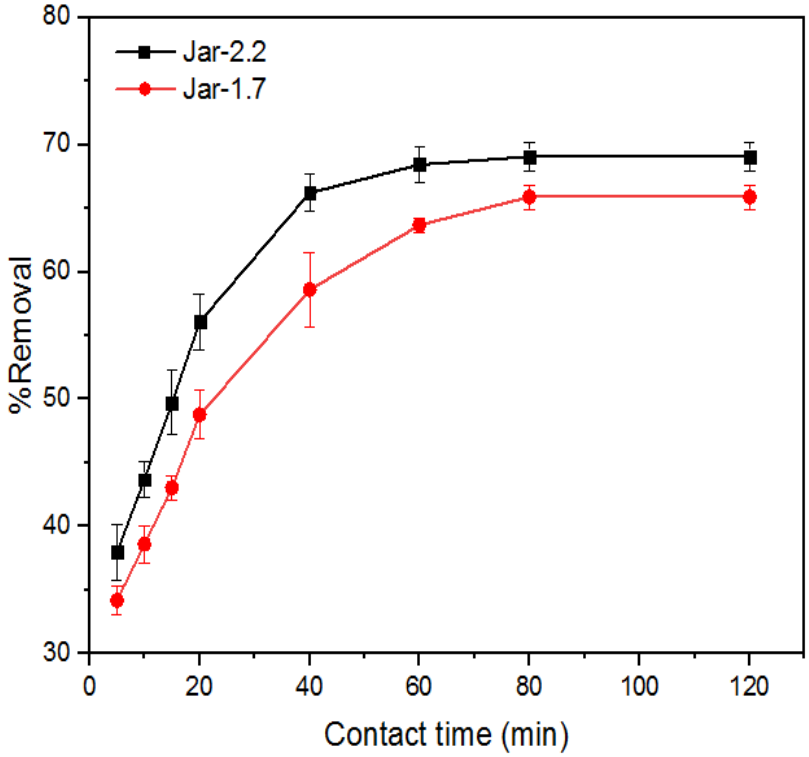

Figure 7.2: Effect of contact time on Cu(II) removal on biogenic jarosite

7.4.2.2 Effect of copper initial concentration

The effect of initial concentration (150 – 500 mg/L) on the uptake of Cu(II) onto jarosite was examined at pH 3, 1 g jarosite dosage, 150 rpm stirring speed, and 80 min contact time. The percentage of copper adsorbed decreased with increasing initial concentration. As presented in Figure 7.3, it can be observed that the copper uptake by jarosite decreased from 69.08 to 48.53% for Jar-2.2 and from 65.90 to 40.72% for Jar-1.7 when the copper initial concentration increased from 150 to 500 mg/L. These observations imply that the ratio of surface active sites to total metal ion concentration was higher in lower metal ion concentrations than in higher metal ion concentrations. A similar finding was made in our prior investigation (Oladipo *et al.*, 2021a).

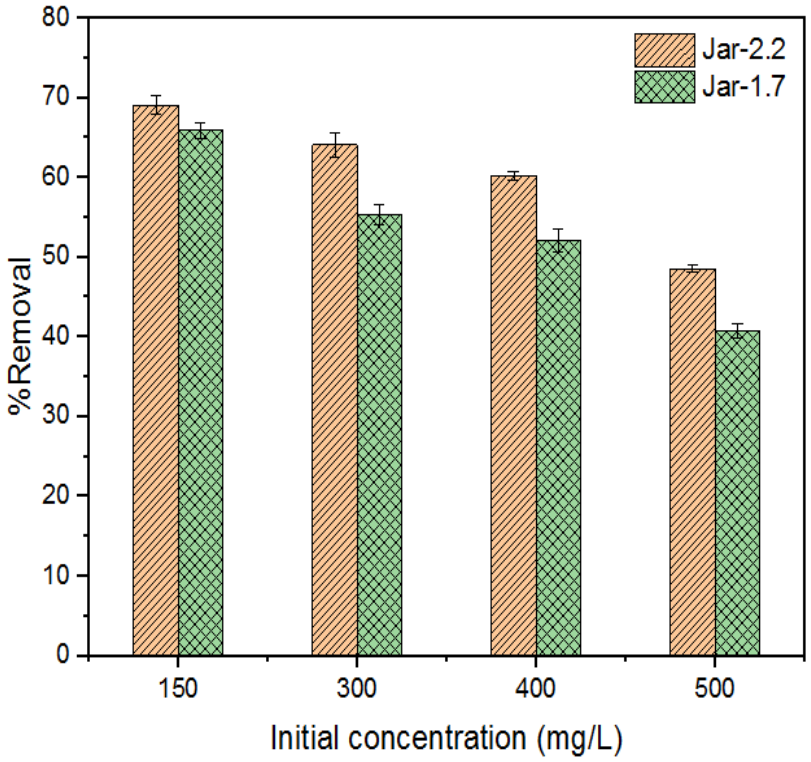

Figure 7.3: Effect of initial concentration on Cu(II) removal on biogenic jarosite

7.4.2.3 Effect of solution temperature

The effect of temperature (30 – 50 °C) on the uptake of Cu(II) onto jarosite was investigated using an initial Cu(II) concentration of 150 mg/L at pH 4, 1 g jarosite dosage, 150 rpm stirring speed, and 80 min contact time. As shown in Figure 7.4, the adsorption efficiency increased from 69.08 to 83.68% for Jar-2.2 and from 65.90 to 77.97% for Jar-1.7 as the temperature increased from 30 to 50 °C, indicating that the sorption process is endothermic. This rise in percentage removal with increasing temperature could be attributed to the copper molecules' mobility increasing as their kinetic energy increased (Igwegbe *et al.*, 2020). Additionally, the increased temperature and mobility associated with it assisted the cationic copper in overcoming the boundary layer limitation at the solid-solution film. The findings in this section are further corroborated by the thermodynamic study, which revealed an endothermic adsorption process.

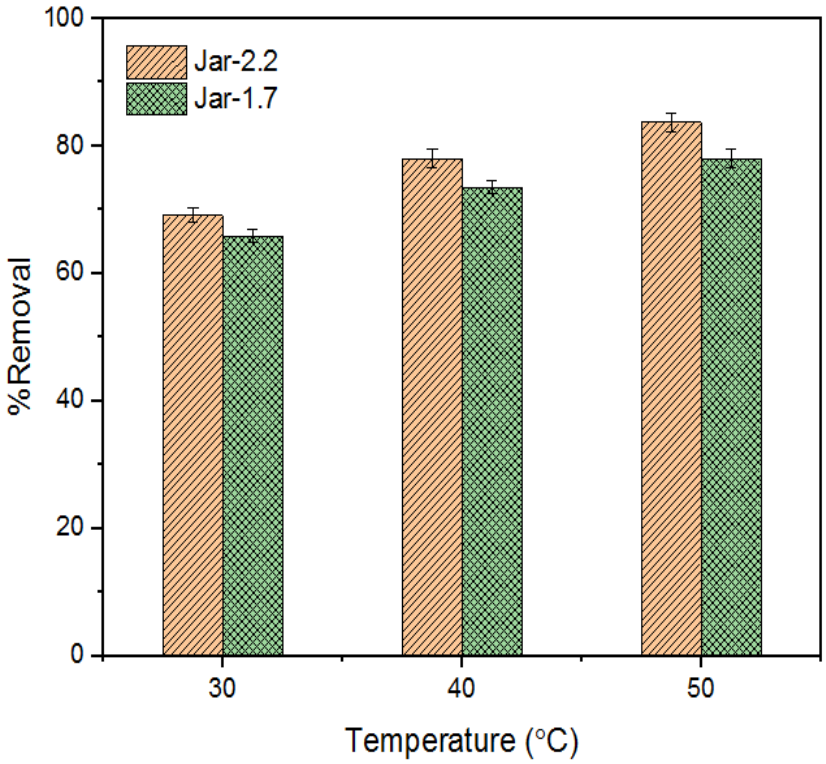

Figure 7.4: Effect of solution temperature on Cu(II) removal on biogenic jarosite

7.4.3 Equilibrium isotherm modeling

In adsorption investigations, adsorption isotherm modeling is significant because it depicts how the adsorbate will interact with the adsorbent and provides an estimate of the adsorption capacity of the adsorbent. It also provides the most appropriate correlations for the design and optimization of an adsorption system. The adsorption isotherms were studied under the following conditions: 1 g jarosite dosage, pH 4, 80 min, 150 rpm, 303 K, and different initial Cu(II) concentrations (150 – 500 mg/L). The Langmuir (Langmuir, 1916) and Freundlich (Freundlich, 1906) models were used for the equilibrium isotherms that described the interaction between Cu(II) uptake onto jarosite.

For the Langmuir isotherm, the slope and intercept of the linear plot of C_e/q_e vs C_e (Figure 7.5a) give the values of q_m and K_L respectively, while for the Freundlich isotherm, the slope and intercept of the linear plot of log q_e vs log C_e (Figure 7.5b) give the values of n_f and K_f respectively. The results of the isotherm analysis are summarized in Table 7.1.

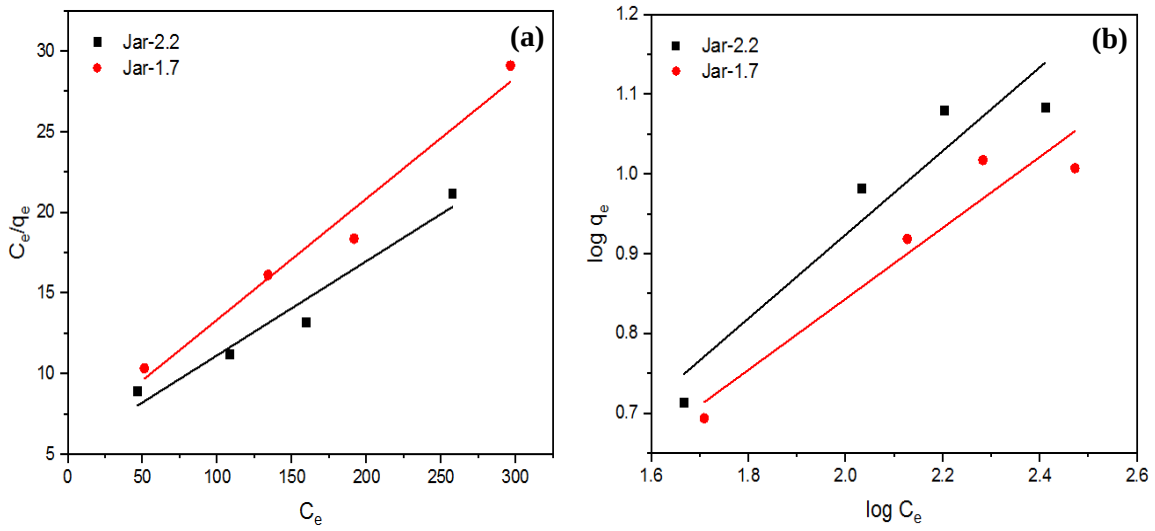

Figure 7.5: (a) Langmuir and (b) Freundlich isotherm model plots for Cu(II) adsorption onto biogenic jarosite

Table 7.1: Isotherms model data for Cu(II) adsorption onto jarosite at 303 K

Isotherms	Constants	Jar-2.2	Jar-1.7
Langmuir model	q_m (mg/g)	17.12	13.32
	b (L/mg)	0.011	0.013
	R_L	0.378	0.342
	R^2	0.9568	0.9734
Freundlich model	n_f	1.904	2.246
	K_f	0.748	0.898
	R^2	0.9057	0.9233

According to the R^2 values, the Langmuir isotherm ($R^2 = 0.9568$ for Jar-2.2 and $R^2 = 0.9734$ for Jar-1.7) was the best fit for representing the adsorption data. This indicates that the surface of jarosite was covered by the monomolecular layer, thus demonstrating monolayer adsorption. The monolayer layer of adsorption has been reported to be a good indicator of chemical adsorption (Ruthven, 1984; Tran *et al.*, 2016). The monolayer adsorption capacity (q_m) at 303 K was 17.12 mg/g for Jar-2.2 and 13.32 mg/g for Jar-1.7. The calculated R_L value in this study ranged between 0 and 1, showing that the adsorption system of Cu(II) ions

onto the biogenic jarosite was favourable. Adsorption is favourable when $0 < R_L < 1$ respectively (Weber and Chakravorti, 1974; Tran *et al.*, 2017).

7.4.4 Adsorption kinetics modeling

Studies of kinetics are useful for the design, optimization, and scale-up of adsorption processes. The adsorption kinetics result was presented under the following investigated conditions: 1 g jarosite dosage, pH 4, 150 rpm, 303 K, 150 mg/L initial Cu(II) concentration, and contact time intervals of 5 – 80 min. The kinetic data necessary for designing and optimizing the removal of Cu(II) ions by jarosite were modeled using pseudo-first-order (Lagergren, 1898), pseudo-second-order (Blanchard *et al.*, 1984), and intra-particle diffusion (Weber and Morris, 1963) models.

For the pseudo-first-order, the slope and intercept of the linear plot of ln (q_e-q_t) vs t (Figure 7.6a) give the value of k_1 and q_e respectively. For the pseudo-second-order, the slope and intercept of the linear plot of t/q_t vs t (Figure 7.6b) give the value of q_e and k_2 respectively. The intra-particle diffusion, the slope and intercept of the linear plot of q_t vs $t^{1/2}$ (Figure 7.6c) give the value of k_{id} and C respectively. The estimated kinetic model parameters in the studied conditions are summarized in Table 7.2.

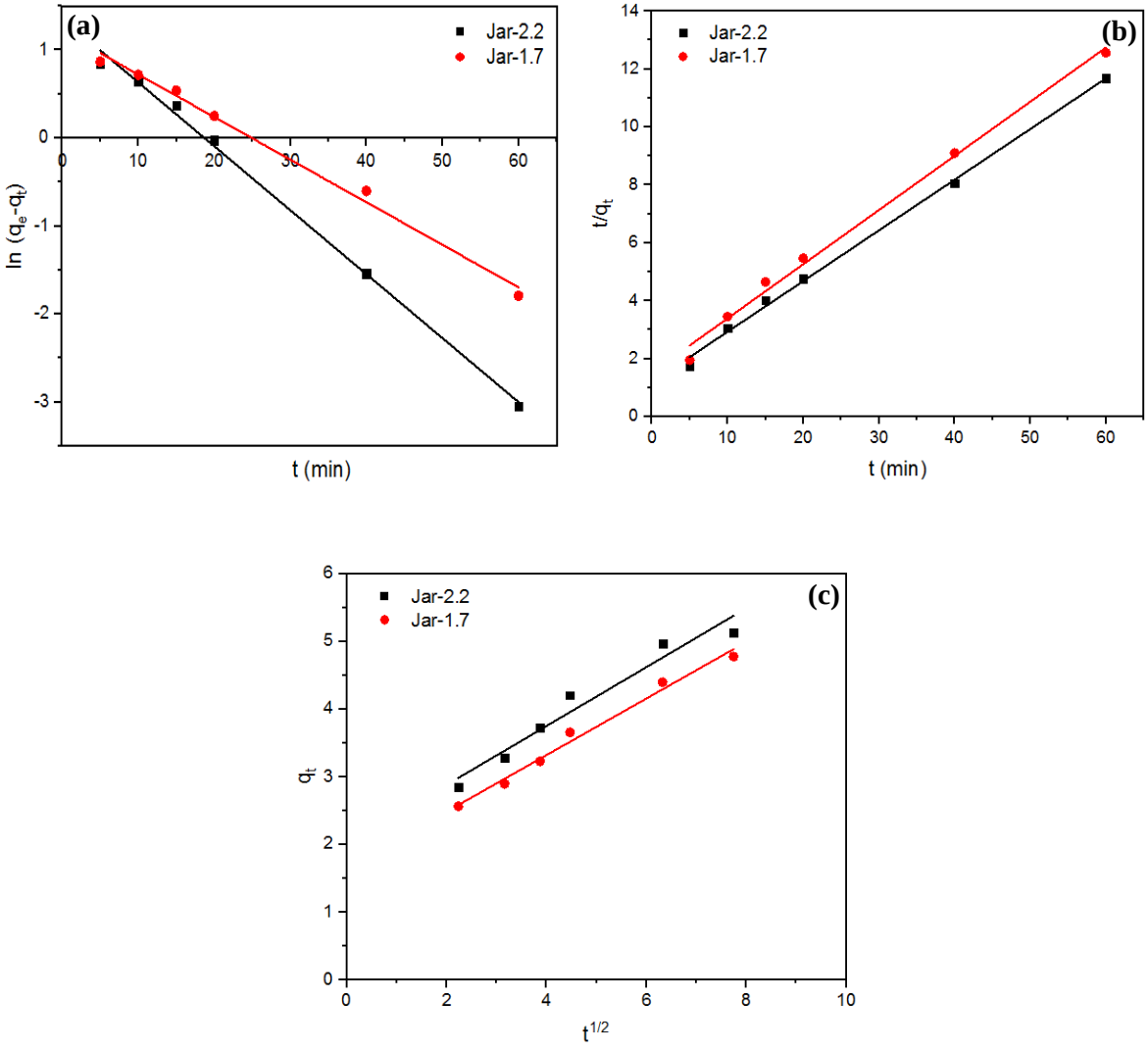

Figure 7.6: (a) Pseudo-first-order, (b) Pseudo-second-order, and (c) Intra-particle diffusion model

Table 7.2: Kinetic model data for Cu(II) adsorption onto jarosite

	Parameters	Jar-2.2	Jar-1.7
Experimental data	$q_{e,\,exp}$ (mg/g)	5.23	4.87
Pseudo-first-order	k_1 (min^{-1})	0.0727	0.0484
	$q_{e,cal}$ (mg/g)	3.89	3.34
	R^2	0.9966	0.9927
Pseudo-second-order	k_2 (g/mg min)	0.0230	0.0259
	$q_{e,cal}$ (mg/g)	5.34	5.71
	R^2	0.9974	0.9942
Intra-particle diffusion	K_{id} (mg/g $min^{0.5}$)	0.435	0.418
	C	2.0096	1.648
	R^2	0.9530	0.9867

The data confirms its best compliance with the pseudo-second-order model for the adsorption process due to its comparatively higher coefficient of determination values (R^2 = 0.9974 for Jar-2.2 and R^2 = 0.9942 for Jar-1.7) than the values for other models (Table 7.2). This is also evident from the insignificant disparities between the pseudo-second-model estimated ($q_{e,\,cal}$ = 5.34 for Jar-2.2 and $q_{e,\,cal}$ = 5.71 mg/g for Jar-1.7) and experimental ($q_{e,\,exp}$ = 5.23 mg/g) values. This indicates that the adsorption kinetics are affected by both the availability of active sites and the concentration of Cu(II) in the solution. The finding suggests that the rate-limiting step in the examined system occurs via chemisorption, which involves the exchange of electrons between the jarosite and Cu(II) ions. It is often assumed in the literature that if the adsorption process is well represented by the pseudo-second-order model, the (adsorbate-adsorbent) chemical reaction at the surface can be thought to constitute the rate-limiting step (Paredes-Quevedo *et al.*, 2021). On the other hand, since non-zero intercepts exist (the lines do not intersect the point of origin) of the plots of the intra-particle diffusion model (Figure 7.6c), this suggests that the adsorption mechanism of Cu(II) onto biogenic jarosite does not include internal diffusion and is therefore

independent of the mass transfer in interior pores. There is no pore-filling mechanism. Thus, external (surface) adsorption occurs.

7.4.5 Activation energy and thermodynamic analysis

The activation energy (E_a) enables the estimation of the energetic barrier that copper ions must overcome before adsorption occurs. The activation energy was calculated using the Arrhenius expression.

The slope of the plot of ln k_2 vs $1/T$ (Figure 7.7) was used to estimate the value of E_a. The activation energy of physical adsorption is usually less than 4.184 kJ/mol (Hill and Root, 2014) and no more than 17.573 KJ/mol (Saha and Chowdhury, 2011). The activation energy required for chemical adsorption is in the range of 4 – 40 kJ/mol (Maleki *et al.*, 2017) since greater force is required for the adsorption process. The activation energy in this investigation was calculated to be 21.01 kJ/mol for Jar-2.2 and 23.39 kJ/mol for Jar-1.7, implying that the rate-limiting step is chemically controlled for both adsorption processes.

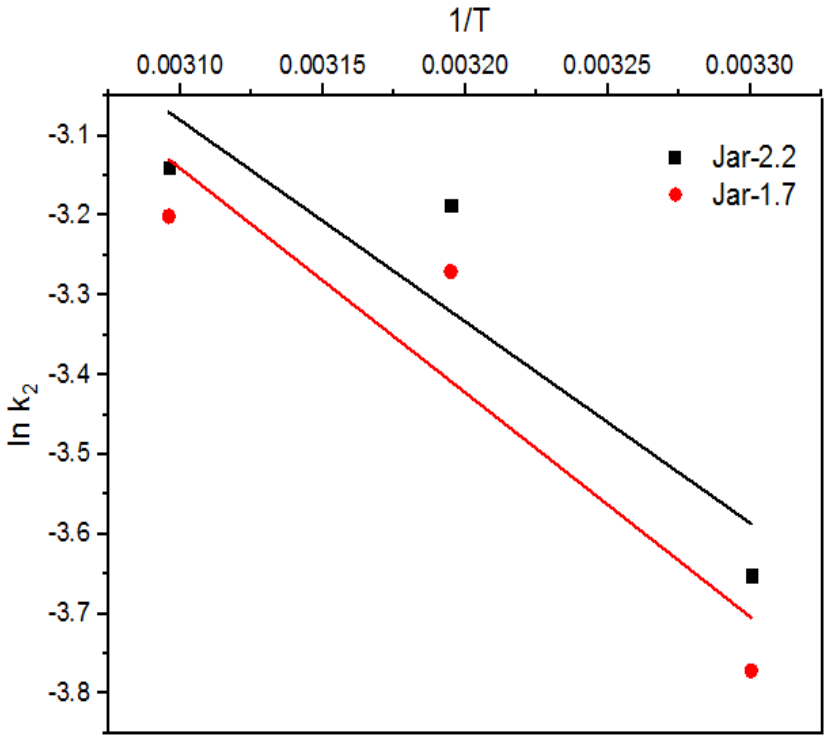

Figure 7.7: Arrhenius plot for Cu(II) adsorption onto biogenic jarosite

The determination of thermodynamic parameters enables the feasibility and real nature of an adsorption system to be determined. After establishing the adsorption equilibrium of the examined systems, thermodynamic data were calculated, namely Gibbs free energy change ($\Delta G°$), entropy change ($\Delta S°$), and enthalpy change ($\Delta H°$).

The slope and intercept of the linear van't Hoff plot of ln K_D vs $1/T$ (Figure 7.8) were used to estimate the values of $\Delta H°$ and $\Delta S°$ respectively. Table 7.3 summarizes the thermodynamic and activation energy data.

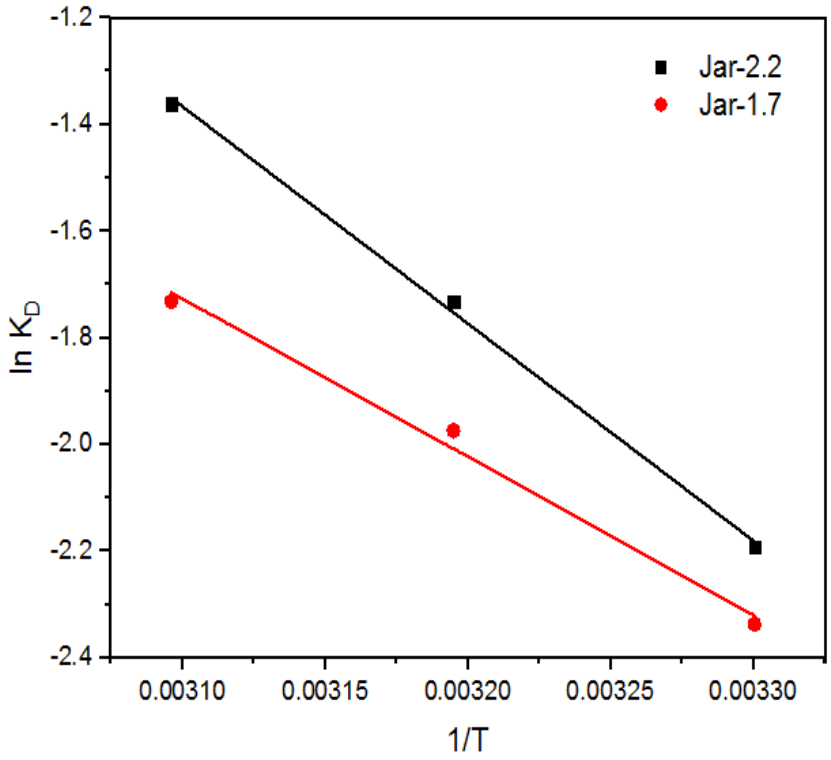

Figure 7.8: van't Hoff plots for Cu(II) adsorption onto biogenic jarosite

Table 7.3: Thermodynamic and activation energy parameters for the adsorption process

Jarosite	ΔH° (kJ/mol)	ΔS° (kJ/mol K)	E_a (kJ/mol)	ΔG° (kJ/mol)		
				303 K	313 K	323 K
Jar-2.2	33.83	0.094	21.01	5.50	4.56	3.63
Jar-1.7	24.65	0.062	23.39	5.85	5.22	4.60

The positive values of $\Delta H°$ confirm that the adsorption process is endothermic. This supports the finding of the parametric analysis, where an increase in adsorption was observed with increasing temperature. The positive values of $\Delta S°$ imply enhanced dissociation at the solid/solution interface. This proved that biogenic jarosite has a high affinity for copper ions during the adsorption process. Similarly, positive values of $\Delta G°$ indicate that the adsorption is non-spontaneous and that ion exchange occurs. The decrease in $\Delta G°$ values with increasing temperature indicates that higher temperatures resulted in a higher sorption rate.

7.4.6 Adsorption mechanism

This section discusses the likely sorption mechanism of copper ion onto jarosite based on the various analyses performed in the study.

Above the pH_{ZPC} values (2.14 and 2.37), the biogenic jarosite powder possessed a net negative surface charge and the adsorption process takes place through electrostatic attraction between the copper ions in solution and the functional groups present on the surface of the adsorbent. Since the pH of the solution (pH_S 4) used throughout the adsorption study is higher than the pH_{PZC}, the deprotonation reactions of the hydroxyl groups available on the surface of the biogenic jarosite occurred as shown in Equation 7.1 and the electrostatic attractions thus occur between the negatively-charged sites on the surface of the biogenic jarosite and Cu(II) cations in the solution as shown in Equation 7.2.

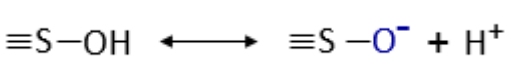

(7.1)

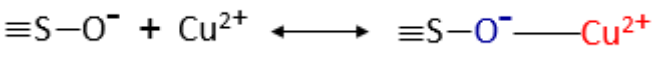

(7.2)

where S represents the surface of the adsorbent

Moreover, the hydroxyl group present on the surface of the biogenic jarosite is a representative surface acidic functional group and could attract the copper molecules through a possible ion-exchange mechanism.

Strictly speaking, industrial heap copper bioleaching is performed at pH 2.0 or lower to maintain a high concentration of the principal bioleaching agent, Fe(III), for copper solubility (Ruan *et al.*, 2011; Gentina and Acevedo, 2013). In fact, microbial activity causes the pH of sulfur-containing leachates to decline more during the duration of a bioleaching run (Mccarthy *et al.*, 2018). Even at these extremely low pH levels (< 2), iron precipitates, particularly jarosite, have been shown in the literature to scavenge metal ions and prevent them from getting into solution (Ju *et al.*, 2011; Liu *et al.*, 2017; Kaksonen *et al.*, 2018; Wang *et al.*, 2018). This was reviewed in Section 2.7 of Chapter 2. As a result, in this present chapter, additional sorption studies were conducted at pH value of 1.5 and solution temperature of 50 °C. These might provide a glimpse of the sorption mechanism that occurs in a typical bioleach heap system at a pH values lower than the pH_{PZC} values (2.14 and 2.37) of biogenic jarosite as demonstrated in this study. To ascertain this, a short investigation was carried out under the following conditions: pH 1.5 and 2, solution temperature of 50 °C, jarosite dosage of 1 g, and contact time of 80 min. The result of the study is illustrated in Figure 7.9.

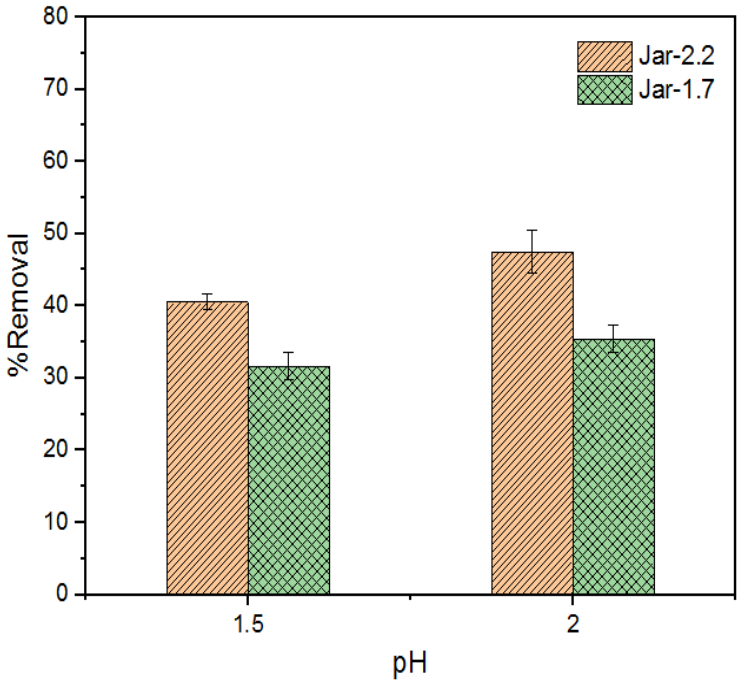

Figure 7.9: Effect of initial pH on biogenic jarosite for copper adsorption

As illustrated in Figure 7.9, the adsorption process of copper still functioned when the pH_S was lower than the pH_{PZC} of jarosite. This result implies that, in the acidic solution for the sorption process, there seems to exist an interaction between the abundant hydrogen (H^+) and the copper ion (Cu^{2+}). This further suggested that certain chemical interactions such as ion exchange, with sufficient energy could overcome the surface-electrostatic repulsive force (Van *et al.*, 2019). The low copper uptake by jarosite (at pH 2: 47.49% for Jar-2.2 and 35.4% for Jar-1.7; at pH 1.5: 40.51% for Jar-2.2 and 31.62 for Jar-1.7) in the investigated conditions could be that the contact time used (80 min) for this sorption process might not have reached equilibrium for the uptake of copper. The adsorption mechanism of copper onto biogenic jarosite is summarised in Figure 7.10.

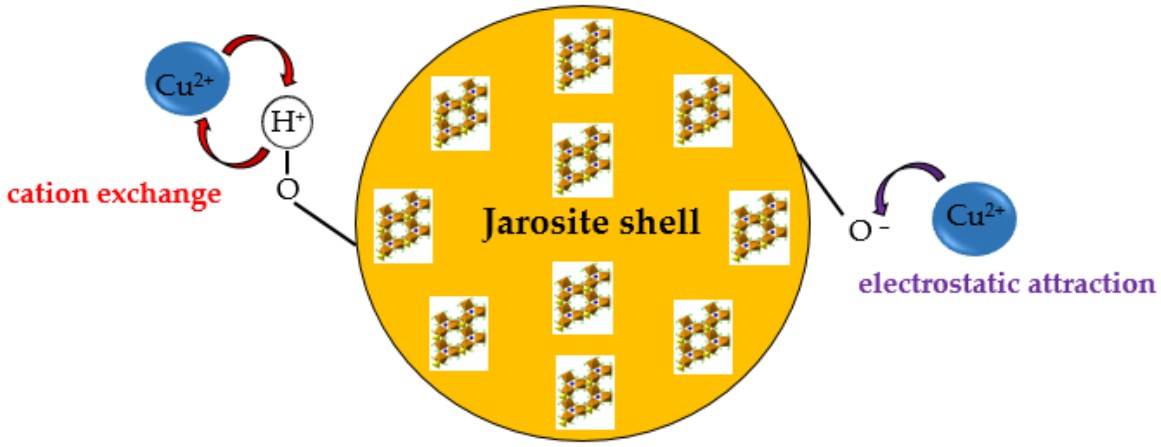

Figure 7.10: Possible mechanism of copper adsorption onto biogenic jarosite

7.5 Implications of surface charge and surface area of jarosite in bioleaching

The impart of iron precipitate (most especially jarosite) on biohydrometallurgical operations was carefully reviewed in Section 2.7 in Chapter 2. While the use of jarosite was demonstrated in this present study to be a promising adsorbent for remediating cationic pollutants from wastewater systems, this adsorbing attribute is quite detrimental during the bioleaching of sulfide minerals. Of notable effect is the scavenging of desired metals by jarosite during bioleaching operations. Based on the findings in this study, to minimize the sorption of metals by jarosite for efficient metal extraction in biohydrometallurgical processes, it is recommended that:

(i) The surface charge of jarosite should be given utmost consideration. In this study, the jarosite formed at pH 2.2 had less positive charge (i.e., more negative charge) which was responsible for its ability to adsorb more copper ions due to the strong electrostatic attraction, as compared to the jarosite formed at pH 1.7. This indicates that the metal adsorption by precipitated iron (jarosite) during bioleaching is caused by the surface charge of such precipitate. Highly positively charged (i.e., less negatively charged) precipitates demonstrated lower adsorption capacity due to the high electrostatic repulsion forces in comparison to less positively charged precipitates, which exhibited high electrostatic attraction forces. Therefore, to increase bioleach efficiency and metal recovery, bioleach conditions should be maintained in such a way that the resulting surface charge on the formed precipitate is more positive. This will aid more sorption of undesirable anions (such as sulfate ions) and less of cationic metals (such as copper).

(ii) The experiments revealed that adsorption of copper is sensitive to the increase in surface area but not sensitive to porosity (pore volume); consequently, for understanding the sorption capacity of jarosite for metal ions, porosity may be considered less important in itself. The kinetic models additionally corroborate this conclusion. Pseudo-second-order kinetic model indicated that the adsorption process occurred via an adsorbate-adsorbent reaction of copper onto the external surface of biogenic jarosites, while the intra-particle diffusion revealed the adsorption process was initiated without mass transport in internal pores.

For proper examination of the scavenging nature of jarosite for metals during bioleaching, it is more important to conduct holistic studies that take into account the interactions (ion exchange and electrostatic attraction) that may occur between adsorbate and the adsorbent surface.

7.6 Surface properties comparison of the precipitates obtained from industrial pyrite bioleaching and laboratory ferrous ion bio-oxidation

The XRD patterns of biogenic iron precipitate samples are shown in Figure 7.11. The jarosite compound formed during the ferrous ion bio-oxidation at the pH levels investigated does

not contain crystalline byproducts. Whereas, in addition to jarosite, secondary minerals (as gangue minerals) such as talc ($Mg_3Si_4O_{10}(OH)_2$) and quartz (SiO_2) were identified on the sample of the industrial precipitate which could be because pyrite mostly occurs at the contact between talc and magnesite bodies (Petrasova *et al.*, 2007; Hredzak *et al.*, 2014).

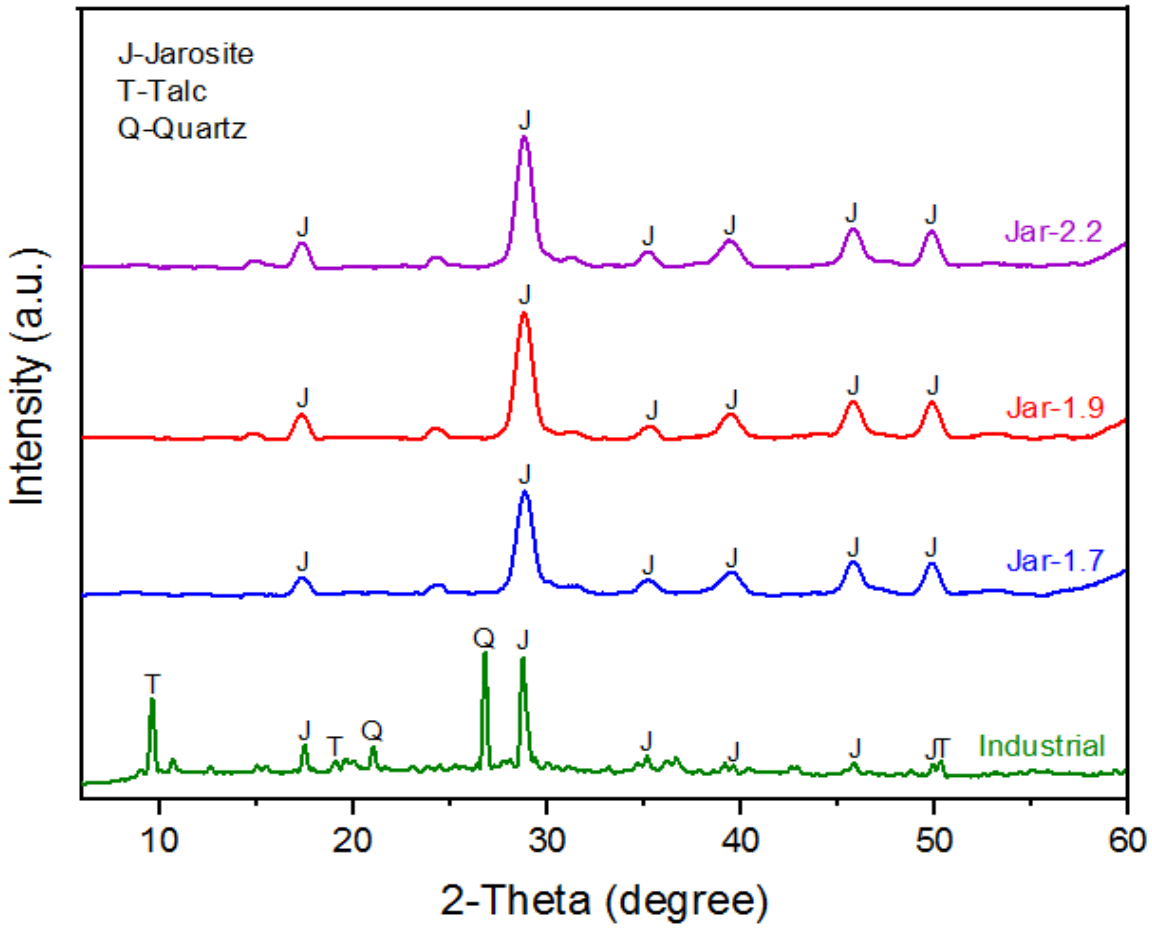

Figure 7.11: XRD patterns of biogenic industrial precipitate from pyrite concentrate and biogenic precipitate produced from ferrous ion oxidation

FTIR spectra for biogenic precipitate (identified as jarosite) generated at pH 1.7 (Jar-1.7), 1.9 (Jar-1.9), 2.2 (Jar-2.2), and the industrial biogenic precipitate samples are illustrated in Figure 7.12. It was observed that the industrial precipitate sample had an additional peak at 1421 cm^{-1} assigned to the bending vibrational mode of $v_4(NH_4^+)$, which suggests that it contained traces of ammoniojarosite (Sasaki *et al.*, 1998). This observed peak was absent in the spectra of the biogenic jarosites generated from the oxidation of ferrous ion at all the

pH levels investigated. Furthermore, the stretching mode of the v(Si–O–Si) band was found at 798 cm^{-1} in the industrial iron precipitate sample (Capeletti and Zimnoch, 2016). This may be due to the presence of talc and quartz as identified from the XRD analysis of the sample. The bands at 667 and 447 cm^{-1} present in the industrial precipitate sample are attributed to $v_4(SO_4^{2-})$ and $v_2(SO_4^{2-})$ bending vibrational modes respectively, of jarosite-group compounds (Sasaki *et al.*, 1998). However, it should be noted that the $v_2(SO_4^{2-})$ peak was not observed in the biogenic jarosites produced from the ferrous ion bio-oxidation process. There are no peaks assigned to the vibrational modes of the Fe–O bond at 400–4000 cm^{-1} in the spectrum of the industrial precipitate sample, which might be due to its overlap with multiple absorption modes of other compounds that are present. All peak assignments are summarized in Table 7.4.

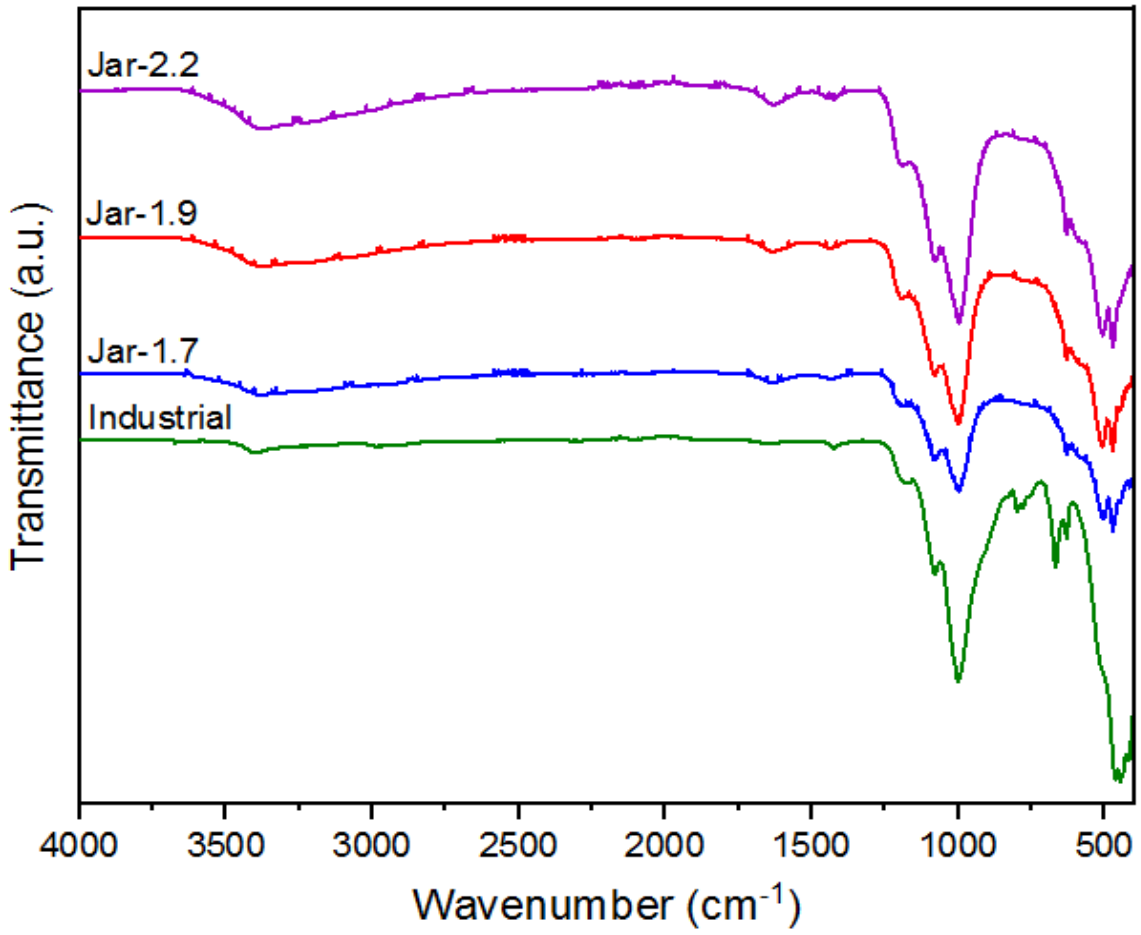

Figure 7.12: FTIR spectra of biogenic industrial precipitate from pyrite concentrate and biogenic precipitate produced from ferrous ion oxidation

Table 7.4: Assignments of infrared wavenumbers of biogenic industrial iron precipitate from pyrite concentrate and biogenic jarosite formed from ferrous ion oxidation

Wave numbers (cm^{-1})				Functional group	Mode of vibration
Jar-1.7	Jar-1.9	Jar-2.2	Industrial		
3362	3365	3369	3399	vOH	stretching
1624	1624	1637	-	$\delta(H_2O)$	bending
-	-	-	1421	$v_4(NH_4^+)$	bending
1189	1189	1196	1176	$v_3(SO_4^{2-})$	stretching
1077	1080	1080	1079	$v_3(SO_4^{2-})$	stretching
997	1000	998	1000	$v_1(SO_4^{2-})$, δ_{OH}	stretching
-	-	-	798	v(Si–O–Si)	stretching
-	-	-	667	$v_4(SO_4^{2-})$	bending
629	629	629	629	$v_4(SO_4^{2-})$	bending
505	506	503	-	Fe–O	stretching
470	471	471	-	Fe–O	stretching
-	-	-	447	$v_2(SO_4^{2-})$	bending

The elemental composition of the samples as identified from the EDS is presented in Table 7.5. The industrial iron precipitate has lower weight fractions of the F, S, and K elements as compared with the biogenic jarosite obtained from the ferrous ion oxidation. Additional elements, namely Mg, Al, Si, Cl, and Ca were detected on the biogenic industrial precipitate sample. This shows that the precipitate is highly heterogeneous in composition and contains the presence of other phases and/or compounds besides K-jarosite. The Fe/S molar ratio obtained for the industrial precipitate is far below the Fe/S standard stoichiometric ratio of 1.5 for K-jarosite (Table 7.5).

Table 7.5: Elemental composition and molar ratio of biogenic industrial iron precipitate from pyrite concentrate and biogenic jarosite formed from ferrous ion oxidation at different pH levels

Element	Elemental composition (%)			
	Jar-1.7	Jar-1.9	Jar-2.2	Industrial
C	20.99	15.17	28.24	9.17
O	56.69	57.70	43.43	54.36
Fe	11.21	14.94	16.45	2.74
S	6.21	6.34	6.63	4.83
K	2.73	2.86	2.93	0.03
P	2.17	2.99	2.33	-
Mg	-	-	-	8.69
Al	-	-	-	0.81
Si	-	-	-	13.72
Cl	-	-	-	0.42
Ca	-	-	-	5.23
Fe/S	1.04	1.35	1.42	0.33
Fe/K	2.88	3.66	3.94	63.52
S/K	2.78	2.71	2.76	187.68

The N_2 adsorption-desorption isotherms for the samples are depicted in Figure 7.13a. The plots all revealed a type-IV isotherm and H3 hysteresis loop patterns (Sing, 1985), showing that the biogenic industrial iron precipitate and biogenic jarosite generated from ferrous ion oxidation are all mesoporous in structure. The adsorption pore-size distribution plots are shown in Figure 7.13b. The majority of the pore diameters were between 2 and 25 nm. This corresponds to the Brunauer–Deming–Deming–Teller (BDDT) classification approach, which classifies pores with diameters ranging from 2 to 50 nm as mesopores (Sing, 1985).

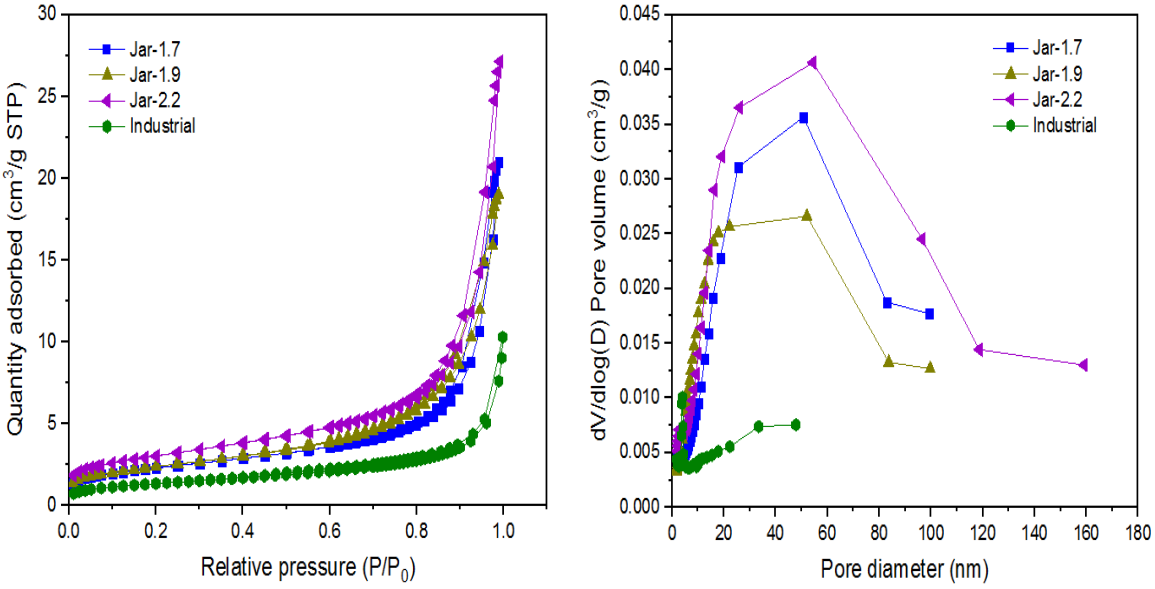

Figure 7.13: (a) N2 adsorption/desorption isotherm; (b) pore-size distribution of biogenic industrial precipitate from pyrite concentrate and biogenic precipitate formed from ferrous ion oxidation

Table 7.6: BET/BJH parameters of biogenic industrial iron precipitate from pyrite concentrate and biogenic jarosite formed from ferrous ion oxidation at different pH levels

Iron precipitate	BET surface area (m^2/g)	Total pore volume (cm^3/g)	BJH average pore size (nm)
Jar-1.7	8.32	0.03	16.15
Jar-1.9	8.58	0.03	13.36
Jar-2.2	11.00	0.04	10.45
Industrial	4.74	0.014	11.61

7.7 Conclusions

This chapter examined the relationship between surface area, pore size, and surface charge of biogenic jarosite for its adsorption of copper from an aqueous solution. The point of zero charge of the jarosite was observed to be 2.14 and 2.37 for jarosite samples synthesized at pH 2.2 (Jar-2.2) and pH 1.7 (Jar-1.7) respectively. Under the same adsorption conditions, Jar-2.2 with a smaller particle size (higher surface area) gave the highest sorption capacity for copper. The best fit for the kinetic investigation of both biogenic jarosites for copper

adsorption was the pseudo-second-order model. This result suggested that the rate-limiting step was chemisorption involving valency forces through sharing or exchange of electrons between jarosite and copper. The Langmuir model also provided the best fit for the isotherm investigation. This suggested monolayer adsorption, indicating that the jarosites have a homogeneous surface. Thermodynamic parameters for the adsorption process obtained over a temperature range of 303 – 323 K revealed that the process was non-spontaneous and endothermic. The mechanism of copper adsorption onto jarosite powder was by cation exchange and electrostatic attraction with no pore-filling mechanism. The result of this study is applicable in the design of iron bio-oxidation and bioleaching processes such that iron precipitation and its scavenging attributes for metals can be well managed.

CHAPTER EIGHT

CONCLUSIONS AND RECOMMENDATIONS

"If the conservation of natural resources goes wrong, nothing else will go right." – M. S. Swaminathan

CHAPTER 8: CONCLUSIONS AND RECOMMENDATIONS

This chapter summarizes the importance of the findings of this thesis in relation to the specified research objectives and concludes with future work prospects.

8.1 Conclusions

This study applied surface chemistry tools to a typical bio-oxidation process to provide new insights into the precipitation of iron and the fate of desired metals during biohydrometallurgical processes. Apart from clogging pipes and heap beds, iron precipitates are known to reduce the extraction efficiency of bioleaching operations by scavenging valuable base metals of interest, and studies have demonstrated that a significant amount of metals can be recovered from the iron precipitate residue of a preceding bioleaching process. In this thesis, fundamental knowledge was obtained of these precipitates regarding their interactions with desired metal ions in order to effectively minimize the loss of metal in biohydrometallurgy. This was achieved by following the approaches outlined below: (i) the influence of initial solution pH values on the amount of iron precipitate generated during bio-oxidation of ferrous ion was examined; (ii) the effect of changes in initial pH on the surface properties of iron precipitate were studied; (iii) the sorption mechanism, kinetics, and thermodynamics of industrial iron precipitate for copper ion retention from an aqueous solution were investigated; and (iv) the significance of surface charge, surface area, and porosity of biogenic iron precipitate on the kinetics and sorption capacity for metal ion was also investigated. In parallel, experiments were conducted and the conclusions drawn below are based on the stated objectives met in accordance with the research questions.

In the first study (Chapter 4), an investigation of the influence of initial solution pH and aging time on the amount of iron precipitate in a CSTR was instigated. The main outcome of the study indicated that the mass of iron precipitate generated increased as the initial solution pH increased.

In the second study (Chapter 5), the effect of initial solution pH was investigated on the surface properties of the microbially synthesized iron precipitate. The XRD patterns of the synthesised biogenic iron precipitates, within the pH values investigated (1.7 – 2.2), showed the precipitate as mainly K-jarosite, $KFe_3(SO_4)_2(OH)_6$. The study revealed a decrease in the average crystallite size (from 8.68 – 8.08 nm) as the influent solution pH increased (from 1.7 – 2.2). The SEM analysis of the jarosite showed the surface morphology to be composed of aggregates of round, elliptical, and/or tabular particles. A trend was observed in the EDS analysis with a decrease in the total content of Fe, S, and K as the synthesis influent pH increased. The XPS spectra for the surface species of the produced biogenic K-jarosite revealed the presence of peaks for Fe(III)–O, hydroxide ($0H^-$), sulfate ion (SO_4^{2-}), polysulfide (S^{2-}), and phosphate ion (PO_4^{3-}) chemical states. The FTIR spectra obtained are consistent with the functional group peculiar in the K-jarosite crystal. In terms of thermal stability, TGA studies showed the dehydroxylation of K-jarosite between 320 – 327 °C and the complete thermal decomposition of yavapaiite between 707 – 716 °C. Most importantly, the study revealed an increase in the surface area (from 8.32 – 11.00 m^2/g) and a decrease in the pore-size distribution (from 16.15 – 10.45 nm) as the influent solution pH increased from 1.7 – 2.2. The chapter concluded that jarosite generated at a higher pH is more porous, has a smaller crystallite size, and higher surface area. This may facilitate metal ion transport and adsorption onto the surface of jarosite particles during bioleaching, thereby hindering the efficient extraction of the desired metal.

In the third study of this thesis (Chapter 6), the kinetics, thermodynamics, and mechanism of copper ion sorption by industrial biogenic iron precipitate from an aqueous solution were investigated. It was shown that the industrial iron precipitate sample was highly heterogeneous in terms of composition and possessed negatively charged functional groups for the uptake of a metal cation such as copper. Consequently, the interaction between the functional ions and metal ions led to a chemisorption process via an ion-exchange mechanism. The pseudo-second-order model best fits the experimental data, signifying its high precision in describing the kinetic constant for Cu(II) adsorption onto biogenic iron precipitate. Thermodynamic parameters showed the process is non-

spontaneous and endothermic. At higher temperatures, the adsorption process for metal ion binding was enhanced, which revealed that increasing the temperature could lead to an expansion in the pore size of the precipitate, helping to ease the diffusion of Cu(II) ions onto the sites difficult to access. The results of this study demonstrate that the entrapment of copper during the high-temperature dissolution of metal-bearing minerals is expected to affect the overall extraction of metal.

This final study (Chapter 7) investigated the relationship between surface area, porosity, and surface charge of biogenic jarosite generated from ferrous ion bio-oxidation for the adsorption of copper from an aqueous solution. Under the same adsorption conditions, jarosite with a smaller particle size (higher surface area) demonstrated an increased sorption capacity for copper compared to jarosite with a larger particle size (lower surface area). The results also showed that in adsorption experiments under positively and negatively charged conditions of pH, jarosite could both adsorb copper, with more copper being adsorbed when the surface of the jarosite was more negatively charged (when the $pH_S > pH_{PZC}$). The kinetic investigation of both biogenic jarosites used for copper adsorption in this study was best fit by a pseudo-second-order model. This result indicated that the rate-limiting phase was chemisorption. The investigation of intra-particle diffusion revealed that the adsorption mechanism is independent of mass transfer in the interior pores (does not include internal diffusion). The Langmuir model offered the best fit for the isotherm investigation, demonstrating monolayer adsorption and a homogeneous surface for the jarosites. Adsorption thermodynamic analysis suggested that the process was non-spontaneous and endothermic. The mechanism of copper adsorption onto biogenic jarosite occurred through cation exchange and electrostatic attraction.

8.2 Recommendations for future research

The studies presented in this thesis have attempted to develop a better understanding of the surface properties of iron precipitates formed during bio-oxidation of ferrous ion at different initial pH levels. The thesis further presented the adsorption of copper ion by industrial precipitate from bioleaching and bio-oxidation processes. The intention was that

this knowledge would help to guide further research in the scavenging of valuable metals by iron precipitates during biohydrometallurgical processes. Based on the major findings and limitations identified in this thesis, the following recommendations for future work are provided below:

- This thesis has established a relationship between surface properties and solution pH conditions for ferrous ion oxidation mediated by mixed mesophilic cultures. It is therefore recommended that studies should be carried out on ferrous ion bio-oxidation mediated by thermophiles. This would help to understand if the precipitate generated under thermophilic conditions follows the same trend as the precipitate produced under mesophilic conditions, in terms of surface properties and adsorption mechanism for metal ions.

- The coexistence of metal ions in different phases (e.g. Ni–Zn–Ca, Cu–Pb–Zn, etc) exists in mineral sulfides due to the diversity of geological and environmental conditions of mined ores. Metal affinities for iron precipitate during bioleaching could be linked to the physicochemical properties of such metal ions (e.g. ionic radius, hydration energy, solubility, electronegativity, etc) and site densities of the precipitates, which can impede target metal extraction. It is recommended that investigations be conducted to identify the distinct types of sites that may be present on iron precipitates (oxides, oxyhydroxides, and hydroxysulfates). Such investigation would address whether the presence of high-energy sites and low-energy sites may explain the adsorption capacity of various iron precipitates for the different metal ions that could be present in a given sulfide mineral.

- In addition to the extraction of base metals during mineral sulfide bioleaching, anions (e.g., phosphate and sulfate) are also dominant ions in iron precipitate residue as demonstrated in the case of jarosite in this study, the presence of which is mostly due to the composition of the synthesis solutions. Thus, the influence of multiple ions coexisting during mineral sulfide dissolution should be considered. Furthermore, the retention of coexisting metal ions on bioleached iron residue can suppress desired metal ions from being extracted during the bioleach operation.

Thus, computer modeling is recommended for calculating the energy of the chemical reactions that occur during the sorption of different ions into the structure of iron precipitate. This would allow an evaluation of the incorporation of the target metal ion into the precipitate crystal structure to be compared to other competing ions. As a result, this would help to model the sorption mechanisms of multiple ions during bioleaching.

- While the findings of this thesis contribute to a better knowledge of the sorption mechanism of iron precipitates in biohydrometallurgical processes, there was no molecular-scale spectroscopic evidence supporting the adsorption mechanism presented in this thesis. Thus, analysis of iron precipitate compounds using X-ray absorption spectroscopy (XAS), extended x-ray absorption fine structure (EXAFS), and X-ray absorption near-edge structure (XANES) spectroscopic techniques that provide direct molecular-scale information about adsorbed metal ions on the surface of iron precipitates should be conducted further. This investigation would provide structural information on the iron precipitate produced from bioleach operation and in particular, its binding forms of metal ions.

- It is also recommended that the kinetics of iron precipitate should be investigated throughout a bio-oxidation and/or bioleaching operation. This would help reveal the rate at which the precipitates are formed and how the change in the degree of crystallinity of the precipitates during aging could influence their sorption capacity for metal ions. The characterization data of the biogenic potassium jarosite from this thesis could be used to guide the interpretation of such an analysis.

REFERENCES

Abdollahi, H., Noaparast, M., Shafaei, S. Z., Manafi, Z., Muñoz, J. A. and Tuovinen, O. H. (2015). Silver-catalyzed bioleaching of copper, molybdenum and rhenium from a chalcopyrite–molybdenite concentrate. *International Biodeterioration & Biodegradation,* 104, 194-200.

Adebisi, G. A., Chowdhury, Z. Z. and Alaba, P. A. (2017). Equilibrium, kinetic, and thermodynamic studies of lead ion and zinc ion adsorption from aqueous solution onto activated carbon prepared from palm oil mill effluent. *Journal of Cleaner Production,* 148, 958-968.

Aguilar-Carrillo, J., Villalobos, M., Pi-Puig, T., Escobar-Quiroz, I. and Romero, F. (2018). Synergistic arsenic (V) and lead (II) retention on synthetic jarosite. I. Simultaneous structural incorporation behaviour and mechanism. *Environmental Science: Processes & Impacts,* 20, 354-369.

Al-Hakkani, M. F., Gouda, G. A. and Hassan, S. H. (2021). A review of green methods for phyto-fabrication of hematite (α-Fe_2O_3) nanoparticles and their characterization, properties, and applications. *Heliyon,* 7, e05806.

Ali, R. M., Hamad, H. A., Hussein, M. M. and Malash, G. F. (2016). Potential of using green adsorbent of heavy metal removal from aqueous solutions: adsorption kinetics, isotherm, thermodynamic, mechanism and economic analysis. *Ecological Engineering,* 91, 317-332.

Angove, M. J., Wells, J. D. and Johnson, B. B. (1999). The influence of temperature on the adsorption of cadmium (II) and cobalt (II) on goethite. *Journal of Colloid and Interface Science,* 211, 281-290.

Antelo, J., Fiol, S., Gondar, D., López, R. and Arce, F. (2012). Comparison of arsenate, chromate and molybdate binding on schwertmannite: Surface adsorption vs anion-exchange. *Journal of Colloid and Interface Science,* 386, 338-343.

Antelo, J., Fiol, S., Gondar, D., Pérez, C., López, R. and Arce, F. (2013). Cu (II) incorporation to schwertmannite: effect on stability and reactivity under AMD conditions. *Geochimica et Cosmochimica Acta*, 119, 149-163.

Bakatula, E. N., Richard, D., Neculita, C. M. and Zagury, G. J. (2018). Determination of point of zero charge of natural organic materials. *Environmental Science and Pollution Research*, 25, 7823-7833.

Barrón, V. and Torrent, J. (2013). Iron, manganese and aluminium oxides and oxyhydroxides.

Barrow, N., Brümmer, G. and Fischer, L. (2012). Rate of desorption of eight heavy metals from goethite and its implications for understanding the pathways for penetration. *European Journal of Soil Science*, 63, 389-398.

Basciano, L. C. and Peterson, R. C. (2008). Crystal chemistry of the natrojarosite-jarosite and natrojarosite-hydronium jarosite solid-solution series: A synthetic study with full Fe site occupancy. *American Mineralogist*, 93, 853-862.

Becker, U. and Gasharova, B. (2001). AFM observations and simulations of jarosite growth at the molecular scale: probing the basis for the incorporation of foreign ions into jarosite as a storage mineral. *Physics and Chemistry of Minerals*, 28, 545-556.

Bevilaqua, D., Diéz-Perez, I., Fugivara, C. S., Sanz, F., Benedetti, A. V. and Garcia Jr, O. (2004). Oxidative dissolution of chalcopyrite by *Acidithiobacillus ferrooxidans* analyzed by electrochemical impedance spectroscopy and atomic force microscopy. *Bioelectrochemistry*, 64, 79-84.

Bhaskar, S., Manu, B. and Sreenivasa, M. (2019). Bacteriological synthesis of iron hydroxysulfate using an isolated *Acidithiobacillus ferrooxidans* strain and its application in ametryn degradation by Fenton's oxidation process. *Journal of Environmental Management*, 232, 236-242.

Bigham, J., Schwertmann, U. and Pfab, G. (1996). Influence of pH on mineral speciation in a bioreactor simulating acid mine drainage. *Applied Geochemistry*, 11, 845-849.

Bigham, J. M., Jones, F. S., Özkaya, B., Sahinkaya, E., Puhakka, J. A. and Tuovinen, O. H. (2010). Characterization of jarosites produced by chemical synthesis over a temperature gradient from 2 to 40 °C. *International Journal of Mineral Processing*, 94, 121-128.

Bishop, J. L. and Murad, E. (2005). The visible and infrared spectral properties of jarosite and alunite. *American Mineralogist,* 90, 1100-1107.

Blanchard, G., Maunaye, M. and Martin, G. (1984). Removal of heavy metals from waters by means of natural zeolites. *Water Research,* 18, 1501-1507.

Bolanz, R. M., Wierzbicka-Wieczorek, M., Čaplovičová, M. r., Uhlík, P., Göttlicher, J. r., Steininger, R. and Majzlan, J. (2013). Structural incorporation of As^{5+} into hematite. *Environmental Science & Technology,* 47, 9140-9147.

Boon, M. (1998). Theoretical and experimental methods in the modelling of bio-oxidation kinetics of sulphide minerals.

Boon, M., Ras, C. and Heijnen, J. J. (1999). The ferrous iron oxidation kinetics of *Thiobacillus ferrooxidans* in batch cultures. *Applied Microbiology and Biotechnology,* 51, 813-819.

Börsig, N., Scheinost, A. C., Shaw, S., Schild, D. and Neumann, T. (2017). Uptake mechanisms of selenium oxyanions during the ferrihydrite-hematite recrystallization. *Geochimica et Cosmochimica Acta,* 206, 236-253.

Breitinger, D., Krieglstein, R., Bogner, A., Schwab, R., Pimpl, T. H., Mohr, J. and Schukow, H. (1997). Vibrational spectra of synthetic minerals of the alunite and crandallite type. *Journal of Molecular Structure,* 408, 287-290.

Brierley, J. and Brierley, C. (2001). Present and future commercial applications of biohydrometallurgy. *Hydrometallurgy,* 59, 233-239.

Capeletti, L. B. and Zimnoch, J. H. (2016). Fourier transform infrared and Raman characterization of silica-based materials. *Applications of molecular spectroscopy to current research in the chemical and biological sciences*, 1-21.

Casas, J. M., Lienqueo, M. E., Cubillos, F. and Herrera, L. (2000). Kinetic modeling of iron precipitation as jarosite in leaching solutions using *Thiobacillus ferroxidans*.

Castro, L., Blázquez, M. L., González, F., Muñoz, J. A. and Ballester, A. (2018). Heavy metal adsorption using biogenic iron compounds. *Hydrometallurgy,* 179, 44-51.

Choppala, G. and Burton, E. D. (2018). Chromium (III) substitution inhibits the Fe (II)-accelerated transformation of schwertmannite. *PloS one,* 13, e0208355.

Chowdhury, F. (2012). *The effect of temperature on the kinetics of microbial ferrous-iron oxidation in a packed column bioreactor.* Cape Peninsula University of Technology.

Chowdhury, F. and Ojumu, T. (2014). Investigation of ferrous-iron biooxidation kinetics by *Leptospirillum ferriphilum* in a novel packed-column bioreactor: Effects of temperature and jarosite accumulation. *Hydrometallurgy,* 141, 36-42.

Chukwuchendo, E. C. and Ojumu, T. V. (2017). Microbial Ferrous Ion Oxidation versus Ferric Ion Precipitation at Low Temperature Conditions. *Solid State Phenomena,* 262, 381-384.

Coates, J. (2000). Interpretation of infrared spectra, a practical approach. *Encyclopedia of Analytical Chemistry*.

Cogram, P. F. (2017). *Capacity and mechanisms of uptake of silver by jarosite family minerals.* Birkbeck, University of London.

Coram, N. J. and Rawlings, D. E. (2002). Molecular relationship between two groups of the genus Leptospirillum and the finding that *Leptospirillum ferriphilum* sp. nov. dominates South African commercial biooxidation tanks that operate at 40 °C. *Applied and Environmental Microbiology,* 68, 838-845.

Córdoba, E., Muñoz, J., Blázquez, M., González, F. and Ballester, A. (2008a). Leaching of chalcopyrite with ferric ion. Part I: General aspects. *Hydrometallurgy,* 93, 81-87.

Córdoba, E., Muñoz, J., Blázquez, M., González, F. and Ballester, A. (2008b). Leaching of chalcopyrite with ferric ion. Part II: Effect of redox potential. *Hydrometallurgy,* 93, 88-96.

Cornell, R. M. and Schwertmann, U. (2003a). *The iron oxides: structure, properties, reactions, occurrences and uses*: John Wiley & Sons.

Cornell, R. M. and Schwertmann, U. (2003b). *The iron oxides: structure, properties, reactions, occurrences, and uses* (Vol. 2): Wiley-vch Weinheim.

Coughlin, B. R. and Stone, A. T. (1995). Nonreversible adsorption of divalent metal ions (MnII, CoII, NiII, CuII, and PbII) onto goethite: effects of acidification, FeII addition, and picolinic acid addition. *Environmental Science & Technology,* 29, 2445-2455.

Craddock, P. T. (1995). *Early metal mining and production*.

Daoud, J. and Karamanev, D. (2006). Formation of jarosite during Fe^{2+} oxidation by *Acidithiobacillus ferrooxidans*. *Minerals Engineering,* 19, 960-967.

Das, G., Acharya, S., Anand, S. and Das, R. (1996). Jarosites: a review. *Mineral Processing and Extractive Metullargy Review,* 16, 185-210.

Das, S., Natarajan, G. and Ting, Y.-P. (2017). *Bio-extraction of precious metals from urban solid waste.* Paper presented at the AIP Conference Proceedings.

Deng, S., He, G., Bichao, W. and Guohua, G. (2020). Pyrite-promoted dissolution of arsenopyrite in the presence of *Sulfobacillus thermosulfidooxidans*. *Journal of Materials Research and Technology,* 9, 9362-9371.

Desborough, G. A., Smith, K. S., Lowers, H. A., Swayze, G. A., Hammarstrom, J. M., Diehl, S. F., Leinz, R. W. and Driscoll, R. L. (2010). Mineralogical and chemical characteristics of some natural jarosites. *Geochimica et Cosmochimica Acta,* 74, 1041-1056.

Deveci, H., Akcil, A. and Alp, I. (2004). Bioleaching of complex zinc sulphides using mesophilic and thermophilic bacteria: comparative importance of pH and iron. *Hydrometallurgy,* 73, 293-303.

Dou, X., Mohan, D. and Pittman Jr, C. U. (2013). Arsenate adsorption on three types of granular schwertmannite. *Water Research,* 47, 2938-2948.

Dreisinger, D. and Abed, N. (2002). A fundamental study of the reductive leaching of chalcopyrite using metallic iron part I: kinetic analysis. *Hydrometallurgy,* 66, 37-57.

Drouet, C. and Navrotsky, A. (2003). Synthesis, characterization, and thermochemistry of K-Na-H_3O jarosites. *Geochimica et Cosmochimica Acta,* 67, 2063-2076.

Dupin, J.-C., Gonbeau, D., Vinatier, P. and Levasseur, A. (2000). Systematic XPS studies of metal oxides, hydroxides and peroxides. *Physical Chemistry Chemical Physics,* 2, 1319-1324.

Dutrizac, J. (1982). *Jarosite-type compounds and their application in the metallurgical industry.* Paper presented at the JOURNAL OF METALS.

Dutrizac, J. (1989). Elemental sulphur formation during the ferric sulphate leaching of chalcopyrite. *Canadian Metallurgical Quarterly,* 28, 337-344.

Dutrizac, J. (2008). Factors affecting the precipitation of potassium jarosite in sulfate and chloride media. *Metallurgical and Materials Transactions B,* 39, 771-783.

Dutrizac, J. E. and Jambor, J. L. (2000). Jarosites and their application in hydrometallurgy. *Reviews in Mineralogy and Geochemistry,* 40, 405-452.

Ehrlich, H. L. (2001). Past, present and future of biohydrometallurgy. *Hydrometallurgy,* 59, 127-134.

Fantauzzi, M., Elsener, B., Atzei, D., Rigoldi, A. and Rossi, A. (2015). Exploiting XPS for the identification of sulfides and polysulfides. *RSC Advances,* 5, 75953-75963.

Feng, K., Wang, X., Zhou, B., Xu, M., Liang, J. and Zhou, L. (2021). Hydroxyl, Fe^{2+}, and *Acidithiobacillus ferrooxidans* Jointly Determined the Crystal Growth and Morphology of Schwertmannite in a Sulfate-Rich Acidic Environment. *ACS omega,* 6, 3194-3201.

Feng, S., Yang, H., Xin, Y., Gao, K., Yang, J., Liu, T., Zhang, L. and Wang, W. (2013). A novel and highly efficient system for chalcopyrite bioleaching by mixed strains of Acidithiobacillus. *Bioresource Technology,* 129, 456-462.

Fernandes, M. M. and Baeyens, B. (2019). Cation exchange and surface complexation of lead on montmorillonite and illite including competitive adsorption effects. *Applied Geochemistry*, 100, 190-202.

Ford, R. G., Bertsch, P. M. and Farley, K. J. (1997). Changes in transition and heavy metal partitioning during hydrous iron oxide aging. *Environmental Science & Technology,* 31, 2028-2033.

Francisco, P. C. M., Sato, T., Otake, T., Kasama, T., Suzuki, S., Shiwaku, H. and Yaita, T. (2018). Mechanisms of Se (IV) co-precipitation with ferrihydrite at acidic and alkaline conditions and its behavior during aging. *Environmental Science & Technology,* 52, 4817-4826.

Freundlich, H. (1906). Over the adsorption in solution. *Journal of Physical Chemistry,* 57, 1100-1107.

Fu, B., Zhou, H., Zhang, R. and Qiu, G. (2008). Bioleaching of chalcopyrite by pure and mixed cultures of *Acidithiobacillus spp.* and *Leptospirillum ferriphilum*. *International Biodeterioration & Biodegradation,* 62, 109-115.

Fu, K.-b., Lin, H., Mo, X.-l., Wang, H., Wen, H.-w. and Wen, Z.-l. (2012). Comparative study on the passivation layers of copper sulphide minerals during bioleaching. *International Journal of Minerals, Metallurgy, and Materials,* 19, 886-892.

Gaboreau, S. and Vieillard, P. (2004). Prediction of Gibbs free energies of formation of minerals of the alunite supergroup. *Geochimica et Cosmochimica Acta,* 68, 3307-3316.

Ganta, P. B., Morshedizad, M., Kühn, O., Leinweber, P. and Ahmed, A. A. (2021). The Binding of Phosphorus Species at Goethite: A Joint Experimental and Theoretical Study. *Minerals,* 11, 323.

Gao, J., Zhang, C.-G., Wu, X.-L., Wang, H.-H. and Qiu, G.-Z. (2007). Isolation and identification of a strain of *Leptospirillum ferriphilum* from an extreme acid mine drainage site. *Annals of microbiology,* 57, 171-176.

Gasharova, B., Göttlicher, J. and Becker, U. (2005). Dissolution at the surface of jarosite: an in situ AFM study. *Chemical Geology,* 215, 499-516.

Gautier, V., Escobar, B. and Vargas, T. (2008). Cooperative action of attached and planktonic cells during bioleaching of chalcopyrite with *Sulfolobus metallicus* at 70 ^{o}C. *Hydrometallurgy,* 94, 121-126.

Gentina, J. C. and Acevedo, F. (2013). Application of bioleaching to copper mining in Chile. *Electronic Journal of Biotechnology,* 16, 16-16.

Ghorbani, Y., Becker, M., Mainza, A., Franzidis, J.-P. and Petersen, J. (2011). Large particle effects in chemical/biochemical heap leach processes–A review. *Minerals Engineering,* 24, 1172-1184.

Ghorbani, Y., Franzidis, J.-P. and Petersen, J. (2016). Heap leaching technology—current state, innovations, and future directions: a review. *Mineral Processing and Extractive Metallurgy Review,* 37, 73-119.

Gramp, J. P., Jones, F. S., Bigham, J. M. and Tuovinen, O. H. (2008). Monovalent cation concentrations determine the types of Fe (III) hydroxysulfate precipitates formed in bioleach solutions. *Hydrometallurgy,* 94, 29-33.

Grishin, S. I., Bigham, J. M. and Tuovinen, O. H. (1988). Characterization of jarosite formed upon bacterial oxidation of ferrous sulfate in a packed-bed reactor. *Applied Environmental Microbiology,* 54, 3101-3106.

Gu, G., Hu, K., Zhang, X., Xiong, X. and Yang, H. (2013). The stepwise dissolution of chalcopyrite bioleached by *Leptospirillum ferriphilum*. *Electrochimica Acta,* 103, 50-57.

Guo, H. and Barnard, A. S. (2013). Naturally occurring iron oxide nanoparticles: morphology, surface chemistry and environmental stability. *Journal of Materials Chemistry A,* 1, 27-42.

Guo, X.-y., Zhang, L., Tian, Q.-h. and Qin, H. (2020). Stepwise extraction of gold and silver from refractory gold concentrate calcine by thiourea. *Hydrometallurgy,* 194, 105330.

Guo, X., Dong, H., Yang, C., Zhang, Q., Liao, C., Zha, F. and Gao, L. (2016). Application of goethite modified biochar for tylosin removal from aqueous solution. *Colloids and Surfaces A: Physicochemical and Engineering Aspects,* 502, 81-88.

Gupta, S. S. and Bhattacharyya, K. G. (2011). Kinetics of adsorption of metal ions on inorganic materials: a review. *Advances in Colloid and Interface Science,* 162, 39-58.

Hackl, R., Dreisinger, D., Peters, l. and King, J. (1995). Passivation of chalcopyrite during oxidative leaching in sulfate media. *Hydrometallurgy,* 39, 25-48.

Han, H., Sun, W., Hu, Y., Jia, B. and Tang, H. (2014). Anglesite and silver recovery from jarosite residues through roasting and sulfidization-flotation in zinc hydrometallurgy. *Journal of Hazardous materials,* 278, 49-54.

Hernández-Lazcano, E., Cerecedo-Sáenz, E., Hernández-Ávila, J., Toro, N., Karthik, T., Mendoza-Anaya, D., Fernández-García, M., Rodríguez-Lugo, V. and Salinas-Rodríguez, E. (2021). Synthesis of hydronium-potassium jarosites: the effect of pH and aging time on their structural, morphological, and electrical properties. *Minerals,* 11, 80.

Hevira, L., Ighalo, J. O. and Zein, R. (2020). Biosorption of indigo carmine from aqueous solution by *Terminalia catappa* shell. *Journal of Environmental Chemical Engineering,* 8, 104290.

Hill, C. G. and Root, T. W. (2014). *Introduction to chemical engineering kinetics and reactor design*: John Wiley & Sons.

Holzwarth, U. and Gibson, N. (2011). The Scherrer equation versus the'Debye-Scherrer equation'. *Nature nanotechnology,* 6, 534-534.

Hredzak, S., Matik, M., Lovas, M., Briancin, J., Stefusova, K. and Zubrik, A. (2014). Research on Pyrite Occurrence and Properties in Talc Ore with the Aim of Its Removal. *Inżynieria Mineralna,* 15.

Hu, S., Lu, Y., Peng, L., Wang, P., Zhu, M., Dohnalkova, A. C., Chen, H., Lin, Z., Dang, Z. and Shi, Z. (2018). Coupled kinetics of ferrihydrite transformation and As (V) sequestration under the effect of humic acids: a mechanistic and quantitative study. *Environmental Science & Technology,* 52, 11632-11641.

Huang, H., Wang, J., Yao, R., Bostick, B. C., Prommer, H., Liu, X. and Sun, J. (2020). Effects of divalent heavy metal cations on the synthesis and characteristics of magnetite. *Chemical Geology,* 547, 119669.

Igwegbe, C. A., Onukwuli, O. D., Ighalo, J. O. and Okoye, P. U. (2020). Adsorption of cationic dyes on Dacryodes edulis seeds activated carbon modified using phosphoric acid and sodium chloride. *Environmental Processes,* 7, 1151-1171.

Jaiswal, A., Banerjee, S., Mani, R. and Chattopadhyaya, M. (2013). Synthesis, characterization and application of goethite mineral as an adsorbent. *Journal of Environmental Chemical Engineering,* 1, 281-289.

Jambor, J. L. (1999). Nomenclature of the alunite supergroup. *The Canadian Mineralogist,* 37, 1323-1341.

Jensen, A. B. and Webb, C. (1995). Ferrous sulphate oxidation using *Thiobacillus ferrooxidan*s: a review. *Process Biochemistry,* 30, 225-236.

Jeon, B.-H., Dempsey, B. A., Burgos, W. D. and Royer, R. A. (2003). Sorption kinetics of Fe (II), Zn (II), Co (II), Ni (II), Cd (II), and Fe (II)/Me (II) onto hematite. *Water Research,* 37, 4135-4142.

Jiang, H. and Lawson, F. (2004). Reaction mechanism for the formation of ammonium jarosite: thermodynamic studies and experimental evidence. *Mineral Processing and Extractive Metallurgy,* 113, 175-181.

Jiménez, A., Hernández, A. and Prieto, M. (2019). Crystallization behaviour of iron-hydroxide sulphates by aging under ambient temperature conditions. *Minerals,* 9, 27.

Jin, J., Shi, S.-y., Liu, G.-l., Zhang, Q.-h. and Cong, W. (2013). Comparison of Fe^{2+} oxidation by *Acidithiobacillus ferrooxidans* in rotating-drum and stirred-tank reactors. *Transactions of the Nonferrous Metals Society of China,* 23, 804-811.

Johnson, D. B. (2009). Extremophiles: acidic environments. *The desk encyclopedia of microbiology*, 463-480.

Johnston, C. P. and Chrysochoou, M. (2016). Mechanisms of chromate, selenate, and sulfate adsorption on Al-substituted ferrihydrite: implications for ferrihydrite surface structure and reactivity. *Environmental Science & Technology,* 50, 3589-3596.

Jolivet, J.-P., Chanéac, C. and Tronc, E. (2004). Iron oxide chemistry. From molecular clusters to extended solid networks. *Chemical Communications*, 481-483.

Jones, C. A. and Kelly, D. (1983). Growth of *Thiobacillus ferrooxidans* on ferrous iron in chemostat culture: influence of product and substrate inhibition. *Journal of Chemical Technology and Biotechnology. Biotechnology,* 33, 241-261.

Jones, F. S., Bigham, J. M., Gramp, J. P. and Tuovinen, O. H. (2014). Synthesis and properties of ternary (K, NH_4, H_3O)-jarosites precipitated from *Acidithiobacillus ferrooxidans* cultures in simulated bioleaching solutions. *Materials Science and Engineering: C,* 44, 391-399.

Ju, S., Zhang, Y., Zhang, Y., Xue, P. and Wang, Y. (2011). Clean hydrometallurgical route to recover zinc, silver, lead, copper, cadmium and iron from hazardous jarosite residues produced during zinc hydrometallurgy. *Journal of Hazardous materials,* 192, 554-558.

Kaksonen, A. H., Boxall, N. J., Gumulya, Y., Khaleque, H. N., Morris, C., Bohu, T., Cheng, K. Y., Usher, K. M. and Lakaniemi, A.-M. (2018). Recent progress in biohydrometallurgy and microbial characterisation. *Hydrometallurgy,* 180, 7-25.

Kaksonen, A. H., Morris, C., Li, J., Wylie, J., Usher, K., Hilario, F. and du Plessis, C. (2019). The fate and impact of contaminants in a biological iron oxidation and jarosite precipitation process. *Minerals Engineering,* 132, 258-267.

Kaksonen, A. H., Morris, C., Rea, S., Li, J., Usher, K. M., McDonald, R. G., Hilario, F., Hosken, T., Jackson, M. and du Plessis, C. A. (2014a). Biohydrometallurgical iron oxidation and precipitation: Part II—Jarosite precipitate characterisation and acid recovery by conversion to hematite. *Hydrometallurgy,* 147, 264-272.

Kaksonen, A. H., Morris, C., Rea, S., Li, J., Wylie, J., Usher, K. M., Ginige, M. P., Cheng, K. Y., Hilario, F. and du Plessis, C. A. (2014b). Biohydrometallurgical iron oxidation and precipitation: part I—effect of pH on process performance. *Hydrometallurgy,* 147, 255-263.

Kakuta, S., Numata, T. and Okayama, T. (2014). Shape effects of goethite particles on their photocatalytic activity in the decomposition of acetaldehyde. *Catalysis Science & Technology,* 4, 164-169.

Karimian, N., Johnston, S. G. and Burton, E. D. (2018). Antimony and arsenic partitioning during Fe^{2+}-induced transformation of jarosite under acidic conditions. *Chemosphere,* 195, 515-523.

Karthikeyan, K., Elliott, H. A. and Cannon, F. S. (1997). Adsorption and coprecipitation of copper with the hydrous oxides of iron and aluminum. *Environmental Science & Technology,* 31, 2721-2725.

Keeling, S., Palmer, M., Caracatsanis, F., Johnson, J. and Watling, H. (2005). Leaching of chalcopyrite and sphalerite using bacteria enriched from a spent chalcocite heap. *Minerals Engineering,* 18, 1289-1296.

Kendall, M. R., Madden, A. S., Madden, M. E. E. and Hu, Q. (2013). Effects of arsenic incorporation on jarosite dissolution rates and reaction products. *Geochimica et Cosmochimica Acta,* 112, 192-207.

Khoshkhoo, M., Dopson, M., Shchukarev, A. and Sandström, Å. (2014). Chalcopyrite leaching and bioleaching: an X-ray photoelectron spectroscopic (XPS) investigation on the nature of hindered dissolution. *Hydrometallurgy,* 149, 220-227.

Kinnunen, P. H. M. and Puhakka, J. A. (2004). High-rate ferric sulfate generation by a *Leptospirillum ferriphilum*-dominated biofilm and the role of jarosite in biomass retainment in a fluidized-bed reactor. *Biotechnology and Bioengineering,* 85, 683-694.

Klauber, C. (2008). A critical review of the surface chemistry of acidic ferric sulphate dissolution of chalcopyrite with regards to hindered dissolution. *International Journal of Mineral Processing,* 86, 1-17.

Knorr, K.-H. and Blodau, C. (2007). Controls on schwertmannite transformation rates and products. *Applied Geochemistry,* 22, 2006-2015.

Koleini, S. J., Aghazadeh, V. and Sandström, Å. (2011). Acidic sulphate leaching of chalcopyrite concentrates in presence of pyrite. *Minerals Engineering,* 24, 381-386.

Kubisz, J. (1971). Studies on synthetic alkali-hydronium jarosites. II. Thermal investigations. *Mineralogia Polonica,* 2, 51-59.

Kumar, B., Smita, K., Sánchez, E., Stael, C. and Cumbal, L. (2016). Andean Sacha inchi (*Plukenetia volubilis* L.) shell biomass as new biosorbents for Pb^{2+} and Cu^{2+} ions. *Ecological Engineering,* 93, 152-158.

Lacey, D. and Lawson, F. (1970). Kinetics of the liquid-phase oxidation of acid ferrous sulfate by the bacterium *Thiobacillus ferrooxidens*. *Biotechnology and Bioengineering,* 12, 29-50.

Lagergren, S. K. (1898). About the theory of so-called adsorption of soluble substances. *Sven. Vetenskapsakad. Handingarl,* 24, 1-39.

Langmuir, I. (1916). The constitution and fundamental properties of solids and liquids. Part I. Solids. *Journal of the American Chemical Society,* 38, 2221-2295.

Lavina, B., Salviulo, G. and Della Giusta, A. (2002). Cation distribution and structure modelling of spinel solid solutions. *Physics and Chemistry of Minerals,* 29, 10-18.

Lazaroff, N., Sigal, W. and Wasserman, A. (1982). Iron oxidation and precipitation of ferric hydroxysulfates by resting *Thiobacillus ferrooxidans* cells. *Applied Environmental Microbiology,* 43, 924-938.

Leduc, L., Trevors, J. and Ferroni, G. (1993). Thermal characterization of different isolates of *Thiobacillus ferrooxidans*. *FEMS Microbiology Letters,* 108, 189-193.

Lee, G., Bigham, J. M. and Faure, G. (2002). Removal of trace metals by coprecipitation with Fe, Al and Mn from natural waters contaminated with acid mine drainage in the Ducktown Mining District, Tennessee. *Applied Geochemistry,* 17, 569-581.

Li, J., Zhang, B., Yang, M. and Lin, H. (2021). Bioleaching of vanadium by *Acidithiobacillus ferrooxidans* from vanadium-bearing resources: Performance and mechanisms. *Journal of Hazardous materials,* 416, 125843.

Li, X., Wei, C., Deng, Z., Li, C., Fan, G., Rong, H. and Zhang, F. (2015). Extraction and separation of indium and copper from zinc residue leach liquor by solvent extraction. *Separation and Purification Technology,* 156, 348-355.

Li, Y., Kawashima, N., Li, J., Chandra, A. and Gerson, A. R. (2013). A review of the structure, and fundamental mechanisms and kinetics of the leaching of chalcopyrite. *Advances in Colloid and Interface Science,* 197, 1-32.

Li, Y., Wei, G., Liang, X., Zhang, C., Zhu, J. and Arai, Y. (2020). Metal Substitution-Induced Reducing Capacity of Magnetite Coupled with Aqueous Fe (II). *ACS Earth and Space Chemistry,* 4, 905-911.

Liang, X., Zhong, Y., Zhu, S., He, H., Yuan, P., Zhu, J. and Jiang, Z. (2013). The valence and site occupancy of substituting metals in magnetite spinel structure $Fe_{3-x}M_xO_4$ (M=

Cr, Mn, Co and Ni) and their influence on thermal stability: An XANES and TG-DSC investigation. *Solid State Sciences,* 15, 115-122.

Liao, R., Yang, B., Huang, X., Hong, M., Yu, S., Liu, S., Wang, J. and Qiu, G. (2021). Combined effect of silver ion and pyrite on AMD formation generated by chalcopyrite bio-dissolution. *Chemosphere,* 279, 130516.

Liao, Y., Zhou, L., Liang, J. and Xiong, H. (2009). Biosynthesis of schwertmannite by *Acidithiobacillus ferrooxidans* cell suspensions under different pH condition. *Materials Science and Engineering: C,* 29, 211-215.

Lima, É. C., Adebayo, M. A. and Machado, F. M. (2015). Kinetic and equilibrium models of adsorption *Carbon nanomaterials as adsorbents for environmental and biological applications* (pp. 33-69): Springer.

Lima, E. C., Cestari, A. R. and Adebayo, M. A. (2016). Comments on the paper: a critical review of the applicability of Avrami fractional kinetic equation in adsorption-based water treatment studies. *Desalination and Water Treatment,* 57, 19566-19571.

Linge, H. (1976). A study of chalcopyrite dissolution in acidic ferric nitrate by potentiometric titration. *Hydrometallurgy,* 2, 51-64.

Liu, C., Ju, S., Zhang, L., Srinivasakannan, C., Peng, J., Le, T. and Guo, Z. (2017). Recovery of valuable metals from jarosite by sulphuric acid roasting using microwave and water leaching. *Canadian Metallurgical Quarterly,* 56, 1-9.

Liu, H.-c., Xia, J.-l. and Nie, Z.-y. (2015). Relatedness of Cu and Fe speciation to chalcopyrite bioleaching by *Acidithiobacillus ferrooxidans*. *Hydrometallurgy,* 156, 40-46.

Liu, H., Lu, X., Li, M., Zhang, L., Pan, C., Zhang, R., Li, J. and Xiang, W. (2018). Structural incorporation of manganese into goethite and its enhancement of Pb (II) adsorption. *Environmental Science & Technology,* 52, 4719-4727.

Liu, H., Xia, J., Nie, Z., Ma, C., Zheng, L., Hong, C., Zhao, Y. and Wen, W. (2016a). Bioleaching of chalcopyrite by *Acidianus manzaensis* under different constant pH. *Minerals Engineering,* 98, 80-89.

Liu, J.-s., Li, B.-m., Zhong, D.-y., Xia, L.-x. and Qiu, G.-z. (2007). Preparation of jarosite by *Acidithiobacillus ferrooxidans* oxidation. *Journal of Central South University of Technology,* 14, 623-628.

Liu, J.-y., Xiu, X.-x. and Cai, P. (2009). Study of formation of jarosite mediated by *Thiobacillus ferrooxidans* in 9K medium. *Procedia Earth and Planetary Science,* 1, 706-712.

Liu, J., Zhu, R., Xu, T., Xu, Y., Ge, F., Xi, Y., Zhu, J. and He, H. (2016b). Co-adsorption of phosphate and zinc (II) on the surface of ferrihydrite. *Chemosphere,* 144, 1148-1155.

Lotfalian, M., Ranjbar, M., Fazaelipoor, M., Schaffie, M. and Manafi, Z. (2015). The effect of redox control on the continuous bioleaching of chalcopyrite concentrate. *Minerals Engineering,* 81, 52-57.

Lv, L., Huang, Y. and Cao, D. (2018). Nitrogen-doped porous carbons with ultrahigh specific surface area as bifunctional materials for dye removal of wastewater and supercapacitors. *Applied Surface Science,* 456, 184-194.

Lv, X., Wang, J., Zeng, X., Liang, Z., He, D., Zhang, Y., Yuan, H., Zhao, H. and Meng, Q. (2021). Cooperative extraction of metals from chalcopyrite by bio-oxidation and chemical oxidation. *Geochemistry,* 81, 125772.

Ma, P., Yang, H., Luan, Z., Sun, Q., Ali, A. and Tong, L. (2021). Leaching of chalcopyrite under bacteria–mineral contact/noncontact leaching model. *Minerals,* 11, 230.

Mabusela, B. (2017). *The effect of initial pH on surface properties of ferric ion precipitates formed during microbial oxidation of ferrous ion by Leptospirillum ferriphilum in a CSTR.* Cape Peninsula University of Technology.

Mabusela, B. and Ojumu, T. V. (2017). *The Effect of Initial Solution pH on Surface Properties of Ferric Ion Precipitates Formed during Biooxidation of Ferrous Ion by Leptospirillum ferriphilum.* Paper presented at the Solid State Phenomena.

Mahmood, T., Saddique, M. T., Naeem, A., Westerhoff, P., Mustafa, S. and Alum, A. (2011). Comparison of different methods for the point of zero charge determination of NiO. *Industrial & Engineering Chemistry Research,* 50, 10017-10023.

Maleki, M., Moradi, O. and Tahmasebi, S. (2017). Adsorption of albumin by gold nanoparticles: Equilibrium and thermodynamics studies. *Arabian Journal of Chemistry,* 10, S491-S502.

Malenga, E. N., Mulaba-Bafubiandi, A. and Nheta, W. (2015). Alkaline leaching of nickel bearing ammonium jarosite precipitate using KOH, NaOH and NH_4OH in the presence of EDTA and Na_2S. *Hydrometallurgy,* 155, 69-78.

Manceau, A., Schlegel, M., Musso, M., Sole, V., Gauthier, C., Petit, P. and Trolard, F. (2000). Crystal chemistry of trace elements in natural and synthetic goethite. *Geochimica et Cosmochimica Acta,* 64, 3643-3661.

Masaki, Y., Hirajima, T., Sasaki, K., Miki, H. and Okibe, N. (2018). Microbiological redox potential control to improve the efficiency of chalcopyrite bioleaching. *Geomicrobiology Journal,* 35, 648-656.

Mazuelos, A., Carranza, F., Romero, R., Iglesias, N. and Villalobo, E. (2010). Operational pH in packed-bed reactors for ferrous ion bio-oxidation. *Hydrometallurgy,* 104, 186-192.

McCarthy, S., Ai, C. and Blum, P. (2018). Enhancement of Metallosphaera sedula bioleaching by targeted recombination and adaptive laboratory evolution *Advances in Applied Microbiology* (Vol. 104, pp. 135-165): Elsevier.

Meng, S., Wang, H., Liu, H., Yang, C., Wei, Y. and Hou, D. (2014). Evaluation of the ability of ferrihydrite to bind heavy metal ions: Based on formation environment, adsorption reversibility and ageing. *Applied Geochemistry,* 45, 114-119.

Meruane, G. and Vargas, T. (2003). Bacterial oxidation of ferrous iron by *Acidithiobacillus ferrooxidans* in the pH range 2.5–7.0. *Hydrometallurgy,* 71, 149-158.

Michel, F. M., Ehm, L., Antao, S. M., Lee, P. L., Chupas, P. J., Liu, G., Strongin, D. R., Schoonen, M. A., Phillips, B. L. and Parise, J. B. (2007). The structure of ferrihydrite, a nanocrystalline material. *Science,* 316, 1726-1729.

Mirabello, G., Lenders, J. J. and Sommerdijk, N. A. (2016). Bioinspired synthesis of magnetite nanoparticles. *Chemical Society Reviews,* 45, 5085-5106.

Mousavi, S., Yaghmaei, S., Salimi, F. and Jafari, A. (2006). Influence of process variables on biooxidation of ferrous sulfate by an indigenous *Acidithiobacillus ferrooxidans*. Part I: Flask experiments. *Fuel,* 85, 2555-2560.

Munagapati, V. S., Yarramuthi, V., Nadavala, S. K., Alla, S. R. and Abburi, K. (2010). Biosorption of Cu (II), Cd (II) and Pb (II) by *Acacia leucocephala* bark powder: Kinetics, equilibrium and thermodynamics. *Chemical Engineering Journal,* 157, 357-365.

Munoz, P., Miller, J. D. and Wadsworth, M. E. (1979). Reaction mechanism for the acid ferric sulfate leaching of chalcopyrite. *Metallurgical Transactions B,* 10, 149-158.

Murphy, P. J., Smith, A. M., Hudson-Edwards, K. A., Dubbin, W. E. and Wright, K. (2009). Raman and IR spectroscopic studies of alunite-supergroup compounds containing Al, Cr^{3+}, Fe^{3+} and V^{3+} at the B site. *The Canadian Mineralogist,* 47, 663-681.

Nazari, B., Jorjani, E., Hani, H., Manafi, Z. and Riahi, A. (2014). Formation of jarosite and its effect on important ions for *Acidithiobacillus ferrooxidans* bacteria. *Transactions of Nonferrous Metals Society of China,* 24, 1152-1160.

Nemati, M., Harrison, S., Hansford, G. and Webb, C. (1998). Biological oxidation of ferrous sulphate by *Thiobacillus ferrooxidans*: a review on the kinetic aspects. *Biochemical Engineering Journal,* 1, 171-190.

Ngoma, I.-M. E. (2015). *Investigating the effect of acid stress on selected mesophilic bioleaching microorganisms.* Cape Peninsula University of Technology.

Nheta, W. and Makhatha, M. E. (2013). *Leaching of nickel from a jarosite precipitate with hydrochloric acid*.

Nourmohamadi, H., Esrafili, M. D. and Aghazadeh, V. (2021). DFT study of ferric ion interaction with passive layer on chalcopyrite surface: Elemental sulfur, defective sulfur and replacement of M^{2+} (M= Cu and Fe) ions. *Computational Condensed Matter,* 26, e00536.

Nurmi, P., Özkaya, B., Kaksonen, A., Tuovinen, O. and Puhakka, J. (2009). Inhibition kinetics of iron oxidation by *Leptospirillum ferriphilum* in the presence of ferric, nickel and zinc ions. *Hydrometallurgy,* 97, 137-145.

Nurmi, P., Özkaya, B., Sasaki, K., Kaksonen, A. H., Riekkola-Vanhanen, M., Tuovinen, O. H. and Puhakka, J. A. (2010). Biooxidation and precipitation for iron and sulfate removal from heap bioleaching effluent streams. *Hydrometallurgy,* 101, 7-14.

Ojumu, T. V. (2008). *The effects of solution conditions on the kinetics of microbial ferrous-iron oxidation by Leptospirillum ferriphilum in continuous culture.* University of Cape Town.

Ojumu, T. V., Hansford, G. S. and Petersen, J. (2009). The kinetics of ferrous-iron oxidation by *Leptospirillum ferriphilum* in continuous culture: the effect of temperature. *Biochemical Engineering Journal,* 46, 161-168.

Ojumu, T. V. and Petersen, J. (2011). The kinetics of ferrous ion oxidation by *Leptospirillum ferriphilum* in continuous culture: The effect of pH. *Hydrometallurgy,* 106, 5-11.

Oladipo, B., Akintunde, A. M., Ajala, S. O., Olatunji, S. O., Falowo, O. A. and Betiku, E. (2020). Phytoextraction of Heavy Metals from Complex Industrial Waste Disposal Sites *Methods for Bioremediation of Water and Wastewater Pollution* (pp. 341-371): Springer

Oladipo, B., Govender-Opitz, E. and Ojumu, T. V. (2021a). Kinetics, Thermodynamics, and Mechanism of Cu (II) Ion Sorption by Biogenic Iron Precipitate: Using the Lens of Wastewater Treatment to Diagnose a Typical Biohydrometallurgical Problem. *ACS Omega*.

Oladipo, B., Ibrahim, T. H., Ajala, S. O., Akintunde, A. M., Taiwo, A. E. and Betiku, E. (2021b). Synthesis of Activated Carbons for Heavy Metals Removal *Green Adsorbents to Remove Metals, Dyes and Boron from Polluted Water* (pp. 1-31): Springer

Olson, G., Brierley, J. and Brierley, C. (2003). Bioleaching review part B. *Applied Microbiology and Biotechnology*, 63, 249-257.

Panda, S., Akcil, A., Pradhan, N. and Deveci, H. (2015). Current scenario of chalcopyrite bioleaching: A review on the recent advances to its heap-leach technology. *Bioresource Technology*, 196, 694-706.

Paredes-Quevedo, L. C., Castellanos, N. J. and Carriazo, J. G. (2021). Influence of Porosity and Surface Area of a Modified Kaolinite on the Adsorption of Basic Red 46 (BR-46). *Water, Air, & Soil Pollution*, 232, 1-17.

Parker, A., Klauber, C., Kougianos, A., Watling, H. and Van Bronswijk, W. (2003). An X-ray photoelectron spectroscopy study of the mechanism of oxidative dissolution of chalcopyrite. *Hydrometallurgy*, 71, 265-276.

Parker, A., Paul, R. and Power, G. (1981). Electrochemistry of the oxidative leaching of copper from chalcopyrite. *Journal of Electroanalytical Chemistry and Interfacial Electrochemistry*, 118, 305-316.

Parkman, R., Charnock, J., Bryan, N., Livens, F. and Vaughan, D. (1999). Reactions of copper and cadmium ions in aqueous solution with goethite, lepidocrocite, mackinawite, and pyrite. *American Mineralogist*, 84, 407-419.

Penev, K. and Karamanev, D. (2010). Batch kinetics of ferrous iron oxidation by *Leptospirillum ferriphilum* at moderate to high total iron concentration. *Biochemical Engineering Journal*, 50, 54-62.

Peng, T., Chen, L., Wang, J., Miao, J., Shen, L., Yu, R., Gu, G., Qiu, G. and Zeng, W. (2019). Dissolution and passivation of chalcopyrite during bioleaching by *Acidithiobacillus ferrivorans* at low temperature. *Minerals,* 9, 332.

Perez, J. P. H., Tobler, D. J., Thomas, A. N., Freeman, H. M., Dideriksen, K., Radnik, J. r. and Benning, L. G. (2019). Adsorption and reduction of arsenate during the Fe^{2+}-induced transformation of ferrihydrite. *ACS Earth and Space Chemistry,* 3, 884-894.

Petersen, J. and Ojumu, T. V. (2007). *The effect of total iron concentration and iron speciation on the rate of ferrous iron oxidation kinetics of Leptospirillum ferriphilum in continuous tank systems.* Paper presented at the Advanced Materials Research.

Petrasova, K., Faryad, S. W., Jerabek, P. and Zackova, E. (2007). Origin and metamorphic evolution of magnesite-talc and adjacent rocks near Gemerská Poloma, Slovak Republic. *Journal of Geosciences,* 52, 125-132.

Pina, P. d. S., Leão, V. A., Silva, C. A. d., Daman, D. and Frenay, J. (2005). The effect of ferrous and ferric iron on sphalerite bioleaching with *Acidithiobacillus sp*. *Minerals Engineering,* 18, 549-551.

Qiao, X., Liu, L., Shi, J., Zhou, L., Guo, Y., Ge, Y., Fan, W. and Liu, F. (2017). Heating changes bio-schwertmannite microstructure and arsenic (III) removal efficiency. *Minerals,* 7, 9.

Qiu, M.-q., Xiong, S.-y., Zhang, W.-m. and Wang, G.-x. (2005). A comparison of bioleaching of chalcopyrite using pure culture or a mixed culture. *Minerals Engineering,* 18, 987-990.

Randall, S., Sherman, D., Ragnarsdottir, K. and Collins, C. R. (1999). The mechanism of cadmium surface complexation on iron oxyhydroxide minerals. *Geochimica et Cosmochimica Acta,* 63, 2971-2987.

Rao, C., Sarma, D. and Hegde, M. (1980). A novel approach to the study of surface oxidation states and oxidation of transition metals by Auger electron spectroscopy. *Proceedings of the Royal Society of London. A. Mathematical and Physical Sciences,* 370, 269-280.

Rawlings, D. E. (2002). Heavy metal mining using microbes. *Annual Reviews in Microbiology,* 56, 65-91.

Rawlings, D. E. (2005). Characteristics and adaptability of iron-and sulfur-oxidizing microorganisms used for the recovery of metals from minerals and their concentrates. *Microbial cell factories,* 4, 1-15.

Rawlings, D. E., Dew, D. and du Plessis, C. (2003). Biomineralization of metal-containing ores and concentrates. *Trends in Biotechnology,* 21, 38-44.

Rodriguez, N. R., Machiels, L., Onghena, B., Spooren, J. and Binnemans, K. (2020). Selective recovery of zinc from goethite residue in the zinc industry using deep-eutectic solvents. *RSC Advances,* 10, 7328-7335.

Rohwerder, T., Gehrke, T., Kinzler, K. and Sand, W. (2003). Bioleaching review part A. *Applied Microbiology and Biotechnology,* 63, 239-248.

Rohwerder, T. and Schippers, A. (2007). Microorganisms involved in bioleaching and nucleic acid-based molecular methods for their identification and quantification. In Donati, E. R. andSand, W. (Eds.), *Microbial Processing of Metal Sulfides* (pp. 3-33). Dordrecht, Netherlands: Springer.

Rouchalova, D., Rouchalova, K., Janakova, I., Cablik, V. and Janstova, S. (2020). Bioleaching of iron, copper, lead, and zinc from the sludge mining sediment at different particle sizes, pH, and pulp density using *Acidithiobacillus ferrooxidans*. *Minerals*, 10, 1013.

Ruan, R., Liu, X., Zou, G., Chen, J., Wen, J. and Wang, D. (2011). Industrial practice of a distinct bioleaching system operated at low pH, high ferric concentration, elevated temperature and low redox potential for secondary copper sulfide. *Hydrometallurgy,* 108, 130-135.

Ruan, R., Zhong, S. and Wang, D. (2010). Life cycle assessment of two copper metallurgical processes: bio-heap leaching and flotation-flash smelting. *Multipurpose Utilization of Mineral Resources,* 3, 33-37.

Ruthven, D. M. (1984). *Principles of adsorption and adsorption processes*: John Wiley & Sons.

Rzepa, G., Bajda, T., Gaweł, A., Debiec, K. and Drewniak, L. (2016). Mineral transformations and textural evolution during roasting of bog iron ores. *Journal of Thermal Analysis and Calorimetry,* 123, 615-630.

Saha, P. and Chowdhury, S. (2011). Insight into adsorption thermodynamics. *Thermodynamics,* 16, 349-364.

Sánchez-España, J. and Reyes, J. (2019). Comparing schwertmannite and hydrobasaluminite dissolution in ammonium oxalate (pH 3.0): implications for metal speciation studies by sequential extraction. *Minerals,* 9, 57.

Sand, W., Gehrke, T., Jozsa, P.-G. and Schippers, A. (2001). (Bio) chemistry of bacterial leaching—direct vs. indirect bioleaching. *Hydrometallurgy,* 59, 159-175.

Sandström, Å., Shchukarev, A. and Paul, J. (2005). XPS characterisation of chalcopyrite chemically and bio-leached at high and low redox potential. *Minerals Engineering,* 18, 505-515.

Sasaki, K. and Konno, H. (2000). Morphology of jarosite-group compounds precipitated from biologically and chemically oxidized Fe ions. *The Canadian Mineralogist,* 38, 45-56.

Sasaki, K., Nakamuta, Y., Hirajima, T. and Tuovinen, O. (2009). Raman characterization of secondary minerals formed during chalcopyrite leaching with *Acidithiobacillus ferrooxidans*. *Hydrometallurgy,* 95, 153-158.

Sasaki, K., Sakimoto, T., Endo, M. and Konno, H. (2006). FE-SEM study of microbially formed jarosites by *Acidithiobacillus ferrooxidans*. *Materials transactions,* 47, 1155-1162.

Sasaki, K., Tanaike, O. and Konno, H. (1998). Distinction of jarosite-group compounds by Raman spectroscopy. *The Canadian Mineralogist,* 36, 1225-1235.

Savage, K. S., Bird, D. K. and O'Day, P. A. (2005). Arsenic speciation in synthetic jarosite. *Chemical Geology,* 215, 473-498.

Schippers, A. (2007). Microorganisms involved in bioleaching and nucleic acid-based molecular methods for their identification and quantification *Microbial processing of metal sulfides* (pp. 3-33): Springer.

Schippers, A. and Sand, W. (1999). Bacterial leaching of metal sulfides proceeds by two indirect mechanisms via thiosulfate or via polysulfides and sulfur. *Applied and Environmental Microbiology,* 65, 319-321.

Schwertmann, U. and Murad, E. (1983). Effect of pH on the formation of goethite and hematite from ferrihydrite. *Clays and Clay Minerals,* 31, 277-284.

Sebastian, A., Nangia, A. and Prasad, M. (2019). Cadmium and sodium adsorption properties of magnetite nanoparticles synthesized from Hevea brasiliensis Muell.

Arg. bark: Relevance in amelioration of metal stress in rice. *Journal of Hazardous materials,* 371, 261-272.

Shannon, R. (1974). Handbook of Chemistry and Physics. *Acta Cryst. A,* 32, 751-767.

Shaw, S., Pepper, S. E., Bryan, N. D. and Livens, F. R. (2005). The kinetics and mechanisms of goethite and hematite crystallization under alkaline conditions, and in the presence of phosphate. *American Mineralogist,* 90, 1852-1860.

Shi, M., Min, X., Ke, Y., Lin, Z., Yang, Z., Wang, S., Peng, N., Yan, X., Luo, S. and Wu, J. (2020). Recent progress in understanding the mechanism of heavy metals retention by iron (oxyhydr) oxides. *Science of the Total Environment*, 141930.

Silverstein, R. M., Webster, F. X., Kiemle, D. J. and Bryce, D. L. (2014). *Spectrometric identification of organic compounds*: John Wiley & Sons

Sing, K. S. (1985). Reporting physisorption data for gas/solid systems with special reference to the determination of surface area and porosity (Recommendations 1984). *Pure and Applied Chemistry,* 57, 603-619.

Siow, K. S., Britcher, L., Kumar, S. and Griesser, H. J. (2018). XPS study of sulfur and phosphorus compounds with different oxidation states. *Sains Malaysiana,* 47, 1913-1922.

Smith, A. M., Hudson-Edwards, K. A., Dubbin, W. E. and Wright, K. (2006). Dissolution of jarosite [$KFe_3(SO_4)_2(OH)_6$] at pH 2 and 8: Insights from batch experiments and computational modelling. *Geochimica et Cosmochimica Acta,* 70, 608-621.

Smith, K. S. (1999). Metal sorption on mineral surfaces: an overview with examples relating to mineral deposits. *Reviews in economic geology,* 6, 161-182.

Smith, S. L. and Johnson, D. B. (2018). Growth of *Leptospirillum ferriphilum* in sulfur medium in co-culture with *Acidithiobacillus caldus*. *Extremophiles,* 22, 327-333.

Sokić, M. D., Marković, B. and Živković, D. (2009). Kinetics of chalcopyrite leaching by sodium nitrate in sulphuric acid. *Hydrometallurgy,* 95, 273-279.

Song, J., Jia, S.-Y., Ren, H.-T., Wu, S.-H. and Han, X. (2015). Application of a high-surface-area schwertmannite in the removal of arsenate and arsenite. *International Journal of Environmental Science and Technology,* 12, 1559-1568.

Spratt, H. J., Rintoul, L., Avdeev, M. and Martens, W. N. (2013). The crystal structure and vibrational spectroscopy of jarosite and alunite minerals. *American Mineralogist,* 98, 1633-1643.

Tang, C., Shu, Y., Zhang, R., Li, X., Song, J., Li, B., Zhang, Y. and Ou, D. (2017). Comparison of the removal and adsorption mechanisms of cadmium and lead from aqueous solution by activated carbons prepared from *Typha angustifolia* and *Salix matsudana*. *RSC advances,* 7, 16092-16103.

Tang, L., Tang, C., Xiao, J., Zeng, P. and Tang, M. (2018). A cleaner process for valuable metals recovery from hydrometallurgical zinc residue. *Journal of Cleaner Production,* 201, 764-773.

Tao, H. and Dongwei, L. (2014). Presentation on mechanisms and applications of chalcopyrite and pyrite bioleaching in biohydrometallurgy–a presentation. *Biotechnology Reports,* 4, 107-119.

Third, K., Cord-Ruwisch, R. and Watling, H. (2002). Control of the redox potential by oxygen limitation improves bacterial leaching of chalcopyrite. *Biotechnology and Bioengineering,* 78, 433-441.

ThomasArrigo, L. K., Kaegi, R. and Kretzschmar, R. (2019). Ferrihydrite growth and transformation in the presence of ferrous iron and model organic ligands. *Environmental Science & Technology,* 53, 13636-13647.

Tokoro, C., Yatsugi, Y., Koga, H. and Owada, S. (2010). Sorption mechanisms of arsenate during coprecipitation with ferrihydrite in aqueous solution. *Environmental Science & Technology,* 44, 638-643.

Tran, H. N., You, S.-J. and Chao, H.-P. (2016). Thermodynamic parameters of cadmium adsorption onto orange peel calculated from various methods: A comparison study. *Journal of Environmental Chemical Engineering,* 4, 2671-2682.

Tran, H. N., You, S.-J., Hosseini-Bandegharaei, A. and Chao, H.-P. (2017). Mistakes and inconsistencies regarding adsorption of contaminants from aqueous solutions: a critical review. *Water Research,* 120, 88-116.

van Hille, R. P., van Zyl, A. W., Spurr, N. R. and Harrison, S. T. (2010). Investigating heap bioleaching: Effect of feed iron concentration on bioleaching performance. *Minerals Engineering,* 23, 518-525.

Van, H. T., Nguyen, L. H., Nguyen, X. H., Nguyen, T. H., Nguyen, T. V., Vigneswaran, S., Rinklebe, J. and Tran, H. N. (2019). Characteristics and mechanisms of cadmium adsorption onto biogenic aragonite shells-derived biosorbent: Batch and column studies. *Journal of Environmental Management,* 241, 535-548.

Velásquez-Yévenes, L., Nicol, M. and Miki, H. (2010). The dissolution of chalcopyrite in chloride solutions: Part 1. The effect of solution potential. *Hydrometallurgy,* 103, 108-113.

Vilcáez, J., Suto, K. and Inoue, C. (2008). Bioleaching of chalcopyrite with thermophiles: temperature–pH–ORP dependence. *International Journal of Mineral Processing,* 88, 37-44.

Villalobos, M., Trotz, M. A. and Leckie, J. O. (2003). Variability in goethite surface site density: evidence from proton and carbonate sorption. *Journal of Colloid and Interface Science,* 268, 273-287.

Viramontes-Gamboa, G., Peña-Gomar, M. M. and Dixon, D. G. (2010). Electrochemical hysteresis and bistability in chalcopyrite passivation. *Hydrometallurgy,* 105, 140-147.

Viramontes-Gamboa, G., Rivera-Vasquez, B. F. and Dixon, D. G. (2007). The active-passive behavior of chalcopyrite comparative study between electrochemical and leaching responses. *Journal of the Electrochemical Society,* 154, C299-C311.

Vishniac, W. and Santer, M. (1957). The thiobacilli. *Bacteriological Reviews,* 21, 195-213.

Volesky, B. (2007). Biosorption and me. *Water Research,* 41, 4017-4029.

Vu, H. P., Shaw, S., Brinza, L. and Benning, L. G. (2010). Crystallization of hematite (α-Fe_2O_3) under alkaline condition: The effects of Pb. *Crystal growth & design,* 10, 1544-1551.

Wang, H., Bigham, J. M. and Tuovinen, O. H. (2006). Formation of schwertmannite and its transformation to jarosite in the presence of acidophilic iron-oxidizing microorganisms. *Materials Science and Engineering: C,* 26, 588-592.

Wang, J., Gan, X., Zhao, H., Hu, M., Li, K., Qin, W. and Qiu, G. (2016a). Dissolution and passivation mechanisms of chalcopyrite during bioleaching: DFT calculation, XPS and electrochemistry analysis. *Minerals Engineering,* 98, 264-278.

Wang, X., Zhu, M., Koopal, L. K., Li, W., Xu, W., Liu, F., Zhang, J., Liu, Q., Feng, X. and Sparks, D. L. (2016b). Effects of crystallite size on the structure and magnetism of ferrihydrite. *Environmental Science: Nano,* 3, 190-202.

Wang, Y.-y., Yang, H.-f., Jiang, B., Song, R.-l. and Zhang, W.-h. (2018). Comprehensive recovery of lead, zinc, and iron from hazardous jarosite residues using direct reduction followed by magnetic separation. *International Journal of Minerals, Metallurgy, and Materials,* 25, 123-130.

Wang, Y., Su, L., Zhang, L., Zeng, W., Wu, J., Wan, L., Qiu, G., Chen, X. and Zhou, H. (2012). Bioleaching of chalcopyrite by defined mixed moderately thermophilic consortium including a marine acidophilic halotolerant bacterium. *Bioresource Technology,* 121, 348-354.

Wang, Z., Xiao, D., Bush, R. T. and Liu, J. (2015). Coprecipitated arsenate inhibits thermal transformation of 2-line ferrihydrite: Implications for long-term stability of ferrihydrite. *Chemosphere,* 122, 88-93.

Wang, Z., Xiao, D., Liu, R., Guo, Y. and Liu, J. (2014). Fenton-like degradation of reactive dyes catalyzed by biogenic jarosite. *Journal of Advanced Oxidation Technologies,* 17, 104-108.

Wanjiya, M., Chowdhury, F. and Ojumu, T. V. (Cartographer). (2015). Solution pH and jarosite management during ferrous iron biooxidation in a novel packed-column bioreactor.

Warren, G., Wadsworth, M. and El-Raghy, S. (1992). Passive and transpassive anodic behavior of chalcopyrite in acid solutions. *Journal of Electronic Materials,* 21, 571-579.

Watling, H., Elliot, A., Maley, M., Van Bronswijk, W. and Hunter, C. (2009). Leaching of a low-grade, copper–nickel sulfide ore. 1. Key parameters impacting on Cu recovery during column bioleaching. *Hydrometallurgy,* 97, 204-212.

Watling, H. R. (2015). Review of biohydrometallurgical metals extraction from polymetallic mineral resources. *Minerals,* 5, 1-60.

Weatherill, J. S. (2018). *Iron Oxyhydroxide Formation in the Enhanced Actinide Removal Plant*: The University of Manchester (United Kingdom).

Weber, T. W. and Chakravorti, R. K. (1974). Pore and solid diffusion models for fixed-bed adsorbers. *AIChE Journal,* 20, 228-238.

Weber, W. J. and Morris, J. C. (1963). Kinetics of adsorption on carbon from solution. *Journal of the Sanitary Engineering Division,* 89, 31-60.

Wei, H., Dong, F., Chen, M., Zhang, W., He, M. and Liu, M. (2020). Removal of uranium by biogenetic jarosite coupled with photoinduced reduction in the presence of oxalic acid: a low-cost remediation technology. *Journal of Radioanalytical and Nuclear Chemistry,* 324, 715-729.

Welch, S. A., Christy, A. G., Kirste, D., Beavis, S. G. and Beavis, F. (2007). Jarosite dissolution I—Trace cation flux in acid sulfate soils. *Chemical Geology,* 245, 183-197.

Welch, S. A., Kirste, D., Christy, A. G., Beavis, F. R. and Beavis, S. G. (2008). Jarosite dissolution II—Reaction kinetics, stoichiometry and acid flux. *Chemical Geology,* 254, 73-86.

Wells, M., Fitzpatrick, R. W. and Gilkes, R. (2006). Thermal and mineral properties of Al-, Cr-, Mn-, Ni-and Ti-substituted goethite. *Clays and Clay Minerals,* 54, 176-194.

Wiltner, A. and Linsmeier, C. (2008). Thermally induced reaction and diffusion of carbon films on Ni (1 1 1) and Ni (1 0 0). *Surface Science,* 602, 3623-3631.

Wu, C., Chen, H., Hong, W., Li, D., Liang, P., Fang, J., Zhang, L. and Lai, C. (2019). Magnetite chemistry and implications for the magmatic-hydrothermal ore-forming process: An example from the Devonian Yuleken porphyry Cu system, NW China. *Chemical Geology,* 522, 1-15.

Wu, Z.-l., Zou, L.-c., Chen, J.-h., Lai, X.-k. and Zhu, Y.-g. (2016). Column bioleaching characteristic of copper and iron from Zijinshan sulfide ores by acid mine drainage. *International Journal of Mineral Processing,* 149, 18-24.

Xiu, W., Guo, H., Zhou, X., Wanty, R. B. and Kersten, M. (2018). Change of arsenite adsorption mechanism during aging of 2-line ferrihydrite in the absence of oxygen. *Applied Geochemistry,* 88, 149-157.

Xu, Z., Lǔ, B., Wu, J., Zhou, L. and Lan, Y. (2013). Reduction of Cr (VI) facilitated by biogenetic jarosite and analysis of its influencing factors with response surface methodology. *Materials Science and Engineering: C,* 33, 3723-3729.

Yang, B., Zhao, C., Luo, W., Liao, R., Gan, M., Wang, J., Liu, X. and Qiu, G. (2020). Catalytic effect of silver on copper release from chalcopyrite mediated by *Acidithiobacillus ferrooxidans*. *Journal of Hazardous materials,* 392, 122290.

Yang, C., Jiao, F. and Qin, W. (2018). Co-bioleaching of chalcopyrite and silver-bearing bornite in a mixed moderately thermophilic culture. *Minerals,* 8, 4.

Yin, G., Song, X., Tao, L., Sarkar, B., Sarmah, A. K., Zhang, W., Lin, Q., Xiao, R., Liu, Q. and Wang, H. (2020). Novel Fe-Mn binary oxide-biochar as an adsorbent for removing Cd (II) from aqueous solutions. *Chemical Engineering Journal,* 389, 124465.

Yin, S., Wang, L., Kabwe, E., Chen, X., Yan, R., An, K., Zhang, L. and Wu, A. (2018). Copper bioleaching in China: Review and prospect. *Minerals,* 8, 32.

Yu, R.-L., Zhong, D.-L., Lei, M., Wu, F.-D., Qiu, G.-Z. and Gu, G.-H. (2011). Relationship and effect of redox potential, jarosites and extracellular polymeric substances in bioleaching chalcopyrite by *Acidithiobacillus ferrooxidans*. *Transactions of Nonferrous Metals Society of China,* 21, 1634-1640.

Zeng, W.-m., Peng, Y.-p., Peng, T.-j., Nan, M.-h., Chen, M., Qiu, G.-z. and Shen, L. (2020). Electrochemical studies on dissolution and passivation behavior of low temperature bioleaching of chalcopyrite by *Acidithiobacillus ferrivorans* YL15. *Minerals Engineering,* 155, 106416.

Zeng, W., Qiu, G., Zhou, H. and Chen, M. (2011). Electrochemical behaviour of massive chalcopyrite electrodes bioleached by moderately thermophilic microorganisms at 48 C. *Hydrometallurgy,* 105, 259-263.

Zhan, Y., Shen, X., Chen, M., Yang, K. and Xie, H. (2021). Bioleaching of tellurium from mine tailings by indigenous *Acidithiobacillus ferrooxidans*. *Letters in Applied Microbiology*.

Zhang, H., Wei, D., Liu, W., Hou, D. and Zhang, R. (2021a). Effect of polyvinyl pyrrolidone on chalcopyrite bioleaching with *Acidithiobacillus ferrooxidans*. *Hydrometallurgy,* 205, 105753.

Zhang, J., Zhang, C., Wei, G., Li, Y., Liang, X., Chu, W., He, H., Huang, D., Zhu, J. and Zhu, R. (2017). Reduction removal of hexavalent chromium by zinc-substituted magnetite coupled with aqueous Fe (II) at neutral pH value. *Journal of Colloid and Interface Science,* 500, 20-29.

Zhang, L., Guo, X.-y., Tian, Q.-h., Zhong, S.-p. and Qin, H. (2021b). Extraction of gold from typical Carlin gold concentrate by pressure oxidation pretreatment-Sodium jarosite decomposition and polysulfide leaching. *Hydrometallurgy*, 105743.

Zhang, L., Wu, J., Wang, Y., Wan, L., Mao, F., Zhang, W., Chen, X. and Zhou, H. (2014). Influence of bioaugmentation with *Ferroplasma thermophilum* on chalcopyrite bioleaching and microbial community structure. *Hydrometallurgy,* 146, 15-23.

Zhang, W.-M. and Gu, S.-F. (2007). Catalytic effect of activated carbon on bioleaching of low-grade primary copper sulflde ores. *Transactions of Nonferrous Metals Society of China,* 17, 1123-1127.

Zhao, F. and Wang, S. (2019). Bioleaching of electronic waste using extreme acidophiles *Electronic Waste Management and Treatment Technology* (pp. 153-174): Elsevier.

Zhao, H.-b., Jun, W., Qin, W.-q., Zheng, X.-h., Lang, T., Gan, X.-w. and Qiu, G.-z. (2015). Surface species of chalcopyrite during bioleaching by moderately thermophilic bacteria. *Transactions of Nonferrous Metals Society of China,* 25, 2725-2733.

Zhao, H., Zhang, Y., Zhang, X., Qian, L., Sun, M., Yang, Y., Zhang, Y., Wang, J., Kim, H. and Qiu, G. (2019). The dissolution and passivation mechanism of chalcopyrite in bioleaching: An overview. *Minerals Engineering*, 136, 140-154.

Zhao, R., Li, Y. and Chan, C. K. (2016). Synthesis of jarosite and Vanadium jarosite analogues using microwave hydrothermal reaction and evaluation of composition-dependent electrochemical properties. *The Journal of Physical Chemistry C,* 120, 9702-9712.

Zhou, H.-B., Zeng, W.-M., Yang, Z.-F., Xie, Y.-J. and Qiu, G.-Z. (2009). Bioleaching of chalcopyrite concentrate by a moderately thermophilic culture in a stirred tank reactor. *Bioresource Technology*, 100, 515-520.

Zhu, J., Gan, M., Zhang, D., Hu, Y. and Chai, L. (2013). The nature of Schwertmannite and Jarosite mediated by two strains of *Acidithiobacillus ferrooxidans* with different ferrous oxidation ability. *Materials Science and Engineering: C,* 33, 2679-2685.

Zhu, M., Legg, B., Zhang, H., Gilbert, B., Ren, Y., Banfield, J. F. and Waychunas, G. A. (2012). Early stage formation of iron oxyhydroxides during neutralization of simulated acid mine drainage solutions. *Environmental Science & Technology,* 46, 8140-8147.

Zhu, W., Xia, J.-l., Yang, Y., Nie, Z.-y., Zheng, L., Ma, C.-y., Zhang, R.-y., Peng, A.-a., Tang, L. and Qiu, G.-z. (2011). Sulfur oxidation activities of pure and mixed thermophiles and sulfur speciation in bioleaching of chalcopyrite. *Bioresource Technology,* 102, 3877-3882.

Zolotov, M. Y. and Shock, E. L. (2005). Formation of jarosite-bearing deposits through aqueous oxidation of pyrite at Meridiani Planum, Mars. *Geophysical Research Letters*, 32.

APPENDICES

Appendix A: Reagents preparation and determination of concentration of iron species

A1.1 Reagents preparation

A1.1.1 Vishniac Trace Metal Solution

Vishniac Trace Metal Solution was prepared according to the method suggested by Vishniac and Santer (1957).

Weigh the reagents accurately and dilute to 1 L volume with distilled water (dH_2O).

- Prepare 6% potassium hydroxide (KOH) by weighing 15 g KOH and diluting to 250 mL with dH_2O.
- Dissolve 50 g EDTA (Ethylenediaminetetraacetic acid disodium salt dihydrate) in 200 mL of 6% KOH using a magnetic stirrer.
- In a separate 500 mL beaker weigh the salts listed below and dissolve in 400 mL dH_2O for 30 minutes using a magnetic stirrer.

Table A.1: Chemical list for Vishniac Trace metal solution

Chemical	Amount (g)
$ZnSO_4.7H_2O$	22.00
$CaCl_2.2H_2O$	9.24
$MnCl_2.4H_2O$	5.06
$FeSO4.7H_2O$	5.00
$(NH_4)_6Mo_7O_{24}.4H_2O$	1.10
$CuSO_4.5H_2O$	1.58
$CoCl_2.6H_2O$	1.62

- Transfer the solution prepared in Step 2 quantitatively into the solution prepared in step 3 and makeup to 1 L with dH_2O by rinsing the 500 mL beaker with 400 mL dH_2O. A deep greenish-brown solution should result.

A1.1.2 Spekker acid

The spekker acid solution was prepared by mixing equal volumes of concentrated sulfuric acid (98% H_2SO_4) and phosphoric acid (85%) with water in a ratio of 3:4 (acid solution:distilled water).

- Measure 600 mL distilled water using a 2 L beaker.
- Carefully add 225 mL of concentrated sulfuric acid (98%) and 225 mL of phosphoric acid (85%) by slowly pouring the acid mixture against the wall of the beaker (caution: rapid addition of the acid mixture to the distilled water will result in heat of mixing which will cause localized boiling, especially when using concentrated H_2SO_4).
- Allow the mixture to cool to room temperature before transferring into a storage bottle.

A1.1.3 Ferric acid

The ferric acid solution was prepared from the spekker acid:

- Measure 600 mL distilled water using a 2 L beaker.
- Slowly and carefully add 150 mL of spekker acid and then 300 mL of concentrated hydrochloric acid (32% HCl) to the distilled water.
- Agitate the mixture using a magnetic stirrer and allow to cool to room temperature before transferring into a storage bottle.

A1.1.4 Stannous chloride solution ($SnCl_2$)

- Weigh out 30 g stannous chloride in a 200 mL beaker.
- Add 100 mL concentrated hydrochloric acid (32%) and agitate at 50 °C until it dissolves completely.
- Allow to cool to room temperature and dilute with 200 mL distilled water.
- Add a small amount of granular tin to the solution to retard precipitation.

A1.1.5 Mercuric Chloride solution ($HgCl_2$)

- Weigh out 50 g mercuric chloride in a 2 L beaker.
- Add 1 L of distilled water and agitate until the solute has dissolved completely (about 2 hours).
- Add a spatula tip of $HgCl_2$ and stir for 2 h before storage.

A1.1.6 Potassium Dichromate solution (0.0149 M $K_2Cr_2O_7$)

- Dry approximately 10 g of $K_2Cr_2O_7$ (molar mass, 294.20 $g.mol^{-1}$) in an oven at 105 – 110 °C for 1 – 2 h. Cool in a desiccator.
- Accurately weigh out 8.78 g of the dried $K_2Cr_2O_7$ into a 100 mL beaker.
- Transfer quantitatively into a 2 L beaker.
- Add 1.5 L of distilled water and agitate until dissolved completely.
- Transfer quantitatively into a 2 L standard volumetric flask and fill to the 2 L mark with distilled water.

A1.1.7 Barium Diphenylamine Sulphonate (BDS) solution ($C_{24}H_{20}BaN_2O_6S_2$)

- Weigh out 1.0 g of barium diphenylamine sulphonate in a 250 mL beaker and add 100 mL of concentrated sulfuric acid (98%). Agitate until the solute has dissolved completely.

A1.2 Determination of ferrous ion concentration by titration with potassium dichromate solution

- Pipette 5 mL of the required aliquot solution into a 125 mL conical flask.
- Add 10 mL of spekker acid solution.
- Add 2 – 3 drops of BDS indicator.
- Titrate the potassium dichromate (0.0149 M $K_2Cr_2O_7$) solution until the first permanent colour change from yellow to intense purple is obtained.

Ferrous-ion concentration may be calculated using Equation A1.1:

$$[Fe^{2+}] = \frac{[K_2Cr_2O_7] \times V_T \times (55.84 \times 6)}{V_{solution}} \quad \text{(A1.1)}$$

Where, $[Fe^{2+}]$ = Ferrous-ion concentration ($g.L^{-1}$)

$K_2Cr_2O_7$ = $K_2Cr_2O_7$ concentration (i.e. 0.0149 M $K_2Cr_2O_7$)

V_T = Titration volume (mL) (amount of 0.0149 M $K_2Cr_2O_7$ added)

$V_{solution}$ = Solution aliquot volume (mL)

A1.3 Determination of total iron concentration by titration with potassium dichromate solution

- Filter 5 mL aliquot of sample solution.
- Pipette the required amount of aliquot (i.e. 5 mL) into a 125 mL conical flask.
- Add 10 mL of spekker acid solution and heat until the mixture boils.
- Add stannous ($SnCl_2$) solution dropwise until the yellow colour disappears completely. Add one extra drop and record the amount of stannous chloride added (note: It is important to record this amount, especially when doing duplicate titrations since it gives some an idea of the amount of $SnCl_2$ required for the next duplicate titrations).
- Allow the solution to cool to room temperature and add 10 mL of mercuric chloride ($HgCl_2$) solution. A silky-white precipitate should appear. If no precipitate forms, too little stannous chloride was added in step 4. If the precipitate is heavy and grey/black, too much stannous chloride was added. In either case, abort the experiment and start over.
- Add 3 – 4 drops of barium diphenylamine indicator solution (BDS) and titrate with the potassium dichromate solution until the first permanent colour change from yellow to intense purple is obtained.

Total iron concentration may be calculated using Equation A1.2:

$$[Fe^{T}] = \frac{[K_2Cr_2O_7] \times V_T \times (55.84 \times 6)}{V_{solution}} \quad \text{(A1.2)}$$

where, $[Fe^T]$ = Total iron concentration ($g.L^{-1}$)

$K_2Cr_2O_7$ = $K_2Cr_2O_7$ concentration (i.e. 0.0149 M $K_2Cr_2O_7$)

V_T = Titration volume (mL) (amount of 0.0149 M $K_2Cr_2O_7$ added)

$V_{solution}$ = Solution aliquot volume (mL)

Appendix B: Standard table and graph

Table B.1: Cu(II) standard table

Concentration (mg/L)	Absorbance
0	0
200	0.147
400	0.286
600	0.411
800	0.541
1000	0.668

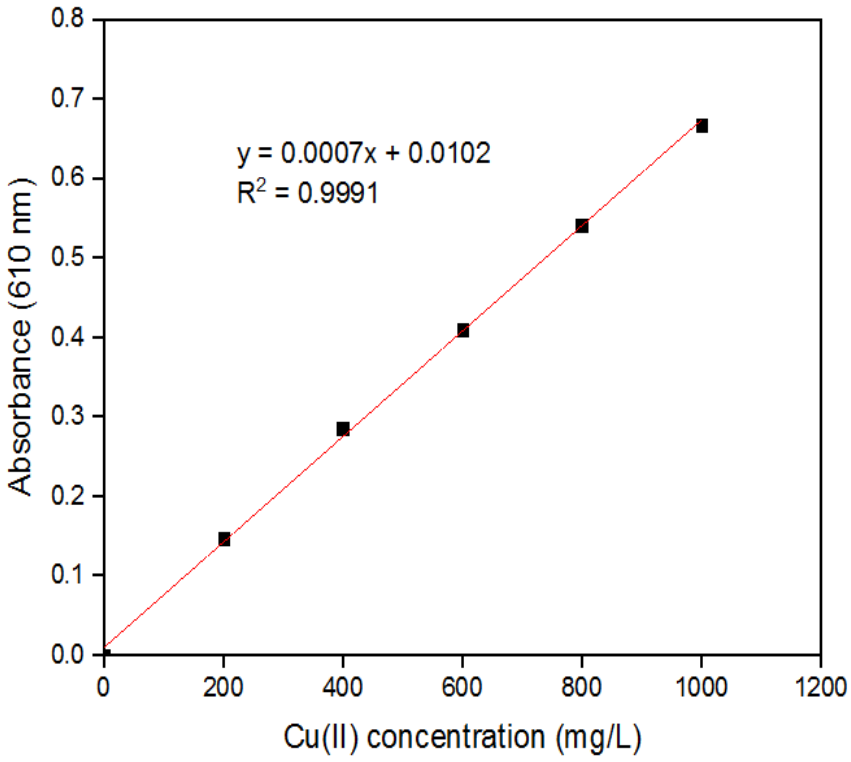

Figure B.1: Graph of absorbance at 610 nm against initial copper concentration (mg/L)

DNA concentration and relative abundance for microbial speciation at the start and completion of experiment

	Universal Bacteria	*Leptospirillum ferriphilum*	*Acidithiobacillus caldus*	Universal Archaea	*Acidiplasma cupricumulans*	*Ferroplasma acidiphilum*	*Archaea (JTC1/2)*	*Cuniculiplasma divulgatum*
Start of experiments	7.25E+06	4.60E+06	2.66E+06	4.76E+05	3.93E+05	1.04E+04	3.20E+05	2.93E+05
Completion of experiments	3.77E+04	5.41E+03	1.79E+02	1.26E+05	0.00E+00	1.05E+03	3.02E+05	2.79E+06

Relative abundance of microorganisms

	Leptospirillum ferriphilum	*Acidithiobacillus caldus*	*Acidiplasma cupricumulans*	*Ferroplasma acidiphilum*	*Archaea (JTC1/2 – Thermoplasmatales)*	*Cuniculiplasma divulgatum*	Bacteria other
Start of experiments	55.5	32.2	4.7	0.1	3.9	3.5	0.0
Completion of experiments	0.2	0.0	0.0	0.0	9.7	89.1	1.0